

**Theoretical and Experimental Investigation of  
Alternative Cathode Catalysts for Proton  
Exchange Membrane Fuel Cells**

Irina Sergeyevna Flyagina

Submitted in accordance with the requirements for the degree of  
Doctor of Philosophy

The University of Leeds  
Energy Technology Innovation Initiative  
Faculty of Engineering

September, 2014



The candidate confirms that the work submitted is her own, except where work which has formed part of jointly authored publications has been included. The contribution of the candidate and the other authors to this work has been explicitly indicated below.

The work in Chapter 3 has appeared in publication as follows:

I. S. Flyagina, K. J. Hughes, M. Pourkashanian, D. B. Ingham, A Theoretical Study of Molecular Oxygen Chemisorption on N, B, or O Doped Carbon Edge Sites, Fuel Cells: From Fundamentals to Systems, 2013.

The work in Chapter 4 has appeared in publication as follows:

I. S. Flyagina, K. J. Hughes, M. Pourkashanian, D. B. Ingham, DFT Study of the Oxygen Reduction Reaction on Iron, Cobalt and Manganese Macrocyclic Active Sites, International Journal of Hydrogen Energy, 2014.

The work in these publications is the candidate's own. Other authors contributed by assisting in the interpretation of the results as well as writing of the papers.

The candidate confirms that appropriate credit has been given within the thesis where reference has been made to the work of others.

This copy has been supplied on the understanding that it is copyright material and that no quotation from the thesis may be published without proper acknowledgement.

The right of Irina S. Flyagina to be identified as Author of this work has been asserted by her in accordance with the Copyright, Designs and Patents Act 1988.



## Acknowledgements

I express my deepest appreciation to Dr. Nikolay B. Abramov (De Montfort University) who supported me and advised at the most challenging stages of the PhD project. My sincere gratitude is to Dr. Sergey P. Dolin (Kurnakov Institute of General and Inorganic Chemistry of Russian Academy of Sciences) who shared with me his profound knowledge in quantum chemistry, helped to design theoretical studies and discuss the results of molecular modelling, and Dr. Alexander A. Markov for consulting on the techniques of computational chemistry. My sincere thanks are also to Detlev C. Mielczarek (University of Leeds) for his active help in procurement and commissioning of the equipment for the project as well as for continuous IT support. Without their invaluable help this dissertation would not have been possible.

I would like to thank the Energy Technology and Innovation Initiative supervisory team: Dr. Kevin J. Hughes, Prof. Mohamed Pourkashanian and Prof. Derek B. Ingham for their continuous help and organisational support. I am also grateful to research technicians Mr. Paul Crosby, Gurdev S. Bhogal and Mr. Mohammed Javed for their prompt help. I thank Prof. Animesh Jha for expressing his interest in my work and broadening the scope of the dissertation, and Prof. Alan Williams for the very helpful discussion of my transfer report. I am also grateful to Dr. Timothy P. Comyn for introducing me to the X-ray diffraction, Dr. Adrian M. Cunliffe, Mr. Simon R. Lloyd and Mr. Peter Thompson for providing laboratory equipment and technical advice on experiments, Dr. Benjamin R. G. Johnson for conducting and explaining the X-ray photoelectron spectroscopy analyses, and Mr. Stuart L. Micklethwaite for conducting the electron microscopy measurements. A special gratitude is to Dr. Mohammed Ismail, my colleague in the fuel cell team, for effective cooperation and sharing his research experience with me. I would also like to thank my friends and colleagues: Davide A. Poggio, James I. Erete, Nahla E. Al-Hazmi, Andrew Dixon, and Dr. Richard M. Gunton (University of Leeds) for their inspiration and help.

Besides my University colleagues and advisors, I would especially like to thank Mr. John Booth (Scientific and Medical Products Ltd.) who introduced me to the key electrochemical techniques and taught operating the electrochemical equipment. I am also very grateful to my family and especially to my grandmother Tamara M. Flyagina for counselling and encouraging throughout my work. Last but not least, I wish to thank the sponsoring company NetScientific Plc. for the sustained financial support.



## Abstract

Proton exchange membrane (PEM) fuel cells offer the potential to provide both efficient and clean energy with the flexibility of conventional energy sources, especially for mobile applications. One of the hurdles impeding the wide-spread use of PEM fuel cells is the high cost of the platinum-based catalysts along with their low durability. A significant reduction of PEM fuel cells costs can be achieved through the development of an alternative low-cost cathode catalyst, which forms the objective of the present thesis.

The theoretical part of the thesis is dedicated to modelling of the active sites in the alternative carbon based catalysts and the oxygen reduction reaction with the aid of computational chemistry methods. The catalyst active sites have been simulated as heteroatom doped graphene and transition metal macrocycles. In doped graphene, the effect of edge and basal planes has been investigated by modelling molecular oxygen chemisorption on a number of possible active sites. The entire mechanistic pathways of the oxygen reduction have been simulated on the surface of the transition metal macrocycles with either an iron, cobalt or manganese central atom.

The experimental part of this thesis focuses on the development and assessment of alternative cathode catalysts for PEM fuel cells. Nitrogen and phosphorus doped carbon catalysts have been synthesized to investigate the effect of heteroatom doping of carbon. In addition, alternative non-carbon catalyst materials have been tested as catalyst supports. The investigated supports have been electrically conductive titanium nitride, tungsten carbide and multiwall carbon nanotubes, and non-conductive silica, titanium dioxide, molecular sieves and faujazite. The activity of synthesized catalysts has been evaluated by electrochemical characterisation while the surface composition of the catalysts has been investigated using physicochemical methods, namely, XRD, XPS, and SEM. Finally, the activity of selected catalysts has been assessed through testing two catalyst candidates in a small scale PEM fuel cell.



## Table of Contents

<b>Acknowledgements .....</b>	<b>v</b>
<b>Abstract .....</b>	<b>vii</b>
<b>Table of Contents .....</b>	<b>ix</b>
<b>List of Figures.....</b>	<b>xv</b>
<b>List of Tables.....</b>	<b>xxv</b>
<b>List of Abbreviations.....</b>	<b>xxvii</b>
<b>Chapter 1 Introduction to Fuel Cells.....</b>	<b>1</b>
1.1 Basic Principle of Fuel Cells .....	2
1.2 Fuel Cell Types and Applications .....	3
1.2.1 Solid Oxide Fuel Cells .....	5
1.2.2 Alkaline Fuel Cells .....	6
1.2.3 Phosphoric Acid Fuel Cells.....	7
1.2.4 Molten Carbonate Fuel Cells.....	8
1.2.5 Direct Methanol Fuel Cells .....	9
1.2.6 Proton Exchange Membrane Fuel Cells.....	10
1.3 Components of Proton Exchange Membrane Fuel Cells .....	11
1.3.1 Membrane.....	11
1.3.2 Electrodes – Catalyst Layers .....	12
1.3.3 Gas Diffusion Layers .....	15
1.3.4 Flow Fields – Current Collectors .....	16
1.4 Research Objectives .....	17
<b>Chapter 2 Review of Theoretical and Experimental Studies of Cathode Catalysts and the Oxygen Reduction Reaction... 19</b>	
2.1 Introduction .....	19
2.2 Oxygen Reduction Reaction.....	20
2.2.1 Thermodynamics .....	20
2.2.2 Kinetics.....	23
2.3 Theoretical Studies of Cathode Catalysts for Fuel Cells.....	26
2.3.1 Computational Chemistry .....	26
2.3.2 Gaussian 09 .....	27
2.3.3 Platinum Based Catalysts .....	28
2.3.4 Nitrogen Doped Carbon Catalysts.....	32

2.3.5 Other Heteroatom Doped Carbon Catalysts.....	37
2.3.6 Transition Metal Macrocyclic Catalysts.....	38
2.4 Experimental Research and Development of Cathode Catalysts for PEM Fuel Cells .....	41
2.4.1 Platinum alloys .....	41
2.4.2 Transition Metal Chalcogenides.....	42
2.4.3 Carbon Catalysts Containing Transition Metals .....	44
2.4.4 Metal-Free Carbon Catalysts.....	47
2.4.4.1 Nitrogen Doped Carbon Catalysts .....	48
2.4.4.2 Other Heteroatom Doped Carbon Catalysts .....	50
2.4.5 Achievements and Challenges .....	52
2.4.6 Catalyst Supports.....	53
2.4.7 Other Types of Non-Precious Catalysts .....	55
2.5 Factors Influencing Catalytic Performance of Cathode Catalysts .....	56
2.6 Summary .....	59
2.7 Research Outlines.....	60
<b>Chapter 3 DFT Modelling of Molecular Oxygen Binding to Heteroatom Doped Carbon Edge Sites.....</b>	<b>62</b>
3.1 Introduction .....	62
3.2 Model Systems .....	62
3.3 Theoretical Method .....	63
3.4 Results and Discussion.....	66
3.4.1 Energies of Molecular Oxygen Binding to N, B, O and Non-Doped Carbon Edges.....	66
3.4.1.1 Non-Doped Carbon Edges.....	66
3.4.1.2 Nitrogen Doped Carbon Edges.....	67
3.4.1.3 Boron Doped Carbon Edges .....	70
3.4.1.4 Oxygen Doped Carbon Edges .....	73
3.4.2 Activation Energies of Molecular Oxygen Binding to N, B, O and Non-Doped Carbon Edges.....	74
3.4.3 Energies of Molecular Oxygen Binding to P, Al, S and Se Doped Carbon Edges.....	77
3.4.4 Activation Energies of Molecular Oxygen Binding to P, Al, S and Se Doped Carbon Edges .....	81
3.5 Conclusion.....	85

<b>Chapter 4</b>	<b>DFT Modelling of the Oxygen Reduction Reaction on Transition Metal Macrocycles.....</b>	<b>86</b>
4.1	Introduction .....	86
4.2	Model Systems .....	86
4.3	Theoretical Method .....	88
4.4	Results and Discussion.....	90
4.4.1	Effect of Macrocycle Structure .....	90
4.4.2	Thermodynamics of the ORR on Fe, Co and Mn Tetraaza-Annulene Model Systems.....	94
4.4.3	Energetics of the ORR on the Fe, Co and Mn N-Coordinated Active Sites .....	98
4.5	Conclusion.....	109
<b>Chapter 5</b>	<b>DFT Modelling of the Catalytic Active Sites on Heteroatom Doped Graphene.....</b>	<b>110</b>
5.1	Introduction .....	110
5.2	Molecular Systems .....	110
5.3	Theoretical Method .....	111
5.4	Proposed Methodology of Modelling the ORR Mechanism in Acid and Alkaline Media .....	112
5.5	Results and Discussion.....	118
5.5.1	Potential Energy Profiles of the Molecular Oxygen Binding .....	118
5.5.2	Atomic Spin Density and Charge Analysis.....	126
5.6	Conclusion.....	130
<b>Chapter 6</b>	<b>Experimental Methods of Catalyst Synthesis and Characterisation .....</b>	<b>131</b>
6.1	Introduction .....	131
6.2	Electrochemical Characterisation Using a Rotating Ring Disk Electrode.....	131
6.2.1	Cyclic Voltammetry .....	131
6.2.2	Linear Sweep Voltammetry .....	133
6.2.3	RRDE Principle .....	134
6.2.4	Analysis of Catalytic Activity towards the ORR using RRDE Data .....	135
6.3	Physicochemical Characterisation.....	137
6.3.1	X-Ray Diffraction .....	138
6.3.2	X-Ray Photoelectron Spectroscopy .....	139
6.3.3	Scanning Electron Microscopy and Energy Dispersive Spectroscopy .....	140

6.4	PEM Fuel Cell Tests .....	141
6.4.1	Polarisation Curves .....	141
6.4.2	Catalyst Durability Evaluation.....	144
6.4.3	Electrochemical Impedance Spectroscopy .....	145
6.5	Experimental Setup .....	147
6.5.1	Equipment for Catalyst Synthesis .....	147
6.5.2	Equipment for Electrochemical Characterisation .....	149
6.5.3	In-house PEM Fuel Cell Test Station.....	150
6.6	Experimental Research Outline.....	151
<b>Chapter 7 Experimental Investigation of Heteroatom</b>		
<b>Doped Carbon Catalysts for PEM Fuel Cells..... 153</b>		
7.1	Introduction .....	153
7.2	Catalyst Ink Preparation for the RRDE Measurements .....	153
7.3	Catalyst Ink Preparation for PEM Fuel Cell Tests .....	154
7.4	Preparation of the Membrane Electrode Assembly.....	155
7.5	RRDE Collection Efficiency Measurement .....	156
7.6	RRDE Characterisation of the Commercial Platinum Catalyst .....	158
7.7	N doped Carbon Catalysts.....	160
7.7.1	LANL1 Catalysts.....	160
7.7.1.1	Synthesis .....	160
7.7.1.2	RRDE Characterisation and the Effect of Sieving .....	161
7.7.1.3	Deactivation of the LANL1 Catalyst.....	164
7.7.2	LANL2 Catalyst .....	165
7.7.2.1	Synthesis .....	165
7.7.2.2	RRDE Characterisation .....	166
7.7.2.3	Reproducibility .....	168
7.7.2.4	Deactivation.....	169
7.7.2.5	Physicochemical Characterisation.....	170
7.7.2.6	PEM Fuel Cell Test .....	172
7.8	P doped Carbon Catalysts .....	174
7.8.1	Synthesis.....	174
7.8.2	RRDE Characterisation.....	177
7.8.3	The Effect of Final Pyrolysis .....	179
7.8.4	Physicochemical Characterisation.....	181
7.9	N and P Co-doped Carbon Catalyst .....	183
7.9.1	Synthesis.....	183

7.9.2 RRDE Characterisation.....	184
7.9.3 Physicochemical Characterisation.....	186
7.10 Glow Discharge Method of Synthesis of Phosphorus Doped Carbon Catalyst.....	188
7.10.1 Synthesis.....	188
7.10.2 Physicochemical Characterisation.....	188
7.10.3 PEM Fuel Cell Test.....	191
7.11 Conclusion.....	192
<b>Chapter 8 Experimental Investigation of Alternative Supports for PEM Fuel Cell Catalysts.....</b>	<b>193</b>
8.1 Introduction .....	193
8.2 Properties of the Alternative Support Materials.....	193
8.2.1 Microporosity and Surface Area .....	193
8.2.2 Thermal Stability.....	194
8.3 ZIF-8 supported N doped catalyst synthesis .....	195
8.3.1 Synthesis.....	195
8.3.2 RRDE Characterisation.....	196
8.3.3 Physicochemical Characterisation.....	198
8.4 Faujazit and Molecular Sieves Supported N Doped Carbon Catalysts .....	200
8.4.1 Faujazit Supported Catalyst.....	200
8.4.2 Molecular Sieves Supported Catalyst .....	203
8.5 Titanium Nitride Supported N doped Carbon Catalysts .....	206
8.5.1 Non-Pyrollysed Catalyst.....	206
8.5.2 The Effect of Pyrolysis.....	209
8.5.3 Physicochemical Characterisation.....	210
8.5.4 Modified Synthesis Technique.....	213
8.6 Tungsten Carbide Supported N doped Carbon Catalyst .....	216
8.6.1 RRDE Characterisation.....	216
8.6.2 Physicochemical Characterisation.....	217
8.7 Multiwall Carbon Nanotubes Supported N Doped Carbon Catalyst ....	219
8.8 Compared Activity of the Synthesised Catalyst.....	220
8.9 Conclusion.....	222
<b>Chapter 9 Conclusions and Future Work.....</b>	<b>223</b>
9.1 Theoretical Findings.....	223
9.1.1 Doped Graphene Edge Sites.....	223

9.1.2 Doped Graphene Planes .....	224
9.1.3 Transition Metal Macrocycles .....	224
9.2 Experimental Findings .....	225
9.3 Future work .....	226
<b>References .....</b>	<b>228</b>

## List of Figures

<b>Figure 1.1</b> Principle of hydrogen fuel cell [8].	2
<b>Figure 1.2</b> Basic Principle of MCFC [12].	8
<b>Figure 1.3</b> Basic Principle of DMFC [13].	9
<b>Figure 1.4</b> Basic Principles of PEM Fuel Cell [1].	10
<b>Figure 1.5</b> Chemical structure of Nafion <sup>®</sup> membrane [1].	12
<b>Figure 1.6</b> Transport of reactants, products, protons, and electrons in a PEM fuel cell cathode [3].	13
<b>Figure 1.7</b> Schematic carbon-supported catalyst particle covered with the thin electrolyte layer [3].	14
<b>Figure 1.8</b> Bipolar plate connects and separates two adjacent cells [1].	16
<b>Figure 1.9</b> Schematics of some common flow field patterns [5].	17
<b>Figure 2.1</b> Oxygen reduction reaction pathways [2].	21
<b>Figure 2.2</b> Electric field gradient ( $E$ ) as a function of the thickness of the electric double layer $d$ at the constant electrode potential $U = 1.23$ V.	23
<b>Figure 2.3</b> Schematic reaction profile for effective and ineffective catalysts [5].	23
<b>Figure 2.4</b> Schematic oxygen reduction reaction. The enthalpies, activation energies and transition states are designated as $\Delta H$ , $E_a$ and TS, respectively.	25
<b>Figure 2.5</b> Models of molecular oxygen chemisorption on platinum [37].	28
<b>Figure 2.6</b> Models of molecular oxygen chemisorption over the Pt(111) monolayer surface [49].	29
<b>Figure 2.7</b> Volcano plot of trends in oxygen reduction activity as a function of OH and O binding energies for different metals [38].	32
<b>Figure 2.8</b> Chemical states of nitrogen in graphene planes [61].	33
<b>Figure 2.9</b> OOH binding to the N doped graphene [69]. The carbon, nitrogen, oxygen and hydrogen atoms are designated by the grey, blue, red and white colours, respectively.	34
<b>Figure 2.10</b> Molecular oxygen binding to a graphite edge doped with graphitic nitrogen [39]. The carbon, nitrogen, oxygen and hydrogen atoms are designated by the grey, blue, red and white colours, respectively.	35
<b>Figure 2.11</b> a) Molecular oxygen bound to a boron doped carbon nanotube [95], and b) boron and nitrogen co-doped carbon nanotube [94]. The carbon, boron, nitrogen and oxygen atoms are designated by the grey, pink, blue and red colours, respectively.	38
<b>Figure 2.12</b> Models of active sites for the ORR with a) Fe (II) and b) Fe(III) oxidation states of the central atom [103].	39

<b>Figure 2.13</b> Transition metal macrocycle active sites based on the structures of a) porphyrine, and b) tetraazaannulene [104]. The carbon, nitrogen and transition metal atoms are designated by the black, blue and brown colours, respectively. ....	39
<b>Figure 2.14</b> Transition metal phthalocyanine structure with molecular oxygen bound to the central metal atom [107]. The carbon, nitrogen, transition metal and oxygen are designated by the grey, blue, purple and red colours, respectively. ....	40
<b>Figure 2.15</b> Theoretical model structures of a) iron-cobalt polyaniline [109], and b) cobalt polypyrrole [36]. The carbon, nitrogen, oxygen and hydrogen are designated by the grey, blue, red and white colours, respectively. The transition metals are designated by the purple and brown colours. ....	41
<b>Figure 2.16</b> Transition metal macrocycles: a) iron phthalocyanine, b) iron porphyrin, c) iron tetraazaannulene [128], and d) cobalt corrin. ....	44
<b>Figure 2.17</b> Proposed active sites with a) two- and b) four-fold coordination of the transition metal to the nitrogen atoms [127, 136]. ....	46
<b>Figure 2.18</b> Common carbon nanostructures [61]. ....	48
<b>Figure 2.19</b> Factors influencing the activity and durability of cathode catalysts. ....	56
<b>Figure 2.20</b> Basic steps of a catalyst synthesis technique. ....	59
<b>Figure 2.21</b> Outline of the theoretical and experimental studies of alternative cathode catalysts for PEM fuel cells. ....	61
<b>Figure 3.1</b> a) Zigzag and b) armchair edge sites of graphene. ....	63
<b>Figure 3.2</b> Generic model systems of the doped carbon edge sites studied here. ....	63
<b>Figure 3.3</b> Initial configurations of the oxygen molecule relative to the model system. ....	65
<b>Figure 3.4</b> Molecular oxygen binding to the non-doped a) naphthalene- and b) graphene-type model systems in the four modifications. The C, O and H atoms are designated by the yellow, red and cyan colours, respectively. ....	67
<b>Figure 3.5</b> Molecular oxygen binding to the graphitic N doped a) naphthalene- and b) graphene-type model systems in the five modifications. The C, O, N and H atoms are designated by the yellow, red, purple and cyan colours, respectively. ....	68
<b>Figure 3.6</b> Molecular oxygen binding to the pyridinic N doped anthracene-type model systems in the four modifications. The C, O, N and H atoms are designated by the yellow, red, purple and cyan colours, respectively. ....	69
<b>Figure 3.7</b> Lone-electron pair of a) graphitic N, and b) pyridinic N. ....	70
<b>Figure 3.8</b> Molecular oxygen binding to the ternary B doped a) naphthalene- and b) graphene-type model systems in the different modifications. The C, O, B and H atoms are designated by the yellow, red, purple and cyan colours, respectively. ....	71

<b>Figure 3.9</b> Molecular oxygen binding to the binary B doped anthracene-type model system in the four modifications. The C, O, B and H atoms are designated by the yellow, red, purple and cyan colours, respectively. ....	72
<b>Figure 3.10</b> Molecular oxygen binding to the O doped anthracene-type model system in the five modifications. The C, O and H atoms are designated by the yellow, red and cyan colours, respectively. ....	73
<b>Figure 3.11</b> Potential energy profile obtained in the IRC calculation for the B doped naphthalene-type system. ....	74
<b>Figure 3.12</b> Pathways of molecular oxygen binding to the non-doped, N doped and B doped naphthalene-type systems with a) one H atom removed, b) two H atoms removed, and c) one H atom removed and (-1) charge for the non-doped or two H atoms removed and (-1) charged for the N, B doped systems. ....	75
<b>Figure 3.13</b> Potential energy profiles of molecular oxygen chemisorption on the O doped anthracene-type system: a) in the end-on mode, and b) with disruption of the heterocycle ring. ....	77
<b>Figure 3.14</b> Geometry optimised Al doped naphthalene-type system modifications with a) one H removed, b) two H removed, and c) two H removed and a (-1) charge. ....	78
<b>Figure 3.15</b> Optimised products of molecular oxygen binding to a) and b) P and Al doped naphthalene-, c) and d) S and Se doped anthracene-type systems. The C, P, Al, S, Se, O and H atoms are designated by the yellow, green, pale-green, olive, orange, red and cyan colours, respectively. ....	79
<b>Figure 3.16</b> Optimised products of molecular oxygen binding to the Al doped systems with a) – c) non-hexagonal and d) disrupted heterocyclic ring structure. ....	80
<b>Figure 3.17</b> Optimised products of molecular oxygen binding with the disruption of the heterocycle ring for the S and Se doped anthracene-type systems with a), d) one H removed, b), e) two H removed, and c), f) two H removed and a (-1) charge. The C, S, Se, O and H atoms are designated by the yellow, olive, orange, red and cyan colours, respectively. ....	81
<b>Figure 3.18</b> Pathways of molecular oxygen binding to the modifications of the P doped naphthalene-type systems. The C, P, O and H atoms are designated by the yellow, green, red and cyan colours, respectively. ....	82
<b>Figure 3.19</b> Pathways of molecular oxygen binding to the modifications of the Al doped naphthalene-type systems. The C, Al, O and H atoms are designated by the yellow, pale-green, red and cyan colours, respectively. ....	83
<b>Figure 3.20</b> Pathways of molecular oxygen binding to the modifications of a) S and b) Se doped anthracene-type systems in the end-on mode and with disruption of the heterocyclic ring. ....	84

**Figure 4.1** Transition metal (a) phthalocyanines, (b) porphyrins, (c) corrins, and (d) tetraaza-annulene model systems in the three sizes: minimal, intermediate and maximal model systems. The C, N, H and transition metal atoms are designated by the grey, blue, light-grey and the purple colours. .... 87

**Figure 4.2** Geometry-optimized structures of the transition metal macrocycles: a) phthalocyanine, b) porphyrin, c) corrin, and d) tetraaza-annulene. The C, N, H and metal atoms are designated by the yellow, purple, cyan and pink colours, respectively. .... 90

**Figure 4.3** Molecular oxygen binding to the four types of Fe macrocycles in minimal, intermediate and maximal sizes. The C, N, O, H and Fe atoms are designated by the yellow, purple, red, cyan and pink colours, respectively. .... 91

**Figure 4.4** Molecular oxygen binding to the four Fe macrocycles. The C, N, O and Fe atoms are designated by the yellow, purple, red and pink colours, respectively, and the interatomic distances are shown in Å. .... 92

**Figure 4.5** Molecular oxygen binding to the four types of neutral and (-1) charged Co macrocycles. The C, N, O and Co atoms are designated by the yellow, purple, red and blue colours, respectively, and the interatomic distances are shown in Å. .... 93

**Figure 4.6** Molecular oxygen binding to the four types of neutral and (-1) charged Mn macrocycles. The C, N, O and Mn atoms are designated by the yellow, purple, red and pink colours, respectively, and the interatomic distances are shown in Å. .... 93

**Figure 4.7** Schematic of the molecular oxygen binding to the active site modelled by the OH-terminated Fe tetraaza-annulene system. .... 95

**Figure 4.8** Thermodynamics of the ORR pathways on the OH-terminated Fe tetraaza-annulene system. .... 95

**Figure 4.9** Thermodynamics of the ORR pathways on the OH-terminated Co tetraaza-annulene system. .... 96

**Figure 4.10** Thermodynamics of the ORR pathways on the OH-terminated Mn tetraaza-annulene system. .... 96

**Figure 4.11** Model systems representing transition metal macrocycle active sites: the large tetraaza-annulene and the small M-4N. .... 98

**Figure 4.12** Potential energy profiles of the ORR elementary steps on the Fe-4N model system: a) molecular oxygen binding; and H addition steps: b) first H; c) second H in the OH-OH pathway; d) second H in the H<sub>2</sub>OO pathway; e) third H in the OH-OH pathway; f) third H in the H<sub>2</sub>OO pathway; and g) fourth H. .... 100

**Figure 4.13** The ORR pathways on the Fe-4N model system. .... 102

**Figure 4.14** Potential energy profiles of the ORR intermediate steps on the Co-4N model system: a) molecular oxygen binding; and H addition steps: b) first H;

c) second H in the OH-OH pathway; d) second H in the H<sub>2</sub>OO pathway; e) third H in the OH-OH pathway; f) third H in the H<sub>2</sub>OO pathway, and g) fourth H. .... 104

**Figure 4.15** The ORR pathways on the Co-4N model system. .... 105

**Figure 4.16** Potential energy profiles of the ORR intermediate steps on the Mn-4N system: a) molecular oxygen binding; and H addition steps: b) first H; c) second H in the two-electron pathway; d) second H in the four-electron pathway; e) third H; f) fourth H. .... 107

**Figure 4.17** The ORR pathways on the Mn-4N model system. .... 108

**Figure 5.1** Generic model systems of a) mono heteroatom doped graphene, b) binary doped graphene with the substituent N, B or P atoms, and c) binary doped graphene with the substituent S and N or P. .... 111

**Figure 5.2** Schematics of the ORR environment in a) acid, and b) alkaline media on a catalyst surface. .... 113

**Figure 5.3** Schematic of the four-electron ORR pathway in acid media on a catalyst surface. The transferred H atoms are designated by the numbers from 1 to 4. .... 113

**Figure 5.4** Schematic of the two-electron ORR pathway in acid media on a catalyst surface. The transferred H atoms are designated by the numbers 1 and 2. ... 115

**Figure 5.5** Schematic of the four-electron ORR pathway in alkaline media on a catalyst surface. The transferred H atoms are designated by the numbers 1 and 2. ... 116

**Figure 5.6** Schematic of the ORR reactants over the catalyst model system. The electric field direction is along the Y axis. .... 117

**Figure 5.7** Geometry-optimized a) N-G, b) P-G and c) B-G systems, and the corresponding potential energy profiles of molecular oxygen binding to the marked atoms (right side). .... 119

**Figure 5.8** a) The 2N-G system, and the potential energy profiles of the molecular oxygen binding to b) C4 atom, and c) all other marked atoms. .... 120

**Figure 5.9** a) The 2P-G system, and the potential energy profiles of molecular oxygen binding to b) the C6, C2, C12, and c) P1, P2 and C4 atoms. .... 121

**Figure 5.10** a) NP-G and b) NB-G systems with the corresponding potential energy profiles of molecular oxygen binding to the marked atoms (right side). .... 122

**Figure 5.11** Three isomeric SN-G model systems a), b), and c), and the corresponding potential energy profiles of molecular oxygen binding to the marked atoms (right side). .... 123

**Figure 5.12** a) SP1-G, b) SP2-G, and c) SP3-G isomeric model systems with the corresponding potential energy profiles of molecular oxygen binding to the marked atoms (right side). .... 124

<b>Figure 5.13</b> Products of molecular oxygen end-on and side-on binding to the binary heteroatom doped model systems: a) 2N-G, b) and c) 2P-G, d) SP2-G, and e) SP3-G.....	125
<b>Figure 5.14</b> Atomic spin densities of the starting and end structures of potential energy profiles of molecular oxygen binding to a) N-G, b) 2N-G, c) P-G, d) 2P-G, and e) SP-G model systems. ....	129
<b>Figure 6.1</b> Cyclic voltammogram of a platinum catalyst in an acid electrolyte [232]. ....	132
<b>Figure 6.2</b> Cyclic voltammogram of a nitrogen doped carbon catalyst in acid electrolyte [233]. ....	133
<b>Figure 6.3</b> LSVs of an alternative carbon based catalysts measured using RRDE [126]. ....	134
<b>Figure 6.4</b> Oxygen reduction reaction on the rotating ring disk electrode [234]. ....	135
<b>Figure 6.5</b> The XRD spectrum of a Fe/N/C catalyst [20]. ....	138
<b>Figure 6.6</b> The XPS spectra of the non-precious FeCo/N/C catalyst: a) survey and b) high resolution of N 1s region [236]. ....	139
<b>Figure 6.7</b> a) SEM image [67], and b) EDS spectrum [179] of alternative carbon-based catalysts. ....	141
<b>Figure 6.8</b> Potential losses and resulting polarization curve in PEM fuel cells [1]. ....	143
<b>Figure 6.9</b> a) Evaluation of PEM fuel cell performance using polarization curves [1], and b) polarization and power density curves in PEM fuel cell tests with two alternative catalysts [137]. ....	143
<b>Figure 6.10</b> Equivalent circuit representing a fuel cell, where $R_e$ is both electronic and ionic resistance, $R_{ct}$ is charge transfer resistance, $Z_w$ is Warburg impedance, C is capacitive resistance [1]. ....	146
<b>Figure 6.11</b> The EIS spectrum at various frequencies of the fuel cell equivalent circuit in the Nyquist form. The frequencies $\omega$ increase from right to left [1]. ....	147
<b>Figure 6.12</b> Photograph of the reflux condenser. ....	148
<b>Figure 6.13</b> Photograph of the tube furnace (1) with gas flow-meter (2), and digital control panel (3). ....	148
<b>Figure 6.14</b> Gas flow-meter calibration. ....	149
<b>Figure 6.15</b> Photograph of the RRDE equipment: (1) potentiostat, (2) rotating ring disk electrode, (3) test cell, (4) electrode rotator, and (5) computer. ....	150
<b>Figure 6.16</b> Photograph of the in-house PEM fuel cell test station: 1) air-breathing PEM fuel cell, 2) potentiostat, 3) and 4) bubbler-type hydrogen and air humidifiers, 5) humidity sensor and reader, 6) and 7) hydrogen and air pressure regulators, 8) and 9) hydrogen and air pressure differential transducers, 10) and 11)	

hydrogen and air back pressure regulators, 12) and 13) mass flow controllers, 15) flow rates control display, and 16) gas leak control monitor. .... 151

**Figure 7.1** Principle of measurement of the empirical collection efficiency: a) LSVs at different electrode rotation speeds [244], and b) calculated collection efficiency as a function of electrode rotation speed [234]. .... 157

**Figure 7.2** Measurement of the empirical collection efficiency on glassy carbon disk and platinum ring electrode in 3 mM  $K_3Fe(CN)_6$  solution: a) and b) LSVs at different rotation speeds in 0.5 M  $H_2SO_4$  and 1 M  $KNO_3$ , respectively; c) and d) empirical collection efficiency as a function of electrode rotation speed in 0.5 M  $H_2SO_4$  and 1 M  $KNO_3$ , respectively. .... 157

**Figure 7.3** RRDE characterisation of the 20% Pt/C catalyst: a) CV in air, b) LSVs at different electrode rotation speeds, and c) Koutecky-Levich plot (the current density data were taken at 0.4 V vs. SHE). .... 159

**Figure 7.4** Electron transfer numbers for the ORR on the 20% Pt/C catalyst plotted versus a) electrode rotation speed, and b) potential. .... 159

**Figure 7.5** Schematic of the LANL1 catalyst synthesis. .... 160

**Figure 7.6** RRDE characterisation of LANL1-ns catalyst: a) CVs in  $N_2$  and air, and b) LSVs at different electrode rotation speeds, shown in the legend. .... 162

**Figure 7.7** RRDE characterisation of LANL1-s catalyst: a) CVs in  $N_2$  and air, and b) LSVs at different electrode rotation speeds, shown in the legend. .... 162

**Figure 7.8** Overlaid RRDE results for the LANL1-s, LANL1-ns and the commercial 20% Pt/C catalysts: a) CVs in air, and b) LSVs at 1200 RPM. .... 163

**Figure 7.9** The RRDE characterisation of the aged LANL1-s catalyst: a) the overlaid CVs in air for the aged and fresh catalyst, and b) LSVs for the aged catalyst at different electrode rotation speeds. .... 164

**Figure 7.10** Schematic of the LANL2 catalyst synthesis. .... 165

**Figure 7.11** RRDE characterisation of the LANL2 catalyst: a) CVs in  $N_2$  and air, b) LSVs at different electrode rotation speeds, shown in the legend, and c) Koutecky-Levich plot (the current density data were taken at 0.1 V vs. SHE). .... 167

**Figure 7.12** Electron transfer numbers for the ORR on the LANL2 catalyst plotted versus a) electrode rotation speed, and b) potential. .... 167

**Figure 7.13** Comparison of the RRDE results for the LANL1-s, LANL2 catalysts, commercial 20%Pt/C and carbon black: a) CVs in air, and b) LSVs at 1200 RPM. .... 168

**Figure 7.14** RRDE results of the LANL-p catalyst: a) CVs in  $N_2$  and air, b) LSVs at different rotation speeds, and c) CVs in air for the LANL-p and LANL2... 169

**Figure 7.15** Deactivation of the LANL2 catalyst in the period of two months a) CVs in air, and b) LSVs at 1200 RPM. .... 170

<b>Figure 7.16</b> The XRD patterns of a) LANL1-s, b) LANL2, and c) LANL1-p catalysts. ....	171
<b>Figure 7.17</b> XPS analysis of the LANL2 catalyst: a) survey, and the deconvoluted high resolution b) C1s, and c) N1s spectra. ....	172
<b>Figure 7.18</b> Polarisation (solid line) and power density (dashed line) of the MEAs with LANL2 (blue) and commercial 20%Pt/C (black) in the in-house PEM fuel cell test. ....	173
<b>Figure 7.19</b> a) The EIS spectra of the MEAs with the LANL2 and commercial 20%Pt/C catalysts, and b) performance stability of the MEA with the LANL2 catalyst in the PEM fuel cell test. ....	174
<b>Figure 7.20</b> Chemical structures of a) triphenylphosphine oxide, b) Met-BozPhos, and c) Met-DuPhos molecules. ....	175
<b>Figure 7.21</b> Schematic of syntheses of the P doped carbon catalysts. ....	176
<b>Figure 7.22</b> RRDE characterisation of the synthesized P doped carbon catalysts: CVs in N <sub>2</sub> and air of the a) LP1-700, and b) LP1-800 b) catalysts; and LSVs of c) LP1-700, and d) LP1-800 catalysts at different electrode rotation speeds. ....	178
<b>Figure 7.23</b> RRDE characterisation of the LP1-700-3-pyr catalyst: a) CVs in N <sub>2</sub> and air, b) LSVs at different electrode rotation speeds, and c) Koutecky-Levich plot (the current density data were taken at 0.1 V vs. SHE). ....	179
<b>Figure 7.24</b> Electron transfer numbers for the ORR on the LP1-700-3-pyr catalyst plotted versus a) electrode rotation speed, and b) potential. ....	180
<b>Figure 7.25</b> Comparison of the RRDE results for the LP1-800, LP1-700 and LP1-700-3-pyr catalysts: a) CVs in air, and b) LSVs at 1200 RPM. ....	181
<b>Figure 7.26</b> The XRD pattern of the LP1-700-3-pyr catalyst. ....	181
<b>Figure 7.27</b> XPS analysis of the LP1-700 catalyst: a) XPS survey; deconvoluted high resolution b) C 1s, and c) P 2p spectra. ....	183
<b>Figure 7.28</b> Chemical structure of diphenyl-2-pyridylphosphine. ....	183
<b>Figure 7.29</b> RRDE characterisation of the NP800 catalyst: a) CVs in N <sub>2</sub> and air, and b) LSVs at different electrode rotation speeds. ....	185
<b>Figure 7.30</b> Comparison of the RRDE results for the NP800, LANL2, LP1-700-3-pyr catalysts and carbon black: a) CVs in air, and b) LSVs at 1200 RPM. ....	186
<b>Figure 7.31</b> The XPS spectra of the NP800 catalyst: a) XPS survey, and the deconvoluted high resolution b) C 1s, c) N 1s, and d) P 2p spectra. ....	187
<b>Figure 7.32</b> The XRD patterns of a) 0.45%P-C coated, and b) uncoated GDLs. ....	189
<b>Figure 7.33</b> The SEM images of a) non-coated, and b) 0.45% P-C coated GDLs, and EDS spectra of c) non-coated, and d) 0.45%P-C coated GDLs. ....	189

<b>Figure 7.34</b> PEM fuel cell test: a) polarisation curve (solid) and power density (dashed) with the 0.60%P-C coated GDL; and b) comparison of polarisation curves with the 0.60%P-C coated GDL and LANL2 as cathode catalysts. ....	190
<b>Figure 7.35</b> The EIS spectra of a) 0.60% P-C coated GDL compared to the LANL2 catalyst, and b) the LANL2 catalyst compared to 20%Pt/C. ....	191
<b>Figure 8.1</b> Schematic of the BLANL2 catalyst synthesis. ....	196
<b>Figure 8.2</b> RDE characterisation of the ZIF-8 supported catalysts: a) CVs in N <sub>2</sub> and air for the BLANL1 catalyst; b) CVs in N <sub>2</sub> and air, and c) LSVs at different electrode rotation speeds for the BLANL2 catalyst. ....	197
<b>Figure 8.3</b> Comparison of the RDE results for the BLANL2 and the LANL2 catalysts: a) CVs in air, and b) LSVs at 1200 RPM. ....	198
<b>Figure 8.4</b> The XRD pattern of the BLANL2 catalyst. ....	198
<b>Figure 8.5</b> The XPS spectra of the BLANL2 catalyst: a) XPS survey; and the deconvoluted high resolution b) C 1s and c) N 1s spectra. ....	199
<b>Figure 8.6</b> RDE characterisation of the FL catalyst: a) CVs in N <sub>2</sub> and air at 1000 RPM, and b) LSVs at different rotation speeds, shown in the legend. ....	200
<b>Figure 8.7</b> The XRD pattern of the FL catalyst. ....	201
<b>Figure 8.8</b> The XPS spectra of the FL catalyst: a) XPS survey, and deconvoluted high resolution b) C 1s, c) N 1s, and d) Si 2p spectra. ....	202
<b>Figure 8.9</b> RRDE characterisation of the ML catalyst: a) CVs in N <sub>2</sub> and air at 1000 RPM, and b) LSVs at different rotation speeds, shown in the legend. ....	203
<b>Figure 8.10</b> The XRD pattern of the ML catalyst. ....	204
<b>Figure 8.11</b> The XPS spectra of the ML catalyst: a) XPS survey; and deconvoluted high-resolution b) C 1s, and c) N 1s spectra. ....	205
<b>Figure 8.12</b> Comparison of the RRDE results for the ML, LANL2, BLANL2, FL catalysts and carbon black: a) CVs, and b) LSVs at 1200 RPM. ....	206
<b>Figure 8.13</b> RRDE characterisation of the Fe-PANI-CoEDA-TiN catalyst: a) CVs in N <sub>2</sub> and air at 1000 RPM for the freshly prepared catalyst and on the next day, and b) LSVs at different electrode rotation speeds (shown in the legend). ....	207
<b>Figure 8.14</b> LSVs after the a) second and b) third measurements for the Fe-PANI-CoEDA-TiN catalyst. ....	208
<b>Figure 8.15</b> RRDE characterisation of the Fe-PANI-CoEDA-TiN-leached catalyst: a) CVs in N <sub>2</sub> and air at 1000 RPM, and b) LSVs at different rotation speeds (shown in the legend). ....	209
<b>Figure 8.16</b> RRDE characterisation of the TL catalysts: a) CVs in N <sub>2</sub> and air at 1000 RPM, and b) overlaid CVs in air for the TL catalyst and carbon black. ....	210
<b>Figure 8.17</b> The XRD patterns of a) the FePANI-CoEDA-TiN, b) FePANI-CoEDA-TiN-leached, and c) TL catalysts. ....	211

<b>Figure 8.18</b> The XPS spectra of the FePANI-CoEDA-TiN-leached catalyst: a) XPS survey, and deconvoluted high-resolution b) C 1s, and c) N 1s spectra. ....	212
<b>Figure 8.19</b> The XPS spectra of the TL catalyst: a) XPS survey and deconvoluted high-resolution b) C 1s, c) N 1s, and d) Si 2p spectra. ....	213
<b>Figure 8.20</b> Schematic of the TL2 catalyst synthesis. ....	214
<b>Figure 8.21</b> RRDE characterisation of the TL2 catalyst: a) CVs in N <sub>2</sub> and air at 1000 RPM, b) LSVs at different electrode rotation rates, and c) overlaid CVs in air for the TL and TL2 catalysts. ....	215
<b>Figure 8.22</b> The XRD patterns of the a) TL2 and b) TL catalysts. ....	216
<b>Figure 8.23</b> RRDE characterisation of the WL catalyst: a) CVs in N <sub>2</sub> and air at 1000 RPM; b) LSVs at different rotation speeds, and c) overlaid CVs in air for the WL catalyst and carbon black. ....	217
<b>Figure 8.24</b> The XRD patterns of a) Fe-PANI-CoEDA-WC and b) WL catalysts. ....	218
<b>Figure 8.25</b> The XPS spectra of the WL catalyst: a) XPS survey and the deconvoluted high resolution b) C 1s, c) N 1s, and d) W 4f spectra. ....	218
<b>Figure 8.26</b> RRDE characterisation of the NL catalyst: a) CVs in N <sub>2</sub> and air at 1000 RPM, and b) LSVs at different rotation speeds (shown in the legend). ....	220
<b>Figure 8.27</b> The XRD pattern of the NL catalyst. ....	220
<b>Figure 8.28</b> Comparison of the RRDE results for NL, LANL2, LP1-700-3-pyr, NP800, BLANL2, FL catalysts and carbon black: a) CVs, and b) LSVs at 1200 RPM. ....	221

## List of Tables

<b>Table 1.1</b> Operating data of various fuel cell system [9].	3
<b>Table 1.2</b> Application areas of PEM fuel cells [2].	4
<b>Table 2.1</b> Energetics of the ORR intermediate steps on a Pt(111) surface.	31
<b>Table 2.2</b> Energetics of the ORR intermediate steps on nitrogen doped carbon.	36
<b>Table 2.3</b> Electrical conductivities of some catalyst support materials.	54
<b>Table 3.1</b> Types of molecular oxygen binding products for the P, Al, S and Se doped model systems.	78
<b>Table 3.2</b> Molecular oxygen binding energies for the P, Al, S and Se doped model system in the five modifications.	79
<b>Table 4.1</b> The formulae for calculating total energies, relative energies and elementary reaction energies of the ORR intermediate steps.	89
<b>Table 4.2</b> Energies (eV) of molecular oxygen binding to the four types of the Fe, Co and Mn macrocycles (neutral and negatively charged).	94
<b>Table 4.3</b> Calculated reaction energies of the ORR elementary steps on the OH-blocked Fe, Co and Mn tetraaza-annulene model systems.	97
<b>Table 4.4</b> Molecular oxygen binding energies for the large tetraaza-annulene and the small M-4N systems.	99
<b>Table 4.5</b> The calculated energies of the ORR elementary steps on the Fe, Co and Mn-4N model systems compared to the OH-terminated tetraaza-annulene (large) model systems.	99
<b>Table 4.6</b> Reaction energies and activation energies of the ORR elementary steps on the Fe-4N model system.	102
<b>Table 4.7</b> Elementary reaction energies and activation energies of the ORR steps on the Co-4N system.	106
<b>Table 4.8</b> Elementary reaction energies and activation energies of the ORR steps on the Mn-4N system.	108
<b>Table 5.1</b> The formulae for calculating the total energies, relative energy levels and elementary reaction energies of the four-electron ORR pathway accounting for the proton donors in acid media.	114
<b>Table 5.2</b> The formulae of calculating the total energies, relative energy levels and elementary reaction energies of the two-electron ORR pathway accounting for the proton donors in acid media.	115

<b>Table 5.3</b> The formulae of calculating the total energies, relative energy levels and elementary reaction energies of the ORR pathways accounting for the proton donors in alkaline media. ....	116
<b>Table 5.4</b> Activation and binding energies of molecular oxygen chemisorption to the binary heteroatom doped model systems. ....	126
<b>Table 5.5</b> Spin densities and natural charges of the C4 and N atoms in the N-G and 2N-G systems in the two spin multiplicity states. ....	127
<b>Table 5.6</b> Spin densities and natural charges of the P atoms in the P-G and 2P-G systems in the two spin multiplicity states. ....	127
<b>Table 5.7</b> Spin densities and natural charges of the P and S atoms in the three SP-G systems in the two spin multiplicity states. ....	127
<b>Table 7.1</b> Elemental composition of the LANL2 catalyst from the XPS analysis. ....	171
<b>Table 7.2</b> Elemental composition of the LP1-700 catalyst derived from the XPS analysis. ....	182
<b>Table 7.3</b> Elemental composition of the NP800 catalyst derived from the XPS analysis. ....	186
<b>Table 7.4</b> Elemental composition of the uncoated and 0.45%P-C coated GDLs derived from the EDS spectra. ....	190
<b>Table 8.1</b> Surface area and porosity of the alternative catalyst supports. ....	194
<b>Table 8.2</b> Thermal stability of the materials utilized as alternative catalyst supports. ....	195
<b>Table 8.3</b> Elemental composition of the BLANL2 catalyst derived from the XPS analysis. ....	199
<b>Table 8.4</b> Elemental composition of the FL catalyst from the XPS analysis. ..	201
<b>Table 8.5</b> Elemental composition of the ML catalyst from the XPS analysis. ..	204
<b>Table 8.6</b> Elemental composition of the FePANI-CoEDA-TiN-leached catalyst from the XPS analysis. ....	211
<b>Table 8.7</b> Elemental composition of the TL catalyst from the XPS analysis. ..	212
<b>Table 8.8</b> Elemental composition of the WL catalyst from the XPS analysis. ..	218

## List of Abbreviations

AAEMFC	Alkaline Anion Exchange Membrane Fuel Cell
AFC	Alkaline Fuel Cell
DFT	Density functional Theory
DMFC	Direct Methanol Fuel Cell
EIS	Electrochemical Impedance Spectroscopy
GDL	Gas Diffusion Layer
HOMO	Highest Occupied Molecular Orbital
IRC	Intrinsic Reaction Coordinate
LUMO	Lowest Unoccupied Molecular Orbital
MCFC	Molten Carbonate Fuel Cell
MEA	Membrane Electrode Assembly
MOF	Metalorganic Framework
MPL	Microporous Layer
MWCNT	Multiwall Carbon Nanotube
ORR	Oxygen Reduction Reaction
PAFC	Phosphoric Acid Fuel Cell
PEM	Proton Exchange Membrane / Polymer Electrolyte Membrane
PTFE	Polytetrafluoroethylene
RRDE	Rotating Ring Disk Electrode
SEM	Scanning Electron Microscopy
SOFC	Solid Oxide Fuel Cell
TS	Transition State
XPS	X-Ray Photoelectron Microscopy
XRD	X-Ray Diffraction
ZIF	Zeolitic Imidazolate Framework
ZPE	Zero-Point Energy



## **Chapter 1**

### **Introduction to Fuel Cells**

At the present time, fossil fuels are utilised in about 80% of the world energy demand, but have two major problems. The first one is that they are limited in amount and sooner or later will be depleted. The second problem is that the use of fossil fuels causes serious environmental problems, such as global warming, climate changes, melting of ice caps, rising sea levels, and so on [1]. Compared to conventional fossil fuel use, the advantages of fuel cells include a high efficiency of energy conversion, low pollution level, low noise and low maintenance costs. Fuel cells also have several performance advantages over batteries. First, fuel cells can achieve higher power and energy capacity, and second, they operate at a constant level as long as fuel is supplied, whereas battery performance deteriorates when the charge level drops [2]. Importantly, fuel cells can be made in any size and their power can range from a few watts up to a megawatt-scale plant with equal efficiency [3]. These advantages render fuel cells preferable over other energy generation devices such as internal combustion engines and batteries [4].

The first fuel cell concept was proposed in 1839 by W. R. Grove, who produced water and electricity by supplying hydrogen and oxygen into a sulfuric acid bath in the presence of porous platinum electrodes. Since then, little progress was made until the middle of the twentieth century. One of the most important milestones in fuel cell history is invention of a polymer electrolyte membrane (PEM) in 1955 by W. T. Grubb in General Electric, who proposed to use a polystyrene membrane as the electrolyte. The second important event in the fuel cell history is the development of electrode catalysts for oxygen reduction and fuel oxidation [3].

The power and energy efficiency of a fuel cell is highly dependent on the thermodynamics, electrode kinetics, electrochemistry, reactant mass transfer, fluid mechanics as well as materials and components constituting the fuel cell. These factors have been addressed throughout the fuel cell history and are now still the major challenges for fuel cell research and development, keeping the fuel cell technology continually evolving [3]. However, the following main technical challenges must be met before the wide-spread fuel cell use: (i) reducing the high system cost and in particular the cost of electrode catalysts, (ii) increasing the system reliability and durability, (iii) development of fuel storage, generation, and delivery technology, (iv) increasing performance and longevity of the components, and (v) development of sensors and online control systems [5]. At present, fuel cells are far more expensive than internal combustion engines [1]. The U.S. Department of Energy

(DOE) has set targets for fuel cell technologies to achieve performance and cost comparable to competing alternatives. For example, the targets for automotive fuel cells include a cost target of \$30/kW by 2015 (\$45/kW by 2010), 5,000-hour durability (equivalent to 150,000 miles), and increased efficiency to 60% [6].

### 1.1 Basic Principle of Fuel Cells

A fuel cell is an electrochemical energy device that converts chemical energy of fuel into direct current electricity [1]. In a fuel cell, a hydrogen rich fuel is fed continuously to the anode (negative electrode), and oxidant, which is often oxygen from air, is fed continuously to the cathode (positive electrode), allowing a fuel cell to generate power for as long as the fuel is supplied [7], as shown in Figure 1.1. Electrochemical reactions take place at the electrodes so that ions flow through the electrolyte, while the electric current flows in the external circuit and performs work on the load.

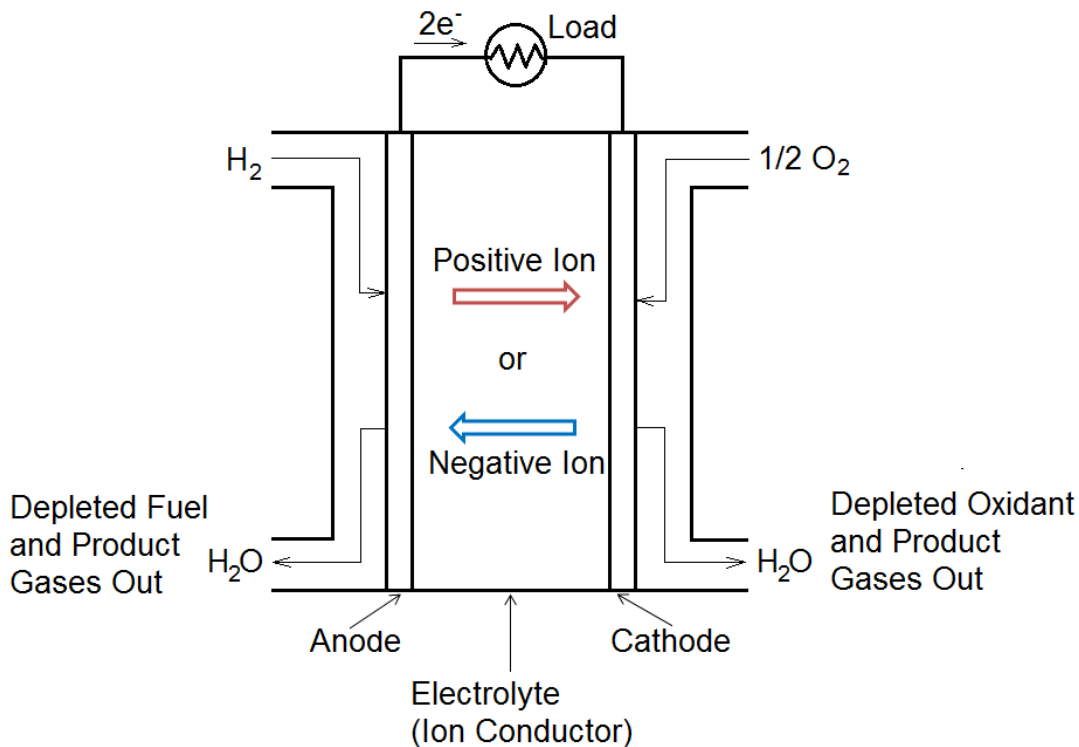


Figure 1.1 Principle of hydrogen fuel cell [8].

Hydrogen undergoes catalytic oxidation at the anode and splits into protons and electrons, and oxygen undergoes a catalytic reduction reaction at the cathode. Both protons and electrons travel from one electrode to the other, using different pathways. Protons travel through the electrolyte and electrons are forced through a separate

pathway via an external circuit with an electric load to the other electrode, where they combine with oxygen to form oxygen ions and ultimately create water or other by-products, such as carbon dioxide (CO<sub>2</sub>). [8].

## 1.2 Fuel Cell Types and Applications

There are at least six types of fuel cells depending on the type of their electrolyte. They are solid oxide fuel cells (SOFCs), alkaline fuel cells (AFCs), alkaline ion exchange fuel cells (AIEFCs), phosphoric acid fuel cells (PAFCs), molten carbonate fuel cells (MCFCs), direct methanol fuel cells (DMFCs), and proton exchange membrane (PEM) or polymer exchange membrane fuel cells (PEMFCs). Table 1.1 lists their typical operation temperature and the state of the electrolyte. [9].

**Table 1.1** Operating data of various fuel cell system [9].

Cell system	Temperature, °C	Electrolyte state
Solid oxide fuel cells	1000 - 1200	Solid
Alkaline fuel cells and alkaline ion exchange fuel cells	100	Liquid
Phosphoric acid fuel cells	60 - 200	Liquid
Molten carbonate fuel cells	500 - 800	Liquid
Direct methanol fuel cells	100	Solid
Proton exchange fuel cells	60 - 100	Solid

Fuel cells can be successfully applied in electricity generation, distributed and portable power generation. A single fuel cell isn't enough to power most devices, therefore fuel cell manufacturers stack them together in a series, hence the name "fuel cell stack". The greater the number of fuel cells in the stack, the higher is the output voltage, and the greater the area of the electrodes, the greater is the current [10]. Since fuel cells can generate power from a fraction of a watt to hundreds of kilowatts, they can be used in almost any application, from stationary power to vehicles of all sizes down to mobile phones, as summarised in Table 1.2. Fuel cell applications can be categorized into four main groups: transportation, stationary power, backup power, and portable power. PEM fuel cells are suitable for all types of applications [2].

The research has been focusing on fuel cells as replacements for internal combustion engines in vehicles. The major driving forces for development of automotive fuel cell technology are their efficiency, low or zero emissions, and fuel that could be produced from indigenous sources rather than imported. The operating time of a vehicle is in the order of 3000 to 5000 hours. The fuel cells for automotive

applications are capable to have a similar lifetime. Buses are considered the most likely type of vehicles for commercializing the fuel cell technology. The expected lifetime of bus engines is higher, because a typical city bus may operate more than 6000 hours per year with a lot of starts and stops. The longer required lifetime and intermittent operation pose a challenge to fuel cell durability [1].

**Table 1.2** Application areas of PEM fuel cells [2].

<b>Level of power</b>	<b>Applications</b>
> 1 MW	Local distributed power station
100 kW–1 MW	Large transportation vehicles: naval ships, submarines, and buses; small portable power station; small stationary power station
10 kW–100 kW	Transportation vehicles: cars and mid-size buses; backup power for mid-size communication station; small power station
1 kW–10 kW	Transportation vehicles: motorcycles, utility vehicles, cars, yachts; various portable power devices used for field working, underwater platform; backup power; uninterruptible power, residential power system
100 W–1 kW	Simple riding devices: bicycles, scooters, and wheelchairs; backpack power; power for exhibition or demo; UPS for small services, terminals, and computers
10 W–100 W	Portable power: for emergency working power supply and military equipment; battery replacements; lighting; signal light power
< 10 W	Small portable power device; cell phone

Applications in stationary power generation include both large-scale utility plants and smaller scale systems, for example, distributed electricity and heat generation in buildings and individual homes [2]. The stationary power fuel cells are expected to operate 40,000 to 80,000 hours (5 to 10 years). Since hydrogen as a fuel is not readily available, fuel cell systems should have a fuel processing section. The majority of contemporary stationary power fuel cell systems use natural gas or propane as fuel. For some applications liquid fuels may be preferable such as fuel oil, gasoline, diesel, methanol, or ethanol [1].

Backup power is a device that provides instantaneous, uninterruptible power. Typical applications for backup power include telecommunications systems, information technology and computer systems, manufacturing processes, security

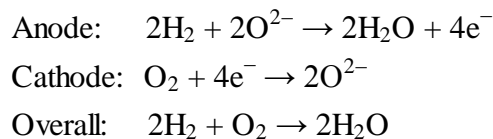
systems, utility substations, and railway applications [1]. Normally, backup power devices use hydrogen as fuel. The operational lifetime requirement for a backup power fuel cell is less than 2,000 hours [2].

Small portable power fuel cells may be divided into two main categories: (i) battery replacements and (ii) portable power generators. They are applied in portable computers, communication and transmission devices, power tools, remote meteorological or other observation systems, and in military gadgets. The critical issue for portable applications is the fuel and its storage. Hydrogen is rarely used because of bulkiness or weight of its storage, and hydrides are used instead. However, such fuel cells must be equipped with suitable reactors where hydrogen is released from hydrides in controlled chemical reaction. Most portable fuel cells use methanol as fuel, or more precisely methanol aqueous solutions, either directly (DMFCs) or via micro-reformers [1].

### 1.2.1 Solid Oxide Fuel Cells

Solid oxide fuel cells (SOFCs) operate at 600-1000 °C and have an electrolyte that is a solid, non-porous metal oxide, usually Y<sub>2</sub>O<sub>3</sub>-stabilized ZrO<sub>2</sub>. The cell is constructed with two porous electrodes that comprise an electrolyte between them. The anode is typically a Ni-ZrO<sub>2</sub> cermet, and the cathode is Sr-doped LaMnO<sub>3</sub> [7]. The fuel can be, for example, hydrogen, CO, or CH<sub>4</sub>, and the oxidant can be CO<sub>2</sub>, O<sub>2</sub>, or air [8].

When an oxygen molecule contacts the cathode/electrolyte interface, it acquires electrons from the cathode. The oxygen ions diffuse into the electrolyte material and migrate to the other side of the cell where they contact the anode. The oxygen ions encounter the fuel at the anode/electrolyte interface and react catalytically, producing water, carbon dioxide, heat, and electrons. The electrons transport through the external circuit, providing electrical energy [7]. The basic reactions at the electrodes are as follows [8]:



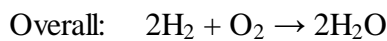
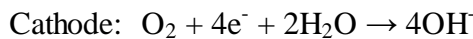
SOFCs have a number of advantages over the other fuel cell types. They allow conversion of a wide range of fuels, including various hydrocarbon fuels. SOFC produce minimal air pollutant emissions and low greenhouse gas emissions. They are not poisoned by carbon monoxide and process it almost as efficiently as hydrogen. SOFCs also benefit from reduced activation voltage losses due to their high operating

temperature. The voltage losses are dominated by the ohmic component [9]. These capabilities have made SOFC an attractive technology for stationary power generation in the 2 kW to 100s MW capacity range [7].

The disadvantages of SOFCs are mostly associated with their high operating temperature (safety, fuel economy). Additional problems arise because the ceramic electrolyte and electrodes are extremely brittle. This is a major disadvantage for vehicular applications where vibrations are common. Thermal cycling further stresses the ceramics and is a major concern for planar fuel cells [9].

### 1.2.2 Alkaline Fuel Cells

Alkaline fuel cells (AFCs) utilize potassium hydroxide (KOH) as an electrolyte of variable concentration, either in aqueous solution or stabilized matrix form. The KOH concentration varies with the operating temperature, increasing from 35 wt% for low temperatures to about 85 wt% for high temperatures. The electrolyte is contained in a porous asbestos matrix, and the catalysts are typically made of nickel and silver [8]. The ion carried by the alkaline electrolyte is a hydroxide ion ( $\text{OH}^-$ ). The half reactions are as follows [9]:



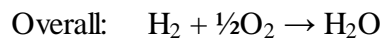
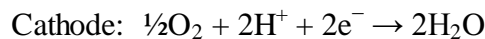
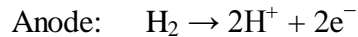
In AFCs, water is formed on the hydrogen electrode and is also needed at the cathode for the oxygen reduction [9]. AFCs are capable of operating over a wide range of temperatures and pressures from 80 to 230°C and 2.2 to 45 atm. High-temperature AFCs use highly concentrated electrolyte, so that the ion transport mechanism changes from aqueous solution to molten salt.

The advantage of AFCs is the capability of achieving very high efficiencies because of the fast kinetics allowed by the hydroxide electrolyte. The oxygen reaction ( $\text{O}_2 \rightarrow \text{OH}^-$ ) in alkaline media is much easier than the oxygen reduction in acidic media. As a result, the activation voltage losses in AFCs are very low. The fast kinetics in AFCs also allows using relatively inexpensive silver or nickel as catalysts, and the cost of the fuel cell stack is thus greatly reduced. However, the greatest problem of AFCs is the increased risk of leakage: potassium hydroxide is highly corrosive and has a natural tendency to leak even through the tightest seals. Another problem is the risk of internal electrolytic short-circuit between two cells if the electrolyte is circulated too vigorously or if the cells are not isolated enough. [9].

Alkaline anion exchange membrane fuel cells (AAEMFCs) are a type of AFCs that is garnering renewed attention. The difference of AAEMFCs from the AFCs is that they employ a solid polymer electrolyte rather than aqueous KOH electrolyte. In this polymer electrolyte, cations are fixed to polymer chains and do not move freely as in the liquid electrolyte. This prevents the deposition of carbonates ( $K_2CO_3$  and  $KHCO_3$ ) on the electrodes and hence the destruction of the catalyst layer. However, the drawback of the AAEMFC is low ionic conductivity and poor chemical stability of the anionic polymer membrane, as well as the impact of its fabrication on the environment [11].

### 1.2.3 Phosphoric Acid Fuel Cells

Phosphoric acid fuel cell (PAFC) was the first fuel cell technology to be commercialized [7]. In PAFCs, the electrolyte is concentrated phosphoric acid ( $H_3PO_4$ ), which allows operation at temperatures over  $100^\circ C$ . The phosphoric acid electrolyte is contained in a silicon carbide matrix, and catalysts are typically made of platinum. Hydrogen-rich fuel is supplied to the anode, where protons and electrons split and start travelling to the cathode, following different pathways through the membrane layer (protons) and via an external circuit (electrons), producing electricity. At the cathode, they combine with oxygen, and water and heat are obtained as by-products [8]:



Although PAFC is the first technology to be marketed, it has a few drawbacks. Basic ones are expensive catalysts (platinum), corrosion by the acidic electrolyte, carbon monoxide poisoning and low efficiency. Additionally, the phosphoric acid electrolyte temperature must be kept above  $42^\circ C$ , which is its freezing point. Freezing and unfreezing the acid unacceptably stresses the fuel cell stack, while keeping it about  $150^\circ C$  is energy consuming, requires extra hardware and adds to the fuel cell cost, complexity, weight, and volume. Most of these issues are minor in the case of stationary applications but are incompatible with a vehicular application. The advantages of PAFCs are utilising the cheap electrolyte, relatively low operating temperature, and reasonable start-up time [9].

### 1.2.4 Molten Carbonate Fuel Cells

Molten carbonate fuel cells (MCFC) operate at 600–700°C. The high operating temperature is needed to achieve sufficient conductivity of the carbonate electrolyte [7]. The electrolyte of the molten carbonate fuel cell is a molten mixture of alkali metal carbonates, usually a binary mixture of lithium and potassium, or lithium and sodium carbonates, which is retained in a ceramic matrix of  $\text{LiAlO}_2$  [12].

Carbon dioxide ( $\text{CO}_2$ ) and oxygen are supplied to the cathode and become converted to carbonate ions  $\text{CO}_3^{2-}$ , which provide the means of ion conduction between the cathode and the anode, as shown in Figure 1.2. At the anode, the carbonate ions are oxidized back into carbon dioxide. Therefore, there is a net transfer of carbon dioxide from cathode to anode in MCFCs [12].

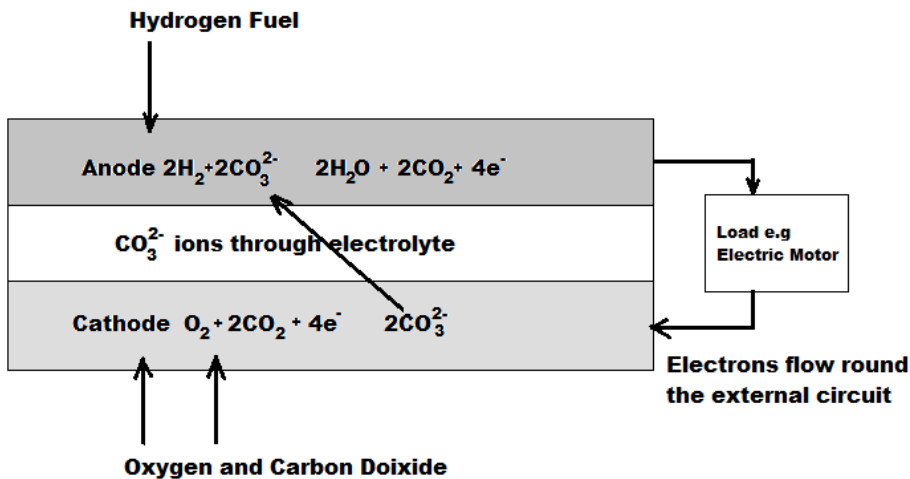


Figure 1.2 Basic Principle of MCFC [12].

A benefit associated with high temperature of MCFCs is the use of low-cost metal components for the electrodes [7]. Further, the fuel for MCFCs is not pure hydrogen, but a mixture of hydrogen with hydrocarbons. The common major advantage of high-temperature fuel cells is their capability to process hydrocarbon fuels directly because the high temperature allows steam reforming of fuel to hydrogen on the electrodes. In addition, high temperatures enhance the kinetics, so that cheap catalyst materials can be used. In summary, the major advantages of MCFCs are the use of hydrocarbon fuels, low-cost catalysts, improved efficiency due to fast kinetics and low sensitivity to poisoning [9].

However, MCFCs pose many problems due to the nature of their electrolytes and the required operating temperatures. The carbonate is an alkali, and is extremely corrosive, especially at high temperatures. The additional fuel consumption associated with heating up the fuel cell is also a problem, worsened by the very high operating temperatures. These problems confine molten carbonate fuel cells to stationary or

steady power applications such as ships. In summary, the major disadvantages of MSFCs are slow start-up and power response, reduced material choice due to high temperature, complex fuel cell system due to CO<sub>2</sub> cycling, and corrosive electrolyte [9].

### 1.2.5 Direct Methanol Fuel Cells

A direct methanol fuel cell (DMFC) is essentially a polymer membrane fuel cell that uses methanol instead of hydrogen as a fuel [1]. The DMFC allows for the direct use of an aqueous, low-concentration (3%) liquid methanol solution as the fuel. Air is the oxidant. As illustrated in Figure 1.3, methanol and water react directly in the anode chamber of the fuel cell to produce carbon dioxide and protons that permeate the polymer electrolyte membrane and react with the oxygen at the cathode [13]. The half-cell reactions are as follows [14]:

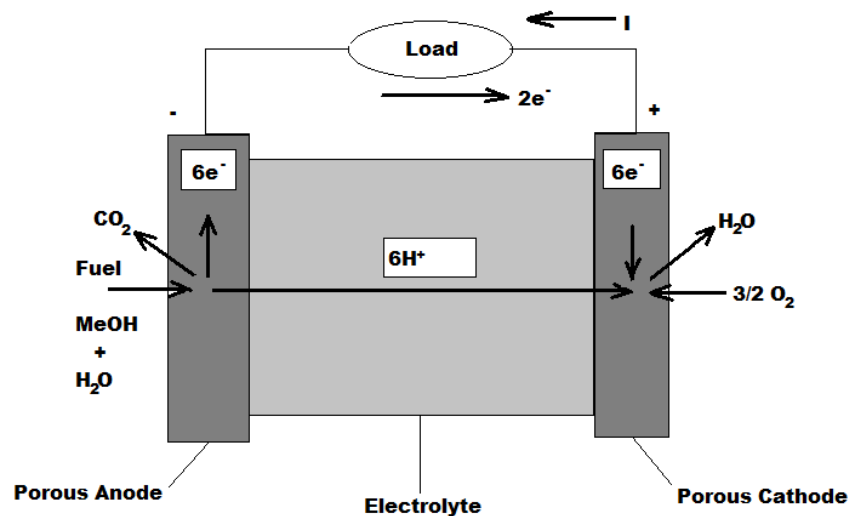
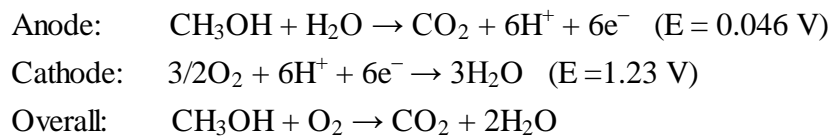


**Figure 1.3** Basic Principle of DMFC [13].

The use of gaseous hydrogen as a fuel presents a number of practical problems, including storage system weight and volume, as well as handling and safety issues, especially for consumer and transportation applications [13]. Therefore, the advantage of DMFC is that its fuel has a relatively high energy density and is a liquid under ambient conditions. However, several problems with the DMFCs result from the cross-over of neutral methanol and its decomposition products from the anode to the cathode side, poisoning the cathode catalyst and causing high voltage losses. In

addition, there are high anode voltage losses due to the slowness of the anode electrochemical reaction [7].

### 1.2.6 Proton Exchange Membrane Fuel Cells

Proton exchange membrane, or polymer electrolyte membrane, fuel cells (PEM fuel cells) use hydrogen as fuel, oxygen or air as oxidant, and a solid polymer membrane as electrolyte [8]. The core of a PEM fuel cell is a polymer membrane that has some unique capabilities. It is largely impermeable to gases but it conducts protons (hence the name, proton exchange membrane). The membrane acts as the electrolyte and is placed between two porous, electrically conductive electrodes. These electrodes are typically made of carbon cloth or carbon fibre paper. At the interface between the porous electrode and the polymer membrane there is a layer with catalyst particles, typically platinum supported on carbon [1].

Figure 1.4 shows the operation principle of PEM fuel cells. Protons, formed from hydrogen at the anode side, travel through the membrane to the cathode side. The electrons travel through electrically conductive electrodes, current collector plates and through the external circuit where they perform useful work (direct electrical current) and come back to the cathode side. At the cathode side, the electrons combine with the protons that went through the membrane and oxygen that is fed to the cathode. Water is created in the electrochemical reaction, and then pushed out of the cell with excess flow of oxygen. [1].

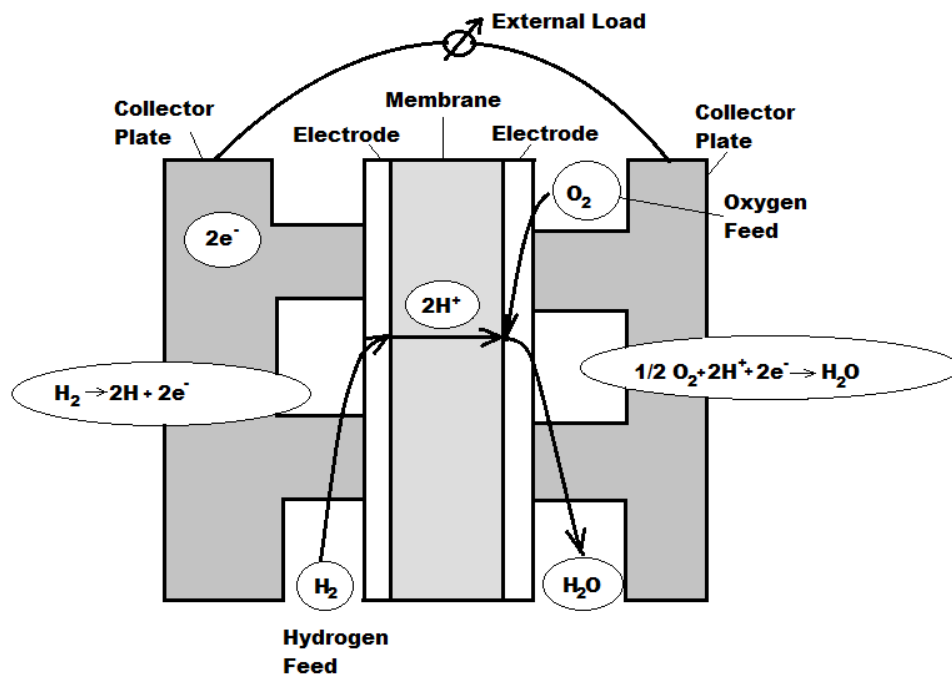
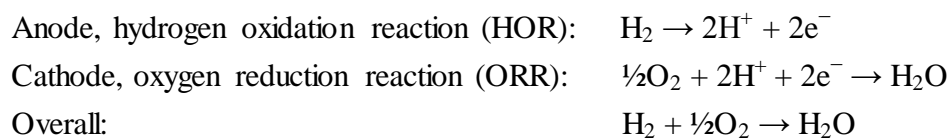


Figure 1.4 Basic Principles of PEM Fuel Cell [1].

The electrochemical reactions on the electrodes in PEM fuel cells are following [8]:



Proton exchange membrane fuel cells have such advantages over the other fuel cell types as high power density and simple design, and therefore are considered to be likely candidates for replacement in all power generation areas, i.e. portable, auxiliary, stationary and automotive power systems [5]. Especially PEM fuel cells are attractive in transport applications, which is confirmed by the fact that since the year 2000 more than 90% of all fuel cell vehicles have been equipped with a PEMFC [15]. However, commercialization of PEM fuel cells is hindered by the particularly high cost of their components, namely, by the electrode catalysts which contain precious metals such as platinum, and the membrane. [1].

### **1.3 Components of Proton Exchange Membrane Fuel Cells**

Since proton exchange membrane fuel cells are investigated in this thesis, their main components and processes are overviewed in the following section, the basic constituent parts of PEM fuel cells are the membrane, electrodes (catalyst layers), gas diffusion layers, and current collectors.

#### **1.3.1 Membrane**

The core of a PEM fuel cell is the polymer electrolyte membrane. [16]. The main function of the membrane is to transport protons from the anode to the cathode; it is possible owing to the membrane polymers which have sulfonic groups and facilitate the transport of protons. The other functions include keeping the fuel and oxidant separated and withstanding harsh conditions, including active catalysts, high temperatures or temperature fluctuations, strong oxidants, and reactive radicals. Thus, the ideal polymer must have excellent proton conductivity, chemical and thermal stability, strength, flexibility, low gas permeability, low water drag, low cost, and good availability [2]. Although the polymer electrolyte membranes are ionic conductors, they do not conduct electrons. The organic nature of the polymer electrolyte membrane structure makes them electronic insulators. As electrons cannot move through the membrane, the electrons produced at one side of the cell must travel through an external wire to the other side of the cell to complete the circuit [16].

The membrane in PEM fuel cells is a type of plastic, a polymer, in which negative ions are rigidly held within the polymer structure, and only positive ions are mobile and carry positive charge through the membrane. In PEM fuel cells, these positive ions are hydrogen ions, or protons. Movement of the hydrogen ions through the membrane in one direction only, from anode to cathode, is essential to a PEM fuel cell operation [16].

One of the most widely used membranes today is Nafion<sup>®</sup>, a polymer created by the DuPont Company. As shown in Figure 1.5, Nafion<sup>®</sup> is a copolymer of tetrafluoroethylene and sulfonyl fluoride vinyl ether and has a semi-crystalline structure. This structure, which resembles Teflon<sup>®</sup>, gives Nafion<sup>®</sup> long-term stability in oxidative or reductive conditions [2]. The Teflon<sup>®</sup>-like component provides mechanical strength and dimensional stability, while the perfluorosulfonic acid component provides proton conductivity [1].

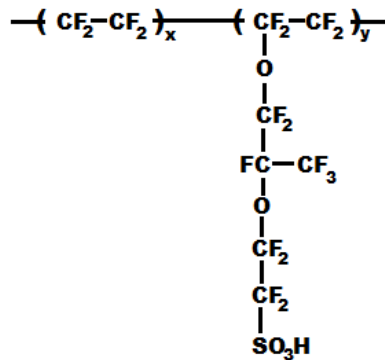


**Figure 1.5** Chemical structure of Nafion<sup>®</sup> membrane [1].

The sulfonyl group SO<sub>3</sub>H has an ionic bond, so the end of the polymer side chain with the sulfonyl group is actually an SO<sub>3</sub><sup>2-</sup> ion with an H<sup>+</sup> ion. Such a polymer is also called an ionomer. The Teflon<sup>®</sup>-like backbone is highly hydrophobic, while the sulfonyl group is highly hydrophilic. Because of their ionic nature, the sulfonyl groups of the side chains tend to cluster, and thus hydrophilic regions are created within the overall structure of the membrane. This is why the membrane can absorb relatively large amounts of water, in some cases up to 50% by weight. Movement of the H<sup>+</sup> ions within the well-hydrated regions makes these membranes proton conductive [1].

### 1.3.2 Electrodes – Catalyst Layers

The membrane in PEM fuel cells is sandwiched between two electrodes. The electrodes are essentially thin catalyst layers pressed between the membrane and porous, electrically conductive substrate. The catalyst layer is the layer where the

electrochemical reactions take place. More precisely, the electrochemical reactions occur on the catalyst surface [1].

Figure 1.6 shows the structure of the electrode – membrane interface. A catalyst layer consists of a porous, three-dimensional structure, with a thickness of 5–30  $\mu\text{m}$ . In supported catalyst layers, the 2–10 nm catalyst particles are physically supported on considerably larger, 45–90 nm carbon particles [5]. The carbon particles contact the polymer electrolyte membrane on one side, and the gas diffusion layer (GDL) on the other [12]. Typically, both electrodes can be applied as thin films and transferred to the membrane or applied directly to the membrane. Alternatively, the catalyst-electrode layer may be deposited onto the GDL and then attached to the membrane [7].

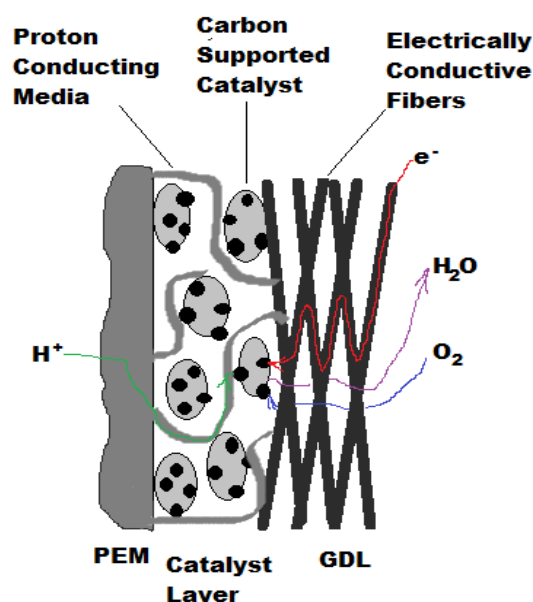


**Figure 1.6** Transport of reactants, products, protons, and electrons in a PEM fuel cell cathode [3].

The catalyst layer is the most complex structure in PEM fuel cells. It must have high electrochemically active surface area and enable facile transport of ions, electrons, reactants, and products [5]. All these species must have access to the catalyst surface [1]. As discussed previously in Section 1.2.6, protons, produced by the oxidation of hydrogen on the anode, are transported through ion conducting polymer membrane to the particles of the cathode catalyst layer. Electrons produced on the anode are transported through the electrically conductive portion of the anode catalyst layer to the anode gas diffusion layer, then to the collector plate, then through an electric load, and finally to the cathode catalyst layer. Gaseous reactants are transported by both diffusion and advection through pores in the catalyst layers.

Liquid water at the cathode is transported through the pores out of the cell along with the excess oxygen [3].

Water is a product of the fuel cell reaction and is carried out of the cell during its operation. However, both the fuel and air entering the fuel cell still must be humidified. This additional water keeps the polymer electrolyte membrane hydrated, and the humidity of the gases must be carefully controlled. Too little water prevents the membrane from conducting the  $H^+$  ions well, and the cell current drops. If the air flow at the cathode is too slow, it cannot carry all the water produced out of the fuel cell, and the cathode “floods”. The cell performance is hurt because not enough oxygen is able to penetrate the excess liquid water to reach the cathode catalyst sites. Thus, “water management” is the key to effective operation of a PEM fuel cell [16].

The best catalyst for both the anode and the cathode so far is platinum; very small particles of which are adsorbed on the surface of larger particles of carbon. Protons, electrons and the reactant gases are involved in the electrode reactions, which take place at the three-phase boundary, namely, ionomer, solid, and void phases, as shown in the Figure 1.7. This active boundary has an infinitesimally small area. However, in practice, some gas may permeate through the polymer, and therefore the reaction zone is larger than a three-phase boundary line [1, 3].

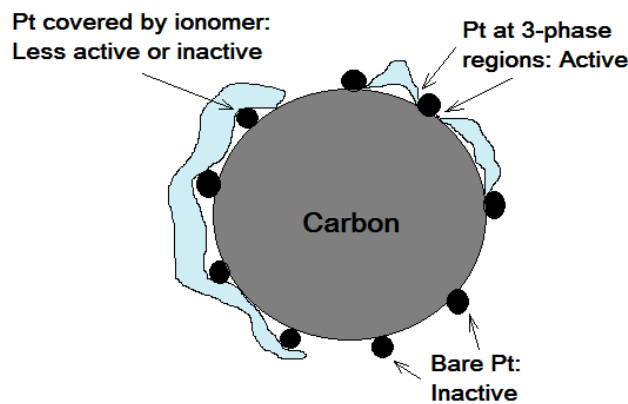


**Figure 1.7** Schematic carbon-supported catalyst particle covered with the thin electrolyte layer [3].

The first generation of PEM fuel cells used platinum black catalysts with loadings of  $4 \text{ mg/cm}^2$  that exhibited excellent long-term performance, but at a prohibitively high cost. A significant amount of research has been directed at reducing platinum loading below  $0.4 \text{ mg/cm}^2$ , and the loadings as low as  $0.014 \text{ mg/cm}^2$  have been achieved [17]. However, development of low cost electrodes is a key issue for the commercialization of PEM fuel cells, particularly given that platinum, presently considered the most effective catalyst, is expensive and in limited supply [18]. In addition, although platinum exhibits superb activity as a catalyst, it suffers from

several drawbacks. For example, platinum is extremely reactive toward and can be poisoned by a variety of contaminants such as halide anions, methanol, carbon monoxide/carbon dioxide via reverse water gas shift reaction, and ubiquitous organics [19]. Therefore, in recent years, the exploration of cost efficient non-noble metal catalysts with the purpose to replace expensive platinum has become a hot research area worldwide [20].

In the effort to develop non-noble catalysts, in particular for the oxygen reduction reaction at the cathode, which is kinetically much slower than the anode hydrogen oxidation reaction, various materials have been explored [20]. Among different non-noble metal catalysts for the PEM fuel cell cathodes, such as pyrolyzed iron/cobalt and nitrogen containing complexes, transition metal chalcogenides, transition metal oxides/carbides/nitrides/oxynitrides/carbonitrides, and enzymatic compounds, pyrolyzed transition metal and nitrogen containing complexes supported on carbon materials are considered the most promising. Unfortunately, when compared to platinum based catalysts in an acidic environment; these promising catalysts still display insufficient activity and stability as cathodes for PEM fuel cells. Therefore, improving the catalytic activity and stability of non-noble metal catalysts is a high priority in PEM fuel cell catalyst development [21].

### **1.3.3 Gas Diffusion Layers**

The layer between the catalyst layer and bipolar plate in PEM fuel cells is called a gas diffusion layer (GDL) [1]. GDLs are critical components in PEM fuel cells. They have three main functions. The first is to allow transport of gases and water to and from the catalyst, and the porous nature of the GDL facilitates this. The second main function is to provide an electrical and thermal connection between the carbon-supported catalyst and the bipolar plate or other current collectors. The third function is to provide structural support for the catalyst layers [2].

Typically, GDLs consist of a woven carbon cloth or a nonwoven fibre paper. The carbon fibre in GDLs is hydrophilic and thus absorbs liquid water into the porous structure, which may result in flooding of a PEM fuel cell. To eliminate the flooding, a hydrophobic additive, typically polytetrafluoroethylene (PTFE, Teflon<sup>®</sup>), is applied onto the carbon fibre to prevent pore blockage with water and manage the internal water distribution. Since the base carbon fibre material is hydrophilic, the resulting Nafion<sup>®</sup> treated GDL is a mixed hydrophobic–hydrophilic structure with channels favouring gas-phase and liquid phase transport, despite the overall hydrophobic behaviour of the surface. The GDLs are characterized mainly by their thickness, porosity, and electrical conductivity [5].

In the addition, a highly dense and hydrophobic microporous layer (MPL) is commonly applied onto a GDL to improve water management. The MPL can be physically bonded to the catalyst layer or GDL inner surface but resides between the catalyst layer and the GDL [5].

### 1.3.4 Flow Fields – Current Collectors

The plates pressed against the outer surface of each GDL serve the dual role of flow field and current collector. In a single fuel cell, these two plates are the last of the components making up the cell. The plates are made of a light-weight, strong, gas-impermeable, electron-conducting material. Graphite or metals are commonly used, although composite plates are now being developed [16]. The bipolar plates comprise almost all the volume of the fuel cell stack (because the membrane electrode assemblies are very thin) and constitute typically about 80% of the mass [12].

As most applications require much higher voltages than that of a single fuel cell, the required voltage is obtained by connecting individual fuel cells in series to form a fuel cell “stack”. If fuel cells were simply lined-up next to each other, the anode and cathode current collectors would be side by side. To decrease the overall volume and weight of the stack, instead of two current collectors, only one plate is used with a flow field cut into each side of the plate, as illustrated in Figure 1.8. This type of plate, called a “bipolar plate”, separates one cell from the next, with this single plate serving to carry hydrogen gas on one side and air on the other [16].

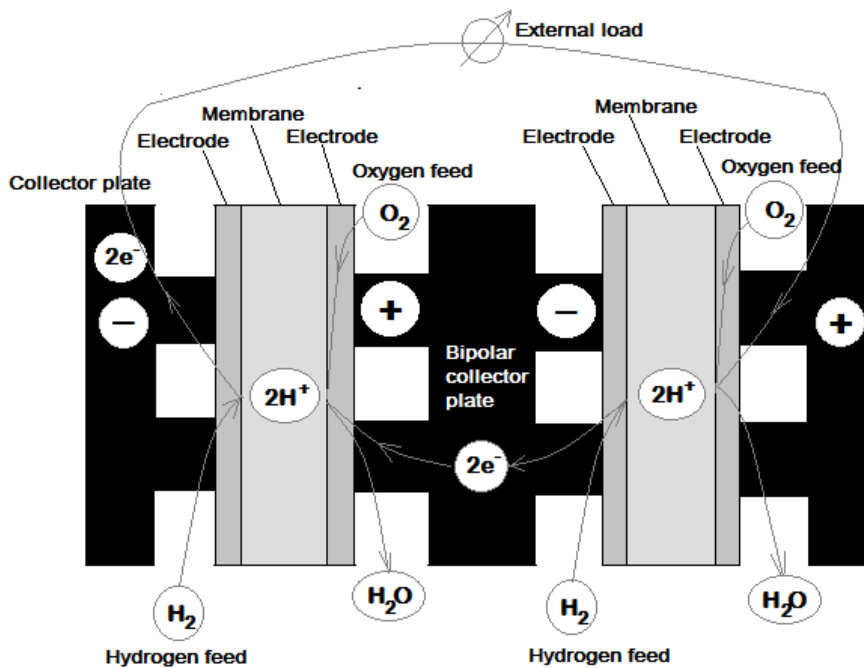
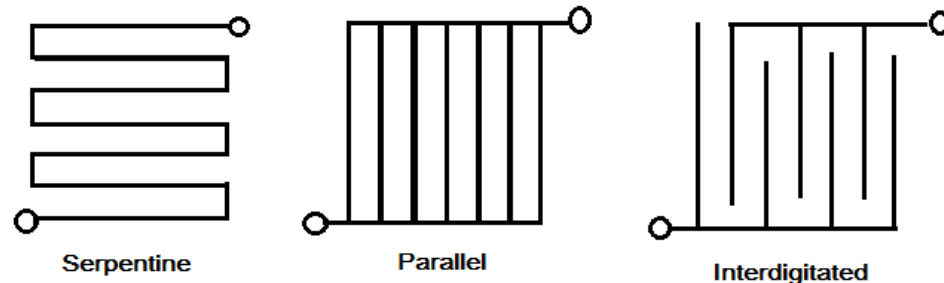


Figure 1.8 Bipolar plate connects and separates two adjacent cells [1].

The bipolar plates have several functions in a fuel cell stack. Their required properties follow from their functions:

- (i) They connect cells electrically in series and conduct current - therefore, they must be electrically conductive [1, 16].
- (ii) They separate the gases in adjacent cells - therefore, they must be impermeable to gases [1].
- (iii) They conduct heat from active cells to the cooling cells or conduits - therefore, they must be thermally conductive [1].
- (iv) They must be able to resist a temperature of 80°C or more, high humidity, and an electrical potential [2].

The side of the bipolar plate next to the GDL contains channels machined into the plate. The channels are used to carry the reactant gas from the point at which it enters the fuel cell to the point at which the gas exits. The pattern of the flow field in the plate as well as the width and depth of the channels have a large impact on the effectiveness of the reactant gases distribution across the membrane electrode assembly. Flow field design also affects water supply to the membrane and water removal from the cathode [16]. Some basic fuel cell flow channel designs are illustrated in the Figure 1.9. Most standard fuel cell designs are a combination of parallel and serpentine channels [5].



**Figure 1.9** Schematics of some common flow field patterns [5].

## 1.4 Research Objectives

One of the hurdles for PEM fuel cell commercialization is that the cost remains too high for wide-spread use of PEM fuel cells. The current state of the art cathode catalysts are based on platinum, which represent the main component to the fuel cell cost [8]. In a PEM fuel cell stack, 56% of the cost comes from the platinum-based catalyst layers which are required both at the anode to catalyze the hydrogen oxidation reaction and at the cathode to catalyze the oxygen reduction reaction [22]. The cathode requires much more platinum than the anode due to the slow rate of oxygen

reduction reaction which is kinetically much slower than the hydrogen oxidation at the anode [23, 24]. Another drawback of platinum-based catalysts is their high sensitivity to contaminants that impacts reliability of PEM fuel cells. [8]. Finally, degradation of platinum based catalysts such as dissolution or sintering of platinum particles is a problem for PEM fuel cell durability [25].

For PEM fuel cell cost reduction, the search for inexpensive, high performance cathode catalysts has taken two different approaches. The first approach is reduction of platinum catalyst usage that can be achieved by alloying platinum with inexpensive metals, e.g. cobalt or iron, and/or by utilizing unique support materials for platinum nanoparticle deposition [22]. However, despite platinum loading has been reduced significantly, the increasing price of platinum renders the efforts ineffective in the last two decades [22, 26]. Therefore, this approach may not be the long-term solution for cost reduction of PEM fuel cells [22, 23]. The other approach is to develop alternatives to platinum, referred to as non-precious catalyst materials [22]. Catalysts free from noble metals have recently attracted much attention [26].

The challenge is that the performance of the best non-precious cathode catalysts is still inferior when compared to platinum in terms of both activity and stability. For a practical non-precious cathode catalyst for PEM fuel cells, the activity and stability goals for 2015 are that the activity must reach a volumetric current density of  $300 \text{ A cm}^{-3}$  at 0.8 V, and the stability must reach 5000 hours at operating temperatures below  $80 \text{ }^\circ\text{C}$ . Despite significant progress in the field, both the activity and stability requirements have not been met yet, and there is still a long way to go in order to reach the practical usage of non-precious cathode catalysts in PEM fuel cell applications [22]. The objective of this thesis is investigation and development of alternative to platinum inexpensive catalysts for cathodes in PEM fuel cells in the effort to meets the cost, performance and durability requirements.

## **Chapter 2**

# **Review of Theoretical and Experimental Studies of Cathode Catalysts and the Oxygen Reduction Reaction**

### **2.1 Introduction**

In PEM fuel cells, the oxygen reduction reaction (ORR) occurs at the cathode side on the catalyst surface and is classified as heterogeneous catalysis. For this reason, the cathode catalysts and the oxygen reduction on them are inextricably connected and investigated jointly. The investigation methods reported in the literature are both theoretical and experimental. The theoretical methods enable us to obtain information on catalysts at the atomic level, of which the most important is the structure of the catalysts and the mechanisms of the ORR, including such thermochemical characteristics as reaction energies, activation energies, electrode potentials, etc. The experimental methods focus on the techniques of development of the catalyst materials, measuring their voltaic performance, e.g. current, voltage or power produced in the electrochemical reactions, and elucidating the nature and structure of the catalysts surface using physicochemical methods of investigation. Theoretical and experimental methods are complementary. Understanding the catalytic oxygen reduction at the atomic level can potentially be used in experimental design and development of catalyst materials. In turn, the experimental methods provide essential information, serving as a basis for theoretical studies, e.g. the chemical nature of the catalyst materials and the favoured reaction pathway.

This chapter reviews the theoretical achievements in elucidating the ORR mechanism with various catalyst models, focusing mostly on non-precious materials, which are reported to deliver the best performance to the date. In connection with this, basic theoretical principles of thermodynamics and kinetics of the catalytic oxygen reduction and general concepts of computational chemistry are described. The sections on experimental investigation of cathode catalysts covers the most significant classes of the catalyst materials, including platinum based.

## 2.2 Oxygen Reduction Reaction

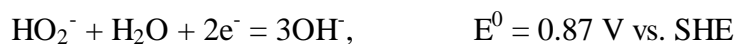
### 2.2.1 Thermodynamics

The oxygen reduction is a multi-step electrochemical reaction, which can occur both in acid and alkali media. The ORR in alkaline media takes place in AFCs, and the ORR in acid media occurs in PAFCs and PEM fuel cells, as discussed in Chapter 1. The oxygen reduction reaction can be either four-electron, or two-electron. The overall reactions with the standard electrode potentials are well known and can be found elsewhere [27, 28]. It follows from these equations that the four-electron oxygen reduction in acid media can yield a substantially higher potential than in alkaline media (1.23 V versus 0.4 V), which is highly beneficial for application in fuel cells. However, it is well known that the ORR is intrinsically much more active in alkaline media than in acid [29]. The following reactions summarize the processes that occur in acid and alkaline media:

Acid media:



Alkaline media:



In acid media, the ORR includes interaction between an oxygen molecule, four protons and four electrons. The reaction mechanism has a number of elementary steps, different reaction intermediates and pathways. In PEM fuel cells, the four-electron pathway of the oxygen reduction yields water, while the two-electron reduction pathway produces hydrogen peroxide, as shown in Figure 2.1. Formation of hydrogen peroxide is not desirable, since it not only reduces the efficiency of the electrochemical reaction, but also deteriorates the catalyst and the cell because of its high reactivity. Hydrogen peroxide can be further reduced to water [2].

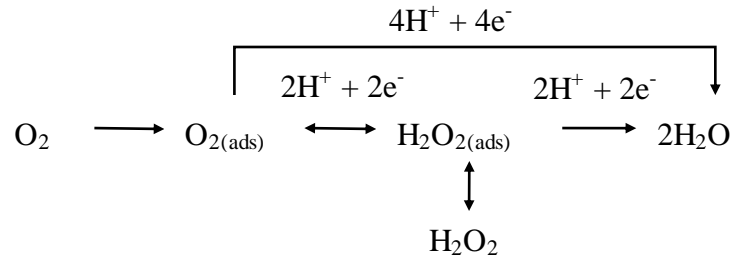


**Figure 2.1** Oxygen reduction reaction pathways [2].

In the absence of the catalyst, the reaction between hydrogen and oxygen in the gas phase is known as hydrogen combustion, which is a highly exothermic process. The energy, or enthalpy, of this chemical reaction is  $286 \text{ kJ mol}^{-1}$  at  $25 \text{ }^\circ\text{C}$ . In a PEM fuel cell, a portion of the reaction enthalpy is converted into useful work – electricity [1]. In fuel cells, this work is the electrical work proportional to the electrode potential. At constant temperature and pressure, the maximal useful work produced by a reacting system is the change in the Gibbs free energy (also known as free energy):  $W = -\Delta G$ , and the dependence of the Gibbs energy change on the electrode potential is expressed as follows [30]:

$$\Delta G = -nFU \quad (2.1)$$

where  $\Delta G$  is the change in the standard Gibbs free energy,  $n$  is number of electrons transferred in the reaction,  $F$  is the Faraday constant, and  $U$  is the reversible potential. For the oxygen reduction over an ideal catalyst, the standard reversible potential, or equilibrium potential  $U^\circ = 1.229 \approx 1.23 \text{ V}$  [1]. The Gibbs free energy is defined from other thermodynamic properties, enthalpy and entropy:

$$G = H - TS \quad (2.2)$$

where  $H$  is the enthalpy,  $T$  is temperature,  $S$  is the entropy. For a spontaneous process, the change in the Gibbs free energy  $\Delta G \leq 0$ .

In several theoretical studies [31-37], the Gibbs free energy includes a linear dependence on the electrode potential according to the technique proposed by Norskov et al. [38]. In this method, the Gibbs free energy of the reaction  $\text{H}^+ + \text{e}^-(U) \rightarrow \text{H}$  is postulated to be as follows:

$$G(\text{H}^+ + \text{e}^-) = \frac{1}{2}G(\text{H}_2) - eU \quad (2.3)$$

where  $G(\text{H}^+ + \text{e}^-)$  is the Gibbs free energy of an aqueous proton and electron,  $G(\text{H}_2)$  is the Gibbs free energy of a gas-phase hydrogen molecule,  $|e|=1.602 \cdot 10^{-19}$  C is the elementary charge, and  $U$  is the electrode potential.

For a reaction which includes an electron transfer step,  $\text{A} + \text{H}^+ + \text{e}^-(U) \rightarrow \text{AH}$ , the Gibbs free energy is given by:

$$\Delta G = \Delta H - T\Delta S + eU - pHk_{\text{B}}T \ln 10 \quad (2.4)$$

where  $\Delta G = G(\text{AH}) - G(\text{A}) - 1/2G(\text{H}_2)$  is the Gibbs free energy of the proton transfer reaction,  $\Delta H$  is the enthalpy change,  $\Delta S$  is the entropy change,  $pH$  is the  $pH$  value,  $k_{\text{B}}$  is the Boltzman constant. In acid media,  $pH = 0$ , and therefore the last term in Equation  $\Delta G = \Delta H - T\Delta S + eU - pHk_{\text{B}}T \ln 10$  (2.4) is nullified. In computational chemistry, the enthalpy is calculated as a sum of the two terms:

$$H = E + ZPE \quad (2.5)$$

where  $E$  is the calculated electronic energy, and  $ZPE$  is the calculated zero point energy correction. Thus, the Gibbs free energy of an electron transfer reaction is calculated as follows:

$$\Delta G = \Delta E + \Delta ZPE - T\Delta S + eU \quad (2.6)$$

The change in the Gibbs free energy of a single electron transfer reaction is obtained based on the calculated changes in the electronic energy,  $ZPE$  correction and entropy. The Gibbs free energy change in a multi-electron reaction can be also obtained by calculating the potential-dependent Gibbs free energy of each species participating in an electron transfer reaction [35]:

$$G(U) = H - TS = E + ZPE - TS + x\left(\frac{1}{2}G(\text{H}_2) - eU\right) \quad (2.7)$$

where  $x$  is the number of electrons/protons transferred in the overall multi-electron reaction.

Another way to account for the effect of an electric field is to specify it in simulations. Since there is a double electric layer at the boundary of the catalyst and electrolyte, it can be idealistically be approximated by a plane capacitor. The electric field correction has been implemented in theoretical studies of the oxygen reduction on a platinum surface [34, 35], and Yeh et al. [34] modelled the electric field at the electrode with a thickness of 3 Å.

The electric field  $E$  is defined by the electrode potential  $U$  and the thickness of the electric double layer  $d$ :  $E = U/d$ . Figure 2.2 illustrates the electric field gradient  $E$  as a function of the electric double layer thickness  $d$  at the constant electrode potential  $U = 1.23$  V. It is clear that the electric field changes dramatically in the short distance within the electric double layer.

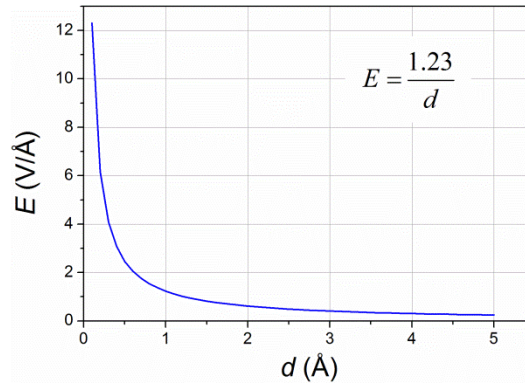


**Figure 2.2** Electric field gradient ( $E$ ) as a function of the thickness of the electric double layer  $d$  at the constant electrode potential  $U = 1.23$  V.

### 2.2.2 Kinetics

The rate of the oxygen reduction reaction at the cathode is significantly lower than that of the hydrogen oxidation reaction at the anode [39]. As the oxygen reduction kinetics in PEM fuel cells are slow, the selection of a proper catalyst is critically important for optimal fuel cell performance. Figure 2.3 illustrates the potential energy profile of a reaction [5].

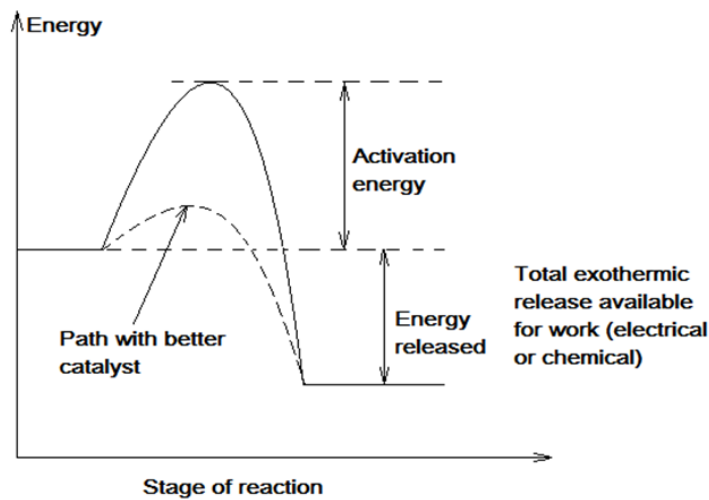


**Figure 2.3** Schematic reaction profile for effective and ineffective catalysts [5].

The energy released when going from reactants to products is the reaction enthalpy. In order to initiate the reaction, the activation energy is required. The activation energy is determined as the difference between the highest energy state of the reacting system, or transition state, and the reactants energy. In the electrochemical oxygen reduction reaction in PEM fuel cells, this activation energy accounts for the loss of potential, or voltage, also known as overpotential [5].

The role of a catalyst in a catalytic reaction is to increase the rate of a chemical reaction by providing an alternative reaction pathway with lower activation energy. A more effective catalyst gives a lower activation energy barrier for the reaction, and therefore lower voltage loss. Also, lower activation energy means that more reaction product forms in the same amount of time. The activation energy is an important parameter in reaction kinetics and can be considered as a measure of the quality of the electrode structure and materials, since it determines the rate of an elementary reaction [5]. Dependence of a reaction rate constant on activation energy is expressed by the well known Arrhenius equation:

$$k = Ae^{-\frac{E_a}{RT}} \quad (2.8)$$

where  $k$  is the rate constant,  $A$  is the pre-exponential factor,  $E_a$  is the activation energy,  $R$  is the universal gas constant, and  $T$  is the temperature.

Interactions between a catalyst and intermediate products of a reaction are critical parameters to evaluate the catalyst's activity. The well-known Sabatier principle suggests that the most active catalysts should bind the reaction intermediate products with a moderate strength. If the interactions are too weak, the reactants would not bind to the catalyst efficiently; on the other hand, if the interactions are too strong, the catalyst would be blocked by the reaction intermediates that impede further reactions [40].

In particular, the ability of a catalyst to interact with molecular oxygen and the degree of this interaction are crucial for the catalytic activity towards the oxygen reduction reaction. Catalysts that bind molecular oxygen too weakly or too strongly are poor candidates. An ideal catalyst should possess an optimum binding energy and also facilitate the dissociation of the strong O–O bond in the oxygen molecule. The direct four-electron pathway requires dissociation of molecular oxygen prior to the transfer of the first electron. The interaction of molecular oxygen with an effective catalyst weakens the O–O bond to such an extent that the bond break is inevitable, and the four-electron reduction occurs with water formation. Catalysts that cannot effectively stretch the O–O bond will only end up with the two-electron reduction product  $H_2O_2$ , which makes the catalyst unstable and degrades the fuel cell system. The most common catalyst in PEM fuel cells for the ORR is platinum, although it

binds molecular oxygen a little too strongly. Thus, finding a better catalyst for the ORR means finding a surface that binds oxygen more weakly than platinum does [2].

The activity of a catalyst towards the oxygen reduction is also influenced by the bond strength of the other intermediate products, namely, OOH, OH, O, and H<sub>2</sub>O<sub>2</sub>. If these interactions are too strong, surface blockage occurs. The OH radical is one of the most important intermediates and is formed in large amounts during the ORR. OH chemisorption is generally believed to be responsible for blocking oxygen adsorption sites [2].

Figure 2.4 illustrates a schematic potential energy profile of the oxygen reduction reaction. The starting point is the reactants, i.e. molecular oxygen and the catalyst. The first step is molecular oxygen chemisorption, or binding to an active site on the catalyst surface to form the first intermediate product. This intermediate may undergo another chemical transformation to form the second intermediate. In the four-electron pathway, the other steps of the ORR include four transfers of proton and electron.

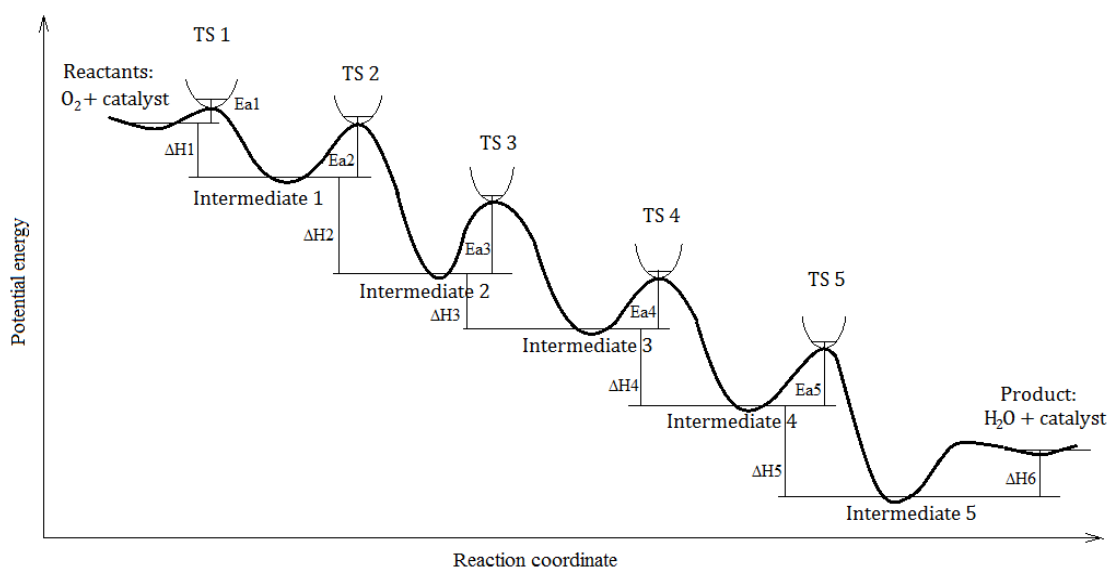


**Figure 2.4** Schematic oxygen reduction reaction. The enthalpies, activation energies and transition states are designated as  $\Delta H$ ,  $E_a$  and TS, respectively.

In order for the ORR to be a spontaneous reaction, the intermediate elementary reactions should be exothermic, i.e. the enthalpies and Gibbs free energies should be negative. An ideal catalyst should have identical Gibbs energies of -1.23 eV of the four proton and electron transfer steps without accounting for the effect of electrode potential, and the activation energies of all steps should be low [41, 42]. Thus, in the oxygen reduction reaction pathway on a catalyst, it is important to find both energies and activation barriers of all elementary steps. The step with highest activation energy

determines the rate of the overall reaction, and is known as the rate limiting step. The rate of a multi-step reaction is determined by the rate of the slowest step.

## 2.3 Theoretical Studies of Cathode Catalysts for Fuel Cells

### 2.3.1 Computational Chemistry

Computational chemistry is one of the most important tools for chemical investigations and applies mathematical and theoretical principles to solving chemical problems [43]. Computational chemistry enables us to study chemical phenomena by running simulations on computers rather than by experimental by examining the reactions and compounds. Modelling of the structure and properties of chemical substances not only supplements experimental methods of investigation, but gives principally new information. Computational experiments enable us to study short-lived, unstable intermediates, transition states and mechanisms of chemical reactions [44, 45]. Methods of computational chemistry can be classified into the three general categories: (i) first principles electronic structure calculations, (iii) semi-empirical methods, and (ii) molecular mechanics [43].

First principles electronic structure methods are based on quantum mechanics and solving the Schroedinger wave equations for electrons inside atoms. In quantum mechanics, energy and other related properties of molecules may be obtained by solving the Shroedinger equation [45]:

$$H\Psi = E\Psi \quad (2.9)$$

where  $H$  is Hamilton operator,  $\Psi$  is wave function, and  $E$  is energy.

The exact solutions of this wave equation cannot be obtained analytically except for the simple systems such as the hydrogen atom or molecule. Various electronic structure methods use some mathematical approximations to obtain the numerical solution of the Shroedinger equation. There are electronic structure methods based solely on the laws of quantum mechanics, and density functional theory methods (DFT), which account for the electron correlation and require relatively less computational resources compared to the correlation methods [45]. Electronic methods provide the most accurate and consistent predictions for chemical systems. The drawback of first principles methods is that they may be costly in terms of computation time [43]. However, DFT methods are known for their computational efficiency and accuracy and often chosen for large systems. The DFT methods are based on Hohenberg-Kohn theorems, according to which the electron density determines the ground-state wave function and all other electronic properties of the

system. The electron density is a function subject to a variational principle and should produce the minimum energy [37].

Semi-empirical methods are also based on quantum mechanics, but replace some calculations with approximations taken from experimental data. Compared to first principles, semi-empirical methods run much faster, but the obtained results are not as reliable and should be correlated to experimental results. Molecular mechanics techniques are purely empirical methods based on the principles of classical physics and neglect the treatment of the electronic structure [43]. In molecular mechanics, atoms are approximated as soft spheres with the van der Waals radius and set constants of net charge and polarizability. Bonds are approximated as a spring-like model. Each particle is surrounded by a “force-field” of electrical effects that interact with the other particles in the simulation [46].

There are a variety of programs for the simulation of chemical phenomena. These programs represent chemical systems effectively in two ways: (i) finite clusters of atoms, and (ii) infinite periodic slabs [47]. The cluster models contain a limited number of atoms and are computationally convenient. They can be efficiently used to describe moderate-size molecular systems and highly dispersed nanoparticles. However, the electronic structure of clusters can be different from the semi-infinite structure of a surface or a bulk material. The slab models represent a surface as a periodic structure along the surface. To represent surfaces and bulk materials, a few slabs are employed, in which the size of the surface unit cell determines the computational time. Periodic slabs are useful in modelling the processes at the electrodes [37, 47]. Depending on which of the two modelling approaches is used, there are two classes of basis sets. The cluster models use localized basis sets, which are linear combinations of atomic functions with their origin in the centre of the cluster atoms. The slab models use delocalized plane wave functions [37].

### **2.3.2 Gaussian 09**

Gaussian 09 [48] is one of the most widely used program packages and has been used to perform all the simulations presented in this thesis. This program enables us to predict the following properties of the molecules and reactions: molecular energies and structures (thermochemical stability), energies and structures of transition states (activation energies), bond and reaction energies, heats of formation, electronic transitions, vibrational frequencies (IR and Raman spectra), potential energy surfaces, reaction pathways and mechanisms, various properties of molecules in gas phase and solution, magnetic shielding effects, etc. [43, 44].

Gaussian simulations include creating an input file, running the program and examining the output file. In the input file, the molecular systems and model

chemistry are specified. The model chemistry includes the choice of computational method and basis set. Model chemistry and type of calculation, e.g. single energy point, geometry optimisation, frequency calculation, etc., are specified in the route section of the input file. The molecular system is the geometric structure of atoms in Cartesian or internal coordinates and the electronic state, i.e. charge and multiplicity [43].

As mentioned in the previous section, there are various methods of electronic structure calculations. In Gaussian, these include the Hartree - Fock method (HF), multiple post Hartree - Fock methods which account for electron correlation (MP2, QCISD, CCSD, etc.), and density functional theory methods (B3LYP, B3PW91, etc.). Basis sets are mathematical representations of the molecular orbitals, i.e. functions that restrict each electron to a particular region of space (orbital) in the molecule. The larger the basis set, the more accurately it represents electron orbitals. Gaussian 09 offers a wide range of standard basis-sets [45].

### 2.3.3 Platinum Based Catalysts

Since platinum is the most active cathode catalyst for oxygen reduction in PEM fuel cells, it has been investigated extensively by computational chemistry methods. Chemisorption of molecular oxygen is the first step of the ORR, and its understanding is crucial in the oxygen reduction catalysis. There are three models of molecular oxygen chemisorption on platinum: (i) end-on (ii) side-on, and (iii) bridge-like, as shown in Figure 2.5 [2, 37].

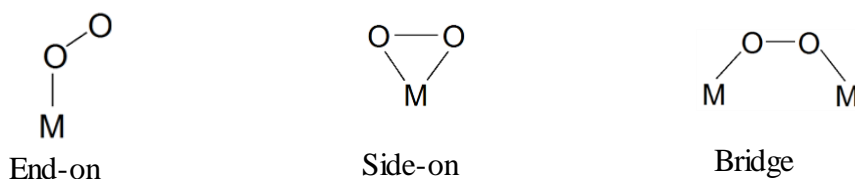


**Figure 2.5** Models of molecular oxygen chemisorption on platinum [37].

Since the radius of a platinum atom is significantly larger than the radius of an oxygen atom, there may be different configurations of molecular oxygen on the surface facet of platinum crystal, designated as Pt(111). Two main configurations are the top-bridge-top and top-hollow-bridge, as illustrated in Figure 2.6 [37, 49]. The bridge (t-b-t) mode of molecular oxygen chemisorption on platinum is the most favourable [37, 50, 51].

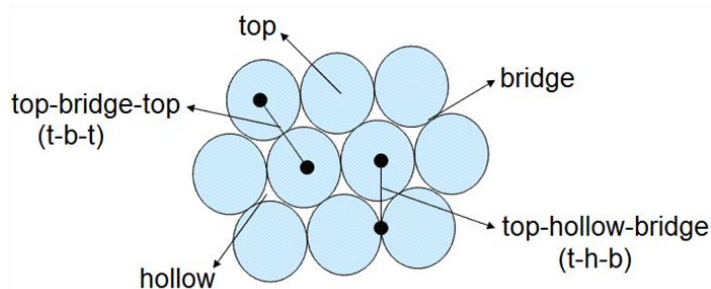
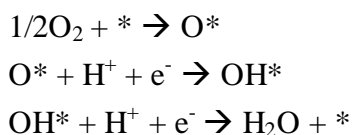


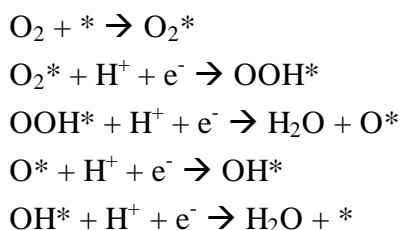
**Figure 2.6** Models of molecular oxygen chemisorption over the Pt(111) monolayer surface [49].

Following the molecular oxygen chemisorption, the ORR can proceed via different reaction mechanisms. Two possible mechanisms of the ORR on platinum are proposed: dissociative and associative, depending on what step the chemisorbed molecular oxygen dissociates [2]:

(i) Dissociative Mechanism (\* denotes a site on the Pt surface):



(ii) Associative Mechanism:



In the dissociative mechanism, no  $\text{H}_2\text{O}_2$  is produced. On a platinum surface, molecular oxygen chemisorption breaks the O-O bond and forms adsorbed atomic O, which further gains two electrons in the two consecutive steps, thus forming water. In the associative mechanism, chemisorbed molecular oxygen is present, and the O-O bond may or may not be broken in the following steps. Therefore, the final product can be either  $\text{H}_2\text{O}$  or  $\text{H}_2\text{O}_2$ , and the latter could be further reduced to water [2].

The question as to which of the two mechanisms occurs on platinum as well as the rate limiting step of the ORR on platinum has been not resolved as yet [37]. According to Goddard et al. [47], the rate limiting step of the ORR in the dissociative mechanism is the reaction  $\text{O}^* + \text{H}^+ + \text{e}^- \rightarrow \text{OH}^*$  with an activation energy of 1.39 eV (32 kcal/mol), and the rate limiting step in the associative mechanism is the dissociation of the chemisorbed OOH group with a barrier of 0.74 eV,. Sidik and

Anderson reported that the molecular oxygen, chemisorbed in the bridge way, easily dissociates at the first electron and proton transfer step with a calculated activation energy of 0.60 eV, which is close to the experimental effective activation energy of 0.44 eV on the Pt(111) in H<sub>2</sub>SO<sub>4</sub> [52]. Later, Ou et al. [51] concluded that the proton-coupled first electron transfer for the OOH\* formation is the rate limiting step, with a calculated activation energy of 0.28 eV.

Since the ORR is an electrochemical reaction, the electrode potential should be accounted for. The influence of the electrode potential on the energetics of the ORR elementary steps was studied for the first time by Norskov et al. The main principle of their technique is shifting the calculated Gibbs energy of an electrochemical reaction linearly by the  $-eU$  term, where  $U$  is the electrode potential [38]. They proposed that the ORR mechanism is dissociative at the equilibrium potential of 1.23 V and is favoured at relatively high potentials, with the rate limiting step being the proton and electron transfer to the chemisorbed molecular oxygen. At lower potentials, e.g. 0.8 V, the dissociative and associative mechanisms compete, and the rate limiting step is molecular oxygen dissociation. At potentials below 0.8 V, the associative mechanism of the ORR dominates, and the rate limiting steps are the proton and electron transfers to chemisorbed O or OH [38].

Later, Janik et al. [35] used the Norskov technique and additionally explicitly accounted for water ambience in order to model the first proton and electron transfer step. They found that the chemisorbed OOH formation is the rate limiting step with activation energy varying between 0.1 and 0.35 eV, depending on the potential. Recently, Yeh and Janik [34] employed a more realistic modelling technique and also showed that the dissociative mechanism is favoured at larger potentials, and the associative mechanism at lower potentials. However, the rate limiting step in the dissociative mechanism is proposed to be the dissociation of the chemisorbed molecular oxygen with activation energies of either 0.63 or 0.72 eV, depending on the model. In the associative mechanism, the proposed rate limiting step is the first electron and proton transfer, and this is in disagreement with the Norskov finding. Further, reduction of the chemisorbed O to OH, and OH to H<sub>2</sub>O at the equilibrium potential have significant activation barriers of 1.2 and 1.6 eV, respectively [34] and thus may be the rate limiting steps [30]. In addition, the experimental activation barrier for the overall ORR is 0.44 eV at the equilibrium potential of 1.23 V, and 0.26 eV at the potential of 0.8 V [35], and the experimental activation energy of dissociation of chemisorbed molecular oxygen is 0.29 eV [53].

Reported in the literature reaction energies and activation barriers of the ORR elementary steps on a Pt(111) surface are summarized in Table 2.1. The calculated energy of molecular oxygen binding fluctuates between circa -0.5 and -1.0 eV. The estimations of the O-O bond dissociation energy in the chemisorbed oxygen molecule

vary slightly more, from 0.2 to circa 0.8 eV. Estimations of activation energy of the first electron and proton transfer vary most significantly, from 0.005 to 0.81 eV. The following ORR steps on platinum were studied to a lesser extent, and the reported activation energy values vary markedly. Thus, all the reviewed studies of platinum as a catalyst for the ORR are rather controversial, and there is no general agreement on the energetics of the elementary steps.

**Table 2.1** Energetics of the ORR intermediate steps on a Pt(111) surface.

ORR intermediate step	Activation energy $E_a$ , eV	Reaction energy $\Delta E$ , eV	Reference
$O_2 + * \rightarrow O_2^*$		-0.49	[47]
		-0.57	[51]
		-0.53	[54]
		-0.72	[55]
		-0.62	[56]
		-0.96	[53]
$O_2 + 2* \rightarrow 2O^*$ or $O_2^* + * \rightarrow 2O^*$	0.20	-1.28 (ads.)	[53]
	0.28		[51]
	0.15	-0.93	[34]
	0.77		[56]
	0.65		[47]
	0.37		[57]
$O_2^* + H^+ + e^- \rightarrow OOH^*$	0.07	-0.23	[53]
	0.20		[51]
	0.81 or 0.31		[35]
	0.67		[34]
	0.005		[54]
$OOH^* + * \rightarrow O^* + OH^*$	0.22	-1.05	[53]
	0.20		[58]
	0.15	-0.93	[34]
	0.74		[47]
$O^* + H^+ + e^- \rightarrow OH^*$	0.03	-0.07	[53]
$OH^* + H^+ + e^- \rightarrow H_2O^*$	0.01	-0.92	[53]
	0.20		[58]
	0.37		[34]
$H_2O^* \rightarrow H_2O + *$	0.08	-0.46	[53]
	0.60		[58]

As mentioned in Section 2.2, the maximum reaction rate of the ORR can be achieved when the intermediate products are bound to the catalyst surface with an optimal strength to weaken the O-O bond and can be easily removed during the reduction steps [2]. When the activity of a catalyst is measured experimentally and graphed as a function of the adsorption bond strengths of OOH, OH or O intermediate products to the catalyst surface, volcano-shaped plots are obtained [30, 59]. Therefore, the adsorption strength of OOH, OH and O on a catalyst surface is an indicator of its

activity. Figure 2.7 illustrates the volcano plot obtained by Norskov et al., plotting the activity of metals as a function of the O and OH binding energies [38]. The volcano plot shows that platinum and palladium, being near the top, are the best catalysts for the ORR. However, there is still room for improvement of the activity of platinum, for example, by alloying with other metals [60].

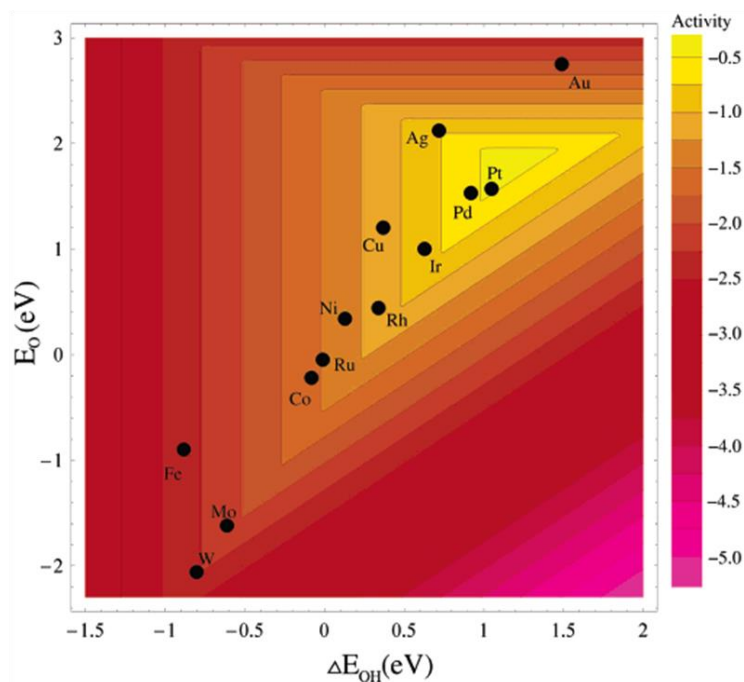


**Figure 2.7** Volcano plot of trends in oxygen reduction activity as a function of OH and O binding energies for different metals [38].

For platinum based catalysts, the adsorption strength of O and OH is too high, and that of OOH is too low. The calculated Gibbs adsorption strengths of chemisorbed O, OH and OOH on a Pt(111) surface are 3.10, 1.84 and 0.47 eV, respectively [30]. An ideal catalyst should bind OOH more strongly, and O and OH more weakly. However, it is not possible to vary the adsorption strengths of these intermediates independently of each other by changing the catalyst, since each of the intermediates binds to the surface via the oxygen atom. At the same time, the adsorption strengths of the O, OH and OOH intermediates are linearly dependent and thus scalable [60]. The suggested ideal Gibbs adsorption strength of OOH is 1.35 eV [30].

### 2.3.4 Nitrogen Doped Carbon Catalysts

Doped carbon materials have attracted significant attention as potential candidates for replacement of platinum in fuel cell cathode catalysts, and this is because they demonstrate certain catalytic activity towards the ORR [61-64]. Several authors have investigated carbon-based metal-free catalysts by means of

computational chemistry. In 2000, Strelko et al. [65] reported that boron, nitrogen and phosphorus doped carbon may have a catalytic activity towards electron transfer reactions. Later, the electron-donor ability of oxygen and nitrogen doped carbon was studied with respect to the oxygen reductive adsorption by evaluating the energy gap between the highest occupied and lowest unoccupied molecular orbital ( $E_{HOMO}$  and  $E_{LUMO}$ ) [66].

Currently, the most promising low-cost cathode catalysts for PEM fuel cells are nitrogen doped carbon based materials, manufactured in the presence of transition metals [24, 67]. Therefore, most of the theoretical studies are dedicated to nitrogen doped carbon [39, 68-74], which is believed to possess high catalytic activity [75, 76]. Generally, the following main forms of nitrogen in graphite are distinguished: (i) pyridinic, (ii) graphitic, (iii) pyrrolic, and (iv) pyridinic N-oxide, as shown in Figure 2.8. The most important and stable forms of doped nitrogen are pyridinic, which exists on the edge of graphite planes and bound to two carbon atoms, and graphitic, which is bound to three carbon atoms. Graphitic and pyrrolic nitrogens donate two p-electrons to the aromatic  $\pi$  system, and pyridinic nitrogen donates one p-electron [61]. It should be added that graphite/graphene structure has basal planes and edges, and the graphitic nitrogen can belong to both basal planes and edges, whereas the pyridinic, pyrrolic nitrogen and pyridinic N-oxide belong to the edges.

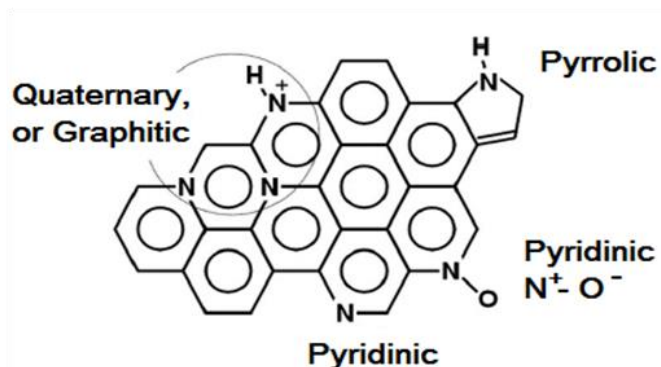


**Figure 2.8** Chemical states of nitrogen in graphene planes [61].

Given the variety of nitrogen positions within graphite/graphene, the active sites on nitrogen doped graphene, where the ORR takes place, are still not unambiguously determined in the literature [39]. The research on nitrogen doped carbon as a catalyst for the ORR has been focusing on both basal planes and edges of graphitic carbon structure, or graphene. Sidik et al. [69] studied the effect of nitrogen doping to graphene basal planes in graphitic position and binding of the OOH group, as shown in Figure 2.9. They showed that carbon radical sites, adjacent to substituent nitrogen in the graphene basal plane, are active towards the oxygen reduction to hydrogen

peroxide. Recently, Zhang et al. [71] investigated nitrogen doped graphene basal planes by calculating the reaction energies and activation barriers of the ORR elementary steps. They also came to the conclusion that carbon atoms in the graphene sheet next to the doped nitrogen atom are the catalytic active sites.

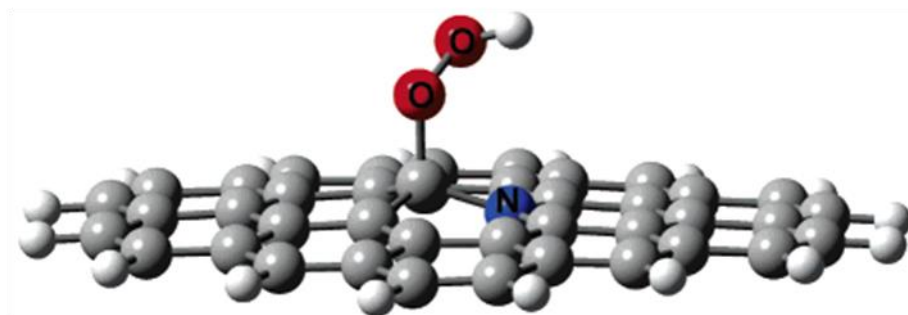


**Figure 2.9** OOH binding to the N doped graphene [69]. The carbon, nitrogen, oxygen and hydrogen atoms are designated by the grey, blue, red and white colours, respectively.

Bao et al. [73] conducted a Gaussian DFT study to investigate molecular oxygen adsorption and the subsequent ORR steps on graphene sheets doped with graphitic nitrogen atom both in the interior and edge positions. According to them, the active sites for the molecular oxygen adsorption are the carbon atoms at the graphitic nitrogen doped zigzag carbon edge.

Graphite edges can be of either zigzag or armchair shape, and the arising question is which of the two structures is more efficient as a catalyst for the ORR. Jiang et al. [77] studied graphene edges theoretically and concluded that the zigzag graphene structure has unique physicochemical properties compared to those of graphene sheet, nanotubes and the armchair edge. Ikeda et al. [39] modelled molecular oxygen adsorption both on the basal planes and the edge (zigzag and armchair) sites of nitrogen doped graphite. They concluded that the ORR is favoured on the zigzag edges of graphene doped with nitrogen in the graphitic position, as illustrated in Figure 2.10.

Since the most stable and abundant chemical states of doped nitrogen in carbon are pyridinic and graphitic, the next question to be addressed is which of the two forms of nitrogen accounts for the catalytic activity in the ORR. In the literature on experimental investigations of nitrogen doped carbon, the active sites are believed to be carbon atoms around either the pyridinic or graphitic nitrogen, both at the carbon edge and basal planes [18, 78-81]. Several experimental reports [18, 61, 75, 82] suggest that the presence of pyridinic nitrogen particularly accounts for the catalytic activity of nitrogen doped carbon. However, the other opinion is that graphitic nitrogen enhances the catalytic activity of the carbon structure [83, 84]. A few studies

report that both pyridinic and graphitic nitrogen doped carbon acts as the catalyst for oxygen reduction [75, 79, 85].

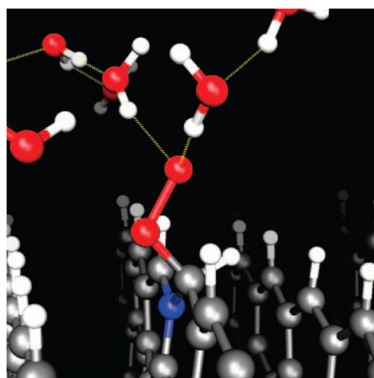


**Figure 2.10** Molecular oxygen binding to a graphite edge doped with graphitic nitrogen [39]. The carbon, nitrogen, oxygen and hydrogen atoms are designated by the grey, blue, red and white colours, respectively.

Pyridinic doped graphite edge sites has been studied by Kurak and Anderson [68], who calculated the adsorption bond strength of the ORR intermediate species and the associated reversible potentials. They concluded that the pyridinic nitrogen doped graphite edge catalyses two-electron oxygen reduction, leading to the formation of hydrogen peroxide. Zhang and Xia [72] studied pyridinic and pyrrolic nitrogen doped graphene as a catalyst for the ORR and found that the carbon atoms, possessing the highest electron density due to the nitrogen doping, are the catalytic active sites. The remaining majority of theoretical studies focus on the graphitic nitrogen in carbon structure [66, 69-71, 73, 74]. The carbon atom next to the substituent graphitic nitrogen is reported to be the active site for the ORR [71, 73, 74]. However, there have been no reported comparative studies of the graphitic and pyridinic doped carbon and there is still uncertainty as to whether pyridinic or graphitic nitrogen in carbon induces the catalytic effect. Thus, there is a disagreement in the theoretical and experimental reports and a gap of knowledge on the chemical state of nitrogen in nitrogen doped carbon catalysts.

Similar to that on platinum, the ORR on nitrogen doped carbon catalysts proceeds through elementary steps including molecular oxygen chemisorption, or binding, and four transfers of protons and electrons. However, the mechanism of the ORR on nitrogen doped catalyst is not established yet. Molecular oxygen binding is crucial for identifying the active catalyst structures. A few authors have reported this step to be a barrierless on nitrogen doped carbon [71, 73], but the binding energy values and interatomic distances between oxygen and surface carbon atoms are controversial between these studies. In contrast, Ikeda et al. [39] reported a significant activation energy of 5 kcal/mol (0.22 eV) for molecular oxygen binding on nitrogen

doped graphite. In addition, Okamoto [86] found that molecular oxygen binding is endothermic for mono and binary nitrogen doped graphene and exothermic only for triply and quaternary nitrogen doped graphene. Thus, there is no unity of opinions in the literature regarding the first step of the ORR on nitrogen doped carbon.

Determining the other steps of the ORR mechanism on doped carbon catalysts is necessary in order to predict whether the materials would catalyse the two- or four-electron pathway. Table 2.2 summarizes theoretical estimations of the reaction energies and activation energies of the ORR elementary steps, reported in the literature. Most of the studies on nitrogen doped carbon do not provide a complete set of energies and activation barriers of the ORR elementary steps. However, there is a general agreement in the values of reaction energies. The reported energies of the first proton and electron transfer vary between circa -0.6 and -1.0 eV. The remaining three proton and electron transfers have markedly higher reaction energies in the range of -2.2 to -4.7 eV. The insufficient information on the thermodynamic and kinetic aspects of the ORR on nitrogen doped carbon catalysts indicates that a detailed investigation is needed.

**Table 2.2** Energetics of the ORR intermediate steps on nitrogen doped carbon.

ORR intermediate step	Activation energy $E_a$ , eV	Reaction energy $\Delta E$ , eV	Reference
$O_2 + * \rightarrow O_2^*$	0.61		[39]
		-0.20	[71]
		-0.06	[73]
$O_2^* + * \rightarrow 2O^*$	0.05	-0.80	[73]
$O_2^* + H^+ + e^- \rightarrow OOH^*$	0.63	-0.96	[71]
		-0.85	[72]
		-0.64	[74]
$OOH^* + * \rightarrow O^* + OH^*$	1.18	0.25	[71]
	1.20		[68]
$OOH^* + H^* \rightarrow O^* + H_2O$	0.55	-2.99	[71]
		-3.53	[72]
		-2.64	[74]
$OOH^* + H^* \rightarrow 2OH^*$	0.72	-2.91	[71]
$OOH^* + H^* \rightarrow H_2O_2$	0.09	-2.21	[71]
$O^* + H^+ + e^- \rightarrow OH^*$	0.54	-2.21	[71]
		-4.66	[72]
$OH^* + H^+ + e^- \rightarrow H_2O^*$	0.22		[39]
	0.82	-2.23	[71]
		-3.77	[72]

### 2.3.5 Other Heteroatom Doped Carbon Catalysts

Doping of other heteroatoms to carbon has received far less attention in the literature than nitrogen. The investigated heteroatoms have been boron [87], phosphorus [88], oxygen [66] and sulphur [89]. However, the nature of the active sites in the heteroatom doped carbon catalysts has not been established yet, and there exist different opinions.

Several authors have reported results of first principles modelling of the ORR on carbon-based metal-free catalysts. In 2000, Strelko et al. [65] reported that boron, nitrogen and phosphorus doped carbon may have a catalytic activity towards electron transfer reactions. Later, they studied oxygen and nitrogen doped carbon and concluded that the presence of oxygen in carbon enhances electron-donor and thus the reductive ability of carbon towards molecular oxygen and other oxidizers. Similar to nitrogen, oxygen has lone-pair electrons that participate in the  $\pi$ -conjugated aromatic structure of carbon [66].

Boron has an atomic radius similar to that of carbon and nitrogen, but one valence electron less than carbon, thus exhibiting electron acceptor properties. Experimental studies of boron doped carbon suggest that the active sites are the boron atoms incorporated into the carbon structure [62], while in boron and nitrogen co-doped carbon, B-N-C moieties are proposed to be responsible for the catalytic activity [84, 90, 91]. The contrary opinion is that the presence of boron does not create new active sites [92], but rather increases the number of the pyridinic nitrogen sites and enhances the asymmetric spin density of carbon atoms [93].

Theoretical studies on boron doped carbon are few. Zhao et al. [94] modelled molecular oxygen adsorption on nitrogen and boron co-doped carbon nanotubes and concluded that molecular oxygen cannot be reduced on this structure. In contrast, recent DFT simulations of molecular oxygen adsorption on boron doped carbon graphene and nanotubes [87, 95] suggest that the substituent boron atom is the active site for the oxygen chemisorption and following reduction, as illustrated in Figure 2.11. However, the effect of boron doping to carbon edge sites has not been addressed so far.

Phosphorus, being in the nitrogen group, has the same number of valence electrons and thus similar electronic properties, e.g. a lone pair of electrons that it can donate in donor-acceptor reactions. However, the electronegativity of phosphorus is lower than those of nitrogen and carbon, while the atomic radius is larger, thus changing its reactivity. The catalytic performance of phosphorus doped carbon towards the ORR has been investigated largely experimentally [93, 96, 97]. In phosphorus doped carbon, phosphorus is believed to create defect active sites in the carbon structure, but the nature of these active sites has not been clarified [97-99]. In

phosphorus, nitrogen and boron co-doped carbon, the presence of phosphorus is suggested to merely increase the number of pyridinic nitrogen active sites [92, 93].

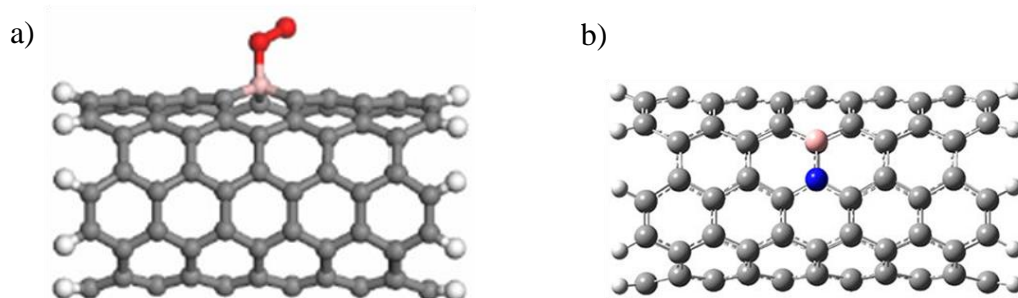


**Figure 2.11** a) Molecular oxygen bound to a boron doped carbon nanotube [95], and b) boron and nitrogen co-doped carbon nanotube [94]. The carbon, boron, nitrogen and oxygen atoms are designated by the grey, pink, blue and red colours, respectively.

Theoretical studies of phosphorus doped carbon are scarce. Bao et al. [100] studied oxygen reduction over a carbon catalyst containing a phosphinate group, and Kaukonen et al. [88] studied the effect of substitution of carbon atoms in graphene with different metal and non-metal heteroatoms, including phosphorus. They proposed that phosphorus atoms doped into double vacancies in graphene can create the active sites for the ORR. However, the latter study did not consider the edge effects in doped graphene, and the proposed coordination number of phosphorus is four, which is exceptionally rare and implies instability of the active site.

Sulphur and selenium possess two more valence electrons than carbon and therefore can also act as donors of electron density. There are a few experimental studies reporting sulphur doped graphene that has an enhanced catalytic activity towards the oxygen reduction [63, 101, 102]. Recently, Zhang et al. [89] investigated sulphur doped graphene edge sites using the DFT method and proposed that the ORR occurs both on the sulphur heteroatom and the adjacent carbon atoms through different mechanisms.

### 2.3.6 Transition Metal Macrocyclic Catalysts

The most prominent experimental results among the non precious catalysts has been demonstrated by nitrogen doped carbon catalysts synthesized in the presence of transition metals, namely iron and cobalt [24, 67]. However, it is still a matter of debate in the literature as to whether the transition metals are an essential part of the catalyst active sites or they merely serve to improve the incorporation of nitrogen into carbon [24, 76].

In recent years, there has been a considerable amount of literature on theoretical investigations of possible active sites in carbon catalysts containing transition metals. In 2004, Anderson and Sidik [103] performed DFT modelling of active sites with the central iron atom coordinated to four nitrogen atoms, illustrated in Figure 2.12. They concluded that the Fe (II), and not the Fe (III) is the active site for the ORR.

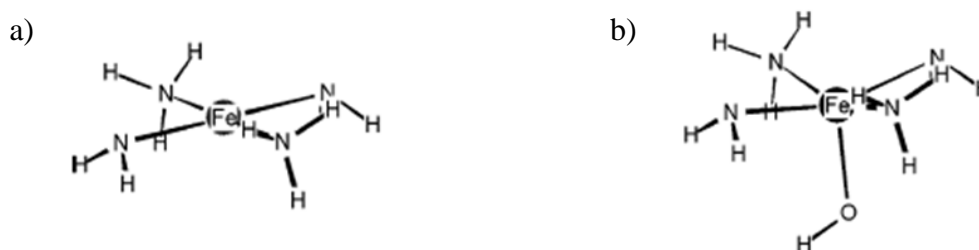


**Figure 2.12** Models of active sites for the ORR with a) Fe (II) and b) Fe(III) oxidation states of the central atom [103].

Recently, Calle-Vallejo et al. [104] studied chemisorption of OOH, OH and O intermediates of the ORR on active sites composed of four pyridinic nitrogen atoms coordinated to the central transition metal atom. The two investigated structures are transition metal porphyrin and tetraazaannulene macrocycle types, illustrated in Figure 2.13. The research group studied a wide variety of transition metal atoms in the macrocycle centre and concluded that the most active sites for oxygen reduction should have the structure of iron and manganese porphyrins. In addition, they proposed that the catalytic behaviour of transition metals can be changed significantly by the structure of macrocycle and the metal oxidation state.



**Figure 2.13** Transition metal macrocycle active sites based on the structures of a) porphyrine, and b) tetraazaannulene [104]. The carbon, nitrogen and transition metal atoms are designated by the black, blue and brown colours, respectively.

The other types of macrocycles studied theoretically in the literature are phthalocyanines [105, 106]. Wang et al. [105] studied molecular oxygen binding to the metal centres in iron and cobalt phthalocyanines. They found that both the end-on and side-on types of oxygen chemisorption are possible on the transition metal macrocycle centres and the binding energies are higher for the iron centre than for

cobalt. It was proposed that the side-on chemisorption should favour the four-electron pathway, while the end-on mode should promote the two-electron pathway of the ORR. Later, Orellana [106] expanded the topic of phthalocyanines by studying also manganese as the central atom; it was concluded that iron and manganese may be the key to increase the ORR rate. Recently, transition metal phthalocyanines and porphyrins have been further investigated as the catalysts for the ORR by He et al. [107]. Using DFT calculations, this group predicted the structures and binding energies of  $O_2$ , OH and  $H_2O_2$  intermediates on the iron and cobalt phthalocyanine molecule, shown in Figure 2.14. They proposed that the type of the central transition metal is the main factor determining the binding energies of the intermediates, which were found to be always lower for the iron centre than for the cobalt centre, which is contradictory to the result obtained by Wang et al. [105]. However, they also concluded that iron and cobalt should promote the four- and two-electron ORR pathways, respectively.

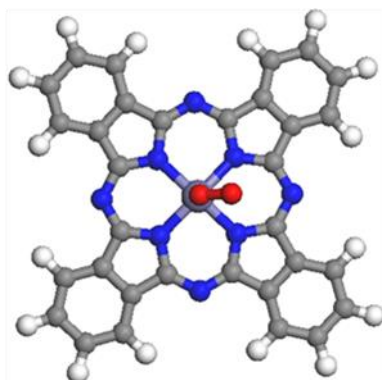


**Figure 2.14** Transition metal phthalocyanine structure with molecular oxygen bound to the central metal atom [107]. The carbon, nitrogen, transition metal and oxygen are designated by the grey, blue, purple and red colours, respectively.

Chen and co-workers performed a DFT modelling of the ORR mechanism on structures representing cobalt polypyrrole and iron and/or cobalt polyaniline [108, 109]. It was concluded that polyaniline, containing both iron and cobalt, has the best catalytic activity for oxygen reduction. Shi et al. [36] studied molecular oxygen binding cobalt polypyrrole solely and suggested that both Co(II) and Co(III) oxidation states could act as the catalytic active centres. It should be noted that the structures of polyaniline or polypyrrole are entirely different from a macrocycle structure and have a transition metal atom coordinated to two nitrogen atoms only, as illustrated in Figure 2.15.

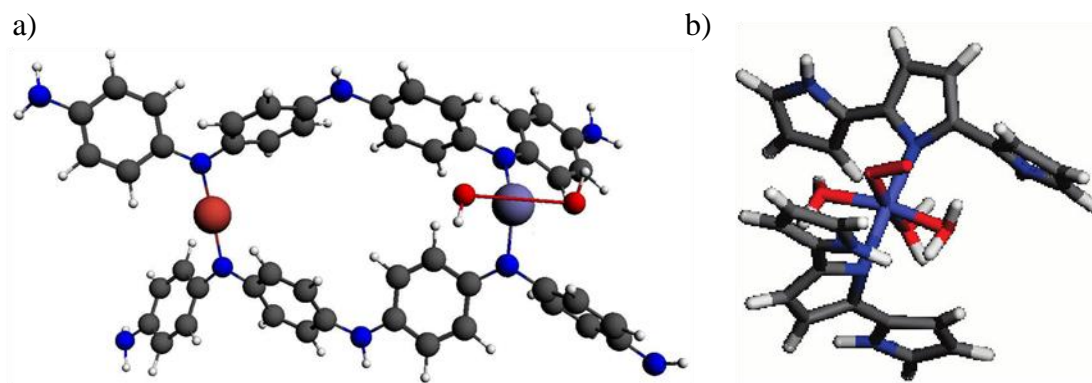


**Figure 2.15** Theoretical model structures of a) iron-cobalt polyaniline [109], and b) cobalt polypyrrole [36]. The carbon, nitrogen, oxygen and hydrogen are designated by the grey, blue, red and white colours, respectively. The transition metals are designated by the purple and brown colours.

It is clear that there is a multitude of various transition metal organic structures that can potentially be the active sites for oxygen reduction. Many questions remain regarding the ORR catalysis on transition metal macrocycles and polymers. The first question is whether the oxygen reduction mechanism is influenced by the type of macrocycle or polymer structure. It is still not clear as to which of the transition metals determines a higher catalytic activity of the macrocycle active sites. Further, although some studies report the thermodynamic parameters of the ORR, such as adsorption or binding energies of the intermediate products, the reaction's pathways have not been studied sufficiently. In addition, to the author's knowledge, the kinetic aspects of the oxygen reduction on transition metal macrocycles have not been investigated.

## 2.4 Experimental Research and Development of Cathode Catalysts for PEM Fuel Cells

### 2.4.1 Platinum alloys

As mentioned in Section 2.3.3, platinum alloys can exhibit enhanced catalytic activity compared to pure platinum. Binary or ternary platinum alloys typically include the first row transition metals such as Ti, V, Cr, Mn, Fe, Co, Ni, and Cu. The alloys can be made in two ways: (i) depositing a transition metal onto carbon-supported platinum (Pt/C), or (ii) depositing platinum and transition metal(s) onto a carbon support simultaneously. The resulting materials need to be sintered at about 1000 °C in order to form a true alloy [3].

The enhanced catalytic activity of platinum alloys towards the ORR in PEM fuel cells is explained through the following effects: (i) strain effects, which are caused by

the size mismatch between the host and foreign atoms, leading to a compression or expansion in the host lattice; (ii) ligand effects, in which the second component (promoter) alters the electronic properties of platinum to affect the adsorption and desorption of the reactants, as well as intermediates and poisons; and (iii) ensemble, or morphological, effects, in which the dilution of platinum with the catalytically inert metal changes the distribution of the active sites, thereby opening different reaction pathways [2, 110, 111].

Platinum-based bimetallic alloys (Pt-M, where M is either Ti, Cr, V, Mn, Fe, Co, Ni, Cu, Y, or Sc, etc.) demonstrated enhanced activity towards the ORR [2, 111]. This was explained by a shortening of the Pt-Pt interatomic distances by alloying, formation of skin platinum which has increased d-electron vacancy of the thin platinum surface layer, caused by the underlying alloy [2, 111], and a weakening in the surface reactivity of platinum, which was defined by the calculated binding energy of oxygen to the catalyst surface [110]. The electronic structure, energy of oxygen binding and the ORR catalytic activity of bimetallic platinum alloys have been studied extensively theoretically. Xu et al. [56] reported that there is a linear relationship between the binding energy of atomic oxygen and the dissociation barrier of molecular oxygen on the alloys of platinum with transition metals. This is due to the principle that the more strongly a material binds atomic oxygen, the more effective it is in dissociating molecular oxygen. Therefore, instead of conducting a complicated and expensive transition-state study, a more affordable atomic binding study can be used to design better oxygen reduction catalysts [2].

However, despite significant achievements in alloying platinum with other metals to form active catalysts, some unsolved problems remain such as complexity of preparation and insufficient durability of platinum alloy catalysts [112]. Another major barrier is the physicochemical instability of the modified catalyst surfaces: transition metals cannot remain stable under the operating condition of a fuel cell cathode and are leached from the alloy surface [2, 110].

#### **2.4.2 Transition Metal Chalcogenides**

An interesting class of cost-efficient catalysts for the ORR are transition metal chalcogenides, i.e. sulphides, selenides or tellurides. These nonstoichiometric crystalline materials have attracted considerable attention because of their tolerance to organic fuels, relatively low cost, promising catalytic activity and high stability [2, 113]. Due to the nonstoichiometric nature of transition metal chalcogenides, their chemical composition varies and a significant number of different chalcogenide compounds have been investigated and reported [114].

In general, the chemical composition of transition metal chalcogenides can be designated as  $M_xM'_yX_z$ , where M, M' are transition metals, X is a chalcogen, either S, Se or Te. The M and M' can be the same or different, if foreign metal atoms replace the base metal in the crystal structure. The transition metals, reported in the literature, are Mo, Ru, Co, Fe, Ni and some others [2, 114]. The unit cell of crystal structure of transition metal chalcogenides is a cluster of metal ions surrounded by several chalcogen ions. For instance, in  $Mo_6S_8$ , each unit cell contains a central octahedral metal cluster with six Mo ions, surrounded nearly cubically by eight sulphur ions [2].

The electrochemical properties of transition metal chalcogenides can be tuned by changing their composition, which in turn is influenced by synthesis conditions, namely, chemical precursors, temperature, pressure and treatment time. The ORR catalysts based on transition metal chalcogenides are prepared using a multitude of techniques, and the challenges are to discover new chalcogenide compositions and develop synthesis methods for preparing the catalysts [114].

Chalcogenides of non-precious transition metals of the IV and VIII groups of the periodic table, e.g. iron and cobalt, have been studied extensively due to their low cost and natural abundance. Various cobalt chalcogenides have been tested as catalysts for the ORR in an acid media. Among them, cobalt sulphide  $Co_3S_4$  has demonstrated the highest activity in the ORR [115]. Substitution of sulphur by selenium or tellurium is believed to affect the ORR activity substantially, since the catalytic activity of cobalt chalcogenides decreases in the order of  $S > Se > Te$ . However, although cobalt selenides and tellurides were not as active and stable as cobalt sulphides, recent studies have achieved considerable improvement in the performance of cobalt selenides in acid media [2, 116].

The nature of transition metal changes the catalytic activity as well. In sulphides, the catalytic activity decreases in the order  $Co > Ni > Fe$ . Further, incorporation of a second transition metal to a chalcogenide can change its catalytic activity. For example, a ternary Co-Ni-S compound is more active than a binary Co-S compound [2], and the ORR activity of cobalt and nickel disulphides decreases as  $(Co,Ni)S_2 > CoS_2 > NiS_2$  [25]. On the contrary, addition of tungsten to cobalt sulphide  $CoS_2$  decreases the activity. Investigating binary transition metal combinations with different formulations of metal and chalcogen is an interesting direction in the research of transition metal chalcogenides as the ORR catalysts [2].

Although non-precious transition metal chalcogenides have displayed some promise as alternative catalysts for PEM fuel cells, the observed activity and stability are still significantly lower than those of commercially available platinum-based catalyst. Therefore, these materials are yet in the research stage [2, 22].

### 2.4.3 Carbon Catalysts Containing Transition Metals

Carbon catalysts with transition metals and nitrogen incorporated into the carbon structure are the most promising for application in PEM fuel cells. These materials are designated as M-N<sub>x</sub>/C, where M = Fe, Co, Mn, Ni, Cu, etc. Development of the M-N<sub>x</sub>/C catalysts started in 1964 from Jasinski's discovery that transition metal porphyrins catalyse the ORR in alkaline media [117]. Later, the catalytic activity of various metal-nitrogen chelate complexes supported on carbon was demonstrated in acidic media. The main types of macrocycles reported are phthalocyanines [105, 107, 118-120], porphyrins [121, 122], corrins/corroles [123-126] and tetraazaannulenes [127, 128]. In these macrocycles, the central transition metal atom is coordinated with four nitrogen atoms within a framework of carbon atoms, as shown in Figure 2.16.

The catalytic activity of the transition metal macrocycle compounds depends on the central transition metal and the macrocycle structure and can be tuned by introducing various substituent functional groups to the macrocycle. Experimental studies show that cobalt porphyrins catalyze the two-electron oxygen reduction, whereas iron complexes catalyze the four-electron oxygen reduction. Importantly, non-pyrolysed transition metal macrocycles are insufficiently active and stable as the ORR catalysts and cannot be applied in PEM fuel cells, but provide a theoretical platform for investigation of the catalytic activity [22].

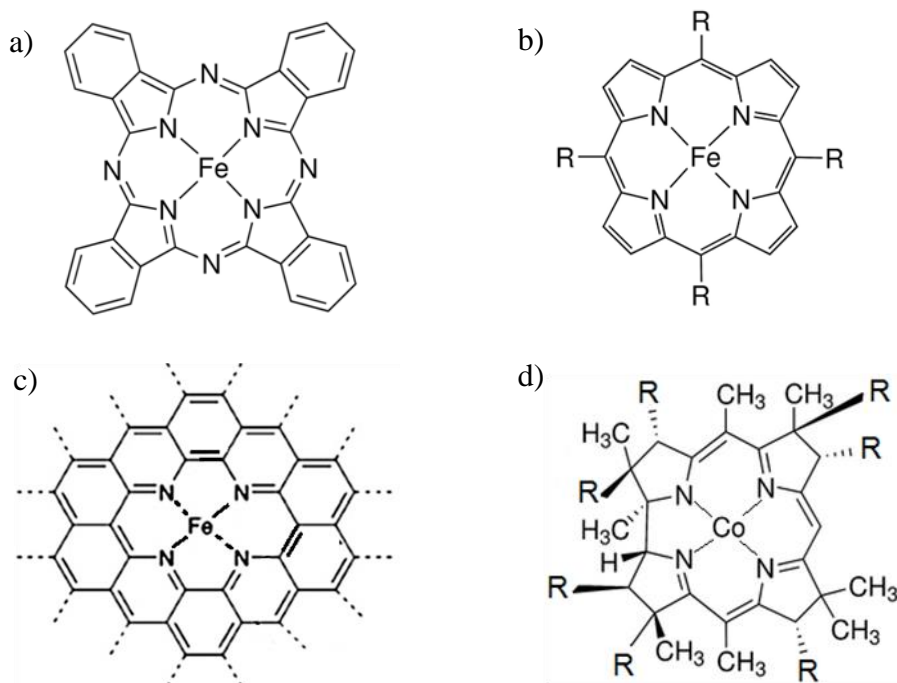


**Figure 2.16** Transition metal macrocycles: a) iron phthalocyanine, b) iron porphyrin, c) iron tetraazaannulene [128], and d) cobalt corrin.

A breakthrough in activity and stability of the M-N<sub>x</sub>/C materials was achieved when heat treatment at temperatures from 400 to 1000 °C (pyrolysis) was introduced to the catalyst synthesis process [22]. In 1989, Yeager and co-workers showed that it is possible to avoid using expensive transition metal macrocycles by heat-treating a metal precursor and a nitrogen precursor impregnated on a carbon black. This discovery led to identifying the essential components needed for forming active sites in M-N<sub>x</sub>/C catalysts, namely (i) a transition metal precursor, (ii) nitrogen precursor, and (iii) carbon [117].

Different non-precious transition metals have been investigated in the synthesis of the M-N<sub>x</sub>/C catalysts, including Fe, Co, Mn, Ni, Cu and Cr. Fe and Co provide the best catalytic activity for the ORR. Moreover, if one catalyst contains two or more different types of metal centres, its ORR activity can be enhanced notably [22]. Chu et al. [129] in their study of the M-N<sub>x</sub>/C catalysts for direct methanol fuel cells revealed that among binary metal catalysts (Co/Fe, V/Fe, Ni/Fe or Cu/Fe), heat treated Co/Fe macrocycles had significantly higher ORR activity than others. Recently, Serov [130] et al. studied tri-metallic catalysts and found that the most pronounced catalytic performance was in the case of combination of Fe with Co, Cu and Mn

A great variety of nitrogen precursors have been utilized for synthesis of M-N<sub>x</sub>/C catalysts [117]. Firstly, the transition metal macrocycles can act as both metal and nitrogen precursors. Secondly, these can be various nitrogen-containing molecules, such as pyridine, bipyridine, phenantroline, glycine, melamine, urea, thiourea, selenourea, ethylene diamine, purine and pyrimidine, cyanamide, nitroaniline, tripyridyl triazine, triethylenetetramine and triethylamine, etc. These molecules can easily form chelate complexes with transition metals and serve as ligands, coordinating to the metal centre via nitrogen atoms. Conductive polymers such as polyaniline (PANI), polypyrrole (PPy), and polyvinylpyridine, display some ORR activity themselves and are nitrogen rich precursors for the M-N<sub>x</sub>/C catalysts [22]. Finally, heat treatment of carbon in the presence of gases such as ammonia or acetonitrile results in formation of nitrogen functional groups in carbon and also leads to carbon's partial gasification. It was demonstrated that in the presence of ammonia, a partial gasification of the disordered carbon phase leads to formation of micropores in the catalysts [22, 131].

Various carbon materials were utilised in the syntheses of the M-N<sub>x</sub>/C catalysts: carbon blacks, carbon nanotubes, oxidized or activated carbons, as well as carbons doped with nitrogen [22]. The introduction of oxygen containing groups to carbon surface is believed to cause an increase in the activity of carbon black for oxygen reduction, which is attributed to the presence of quinone groups [116]. The presence of nitrogen in carbon improves the activity towards oxygen reduction compared to the oxidized carbon, which does not contain nitrogen. In addition, the modification with

nitrogen significantly decreases the percentage of hydrogen peroxide produced during oxygen reduction in comparison with oxidized carbon. Thus, the incorporation of nitrogen groups onto the carbon support greatly improves both the catalyst's activity and selectivity towards the ORR [116].

A porous carbon framework can be obtained using a silica template method of catalyst synthesis, a technique proposed by Ziegelbauer et al. [19], in which amorphous fumed silica is dispersed with cobalt porphyrin and subsequently pyrolyzed. The silica template is removed by etching with potassium hydroxide (KOH). The etching out of silica particles results in the unique morphology of the material with a hollow spherical structure that provides a high surface area for catalytically active sites [128].

From a fundamental point of view, a catalyst's activity and stability towards the ORR relies on knowing its active site structure. Pyrolysis causes changes in the structure of macrocycles, chelate complexes and conductive polymers, and this imposes uncertainty regarding what surface moieties serve as catalytic active sites for the ORR. At present, active site structures are still a subject of controversy [22]. Experimental literature presents two opinions on the nature of active sites in M-N<sub>x</sub>/C catalysts. The first one is that the transition metal centre coordinated by nitrogen atoms is the active site for the ORR. In these active sites, the number of nitrogen atoms coordinated with the metal atom is not unambiguously determined: some authors propose that the metal atom is coordinated to two nitrogen atoms (M-N<sub>2</sub>/C) [19, 132, 133], and some authors believe the metal should be bound to four-bond nitrogen atoms [119, 121, 134, 135], as illustrated in Figure 2.17.

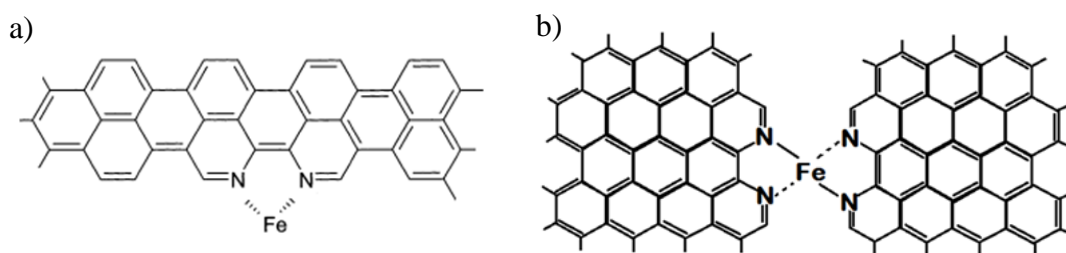


**Figure 2.17** Proposed active sites with a) two- and b) four-fold coordination of the transition metal to the nitrogen atoms [127, 136].

The second opposite opinion on the nature of the ORR active sites is that they are metal free, since the M-N<sub>x</sub>/C moieties decompose at high temperatures. It is proposed that the transition metal is not a part of the active site structure but serves to catalyze the incorporation of nitrogen to carbon structure, which is active for the ORR [22, 75, 137-139]. This hypothesis is confirmed by the fact that activity can improve after treatment with acids, which removes transition metals from the catalyst's surface

[76, 116, 140]. Thus, the exact role of transition metals in the M-N<sub>x</sub>/C catalysts remains unknown and further detailed investigations are required.

Importantly, the M-N<sub>x</sub>/C catalysts exhibited the highest activity and stability amongst the other non-precious catalysts tested in PEM fuel cells [24, 136, 137]. One of the most active non-precious metal catalysts was synthesized in 2009 by Lefevre et al. [136]. The authors used carbon black as a support material, 1,10-phenanthroline and ammonia as nitrogen precursors and iron acetate as a metal precursor. Briefly, the micropores of the carbon black were filled with a mixture of iron acetate and 1,10-phenanthroline as a pore filler. Then the filled carbon support was exposed to two pyrolysis procedures, the first being at 1050 °C in argon, and the second at 950 °C in ammonia. Later, the same research group modified the synthesis procedure by utilizing a different support material, namely, Zn(II) zeolitic imidazolate framework (ZIF-8). This M-N<sub>x</sub>/C catalyst displayed the highest reported to date catalytic activity towards the ORR with volumetric current density of 230 A cm<sup>-3</sup> at a cell voltage of 0.8 V [67]. However, the stability of the catalyst is still insufficient under PEM fuel cell operation conditions.

Los Alamos National Laboratory [141] developed Fe and Co containing catalyst which demonstrates excellent combination of high activity and long-term stability. The reported power density is 0.55 W cm<sup>-2</sup> at 0.38 V, and the durability is 700 hours at 0.4 V with current density decline 3%. The authors employed iron (III) chloride and cobalt (II) nitrate as metal precursors, polyaniline as a nitrogen source and carbon black as a catalyst support. The synthesis procedure includes mixing the carbon black, aniline, the iron and cobalt salts, followed by polymerization of aniline by an oxidant, pyrolysis at 900 °C in nitrogen gas, leaching in sulphuric acid solution, and second pyrolysis in the same conditions.

Although great progress has been achieved in the research and development of M-N<sub>x</sub>/C catalysts, there are still challenges in both the activity and stability. The volumetric activity of the most active non-precious metal catalyst is still well below the 2015 target of 300 A cm<sup>-3</sup> [22]. Fuel cell stability tests for non-precious cathode catalysts are generally run at low current densities or low power levels, and the lifetime is also far shorter than required. Therefore, improving both the ORR activity and stability are the major short and long term focuses of research and development of non-precious metal catalysts [22].

#### **2.4.4 Metal-Free Carbon Catalysts**

Common carbon nanostructures are single-walled carbon nanotubes, multi-walled carbon nanotubes, onion, stacked platelets and stacked cups, as illustrated in Figure 2.18. They have different morphology, crystallinity and surface area. These

nanostructures are formed in conditions similar to those used to prepare catalysts for the ORR. The type of obtained nanostructure is controlled by temperature, pressure, atmosphere and metal catalysts. The surface of onion and nanotube structures consists of basal planes predominantly, whereas carbon fibres with stacked platelet or stacked cup structures have significant edge site exposure [61].

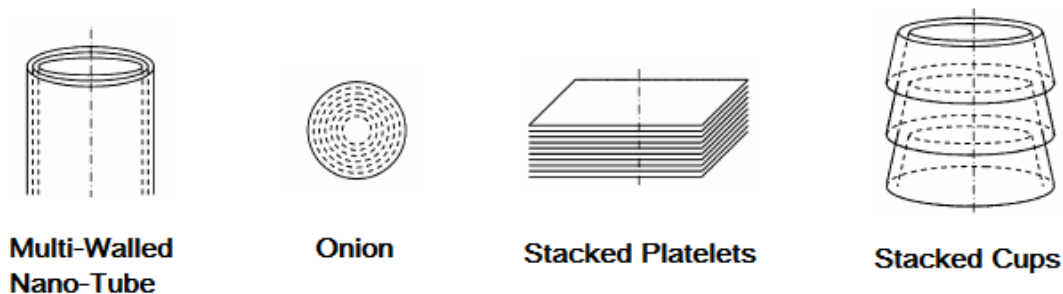


**Figure 2.18** Common carbon nanostructures [61].

Several catalytic reactions have a faster kinetics on carbon edge sites compared basal planes. This is attributed to the ability of carbon edge sites to chemisorb molecular oxygen more readily, e.g. carbon combusts faster at the edges and defect sites. In addition to the electron-donating effect of nitrogen, carbon edge sites may further improve the activity towards the ORR [61].

The building block of most of the carbon nanostructures is graphene, which is a one atom thick layer consisting of conjugated benzene rings. Graphene possesses exceptional physical properties: high electrical and thermal conductivity, as well as high stability and mechanical strength. By means of chemical modifications, it is possible to change the electrical and physicochemical properties of graphene for specific purposes through changing its energy band gap. As graphene is a polyaromatic system, it is capable of additive reactions with active reagents leading to the formation of covalent bonds [142]. Graphene is prepared by various methods, including micromechanical exfoliation, epitaxial growth, chemical vapour deposition (CVD) and chemical exfoliation of graphite (Hummers method) [143].

#### **2.4.4.1 Nitrogen Doped Carbon Catalysts**

Experimental research efforts have been focusing primarily on investigating nitrogen doped carbon as the ORR catalyst [18, 79, 80, 82, 83, 140, 144-154]. The main reported carbon nanostructures modified with nitrogen are graphene [18, 78, 145, 146, 148, 153-155], carbon nanotubes [79, 80, 140, 147] and mesoporous spheres (onion-type nanostructure) [152]. The literature on various nitrogen doped

nanostructures, especially graphene and nanotubes, is abundant, and only the most recent studies are briefly mentioned herein.

Oh et al. [79] studied carbon black, nanotubes and platelet nanofibres modified with nitrogen as the ORR catalysts and suggested that the catalytic activity is influenced by the type and content of a nitrogen functional group which in turn strongly depends on the carbon nanostructure, but does not depend on the surface area. They concluded that carbon platelet nanofibres have the highest ORR activity due to the highest degree of edge plane exposure and higher overall nitrogen content despite having the smallest surface area.

Some of the nitrogen doped carbon catalysts have been synthesized in the presence of transition metals but their surface is metal-free. For instance, Matter et al. [76] synthesized different nitrogen doped carbon nanostructures by pyrolysis of acetonitrile over silica and magnesia supports using Fe, Co and Ni particles. Also they found that stacked cup structure with many edge sites, enriched with nitrogen, is the most active for the ORR. The importance of the edge plane defects and the nitrogen content in nitrogen doped carbon nanotubes was confirmed later by other research groups [80, 140]. Popov's group reported syntheses of nitrogen doped carbon using transition metal salts [75, 137, 138].

These nitrogen doped carbon catalysts do not contain transition metals on the surface, but are covered with graphitic layers in the form of nanotubes or fibres. Recently, Tang et al. [156] synthesized nitrogen doped carbon nanotubes from ferrocene, nickelocene and cobaltocene using chemical vapour deposition. In the obtained material, the transition metals were encapsulated inside a stacked-cup carbon structure. The catalytic action of transition metal atoms in formation of nitrogen doped carbon nanostructures has been also corroborated by Sevilla et al. [157] in their report on the synthesis of nitrogen doped mesoporous carbon using polypyrrole and silica xerogel.

Nitrogen doped graphene as the ORR catalyst has been reported most frequently. This material is typically prepared by reducing graphene oxide (GO) in the presence of other compounds as nitrogen sources such as polyaniline [85, 148, 153], cyanamide [158], urea [78], melamine [83] 1,2-diaminobenzene [145], ammonia [82] by heat treatment, hydrazine [18], etc. Carbon nitride ( $C_xN_y$ ) is a carbonaceous material with very high nitrogen content, including both pyridinic and graphitic nitrogen moieties. This material can be obtained through the pyrolysis of cyanamide, melamine, or ethylenediamine on carbon. However, the low electrical conductivity of carbon nitrides impedes their application in fuel cells [83, 146]. A catalyst based on the combination of carbon nitride and graphene was reported to have an excellent catalytic performance for the ORR, including high activity, selectivity and long-term durability [146].

Importantly, although most fuel cells, including PEM, operate in acid electrolytes, a great number of the experimental studies of nitrogen doped carbon focus on alkaline electrolytes [82, 83, 140, 144-153]. In alkaline media, nitrogen doped carbon catalysts can exhibit a comparable or even higher activity than platinum [82, 147, 152], but in acid media, the activity is still insufficient [101, 144]. In acid and alkaline media, hydrated protons (hydronium ions) and hydroxyl anions, respectively, play a key role in the oxygen reduction. The detailed schematics of the ORR mechanism in acid and alkaline media are presented in a review by Wong et al. [149] and a theoretical study by Nilekar et al. [159]. However, to the author's knowledge, the substantial differences in the oxygen reduction kinetics on the same carbon based catalysts in acid and alkaline media have not been explained.

#### **2.4.4.2 Other Heteroatom Doped Carbon Catalysts**

In an effort to improve the ORR activity of carbon, other non-metal heteroatoms have been incorporated into carbon. Among these elements are boron, oxygen, phosphorus, and chalcogens (S, Se, Te). Boron has been reported to improve the catalytic performance of carbon both as a sole substituent heteroatom [62, 95], in binary combination with nitrogen [64, 84, 90, 91] and tertiary combination with nitrogen and phosphorus [92, 93]. In these studies, boron has been incorporated into the carbon structure using various techniques and compounds as sources of boron, e.g. triphenylborane, boron oxide, boron fluoride, boran-tert-butylamine, etc. Yang et al. [95] synthesized boron doped carbon nanotubes and found that the catalytic performance enhances with increasing boron content and approaches to that of platinum in alkaline media. The proposed active sites for the ORR in boron doped carbon are the substituent boron atoms.

Simultaneous doping of carbon with nitrogen and boron was reported to exhibit higher catalytic activity towards the ORR compared to pristine carbon as well as solely nitrogen or boron doped carbon [64, 90]. The higher catalytic activity is attributed to the presence of B-N-C moieties, Zhu et al. [84]. The synergetic effect of boron and nitrogen co-doping has been also confirmed by Liu et al. [91]. In alkaline media, the boron and nitrogen co-doped nanodiamond showed higher catalytic activity than platinum. However, in acid media the performance of boron and nitrogen doped carbon catalysts is still far below than that of platinum [92].

The electrochemical performance of phosphorus doped carbon towards the ORR has been tested by a few research groups in alkaline media [96-98]. The catalysts have been synthesized using different techniques with either triphenylphosphine or phosphoric acid as a source of phosphorus. Wu et al. [98] prepared phosphorus doped carbon in the presence of cobalt. The catalyst has shown activity in alkaline media

comparable to that of platinum. It was observed that the introduced cobalt enhances the ORR activity, although being absent on the catalyst surface.

Binary doping of carbon with phosphorus and other non-metal elements has been reported in a few studies: phosphorus with nitrogen [92, 93, 99], and phosphorus with silicon [160]. It was found that phosphorus and nitrogen co-doped carbon shows higher catalytic activity in acid media than solely nitrogen or binary nitrogen and boron doped carbon. The synergetic effect of co-doping has been assigned to an enhancement of electron density and a decrement of the band gap [92]. However, phosphorus content in the co-doped carbon should be optimal, since a high amount of phosphorus disrupts carbon network and therefore lowers the ORR activity [99].

Ternary combinations of heteroatoms doped to carbon have been phosphorus, nitrogen and sulphur [161], and phosphorus, nitrogen and boron [93]. Co-doping of phosphorus and sulphur to nitrogen doped carbon has improved its catalytic activity in acid media. This enhancement was ascribed to an increase of carbon edge sites and the portion of pyridinic nitrogen. Similarly, ternary phosphorus, nitrogen and boron co-doped carbon displayed a higher ORR activity in acid media than carbon doped with binary combinations of these elements. The role of phosphorus is suggested to be a charge delocalization of carbon atoms and creating carbon morphology with high edge exposure, whereas the role of boron is deemed to be increasing the portion of pyridinic nitrogen sites.

Oxygen doped carbon as a catalyst for the ORR has been reported in very few studies [66, 151]. However, since the majority of reported synthesis methods involve pyrolyses, acid leaching, and use of oxygen containing materials, e.g. graphene oxide, it is difficult to avoid incorporation of oxygen into a carbon catalyst structure. The presence of significant amounts of oxygen in these catalysts is detected by physicochemical methods of material investigation, in particular, X-ray photoelectron spectroscopy [18, 78, 82, 85, 148, 152, 155]. Frequently, oxygen is the most abundant element after carbon in these catalysts, but its impact on the catalytic activity is not discussed in the literature. Importantly, in heteroatom doped carbons, especially boron, phosphorus or sulphur doped carbons, the content of oxygen is several times higher than that of the doped heteroatoms [63, 84, 97, 98, 160, 162, 163]. In fact, these materials are oxygen modified carbons with trace amounts of other elements, the effect of which should be negligible due to the low concentrations. Thus, omitting possible effect of large amounts of oxygen is a serious weakness in the existing literature on experimental development of doped carbon based catalysts.

Chalcogen doped/modified carbons have been synthesized and tested as potential catalysts for the ORR, with sulphur [63, 102, 162] or selenium [164] as the heteroatoms. In these catalysts, the oxygen content is markedly higher than that of the chalcogens. The substituent sulphur and selenium atoms are believed to exist in

thiophene-like form. In contrast, tellurium modified carbon [165] contained a relatively high percentage of the chalcogene, circa 5%, in the form of tellurium nanoparticles deposited on carbon. However, moderate catalytic activity of S, Se and Te doped/modified carbon catalysts provides room for further improvement. Also, sulphur and selenium have been co-doped to carbon with nitrogen [101, 163, 166, 167]. The co-doped nitrogen and chalcogen carbon catalyst have considerable amounts of oxygen and nitrogen and very small amounts of chalcogens (< 1%). In alkaline media, the catalytic performance of these materials is comparable or higher than that of platinum, but in acid media the activity is low.

Finally, syntheses of halogen modified carbon based catalysts have been reported, namely, fluorine [168], fluorine with nitrogen [169], and iodine [170] doped carbon. In addition to significantly larger content of oxygen, fluorine is present in C-F bonds on carbon edges, and iodine is both in an elemental state and in the form of iodide ( $I^-$ ), triiodide ( $I_3^-$ ), or pentaiodide ( $I_5^-$ ) ions. The electrochemical tests in alkaline media show that the activity of these catalysts is slightly higher than that of platinum.

#### **2.4.5 Achievements and Challenges**

One of the most promising carbon based cathode catalyst for PEM fuel cells was demonstrated by Popov's research group in a series of experimental reports [116, 138, 171]. Their carbon composite catalysts were synthesized using carbon black and simple nitrogen containing organic molecules in the presence of iron and cobalt salts. The transition metals were removed from the catalyst surface by acid-leaching, and the remaining metal particles were encased inside the carbon structure and absent on the catalyst surface. The catalytic activity was assigned to pyridinic and graphitic nitrogen groups which increased the electron-donor properties of carbon. The role of transition metals was to facilitate the incorporation of nitrogen to carbon. [116]. The catalyst showed good activity in terms of the onset potential, which was as high as 0.87 V versus a normal hydrogen electrode, and also notable selectivity, generating less than 1% of hydrogen peroxide. A PEM fuel cell test also exhibited good performance with a current density of 2.3 A cm<sup>-2</sup> at 0.2 V, as well as durability with 480 hours of continuous operation and no significant performance degradation.

It should be emphasized that many of the studied metal free carbon catalysts show an activity superior to that of platinum in alkaline media, but the performance of the same materials in acid media is still very low [29, 101]. This means that these carbon based catalysts have high promise for use in alkaline fuel cells, but they are not suitable for PEM fuel cells. Thus, the activity and durability of the existing carbon based catalysts have not achieved the level of commercially available platinum [18].

The nature of the active sites in the heteroatom doped carbon catalysts is still not established. In nitrogen doped carbon, the major uncertainty is whether pyridinic or graphitic nitrogen provide active sites for the ORR, or whether the reaction is promoted simply due to an abundance of highly active carbon edge or defect sites [144]. Controversial opinions on the oxygen reduction active sites exist with respect to other heteroatom doped carbon materials. In boron doped carbon, the active sites are deemed to be either substituent boron atoms [62] or B-N-C moieties in boron and nitrogen doped carbon [84, 90, 91]. Conversely, the presence of boron does not create new active sites [92] but increases the number of the pyridinic nitrogen sites and enhances asymmetric spin density of carbon atoms [93]. In phosphorus doped carbon, phosphorus is believed to create defect active sites in carbon, but the nature of these active sites is not specified [97-99]. Conversely, presence of phosphorus in carbon is suggested to merely increase the number of pyridinic nitrogen active sites [92, 93]. In addition, the presence of large amounts of oxygen in any carbon based catalyst is generally ignored, although it may change the electronic structure of carbon materials to a far greater extent than the rest of the doped heteroatoms.

#### **2.4.6 Catalyst Supports**

A considerable amount of literature has been published on various materials as supports for both platinum and non-platinum catalysts for PEM fuel cells. The support materials reported in the literature can be divided into two groups: carbon based and non-carbon. The most widely utilized carbon based supports are graphene oxide (GO) [18, 62, 78, 83, 145, 146, 148, 154, 158, 164, 170, 172-174], reduced graphene oxide (rGO) [18, 155, 175-179], and carbon nanotubes (CNTs) [118, 140, 147, 164, 180-184]. A special class of organic materials proposed as catalyst supports are metal organic frameworks (MOF) [185, 186]. A subclass of MOFs, named zeolitic imidazolate framework (ZIF), has been successfully used to synthesise a Fe-N<sub>x</sub>/C catalyst with unequalled activity towards the ORR [67].

Electronic conductivity and porosity are the factors to be considered in the design of fuel cell catalysts. Sufficient electronic conductivity of a support material is 0.1 S cm<sup>-1</sup> [187]. This is five times greater than the proton conductivity of the ionomer membrane in PEM fuel cells and therefore does not impose significant Ohmic losses in the catalyst layer. However, compared to pristine carbon materials, heteroatom doped carbons have a lower conductivity [188]. Table 2.3 shows the electronic conductivities of a few materials reported in the literature as possible catalyst supports. Also, the support material should be microporous. The porosity of carbon is circa 80%, and the pore diameter varies between 20 – 100 nm. The high porosity

entails that the catalyst supports should provide a high surface area of more than 50 m<sup>2</sup> g<sup>-1</sup> [187].

Besides carbon based materials, inorganic compounds have been reported as alternative catalyst supports. Although it is an electrical insulator, silica (silicon dioxide SiO<sub>2</sub>), has been also reported as a catalyst support owing to its high stability in an acidic media [137, 189, 190]. In these studies, the silica support was encapsulated within the carbon catalysts. Silica was also used as a removable template to form a porous structure of a carbon catalyst [137, 191, 192].

**Table 2.3** Electrical conductivities of some catalyst support materials.

Material name	Formula	Electronic conductivity, S/cm	Reference
Carbon black (Vulcan XC-72)	C	0.71	[76]
Carbon nanotubes	C	0.45	[193]
Titanium dioxide (titania)	TiO <sub>2</sub>	1.47×10 <sup>-6</sup>	[194]
Niobium doped titania	5 at% Nb/TiO <sub>2</sub>	1×10 <sup>-4</sup>	[195]
Titanium nitride	TiN	850	[196]

Titania (titanium oxide, TiO<sub>2</sub>) is a semiconductor and has much lower electronic conductivity than carbon black, as shown in Table 2.3. However, titania was utilized in the syntheses of platinum based catalysts [194]. There are two strategies to substantially increase the electronic conductivity of inorganic oxides: (i) doping with n-type donors of electron density, e.g. doping titania with niobium (Nb) [195], and (ii) combining the inorganic oxide with carbon to make composite/hybrid materials [196, 197]. Several studies reported niobium doped titania [195, 197], titania combined with carbon as a composite support [194, 197, 198], and various non-stoichiometric compounds of titanium such as nitrides [196], oxy-nitrides [199], and oxy-carbonitrides [200, 201]. Although titania based support materials possess a lower conductivity than carbon, they may increase durability of cathode catalysts for PEM fuel cells [197, 198].

Tungsten carbide (WC) has a high chemical stability and electronic conductivity and has been utilized recently as an alternative support in cathode catalysts for PEM fuel cells [202, 203]. The tungsten carbide supported catalysts, both platinum and metallorganic, are considerably less active than the commercial platinum catalyst. In addition, tungsten carbide is reported to be unstable under highly oxidizing conditions of the ORR and can easily form tungsten oxides [202].

### 2.4.7 Other Types of Non-Precious Catalysts

Non-precious metal carbides, oxides, oxynitrides and carbonitrides have been considered as inexpensive alternative catalysts for fuel cell applications in recent years [22]. Transition metal carbides and nitrides have attracted scientific interest due to their good electrical conductivity, corrosion resistance, and catalytic activity. Several transition metal carbides such as tungsten, titanium, and tantalum show some activity towards the oxygen reduction in acid media. The electronic structure of tungsten carbide is similar to that of platinum. Properties of transition metal carbides can be modified by alloying them with other metals, for instance tantalum [2]. However, the ORR activity of these materials is low, which is attributed to the inherently large band gap and low electronic conductivity [22]. Moreover, stability of transition metal carbides in acid media is low and hinders their application in PEM fuel cells.

Transition metal nitrides are more stable in acidic conditions and under high electrode potentials. Titanium, cobalt, molybdenum, niobium and tungsten nitrides have been reported [2]. Carbon supported tungsten nitride ( $W_2N/C$ ) exhibited good stability after 100 hours of operation. However, the catalytic activity of these materials is relatively low [22]. Non-precious metal oxides also possess suitable stability in acidic and oxidizing conditions. Zirconium, cobalt, titanium, tin and niobium oxides have been explored, and the ORR activity of these compounds was ranked as follows:  $ZrO_{2-x} > Co_3O_{4-x} > TiO_{2-x} = SnO_{2-x} > NbO_{5-x}$ . However, their low catalytic activity and insulator properties indicate that they may not be used as efficient cathode catalysts in PEM fuel cells [22]. Several studies have been published on the oxygen reduction activity of carbon supported manganese oxides in an alkali media [41, 204-208]. These manganese oxide catalysts attracted particular attention because they demonstrated the ORR activity and stability in alkaline media approaching to that of commercially available platinum catalyst.

Transition metal oxynitrides are another class of materials which show some catalytic activity towards the oxygen reduction. Oxynitrides are formed by substitutional doping of metal oxides with nitrogen. The substitutional doping can reduce the large inherent band gap of metal oxides, enhancing the electronic conductivity, which is important in the ORR catalysis. Transition metal carbonitrides, e.g. chromium, cobalt and nickel carbonitrides have also been explored as the ORR catalyst materials [22]. Tantalum and zirconium oxynitrides were investigated as ORR electrocatalysts. A range of various inorganic non-stoichiometric compounds have been investigated as catalysts for the ORR in acid and alkaline media: zirconium oxynitrides [209], titanium, tantalum and niobium nitrides, carbides, oxy-nitrides and oxy-carbides [210, 211]. Carbon composites of these inorganic compounds show an improved catalytic activity in acid media, but it is still far below that of platinum [209].

## 2.5 Factors Influencing Catalytic Performance of Cathode Catalysts

There are several important factors that influence the activity and stability of cathode catalysts for fuel cells [22], as illustrated in Figure 2.19. The factors are divided here into chemical and physical. The chemical factors are related to the materials of the catalyst support, nitrogen or another heteroatom precursor and transition metal precursors. The physical factors encompass various synthesis methods and temperature and duration of pyrolyses.

Reported in the literature support materials are either carbon based or non-carbon inorganic compounds. Carbon based materials are ideal support for PEM fuel cell catalysts, since they have the essential properties of high electronic conductivity and large surface area. The most widely used carbon support materials are carbon blacks, e.g. Vulcan XC-72 [131], Ketjen Black EC-300J [24], Black Pearl 2000 [136], graphene oxide [175] and activated carbon [212]. In addition, various organic compounds such as glycine [26], aminoantipyrine [29], pyridyl pyrazine [20] etc., carbonized at high temperatures, can be the sources of carbon for the catalysts. As mentioned in Section 2.4.4, various carbon materials have different nanostructure, surface morphology, porosity, surface area and graphitization degree.

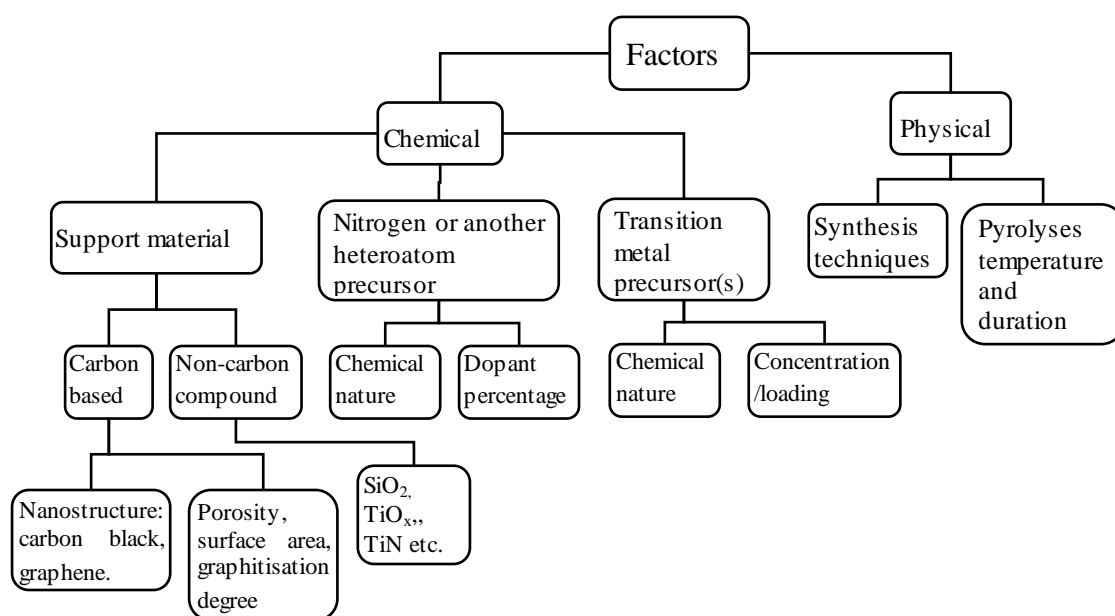


**Figure 2.19** Factors influencing the activity and durability of cathode catalysts.

Properties of carbon such as nanostructure and porosity influence the resulting ORR activity and stability of pyrolysed carbon based catalysts significantly. The ORR activity depends on the catalyst's pore volume and surface area: large surface area

implies high density of the catalyst's active sites. However, highly porous catalysts can degrade rapidly under PEM fuel cell operational conditions due to a low degree of graphitisation. Thus, there is a trade-off between the activity and stability of carbon based catalysts [22].

There are several ways of developing carbon catalysts with high surface area. First, the utilisation of carbon supports with high surface area, e.g. multi- and single-walled carbon nanotubes [182, 184], graphene [18], etc. Heat treatment of the catalyst with ammonia gas (ammonia etching) results in a partial evaporation of disordered carbon phase [131, 136, 213] and increases the porosity of a catalyst. Finally, silicon or silica hard template synthesis methods enable us to create highly porous carbon structures [19, 137, 189].

A catalyst support should have a good corrosion resistance, since cathode catalysts operate in a chemically aggressive PEM fuel cell environment: high oxygen concentration, low pH, high potential. The drawback of carbon based supports is their thermodynamic instability in PEM fuel cell operating conditions if voltages rise above 0.9 V [196]. The corrosion of carbon is described by the reaction [197]:



In order to solve the stability problem, novel catalyst supports that are not based on high surface area carbons, but made of alternative materials, have drawn the attention of researchers. Various inorganic compounds have been utilized in combination with carbon, such as silica [76, 214], titania [194, 195, 197, 198], titanium nitride [196], tungsten carbide [202, 203], etc.

Many of organic molecules have been reported in the literature as the sources of nitrogen in catalyst syntheses, as discussed in Sections 2.4.3 and 2.4.4. A few research groups have studied the dependence of the ORR catalytic activity of nitrogen doped carbon catalysts on nitrogen precursors, utilized in the syntheses, and the content of doped nitrogen. The nitrogen precursor determines the content of nitrogen doping in the pyrolysed nitrogen doped carbon catalysts and hence the ORR activity [128]. Maruyama et al. [26] used a few different aminoacids containing more than one nitrogen atom in the molecule as the nitrogen precursors and found that the catalytic activity increases with the number of nitrogen atoms in the aminoacids. The same effect was confirmed later by other research groups [80, 140, 215, 216]. In these studies, the contents of nitrogen in the pyrolysed carbon catalysts varied between 1 and 11%. However, the optimal content of doped nitrogen has not been accurately established as yet. Rao et al. [216] reported that a nitrogen content of 8.4 % exhibited the best ORR performance, and a further increase in the concentration of doped nitrogen reduces the catalytic activity. In addition, the effect of concentration of other

heteroatoms, e.g. boron, phosphorus, sulphur, etc., on the ORR activity of doped carbon catalysts has not been studied as yet.

Although transition metals may or may not be a part of the active sites of the catalysts for the ORR, their presence significantly improves the activity and stability of cathode catalysts. Transition metal nature and loading has an effect on the ORR activity of carbon based catalysts [217, 218]. As mentioned in Section 2.4.3, among many investigated transition metals, iron and/or cobalt have the most pronounced effect on the catalytic performance of carbon catalysts. The precursors of transition metals are typically inorganic salts of the metals, e.g. sulphates [171], nitrates [219], chlorides [220] or acetates [67]. The effect of transition metal precursor was studied by Yuan et. al. [221] using cobalt nitrate, chloride, acetate and oxalate in the carbon catalyst syntheses. They found that using cobalt acetate results in a better electrochemical performance. However, the effects of different iron salts on the catalytic activity have not been reported so far.

The optimal content of transition metals in carbon catalysts varies in different studies. However, there is a common trend in the effect of metal loading on the ORR activity. At low relative metal contents, which are study dependent, the activity of carbon catalysts increases with increasing the metal content up to a maximum saturation point in which a plateau of ORR activity is observed [22]. For instance, Hu et al. studied the effect of iron loading in metallorganic catalysts and found that the ORR activity increased with the iron content growing from 0 to 3%, but further addition of iron up to 10% resulted in a decrease in the activity [222].

Figure 2.20 illustrates a schematic of a metallorganic carbon based catalyst synthesis technique which can vary significantly in different studies, but the basic procedures are common. In general, three major materials are necessary for the synthesis: catalyst support, transition metal precursor and nitrogen precursor, all of which are discussed in Sections 2.4.3 and 2.4.4. These components are brought together in a way that depends on the chemical nature of the nitrogen precursor. If a nitrogen precursor can polymerize, polymerization is used to apply it onto a support material; if it is chemically stable, precipitation or impregnation of a porous catalyst support is conducted. For instance, the Zelenay research group used a facile technique of polymerization of aniline as a nitrogen source [24, 141, 220], the Dodelet group impregnated a stable nitrogen precursor (1,10 phenantroline) to the pores of a support material [223, 224], and Yang et al. used precipitation of cyanamide onto graphene oxide [219].

Depending on the ways of combining the three components, the next step may be the evaporation of solvent, e.g. in the case of formation of polyaniline [24]. The heat treatment, or pyrolysis, is crucial for annealing a catalyst structure and improving its stability, as mentioned in Section 2.4.3. The most common pyrolysis temperatures

reported in the literature typically are the range of 700 – 1000 °C [22, 67]. Acid leaching, i.e. treating the catalyst with a diluted acid solution is used to remove inactive particles or impurities from the surface [138]. In several reports, acid leaching is followed by a second pyrolysis performed in order to improve the catalyst's activity and stability [220].

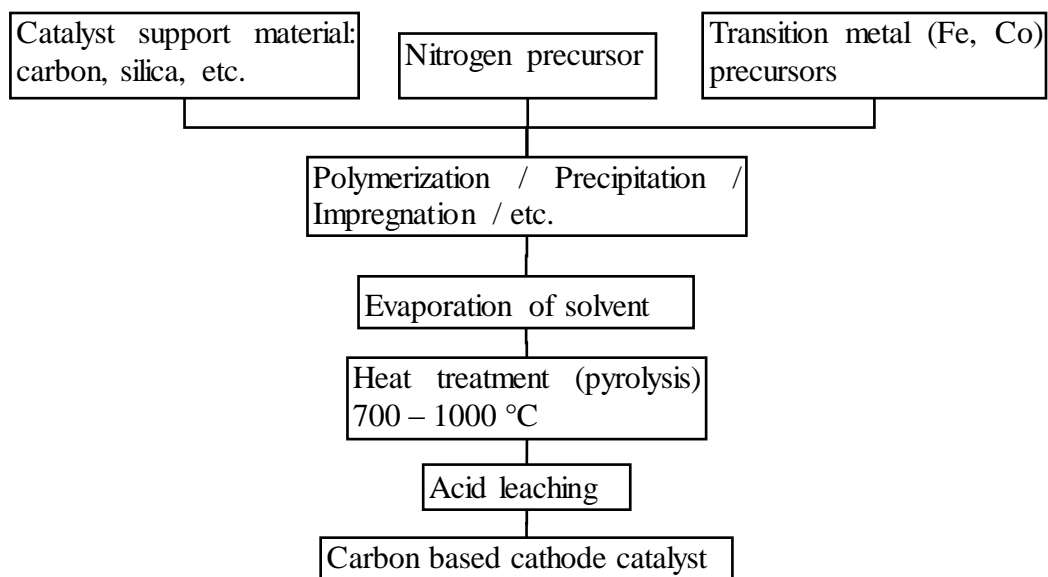


**Figure 2.20** Basic steps of a catalyst synthesis technique.

The optimal temperature pyrolysis of carbon catalysts is dependent on the precursor materials and pyrolysis environment, and it is determined experimentally by trial and error [22, 171]. Different pyrolysis temperatures in inert environments have varying effects on both ORR activity and stability of the synthesized catalysts. Normally, carbon catalysts displaying the highest activity towards ORR can be synthesized at pyrolysis temperatures between 500 and 800 °C in inert environments (N<sub>2</sub> or Ar). In this temperature range, it has been proposed that thermal annealing occurs between carbon, nitrogen and metal groups, creating some catalytically active sites responsible for the ORR activity observed through electrochemical measurements. In addition, pyrolysis temperatures in the range of 500 - 800 °C result in a high catalyst activity but a limited stability, whereas temperatures above 800 °C lead to a high stability, but the ORR activity is inferior to that resulting from the lower temperatures [22, 171].

## 2.6 Summary

Although platinum and platinum alloys show high activity as catalysts for the ORR in PEM fuel cells, their high cost and low durability are significant barriers for

commercialisation. Carbon based catalysts are promising alternatives to platinum based ones. The most active catalysts so far are nitrogen doped carbons synthesised in the presence of iron and cobalt. Although the transition metals are essential for high catalytic activity, their role in catalysing the oxygen reduction reaction is not established yet. Besides nitrogen, there have been several experimental attempts to develop boron, phosphorus and other heteroatom doped carbon catalysts. However, in these catalysts, the contents of the heteroatoms are negligibly small compared to the content of oxygen. Thus, the problem is to find an efficient technique of doping carbon with the heteroatoms. The structure of active sites of nitrogen, boron, or phosphorus doped carbons also remains unknown; consequently, the mechanism of the ORR on these active sites provided the motivation for this thesis.

## 2.7 Research Outlines

This thesis is dedicated to searching for alternative non-platinum cathode catalysts for PEM fuel cells both theoretically and experimentally. Figure 2.21 illustrates the structure of the studies.

The theoretical part of the thesis is dedicated to the fundamental understanding of the oxygen reduction reaction in PEM fuel cells and its relation to the active site structures and composition of the cathode catalysts. In an effort to predict the active site structures, three carbon based model systems are investigated: carbon edge sites, transition metal macrocycles and graphene basal planes. In order to find the catalyst active sites, reaction energies and activation energies of the multi-step oxygen reduction are determined. Reaction energies show the *potential* and *direction* of spontaneous reactions, and activation energies indicate *how fast* the reaction can occur. The activation energies for the alternative catalysts are desired to be lower than those for platinum in order to ensure that the rate of the oxygen reduction reaction on the alternative cathode catalyst is fast enough.

The experimental part and the thesis focus on the research and development of alternative cathode catalysts for PEM fuel cells. Several catalyst materials are synthesized using techniques reported in the literature as well as novel techniques with different precursor materials and modified procedures. Each synthesized catalyst is tested, or characterized, using electrochemical equipment, which simulates the oxygen reduction in PEM fuel cells. Current density and voltage are the experimental measures of the catalytic activity of the oxygen reduction reaction. These parameters are compared against those of platinum to identify the best performing alternative catalyst. The surface structures and compositions of the selected synthesized catalysts are investigated using physicochemical methods such as X-ray diffraction, X-ray

photoelectron spectroscopy and scanning electron microscopy. The catalysts that have shown the best performance in the electrochemical characterization are tested using in-house manufactured PEM fuel cells. The fuel cell performance of the catalysts is measured as current density as a function of cell voltage.

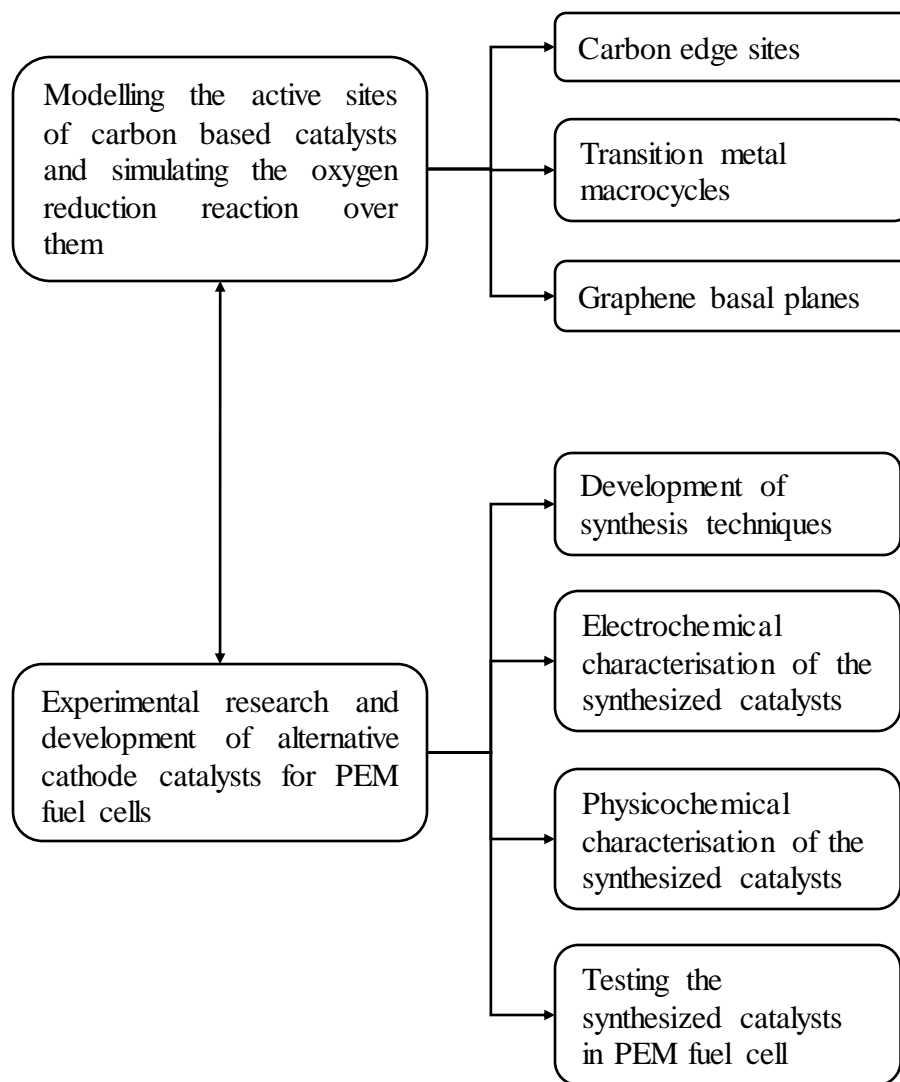


**Figure 2.21** Outline of the theoretical and experimental studies of alternative cathode catalysts for PEM fuel cells.

## Chapter 3

### DFT Modelling of Molecular Oxygen Binding to Heteroatom Doped Carbon Edge Sites

#### 3.1 Introduction

In this chapter, carbon edge sites are investigated theoretically by means of DFT simulations. Non-doped and nitrogen (N), boron (B), phosphorus (P), aluminium (Al), oxygen (O), sulphur (S) and selenium (Se) doped carbon (C) edge sites are modelled. The catalytic effect of graphitic and pyridinic N, as well as tertiary and binary B doping of carbon edge sites is addressed.

Since molecular oxygen binding is a first step in the ORR, this reaction is modelled in the present chapter and used for predicting the most promising catalytic structures of doped and non-doped carbon edge sites. Possible products of molecular oxygen binding to the doped carbon edge are modelled. Further, chemisorption energies are calculated to estimate the thermodynamic favourability of the reactions, and activation energies are obtained to evaluate kinetic favourability of molecular oxygen binding to different active sites in doped carbon edges. Using these data, detailed diagrams of molecular oxygen binding pathways are obtained for various possible sites on doped and non-doped carbon edges.

#### 3.2 Model Systems

Carbon materials consist of both ordered (graphitic) and disordered (amorphous) regions. The ordered regions are composed of graphene domains, and the disordered regions consist of a three-dimensional network of interconnected small fragments of graphene [79, 101, 225].

The graphene edge sites can be in the forms of zigzag and armchair, illustrated in Figure 3.1. Since it has been reported that the zigzag edge sites exhibit a higher reactivity towards the ORR [39, 77], the graphene edge sites in this work are studied using the zigzag model only. Model systems employed in this study represent these two phases of carbon and are the finite-size graphene fragments terminated with C-H bonds, as shown in Figure 3.2. The systems with two and three conjugated aromatic rings represent the disordered carbon phase and are further referred to as the naphthalene- and anthracene-type. The system with eight aromatic rings represents the ordered regions of carbon and is referred to as the graphene-type.

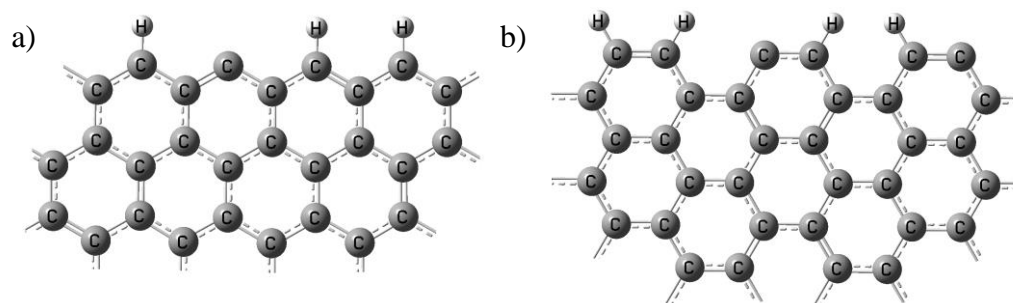


**Figure 3.1** a) Zigzag and b) armchair edge sites of graphene.

Doping of N and B to carbon has been studied using all three model systems. In the naphthalene- and graphene- type systems the heteroatoms were placed in the graphitic position to model the graphitic N and the ternary B doping. In the anthracene-type systems, N and B were placed in the central position to model pyridinic N and binary B doping. The P and Al doping of carbon was studied using the naphthalene- and graphene-type systems, with the heteroatoms placed in the central “graphitic” position. The O, S and Se doped carbon was studied using the anthracene-type model system.

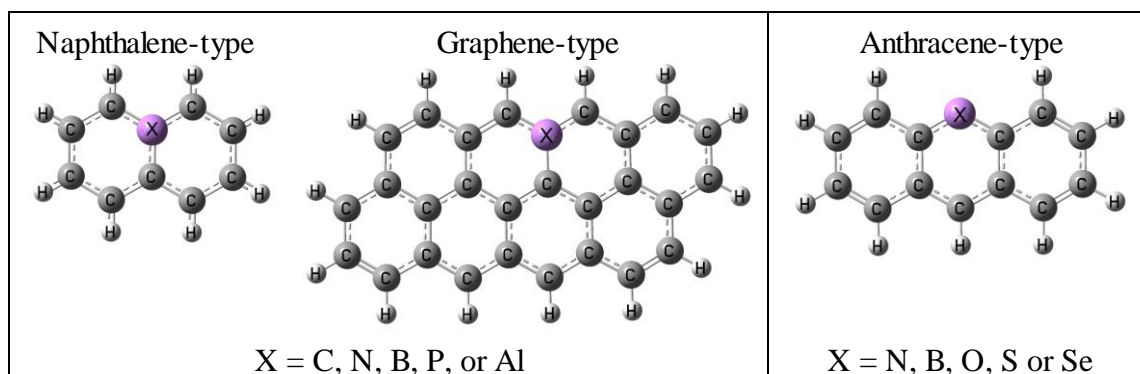


**Figure 3.2** Generic model systems of the doped carbon edge sites studied here.

### 3.3 Theoretical Method

The boundaries of carbon edge sites can be partially terminated with hydrogen (H) atoms, or other functional groups such as hydroxyl, acetoxy, etc. [226, 227]. For simplicity, the partial termination of carbon edges has been modelled by removing one or two H atoms from the edge of the model systems. Since the cathode of a fuel cell is a negatively charged environment, the catalyst surface bears a negative charge. To account for this, a (-1) charge has been assigned to the model systems. A combined effect of the partial H termination and a negative charge on the catalyst has been simulated by removing one or two H atoms and assigning a (-1) charge to the model

systems at the same time. Thus, a few modifications of the generic model systems with different charge ( $Z$ ) have been used to study molecular oxygen binding, or chemisorption on the doped carbon edge sites.

To represent the non doped carbon edge sites, four modifications of the generic model systems have been used:

- (i) fully H-terminated ( $Z = 0$ ),
- (ii) one H atom removed ( $Z = 0$ ),
- (iii) one H atom removed and negatively charged ( $Z = -1$ ), and
- (iv) two H atoms removed ( $Z = 0$ ).

To represent the graphitic N, ternary B, P, Al, O, S and Se doped carbon edge sites, five modifications have been employed:

- (i) fully H-terminated ( $Z = 0$ ),
- (ii) fully H-terminated and negatively charged ( $Z = -1$ ),
- (iii) one H atom removed ( $Z=0$ ),
- (iv) two H atoms removed ( $Z = 0$ ), and
- (v) two H atoms removed and negatively charged ( $Z = -1$ ).

The pyridinic N and binary B doped anthracene model systems have been studied in four modifications:

- (i) one H removed from the heteroatoms ( $Z = 0$ ),
- (ii) one H removed from the heteroatoms and negatively charged ( $Z = -1$ ),
- (iii) H terminated heteroatoms ( $Z = 0$ ), and
- (iv) H terminated heteroatoms and negatively charged ( $Z = -1$ ).

The spin multiplicities of the model systems have been allowed to relax, i.e. the electronic energy of each system has been obtained with two spin multiplicities: (i) the lowest,  $M = 1$  or  $2$ , and (ii) the next higher,  $M = 3$  or  $4$ , depending on the electronic structure. The multiplicity with lower electronic energy has been taken as the ground state.

During the oxygen reduction on a catalyst, the oxygen molecules approach the catalyst surface from various directions. This has been accounted for by different initial orientations of the oxygen molecule over the model systems prior to geometry optimisations. Three main orientations of the oxygen molecule investigated have been in-plane, parallel to the edge, and perpendicular to it, as shown in Figure 3.3.

The simulations have been performed with the B3LYP hybrid DFT method in Gaussian 09 [48] in combination with two split-valence basis sets: augmented with both polarization and diffuse functions 6-311++G(d,p) in the case of non-doped, N, B, P and Al doped systems, and 6-31G(d) for O, S and Se doped anthracene-type systems. The model systems have been geometry-optimized in order to obtain the structures corresponding to the local minima on the potential energy surface (PES). Subsequent frequency calculations have been carried out in order to ensure that the

obtained molecular structures correspond to the minima rather than to saddle points on the PES. Zero point energy (ZPE) corrections, obtained in the frequency calculations, have been taken into account in calculated electronic energies.

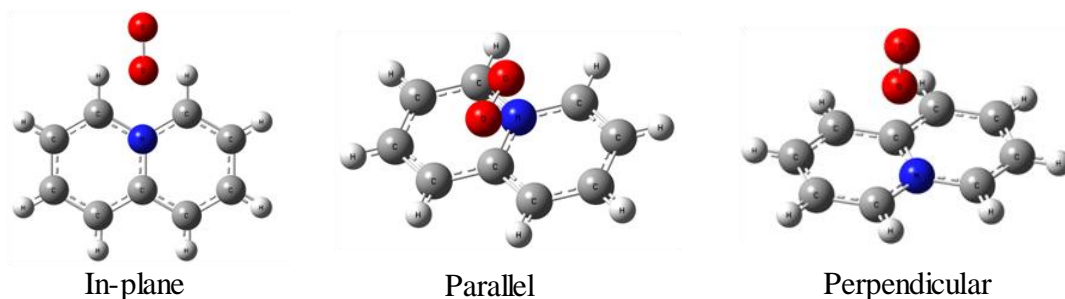


**Figure 3.3** Initial configurations of the oxygen molecule relative to the model system.

Transition states (TS) connecting the reactants and products of molecular oxygen binding to the N and B doped naphthalene-type model systems have been obtained using the QST3 procedure and subsequently verified using the intrinsic reaction coordinate (IRC) [45] calculations launched from the TS points. In the case of convergence problems, relaxed potential energy surface (PES) scans have been performed to locate the TS.

In order to examine the pathways of molecular oxygen binding to the P, Al, O, S and Se doped naphthalene-type model systems, the technique of relaxed PES scan calculations have been employed. In the case of the P and Al doped systems, the scanned coordinates were the distances between one of the atoms of the oxygen molecule and either (i) the doped heteroatom, or (ii) the adjacent C atom. The O-P and O-Al distances were reduced from 3.5 Å down to 1.5 and 1.6 Å, respectively, and the O-C distance was reduced from 3.5 Å down to 1.2 Å. In the case of the O, S and Se doped anthracene-type systems, the scanned coordinates were the distances between one of the atoms of the oxygen molecule and either (i) the valence unsaturated C atom at the edge, or (ii) the C atom adjacent to the heteroatom. The distances were reduced from 3.0 to 1.3 Å, and from 2.3 to 1.1 Å, respectively. In the scan calculations, the step size has been set to 0.1 Å. Smaller step sizes have been used in a few calculations to obtain finer resolution potential energy profiles. In order to account for the triplet spin state of molecular oxygen, the spin multiplicities in the scan calculations have been set either 3 or 4, depending on the electronic structure.

The relative energies in the potential energy profiles of molecular oxygen binding have been calculated as the energy difference between each scan point and the minimum energy point. The starting, maximum and minimum energy points of the scan calculations have been taken as the reactant complexes, transition states (TS) and reaction products, respectively. Molecular oxygen binding energies (product relative

energy levels), TS energy levels and relative energies of reactant complexes have been calculated as follows:

$$\Delta E = E - (E_{\text{Substrate}} + E_{\text{O}_2}) \quad (3.1)$$

where  $\Delta E$  is one of the calculated energy parameters,  $E$  is energy of either a product, or a TS, or a reactants complex,  $E_{\text{Substrate}}$  is the energy of a model system, and  $E_{\text{O}_2}$  is the energy of the oxygen molecule in the triplet spin state. The sum of  $E_{\text{Substrate}}$  and  $E_{\text{O}_2}$  is further referred to as the energy of reactants. Activation energies have been calculated as the difference between the TS energy levels and relative energies of reactant complexes.

## 3.4 Results and Discussion

### 3.4.1 Energies of Molecular Oxygen Binding to N, B, O and Non-Doped Carbon Edges

Firstly, structures of the non doped, N, B and O doped carbon model systems have been geometry-optimised. The ground states of all the systems have been found to have the lowest spin multiplicity, namely 1 or 2, depending on the electronic structure. The spin multiplicities of the ground states of the optimised products vary, being either the lowest (1 or 2) or the next higher (3 or 4).

#### 3.4.1.1 Non-Doped Carbon Edges

Figure 3.4 a) and b) show the relative energies of the products of molecular oxygen binding to the non doped naphthalene- and graphene-type systems, respectively. Optimised structures of the four modifications of the generic model systems are shown on the top, and the corresponding products are arranged in the columns below.

It can be observed that molecular oxygen does not bind to the fully H-terminated carbon edge sites, and the calculated relative energy of the products, or binding energy, is close to zero or endothermic (0.7 eV). In the case of systems with one H removed, products with the end-on chemisorbed oxygen molecule are the most thermodynamically stable. The calculated relative energies are similar for the naphthalene- and graphene-type systems: -1.7 and -2.0 eV for the neutral systems, and -2.6 and -2.5 eV for the (-1) charged systems, respectively. The benzoquinone-type products obtained for the systems with two H removed are the most

thermodynamically stable, since their calculated relative energies are -5.6 eV and -8.0 eV for the naphthalene- and graphene-type systems, respectively.

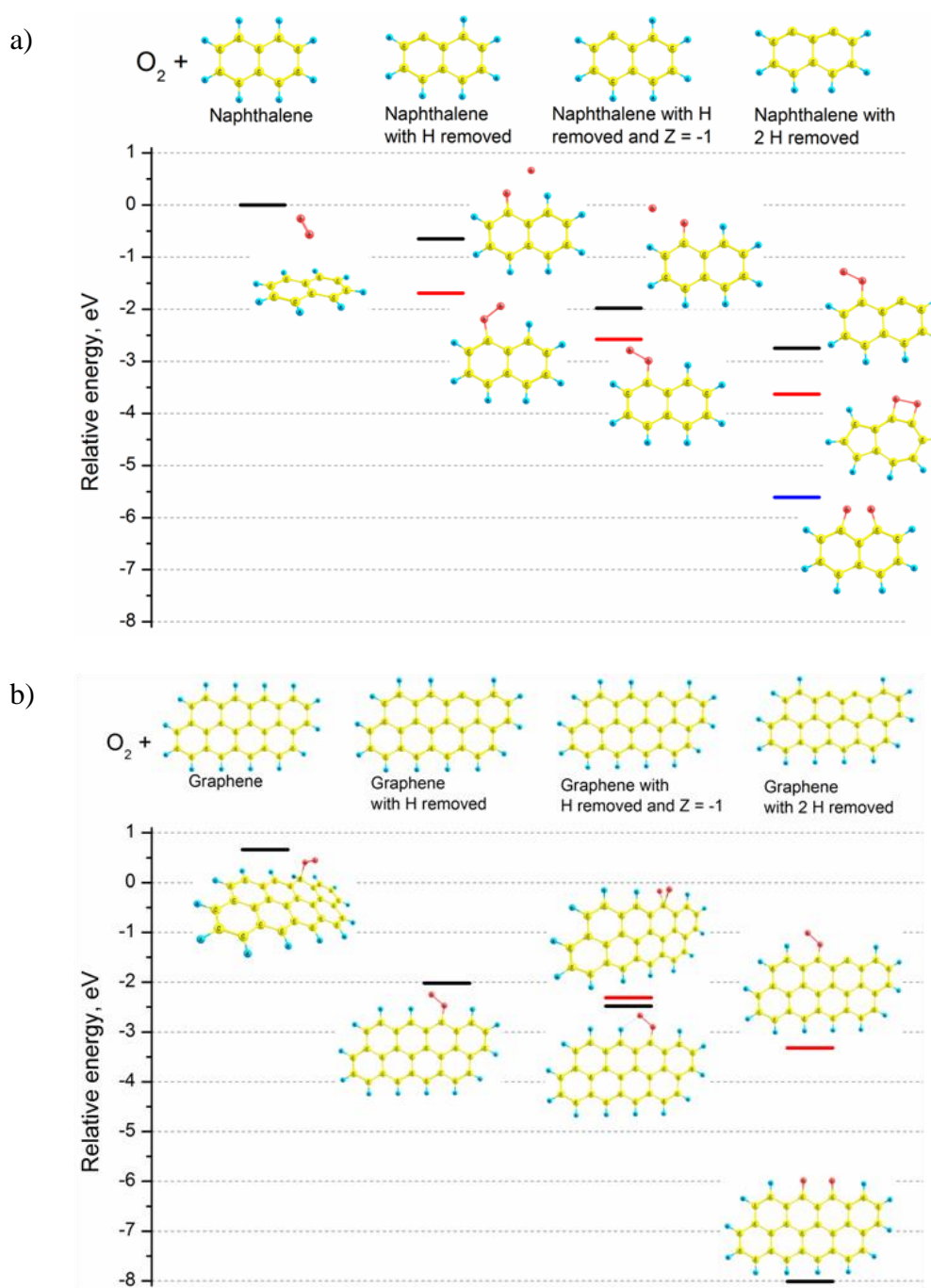


**Figure 3.4** Molecular oxygen binding to the non-doped a) naphthalene- and b) graphene-type model systems in the four modifications. The C, O and H atoms are designated by the yellow, red and cyan colours, respectively.

### 3.4.1.2 Nitrogen Doped Carbon Edges

Figure 3.5 a) and b) shows the relative energies of products of molecular binding to the carbon model systems doped with graphitic N. In contrast to the non doped

carbon systems, the N doped fully H terminated graphene-type system binds the oxygen molecule to the C atom adjacent to N, with the calculated relative energy of the product being -0.2 eV.

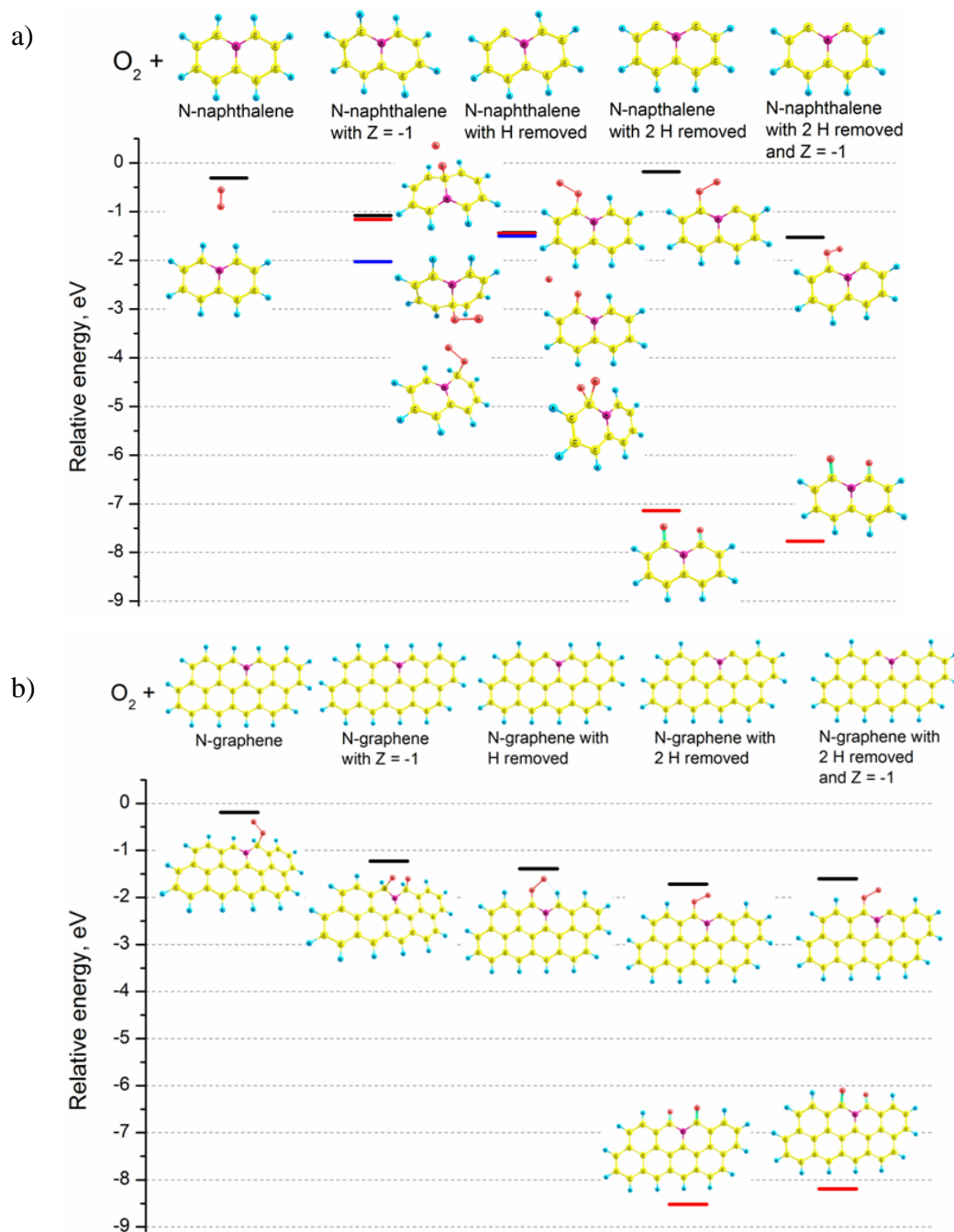


**Figure 3.5** Molecular oxygen binding to the graphitic N doped a) naphthalene- and b) graphene-type model systems in the five modifications. The C, O, N and H atoms are designated by the yellow, red, purple and cyan colours, respectively.

The negatively charged fully H-terminated systems also bind molecular oxygen to the C atoms adjacent to the substituent N. As can be observed, the oxygen molecule can bind to the C atoms both in the end-on and bridge configurations, with the

calculated relative energies varying from -1.0 to -2.0 eV. The bridge configuration of the chemisorbed oxygen molecule on the graphene-type system is structurally similar to that reported by Bao et al. [73]. This indicates that doping of carbon edges with graphitic N enhances molecular oxygen binding compared to non-doped carbon.

In the case of the N doped model systems with valence unsaturated C atoms, two main types of the most stable products have been identified: (i) end-on products with the relative energy circa -1.5 eV, and (ii) benzoquinone-type products with highly exothermic relative energies varying from -7.1 to -7.8 eV for the naphthalene-type and from -8.2 to -8.5 eV for the graphene-type systems.

The simulation results of molecular oxygen binding to the anthracene-type model systems, doped with pyridinic N, are shown in Figure 3.6. It is clear that the oxygen molecule does not bind to the neutral and negatively charged N doped anthracene-type systems and drifts away, with the calculated relative energies of the optimized products being negligibly small. In the case of N-H terminated model systems, the oxygen molecule either coordinates to the H atom with a noticeable exothermic effect, or forms the OOH group that detaches from the model system. This indicates that the pyridinic N doped carbon edge sites do not intrinsically initiate molecular oxygen binding, compared to the graphitic N doped carbon edge sites.

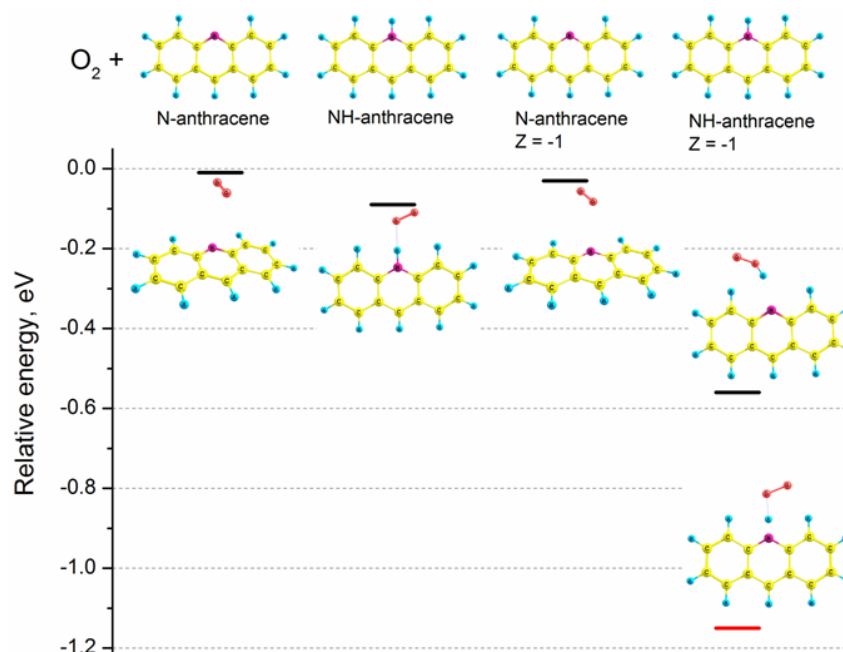


**Figure 3.6** Molecular oxygen binding to the pyridinic N doped anthracene-type model systems in the four modifications. The C, O, N and H atoms are designated by the yellow, red, purple and cyan colours, respectively.

To explain the differences between the graphitic and pyridinic N doped carbon edge sites, the spatial orientation of the lone-electron pair of N atom in these positions

can be addressed. Figure 3.7 illustrates the graphene fragments doped with the graphitic and pyridinic N. The lone-electron pair in the graphitic N is oriented perpendicularly to the carbon framework and therefore participates in the delocalized  $\pi$  system of the aromatic rings. Thus, the adjacent C atoms are subject to the two opposite effects: (i) an electron density shift towards the N atom along the  $\sigma$  bonds due to the higher electronegativity of N, known as the inductive effect, and (ii) an electron density shift towards the C atoms due to the lone-electron pair of N in the  $\pi$  system, known as the mesomeric effect. The mesomeric effect in the graphitic N doped system is proposed to be crucial in the increasing the electron density on the adjacent C atoms enabling them to serve as the molecular oxygen binding sites. In contrast, in the pyridinic doped graphene, the lone-electron pair of N is in-plane with the carbon framework and thus does not participate in the aromatic delocalized  $\pi$  system. The C atoms adjacent to N are subject to the inductive effect of shifting the electron density towards the heteroatom, and the decreased electron density of the adjacent C atoms does not favour molecular oxygen binding.

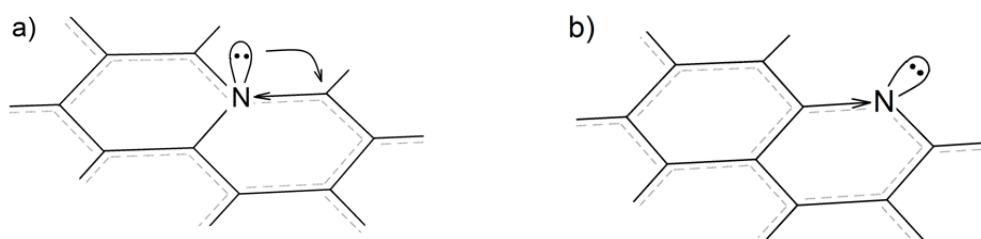


**Figure 3.7** Lone-electron pair of a) graphitic N, and b) pyridinic N.

### 3.4.1.3 Boron Doped Carbon Edges

Figure 3.8 a) and b) shows molecular oxygen binding to the ternary B doped naphthalene- and graphene-type systems. Relative energies of the optimized products are arranged in the columns corresponding to the modifications of the generic model systems. It can be observed that the H terminated edges of the B doped model systems of both sizes do not bind the oxygen molecule, similar to the non-doped model systems. As opposed to the N doped, the negatively charged B doped systems do not facilitate molecular oxygen binding, since the calculated relative energies are close to zero for the systems of both sizes. The binding products for the valence unsaturated B doped model systems can be divided into the two major groups: (i) end-on products with the relative energies ranging from -1.2 to -2.8 eV, and (ii) benzoquinone-type products with highly exothermic relative energies from -5.6 to -6.7 eV for the naphthalene-, and from -7.7 to -7.8 for the graphene-type systems.

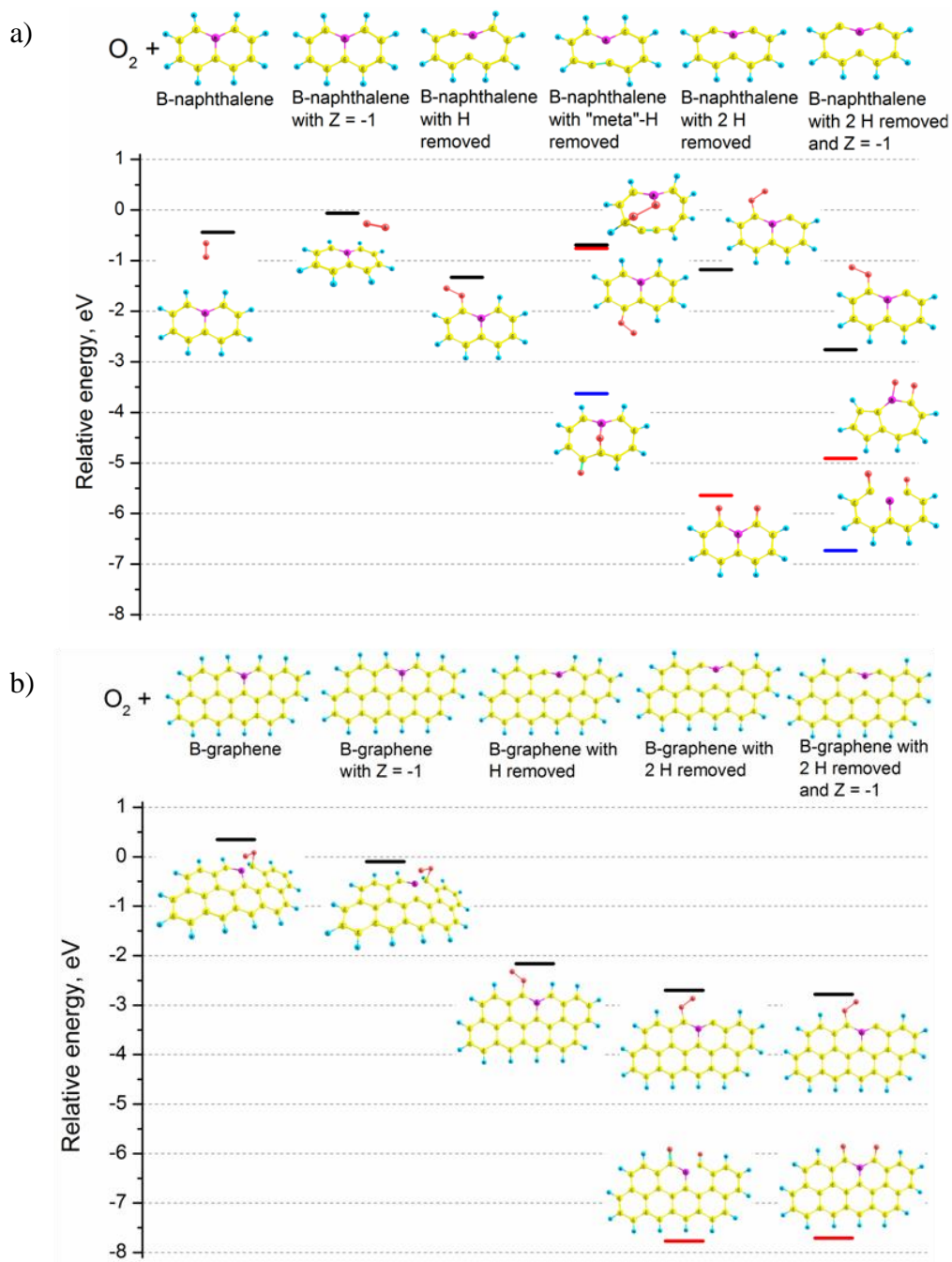


**Figure 3.8** Molecular oxygen binding to the ternary B doped a) naphthalene- and b) graphene-type model systems in the different modifications. The C, O, B and H atoms are designated by the yellow, red, purple and cyan colours, respectively.

It should be emphasized that the oxygen molecule chemisorbs on the C atoms rather than B atoms of the ternary B doped carbon edge systems. This can be explained by two reasons. First, the valence unsaturated edge C atoms are spacially more exposed to the molecular oxygen attack, and second, they have an increased electron density due to carbon's higher electronegativity compared to boron (the inductive effect).

In the case of B doped naphthalene-type systems, three optimized products have structures with disrupted heterocyclic rings. The calculated relative energies of these products vary between -3.5 and -4.9 eV, i.e. they are significantly exothermic. This indicates that in the disordered phase of B doped carbon, molecular oxygen binding may result in formation of strong bonds between the B and O atoms. The suggested explanation of this is that the B-O bond strength (8.35 eV) is substantially higher than the B-C bond strength (4.64 eV) [228]. Therefore, molecular oxygen binding can cause chemical changes in the structure of a B doped carbon catalyst during the ORR in a fuel cell.

The simulation results of molecular oxygen binding to the binary B doped anthracene-type systems are shown in Figure 3.9. It can be observed that the B anthracene-type system chemisorbs the oxygen molecule to the B atom to form products with significant relative energies, namely, -2.2 and -2.6 eV. In contrast, the B-H terminated binary B doped system does not chemisorb molecular oxygen. The negatively charged B doped system binds the oxygen molecule in the end-on configuration with a high exothermic effect of -1.4 and -3.3 eV. The negatively charged B-H terminated system yields the products with different structures and lower relative energies. It is clear that the oxygen molecule binds solely to the B atom of the anthracene-type systems.

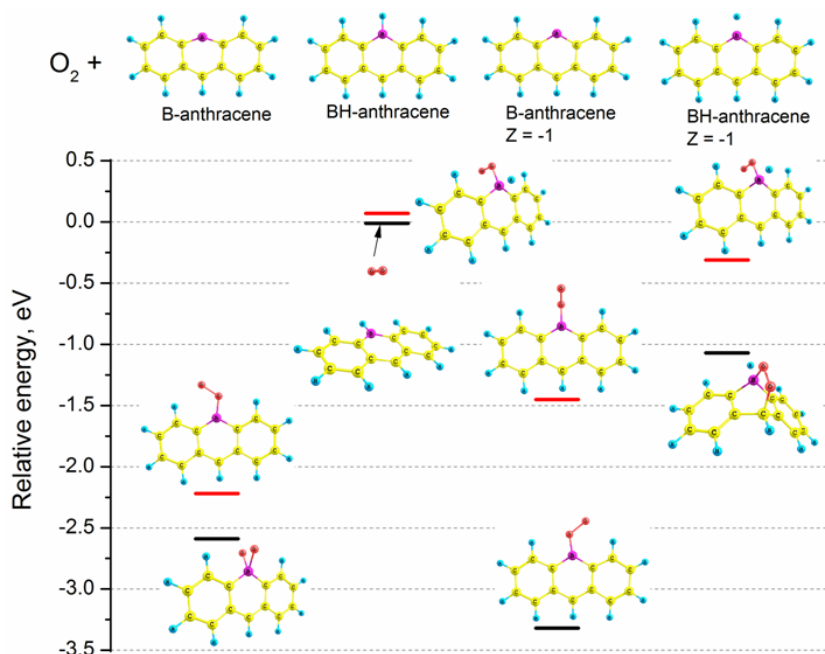


**Figure 3.9** Molecular oxygen binding to the binary B doped anthracene-type model system in the four modifications. The C, O, B and H atoms are designated by the yellow, red, purple and cyan colours, respectively.

Summarizing the modelling results of molecular oxygen binding to both the ternary and binary B doped carbon edge sites, two opposite effects of B doping are identified. On one hand, the substituent B atom in the ternary position may increase the electron density of the adjacent edge C atoms via the inductive effect, enabling these edge C atoms to serve as the active sites for molecular oxygen binding. On the other hand, due to the strong B-O bonds and incorporation of O into the carbon framework, chemical composition of the B doped carbon can change through the formation of various B-O-C species.

### 3.4.1.4 Oxygen Doped Carbon Edges

The effect of O doping to carbon edge sites towards the molecular oxygen chemisorption is illustrated in Figure 3.10. It is clear that the fully H-terminated O doped system does not bind the oxygen molecule. Similar to the N, B and non-doped systems, the valence unsaturated C atoms of the O doped systems bind the oxygen molecule in the end-on and bridge configurations. The optimized structure of one chemisorption product has a disrupted heterocyclic ring with benzoquinone-type groups. The calculated relative energy of this product is significantly exothermic, namely -4.7 eV. This suggests that chemical structure of O doped carbon catalysts may change irreversibly during the ORR.

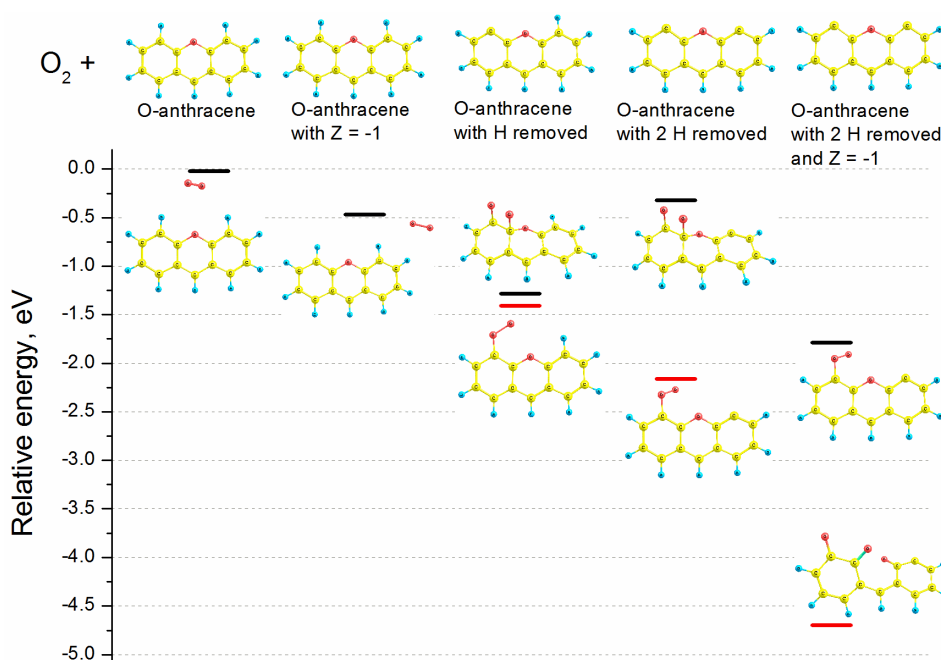


**Figure 3.10** Molecular oxygen binding to the O doped anthracene-type model system in the five modifications. The C, O and H atoms are designated by the yellow, red and cyan colours, respectively.

### 3.4.2 Activation Energies of Molecular Oxygen Binding to N, B, O and Non-Doped Carbon Edges

The end-on and benzoquinone-type products are the main thermodynamically stable products of molecular oxygen binding and have been obtained for the following modifications of the doped and non-doped model systems: (i) one H atom removed ( $Z = 0$ ), (ii) two H atoms removed ( $Z = 0$ ), and (iii) one H atom removed and negatively charged ( $Z = -1$ ) in the case of the non-doped systems or two H atoms removed and negatively charged ( $Z = -1$ ) for the doped ones. The activation energies of the reactions leading to these products have been sought only for the smaller naphthalene-type systems for the purpose of reducing the computational time.

As mentioned in Section 3.3, in order to verify that the found transition state connects correct reactant and product systems, IRC calculations have been performed for each transition state structure. Figure 3.11 illustrates an IRC calculation performed for the molecular oxygen binding to the B doped naphthalene-type system. The maximum energy point corresponds to the transition state and connects the reactants (the oxygen molecule and the B doped model system) on the left and the product on the right.

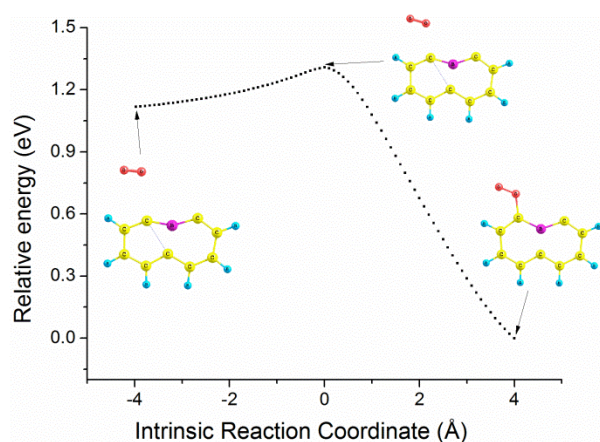
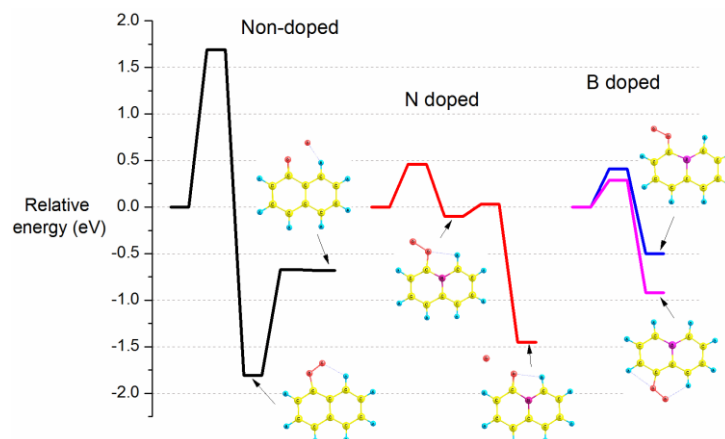


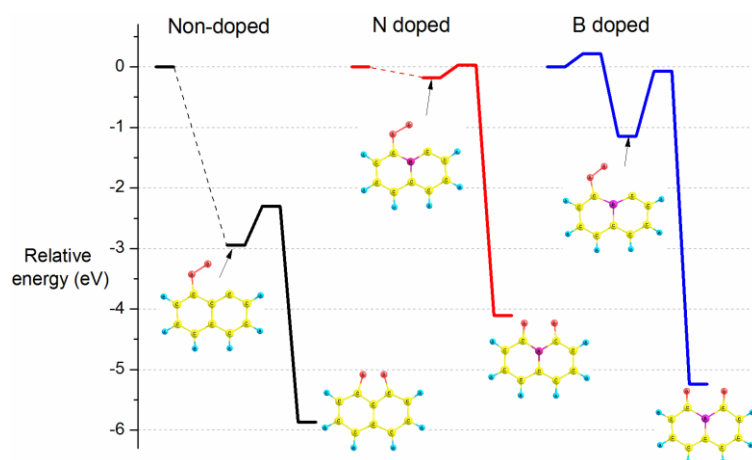
**Figure 3.11** Potential energy profile obtained in the IRC calculation for the B doped naphthalene-type system.

Investigation of transition states for the end-on and benzoquinone-type products resulted in obtaining the pathways of molecular oxygen binding to the non-doped, N and B doped naphthalene-type systems, illustrated in Figures 9 a), b) and c), respectively. The dashed lines designate that the transition states have not been found using the QST3 method due to convergence problems, and the PES scan calculations, performed instead, revealed that the reactions proceed without activation. The structures of optimized products are illustrated near the corresponding energy levels.

a) one H removed



b) two H removed



c) two H removed and -1 charged

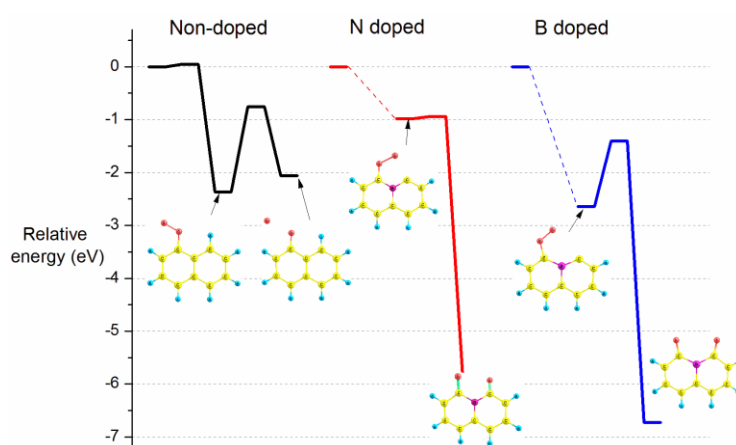


**Figure 3.12** Pathways of molecular oxygen binding to the non-doped, N doped and B doped naphthalene-type systems with a) one H atom removed, b) two H atoms removed, and c) one H atom removed and (-1) charge for the non-doped or two H atoms removed and (-1) charged for the N, B doped systems.

It has been found that the oxygen molecule binds to the model systems in two steps: (i) end-on chemisorption, and (ii) subsequent dissociation of the O-O bond. In Figure 3.12 a), the effect of a heteroatom doping is clearly observed, since the

activation energies of both steps are more than four times higher in the case of the non-doped system than the N and B doped ones. Activation energies of the end-on oxygen chemisorption are comparable for the N and B doped systems, varying from 0.3 to 0.5 eV. The second step of the O-O bond dissociation on the N doped system is 0.13 eV, and it was not found for the B doped system since the geometry optimisation does not result in the products with the dissociated O-O bond. Instead, the effect of the B atom position relative to the valence-unsaturated C atom has been investigated. The relative binding energies and activation barriers have been obtained for the *ortho*- and *meta*-isomers. It can be observed that the *ortho*-isomer displays slightly higher activation barrier towards the end-on oxygen chemisorption than the *meta*-isomer.

In Figure 3.12 b), the end-on oxygen chemisorption is barrierless for the non-doped and N doped naphthalene-type systems, but for the B doped system, the activation energy is 0.35 eV. At the O-O bond dissociation step, the N doped system demonstrates the lowest activation barrier of 0.26 eV, which is 2.5 and 4 times lower than the activation barriers for the non- and B doped systems, respectively. In Figure 3.12 c), the O-O bond dissociation has a significantly lower activation energy in the case of the N doped system as compared to the B and non-doped ones, and this indicates that the O-O bond dissociation is more favourable on the N doped carbon rather than on the B and non-doped carbon.

For the O doped anthracene-type systems, the most stable products of molecular oxygen chemisorption have been the end-on and with the disrupted heterocyclic ring. Relaxed PES scan calculations have been performed in order to investigate the pathways of the formation of these products, as described in Section 3.3. The potential energy profiles have been plotted as functions of the distance between one of the atoms of the oxygen molecule and an edge carbon atom of the O doped anthracene-type system, as illustrated in Figure 3.13 a) and b). Each point in the graphs is the optimised energy of the molecular system at the given fixed distance between the oxygen molecule and the edge C atom.

The end-on molecular oxygen chemisorption on the O doped anthracene-type system with one valence unsaturated C atom is a barrierless process, since the energy in Figure 3.13 a) gradually decreases to a minimum with the decreasing the scanned distance. If the oxygen molecule approaches the C atom next to the substituent O in the anthracene-type system with two valence-unsaturated C atoms, the heterocyclic ring split, as shown in Figure 3.13 b). The activation barrier for this reaction, calculated as the difference between the maximum energy point and the energy of reactants, is circa 0.6 eV, i.e. relatively low. This suggests that molecular oxygen chemisorption on O doped carbon edge sites may lead to an irreversible oxidation of carbon. Since this process underlies a chemical degradation of a carbon catalyst structure, O doping to carbon should be avoided.

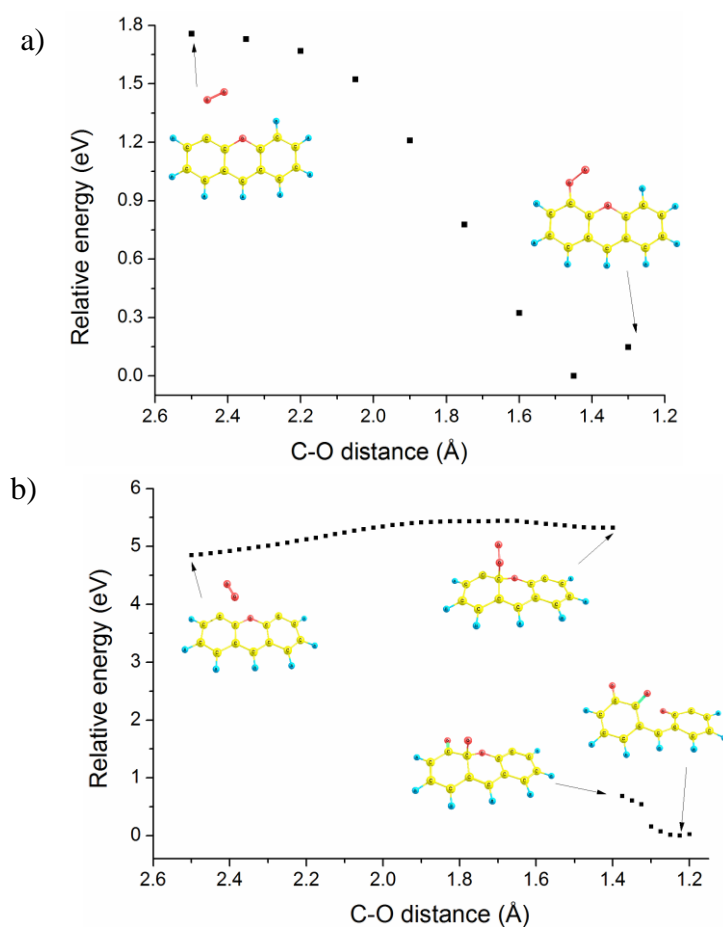


**Figure 3.13** Potential energy profiles of molecular oxygen chemisorption on the O doped anthracene-type system: a) in the end-on mode, and b) with disruption of the heterocycle ring.

### 3.4.3 Energies of Molecular Oxygen Binding to P, Al, S and Se Doped Carbon Edges

All optimized P, Al, S and Se doped model systems have the lowest ground state multiplicity, namely 1 or 2, depending on the electronic structure. The P, S and Se doped systems retain the hexagonal ring structure after optimization, and the optimized Al doped systems have non-hexagonal rings, as illustrated in Figure 3.14. This indicates that the disordered phase of Al doped carbon may partially have an asymmetric non-hexagonal heterocycle ring structure, in which the Al atom is bound to two C atoms in a heptagonal ring.

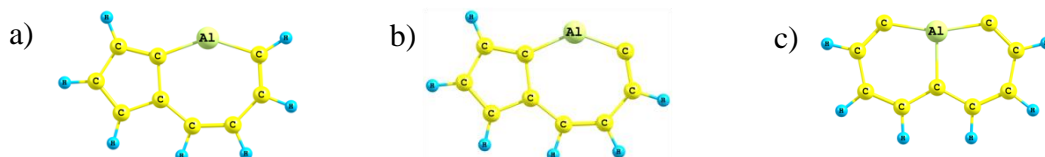


**Figure 3.14** Geometry optimised Al doped naphthalene-type system modifications with a) one H removed, b) two H removed, and c) two H removed and a (-1) charge.

The ground state spin multiplicities of the optimized products of molecular oxygen binding to the P, Al, S and Se systems vary, being either the lowest (1 or 2) or the next higher (3 or 4). The products have different structures and therefore have been classified into nine groups based on similarities and common functional groups. Table 3.1 lists the nine product groups designated by the letters A to I, the structures of which can be found in Tables A1 – A6 of the Appendix A. The calculated molecular oxygen binding energies are summarised in Table 3.2 only for the most thermodynamically stable exothermic products.

**Table 3.1** Types of molecular oxygen binding products for the P, Al, S and Se doped model systems.

Product label	Description of the molecular oxygen binding mode or the product
A	Van-der-Waals complex
B	End-on binding to the heteroatom
C	End-on binding to a C atom
D	Side-on binding along the C-heteroatom or a C-C bond
E	Product with benzoquinone groups
F	Product with a benzoquinone group and oxidized heteroatom
G	Product with non-hexagonal heterocyclic ring
H	Incorporation of O to the Al-C structure
I	Disruption of the heterocyclic ring

The difference in the molecular oxygen binding to the fully H-terminated P, Al, and S, Se doped systems is illustrated in Figure 3.15. The oxygen molecule coordinates or binds to the P and Al atoms in the end-on mode (B type products), with the calculated binding energies being -0.91 and -0.32 eV for the P doped, and -0.3 and -1.0 eV for the Al doped naphthalene- and graphene-type systems, respectively. In contrast, for the S or Se fully H terminated systems, the ground state products are just Van-der-Waals complexes with small relative energies of -0.02 and -0.08 eV, respectively. Stable products with O-S and O-Se chemical bonds have been obtained with multiplicities that do not represent the ground states, and are substantially endothermic, with the relative energies being 2.32 and 1.85 eV, respectively.

**Table 3.2** Molecular oxygen binding energies for the P, Al, S and Se doped model system in the five modifications.

	Product label	O <sub>2</sub> binding energy, eV				
		Fully H terminated	Z = -1	One H removed	Two H removed	Two H removed and Z = -1
P doped naphthalene	A	-0.16				
	B	-0.91	-1.43 -2.61			
	C		-0.86	-1.00	-1.47	-1.72
	D			-1.83	-1.88	-1.57
	E				-6.75	-5.59
P doped graphene	B	-0.32	-0.96			
	D			-1.68	-1.93	-0.92
	F			-4.97	-5.80	-5.29
	E					-7.40
Al doped naphthalene	A	-0.01				
	B	-0.26	-0.91			
	D		-1.38	-1.84	-2.11	-3.80
	C			-1.05	-1.17	-3.24
	G			-2.55		-5.67
	H			-4.98		
Al doped graphene	E				-9.26	-11.13
	D	-1.00	-1.76	-3.02	-4.06	-3.86
	C			-2.31		
	G					-5.23
S doped anthracene	E					-8.32
	A	-0.02	-0.37			
	D			-1.22	-1.31	-0.86
	I			-1.91	-2.00	-1.82
Se doped anthracene	C			-2.28	-2.35	-2.19
	A	-0.08	-0.39			
	D			-1.74		-1.03
	I			-2.38	-1.11	-4.63
Se doped anthracene	C			-2.73	-2.11	-2.63

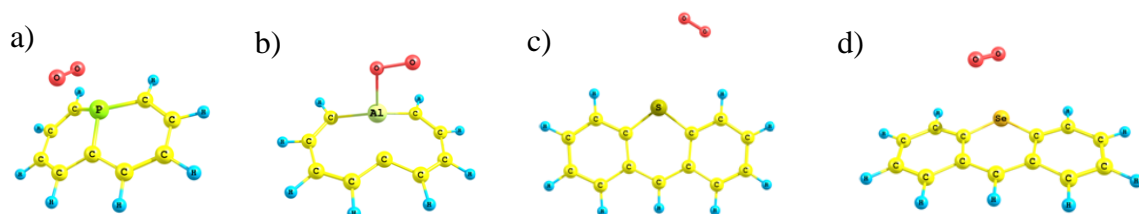


**Figure 3.15** Optimised products of molecular oxygen binding to a) and b) P and Al doped naphthalene-, c) and d) S and Se doped anthracene-type systems. The C, P, Al, S, Se, O and H atoms are designated by the yellow, green, pale-green, olive, orange, red and cyan colours, respectively.

Assigning a (-1) charge to the heteroatom doped model systems results in an increased stability of the molecular oxygen binding products. However, the ground state products in the case of the S and Se doped systems are still Van-der-Waals complexes with the respective binding energies of -0.37 and -0.39 eV. The products with O-S and O-Se bonds have relative energies of 1.16 and 0.85 eV. These findings suggest that that molecular oxygen is not likely to bind to the S or Se heteroatoms in carbon edges, and the presence of S or Se does not facilitate molecular oxygen chemisorption. In contrast, the heteroatoms in the P and Al doped systems bind the oxygen molecule either in the end-on or side-on dissociative mode with exothermic effects (B and D type products).

The products of molecular oxygen binding to the valence unsaturated P, Al, S and Se doped systems have several similarities and are either the end-on (C type), side-on parallel to the C-heteroatom or C-C bond (D type), with benzoquinone groups (E type), and with non-hexagonal or disrupted heterocyclic rings in the cases of Al, S and Se doping (G, H and I types). The products with benzoquinone groups have the highest calculated binding energies for the P and Al doped model systems and are the most thermodynamically stable.

Importantly, the some of the products of molecular oxygen binding to the Al doped systems are markedly different from the other heteroatom doped systems. These products either have the non-hexagonal structure of the heterocycle rings (G type), or the O atom is incorporated into the Al-C structure (H type), as illustrated in Figure 3.16. This may be due to the significantly higher strength of Al-O bonds than Al-C bonds [228] and cause changes in the chemical structure of Al doped carbon catalysts during the ORR, resulting in the formation of stable Al-O-C species.

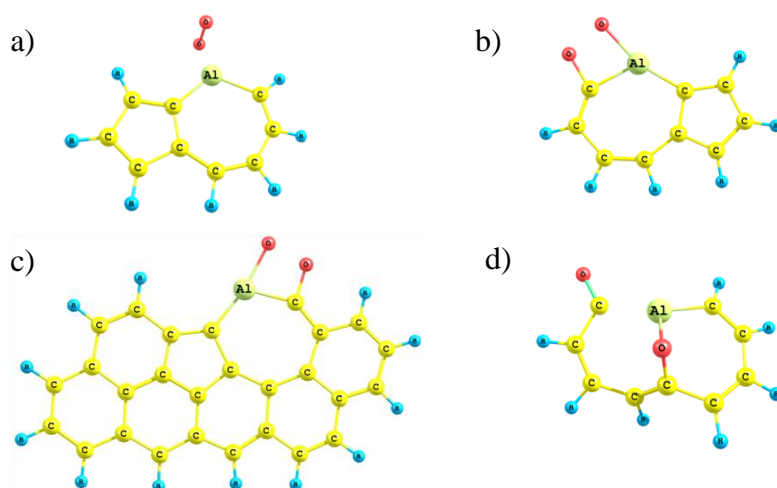


**Figure 3.16** Optimised products of molecular oxygen binding to the Al doped systems with a) – c) non-hexagonal and d) disrupted heterocyclic ring structure.

In the case of the S and Se doped systems, products with disrupted heterocyclic rings have also been obtained (the I type). In some of the products, the heteroatoms are oxidized, as illustrated in Figure 3.17. This indicates that S and Se doped carbon edge sites in the disordered carbon phase are thermodynamically unstable and may be oxidized with the disruption of the heterocyclic ring structure and formation of various S and Se acidic groups.

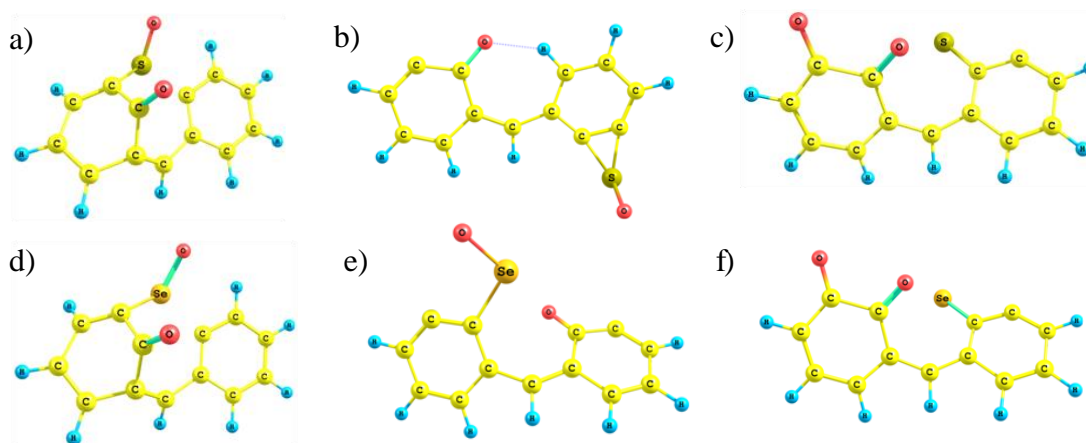


**Figure 3.17** Optimised products of molecular oxygen binding with the disruption of the heterocycle ring for the S and Se doped anthracene-type systems with a), d) one H removed, b), e) two H removed, and c), f) two H removed and a (-1) charge. The C, S, Se, O and H atoms are designated by the yellow, olive, orange, red and cyan colours, respectively.

### 3.4.4 Activation Energies of Molecular Oxygen Binding to P, Al, S and Se Doped Carbon Edges

The activation barriers of molecular oxygen binding have been investigated for the P and Al, naphthalene- and the S and Se anthracene-type systems. The potential energy profiles of molecular oxygen binding have been obtained using the technique of relaxed PES scan calculations, the illustrations of which can be found in Figures A1 – A3 of the Appendix A.

Figure 3.18 shows the schematic pathways of molecular oxygen binding to the P doped naphthalene-type system modifications with (i) a (-1) charge, (ii) one H removed, (iii) two H removed, and (iv) two H removed and a (-1) charge. In the case of the (-1) charged system, the potential energy decreases from the reactants level to -1.55 eV, and the first intermediate product with the oxygen molecule bound to the P atom forms without an activation barrier. In order to break the O-P bond and form the second intermediate product, an activation barrier of 0.61 eV (TS 1) has to be overcome. A second activation barrier of 0.21 eV (TS 2) has to be transited in order to

form a covalent O-C bond. Thus, the oxygen molecule preferentially binds to the substituent P atom of the negatively charged model system.

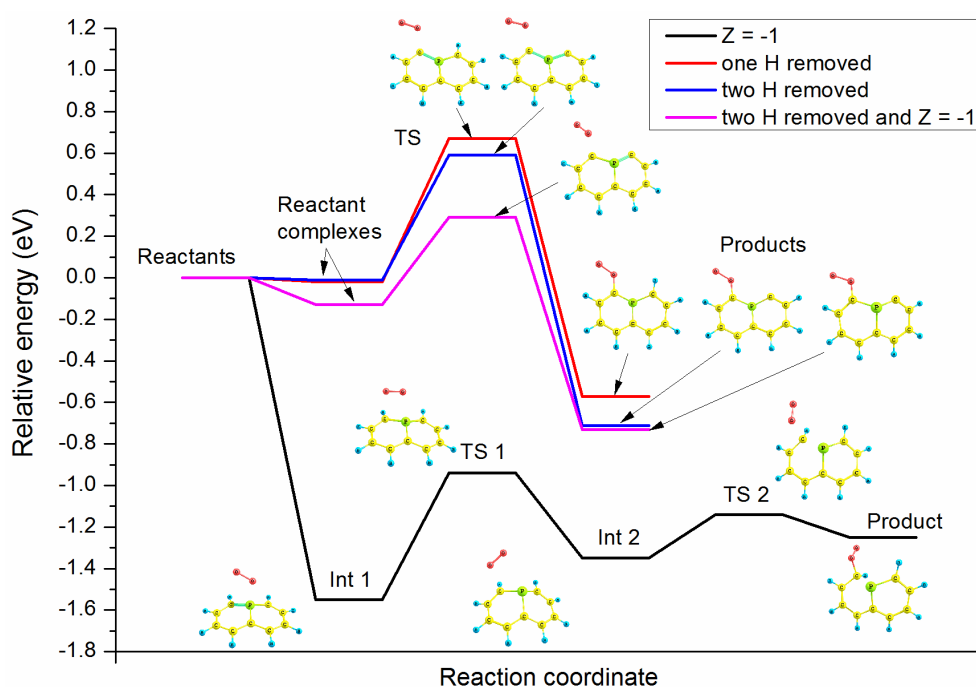


**Figure 3.18** Pathways of molecular oxygen binding to the modifications of the P doped naphthalene-type systems. The C, P, O and H atoms are designated by the yellow, green, red and cyan colours, respectively.

For the remaining three system modifications, it has been found that the oxygen molecule binds only to the valence unsaturated C atoms. The activation barriers estimated with the reference to the reactant complexes are 0.69, 0.60 and 0.42 eV for the systems with one H removed, two H removed, and two H removed and a (-1) charge, respectively. This suggests that molecular oxygen is kinetically favourable to bind to substituent P atoms in carbon edge planes rather than the valence unsaturated C atoms, and the P atoms can serve as the active sites for the ORR.

Figure 3.19 illustrates the pathways of molecular oxygen binding to the Al doped naphthalene-type system modifications with (i) a (-1) charge, (ii) one H removed, (iii) two H removed, and (iv) two H removed and a (-1) charge. In the first two cases, the oxygen molecule chemisorbs to the substituent Al atoms without activation barriers (see Figure A2, Appendix A). In the third case, there is a possibility of molecular oxygen binding to either the Al or adjacent C atom, with the former reaction being barrierless and the latter reaction passing through the two potential barriers of 0.32 eV (TS 1) and 0.26 eV (TS 2). Finally, the system with two H removed and a (-1) charge (the fourth case) binds the oxygen molecule to either the Al or the adjacent C atom without activation barriers.

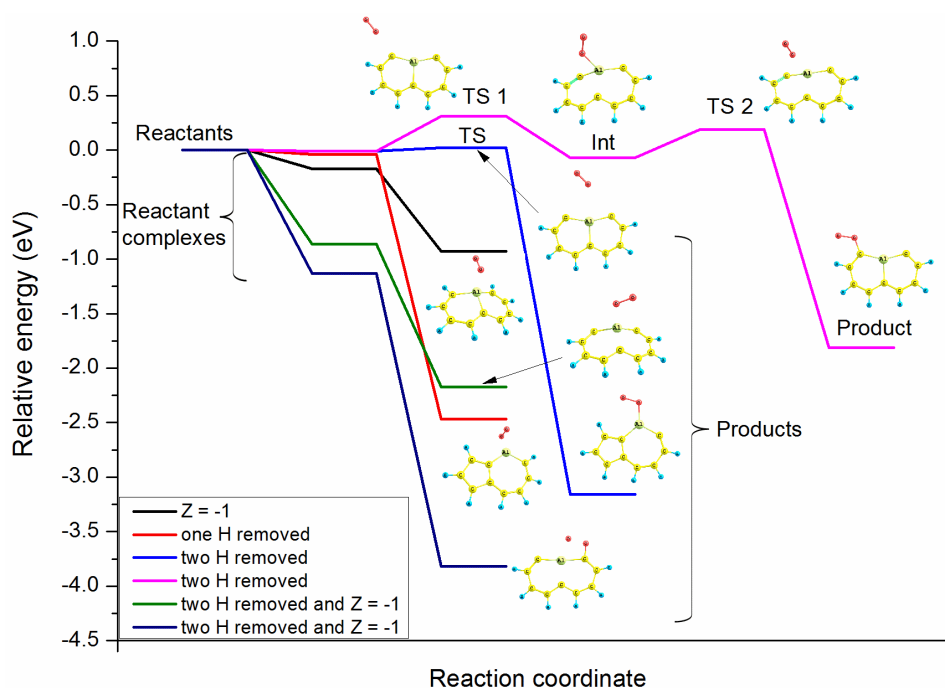


**Figure 3.19** Pathways of molecular oxygen binding to the modifications of the Al doped naphthalene-type systems. The C, Al, O and H atoms are designated by the yellow, pale-green, red and cyan colours, respectively.

Thus, only one pathway of molecular oxygen binding on the Al doped naphthalene-type system has relatively significant activation barriers. The virtual absence of activation barriers in all other cases indicates that molecular oxygen can bind preferentially to the substituent Al atom, yielding various products. The presence of the valence unsaturated C atoms may facilitate the dissociation of the O-O bond. Therefore, the substituent Al atoms in carbon edges can serve as the active sites of molecular oxygen binding and further the ORR. However, molecular oxygen binding to the substituent Al atoms without activation barriers indicates the ease of changing the chemical structure of Al doped carbon edge sites towards the oxidation of Al atoms.

Activation barriers of molecular oxygen binding to the S and Se doped anthracene-type systems have been examined for the end-on products and the products with the disrupted heterocyclic ring, since they are the most thermodynamically stable. Figure 3.20 shows the pathways of molecular oxygen binding to the S and Se doped model systems derived from potential energy profiles illustrated in Figure A3, Appendix A.

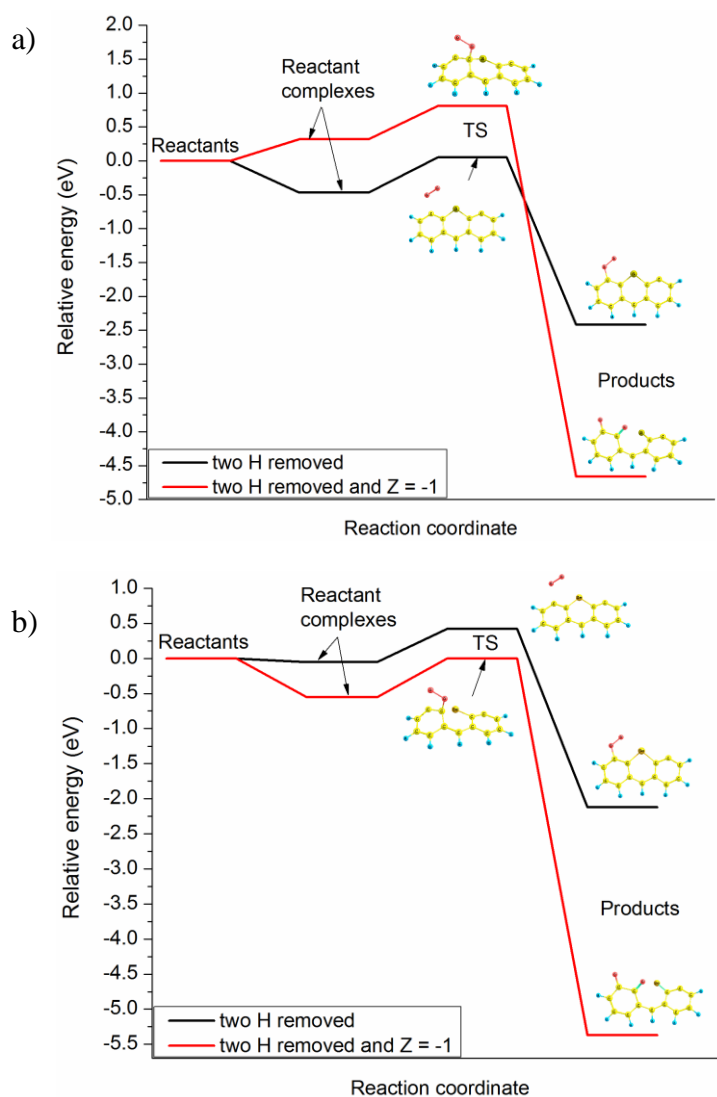


**Figure 3.20** Pathways of molecular oxygen binding to the modifications of a) S and b) Se doped anthracene-type systems in the end-on mode and with disruption of the heterocyclic ring.

The oxygen molecule binds to the S or Se doped model systems in the end-on mode with the activation barriers of 0.52 and 0.47 eV, respectively. The disruption of the S and Se heterocyclic rings has slightly higher activation barriers than the end-on molecular oxygen binding. For the S doped system, the reactants complex energy is 0.31 eV higher than the energy of the isolated reactants and therefore adds to the activation barrier, which is the sum of the reactants complex and the TS relative energies, i.e. 1.13 eV. The high activation energy of the S heterocyclic ring disruption indicates that this reaction is hindered kinetically. The calculated activation energy of the Se heterocyclic ring disruption is 0.55 eV, and this is comparable to the activation energy of the end-on binding of molecular oxygen. The activation barriers of circa 0.5 eV activation energies of molecular oxygen binding to the Se doped system in both

modes suggests that Se doped carbon edge sites can be oxidized easily during the ORR with irreversible disruption of the heterocyclic ring.

### 3.5 Conclusion

In this chapter, molecular oxygen chemisorption has been studied on the nitrogen, boron, phosphorus, aluminium, oxygen, sulphur or selenium and non-doped carbon edge sites as a first step of the oxygen reduction reaction in fuel cells by means of the DFT simulations. The presence of oxygen, sulphur or selenium in carbon edge sites does not facilitate molecular oxygen binding, but can lead to an irreversible oxidation and thus chemical degradation of the carbon structure. This suggests that oxygen, sulphur or selenium doped carbons may be inefficient and unstable as cathode catalysts for fuel cells.

In boron doped carbon edges, the sites for molecular oxygen chemisorption are proposed to be the valence unsaturated carbon atoms rather than the substituent boron atom. However, the active sites of the same nature can also exist on non-doped carbon edges. The major shortcoming of boron doped carbon is that boron-oxygen bonds are stronger than boron-carbon bonds. This may cause formation of various B-O-C species and change the chemical structure of a boron doped carbon catalyst.

Chemisorption of molecular oxygen on the aluminium doped carbon is barrierless, and the substituent aluminium atoms can serve as the chemisorption sites. However, oxidation of the aluminium doped carbon edge sites is also possible due to aluminium's strong affinity towards formation of strong bonds with oxygen. For this reason, aluminium doped carbon may have insufficient chemical stability as a catalyst for the oxygen reduction.

The presence of graphitic nitrogen in carbon edge planes enhances molecular oxygen chemisorption on the adjacent edge carbon atoms compared to carbon with pyridinic nitrogen groups. Graphitic rather than pyridinic nitrogen is responsible for the improved catalytic properties of carbon edges, since its lone-electron pair is in-plane with the aromatic  $\pi$  system of electrons and donates the electron density to the adjacent carbon atoms. The edge carbon atoms adjacent to the substituent graphitic nitrogen are the sites of molecular oxygen chemisorption.

In phosphorus doped carbon edges, the substituent phosphorus atom along with the valence unsaturated carbon atoms can serve as the oxygen chemisorption sites. In addition, the disordered phase of phosphorus doped carbon is likely to retain its structure in the interaction with molecular oxygen. This suggests that phosphorus doped carbon edge sites may be efficient and stable in the oxygen reduction.

## Chapter 4

# DFT Modelling of the Oxygen Reduction Reaction on Transition Metal Macrocycles

### 4.1 Introduction

In the present chapter, the active sites of PEM fuel cell cathode catalysts are modelled based on structures of transition metal macrocycles. The transition metal centres under investigation are iron (Fe), cobalt (Co) and manganese (Mn), since these have been reported in the literature most frequently. In addition, Fe, Co and Mn have similar atomic radii. The macrocycle structures chosen for the study are phthalocyanine, porphyrin, corrin and tetraaza-annulene. Herein, the effect of a central transition metal, macrocycle structure and a macrocycle size are investigated with respect to the oxygen reduction reaction.

The effects of the macrocycle structure and size are studied by the modelling of molecular oxygen chemisorption, or binding, to the four types of macrocycles with either Fe, Co or Mn central atoms. The effect of the central transition metal atom is investigated using one selected macrocycle structure. Further, thermodynamic pathways of the oxygen reduction are constructed as potential energy profiles, including all the intermediate steps. Finally, a modified model of the transition metal active sites is suggested, and the refined ORR pathways are obtained with activation barriers for all the intermediate steps.

### 4.2 Model Systems

The model systems of phthalocyanine, porphyrine, corrin and tetraazaannulene macrocycles used in this study are illustrated in Figure 4.1 in the three sizes referred to as the minimal, intermediate and maximal. The common property of all the macrocycles is that their central parts have a transition metal coordinated to four N atoms. However, there are also structural differences. In phthalocyanine, there are eight N atoms, four of which are not connected directly to the central metal atom. In corrins, the coordination framework around the central transition metal is asymmetric unlike in the other macrocycles. In tetraaza-annulenes, the structure of coordination is different from that of in phthalocyanines and porphyrins. The illustrated macrocycles are employed as initial structures in the search for optimal model systems, representing organometallic active sites in the ORR catalysts.

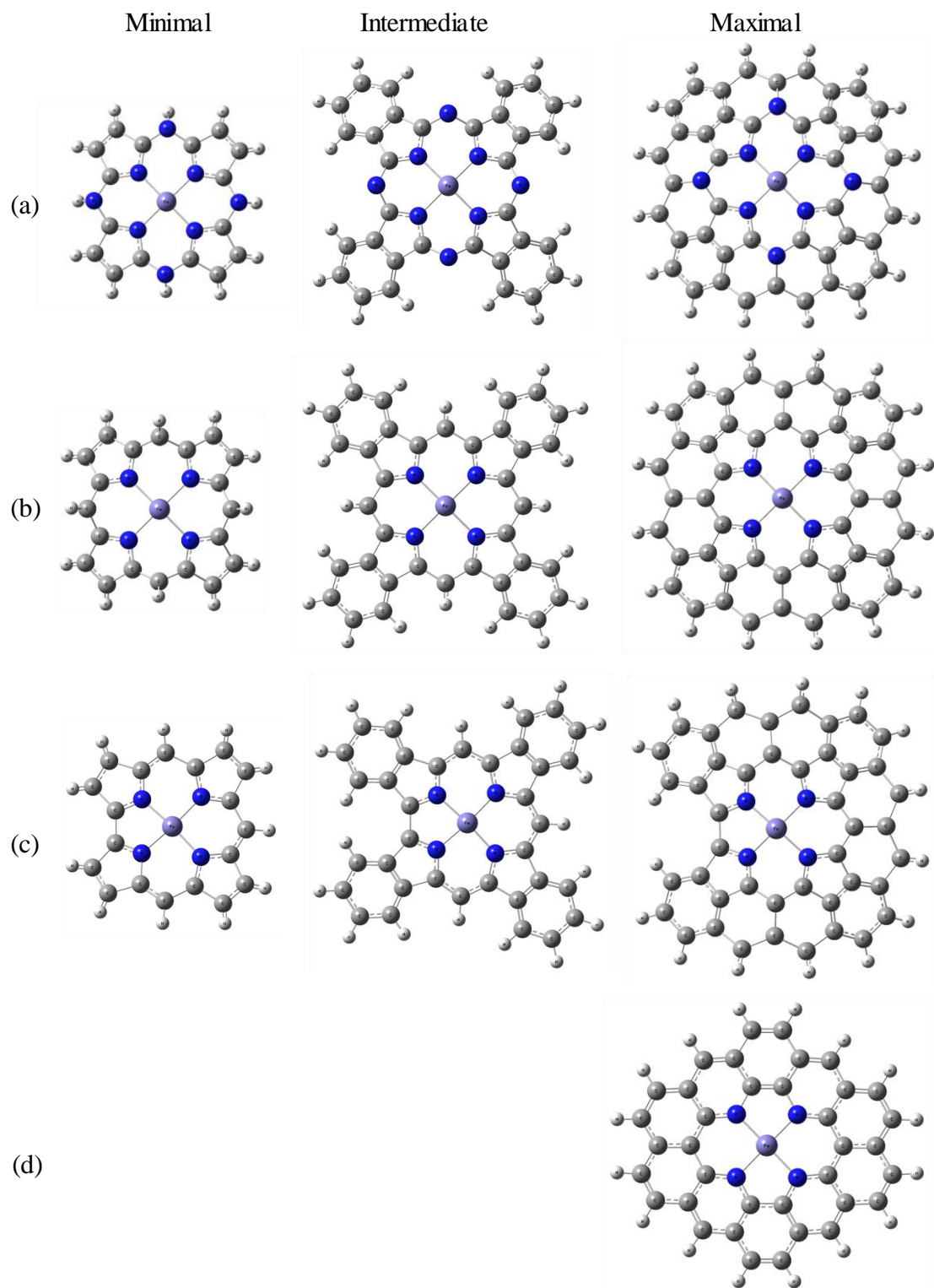


**Figure 4.1** Transition metal (a) phthalocyanines, (b) porphyrins, (c) corrins, and (d) tetraaza-annulene model systems in the three sizes: minimal, intermediate and maximal model systems. The C, N, H and transition metal atoms are designated by the grey, blue, light-grey and the purple colours.

### 4.3 Theoretical Method

All calculations have been performed in Gaussian09 [48] using a model chemistry with the B3LYP hybrid DFT method and the split-valence polarised basis set 6-31G(d). The effect of aquatic medium existing at the cathode in PEM fuel cells has been accounted for by the polarized continuum model (PCM) of the self-consistent reaction-field (SCRF), in which water is represented as a continuum of uniform dielectric constant [45].

The macrocycle model systems have been geometry-optimised with the lowest spin multiplicity, namely,  $M = 1$  or  $2$ , depending on the electronic structure. The spin multiplicities of the molecular oxygen binding products have been allowed to relax, i.e. their structures have been optimized with two spin multiplicities: (i) the lowest,  $M = 1$  or  $2$ , and (ii) the next higher,  $M = 3$  or  $4$ . Products with lower electronic energies have been taken as ground states to calculate molecular oxygen binding energies. Products of the other elementary steps of the ORR have been optimised with the lowest multiplicity  $M = 1$  or  $2$ . In addition,  $O_2$ ,  $H$ ,  $H_2O_2$ , and  $2H_2O$  molecules have been optimised separately at their ground state multiplicities. Since the cathode in PEM fuel cells is a reservoir of electrons, the effect of a negative charge has been accounted for by assigning a (-1) charge to the catalyst model systems.

Oxygen molecules can attack a catalyst surface at various angles. In order to account for this, two basic configurations of the oxygen molecule over the model systems have been used prior to geometry optimization: (i) side-on configuration in which the oxygen molecule is parallel to a model system's surface with the molecule's centre of mass above the metal atom, and (ii) end-on configuration in which the oxygen molecule is perpendicular to the model system's surface and aligned with the metal atom. Molecular oxygen binding energies have been calculated using Equation 3.1. The electron affinities of the macrocycle model systems have been calculated as follows:

$$EA = E_{\text{Neutral}} - E_{\text{Charged}}$$

where  $EA$  is the electron affinity,  $E_{\text{Neutral}}$  is the energy of a neutral catalyst model system, and  $E_{\text{Charged}}$  is the energy of a catalyst model system with a (-1) charge.

The addition of the four hydrogen (H) atoms in the course of the ORR has been modelled by consequent introduction of the H atoms to products of molecular oxygen binding to the model systems. The product of the first H addition is the OOH chemisorbed on a model system. The second H addition can result in the formation of either hydrogen peroxide  $H_2O_2$ , or water oxide  $H_2O-O$ , or di-hydroxyl  $OH-OH$ , chemisorbed on a model system. Formation of hydrogen peroxide terminates the two-electron ORR pathway and is not desirable, since presence of hydrogen peroxide in

PEM fuel cells causes deterioration of both the catalyst layer and the electrolyte membrane. Formation of chemisorbed water oxide  $\text{H}_2\text{O-O}$  or di-hydroxyl  $\text{OH-OH}$  allows for the four-electron ORR pathway. The third H addition results in  $\text{H}_3\text{O}_2$  formation. The fourth H addition terminates the four-electron ORR pathway and yields two  $\text{H}_2\text{O}$  molecules. Thus, investigation of the ORR intermediate steps includes obtaining optimised structures of the  $\text{O}_2$ ,  $\text{OOH}$ ,  $\text{H}_2\text{O}_2$ ,  $\text{H}_2\text{O-O}$ ,  $\text{OH-OH}$ ,  $\text{H}_3\text{O}_2$  and  $\text{H}_2\text{O}$  species chemisorbed on the model systems.

Table 4.1 lists the ORR intermediate steps and formulae used to calculate their total energies, relative energy levels and elementary reaction energies. The total energies of the intermediate steps have been calculated based on the principle of mass conservation: the total sum of nuclei remains constant and includes two O atoms of the oxygen molecule, four H atoms and atoms constituting a catalyst model system. In order to calculate relative energy levels of the ORR intermediate steps, total energy of the reactants has been set as a reference and subtracted from energies of each of the following ORR steps. The elementary reaction energies have been calculated as the difference between two neighbouring relative energy levels. In order to calculate activation energies of the ORR elementary steps, relative energy levels of transition states have been calculated similarly, with the energies of products being replaced by the TS energies.

**Table 4.1** The formulae for calculating total energies, relative energies and elementary reaction energies of the ORR intermediate steps.

Reaction/state	Total energy formula	Relative energy level, eV	Elementary reaction energy, eV
Reactants	$E_0 = E_{\text{catalyst}} + E_{\text{O}_2} + 4 \cdot E_{\text{H}}$	0	0
$\text{O}_2$ binding	$E_1 = E_{\text{O}_2\text{-catalyst}} + 4 \cdot E_{\text{H}}$	$E_1 - E_0$	$E_1 - E_0$
First H addition	$E_2 = E_{\text{OOH-catalyst}} + 3 \cdot E_{\text{H}}$	$E_2 - E_0$	$E_2 - E_1$
Second H addition (two-electron pathway)	$E_3 = E_{\text{H}_2\text{O}_2\text{-catalyst}} + 2 \cdot E_{\text{H}}$	$E_3 - E_0$	$E_3 - E_2$
$\text{H}_2\text{O}_2$ desorption	$E_{\text{H}_2\text{O}_2\text{desorp.}} = E_{\text{catalyst}} + E_{\text{H}_2\text{O}_2}$	$E_{\text{H}_2\text{O}_2\text{desorp.}} - E_0$	$E_{\text{H}_2\text{O}_2\text{desorp.}} - E_3$
Second H addition (four-electron pathway)	$E_4 = E_{\text{H}_2\text{OO-catalyst}} + 2 \cdot E_{\text{H}}$	$E_4 - E_0$	$E_4 - E_2$
Third H addition	$E_5 = E_{\text{H}_3\text{O}_2\text{-catalyst}} + E_{\text{H}}$	$E_5 - E_0$	$E_5 - E_4$
Fourth H addition	$E_6 = E_{\text{H}_2\text{O-catalyst}}$	$E_6 - E_0$	$E_6 - E_5$

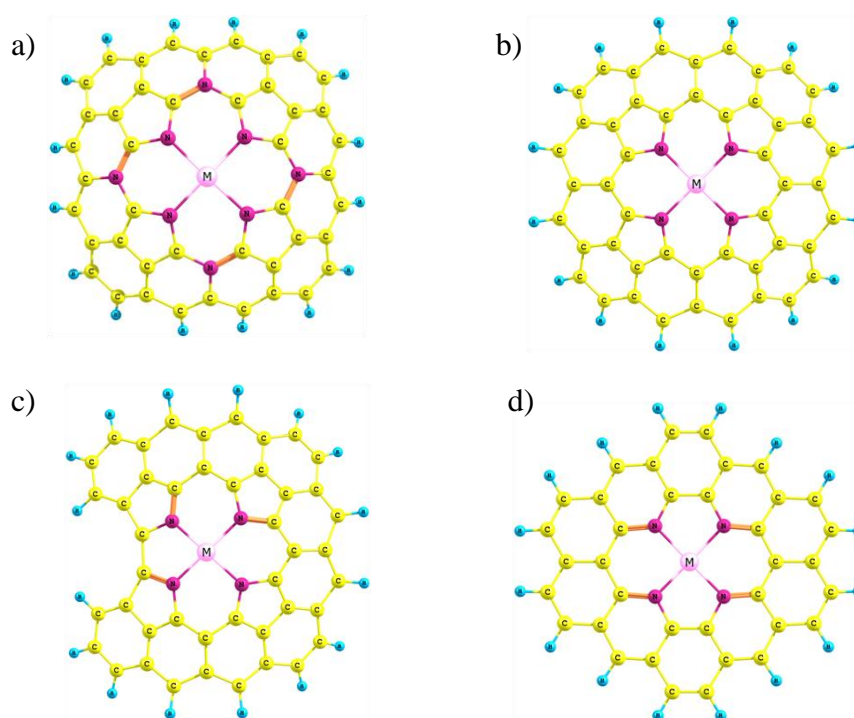
The technique of relaxed potential energy surface (PES) scan calculations has been used to evaluate activation barriers of the ORR intermediate steps. Molecular oxygen binding to the transition metal centres has been modelled by reducing the

distance between one of the atoms of the oxygen molecule and the metal centre from 2.5 Å to circa 2.1 Å by taking a few steps of approximately 0.03 Å step size. The H addition steps were modelled by reducing the distance between the H atom and an O atom from 2 to circa 0.95 Å with a step size of approximately 0.086 Å. At each point, molecular systems were optimized at the given fixed distance between the oxygen molecule and the metal or H atom.

## 4.4 Results and Discussion

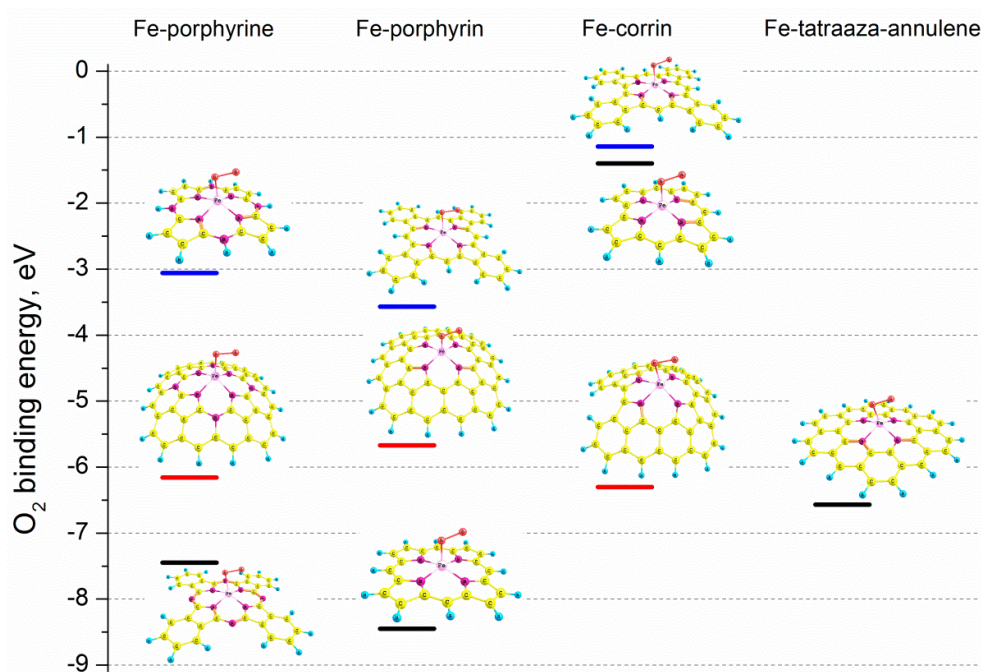
### 4.4.1 Effect of Macrocycle Structure

Figure 4.2 illustrates optimised geometries of the four macrocycle model systems representing the active sites with either Fe, Co or Mn central atom: phthalocyanine, porphyrin, corrin and tetraaza-annulene. Importantly, the optimised structure of the tetraaza-annulene system is almost planar, whereas the structures of the remaining three macrocycle systems have a semi-spherical shape. Since the optimized phthalocyanine, porphyrin and corrin model systems are semi-spherical, molecular oxygen binding has been investigated on both the convex and concave sides.



**Figure 4.2** Geometry-optimized structures of the transition metal macrocycles: a) phthalocyanine, b) porphyrin, c) corrin, and d) tetraaza-annulene. The C, N, H and metal atoms are designated by the yellow, purple, cyan and pink colours, respectively.

The effect of the macrocycle model system size has been investigated for Fe atom in the centre. It should be noted, that these calculations have been performed in HF/3-21G model chemistry, which is not reliable for obtaining quantitative values [45]. However, it has been used for a qualitative assessment of the model size effect. Figure 4.3 shows molecular oxygen binding energies for the four Fe macrocycles arranged in columns, with each of the macrocycles in the minimal, intermediate and maximal sizes. The optimized product structures are shown next to the corresponding energy levels. It is clear that the binding energies vary significantly depending on the model system size. However, binding energies for the maximal size macrocycle systems fluctuate in relatively narrow range, namely from -5.5 eV to -6.6 eV. For this reason, further simulations are performed using the maximal size systems.



**Figure 4.3** Molecular oxygen binding to the four types of Fe macrocycles in minimal, intermediate and maximal sizes. The C, N, O, H and Fe atoms are designated by the yellow, purple, red, cyan and pink colours, respectively.

Figure 4.4 shows molecular oxygen binding energies for the four Fe macrocycles. The central parts of the optimized structures with interatomic distances designated in Å are shown adjacent to the corresponding energies. It can be observed that the molecular oxygen binds to the Fe centre both in the side-on and end-on configurations, and all the calculated binding energies vary in the range of -1.3 to -2.3 eV. Further, the calculated binding energies for each of the macrocycles vary noticeably depending on the local geometry of the reaction centre, i.e. the Fe-O, Fe-N and O-O interatomic distances.

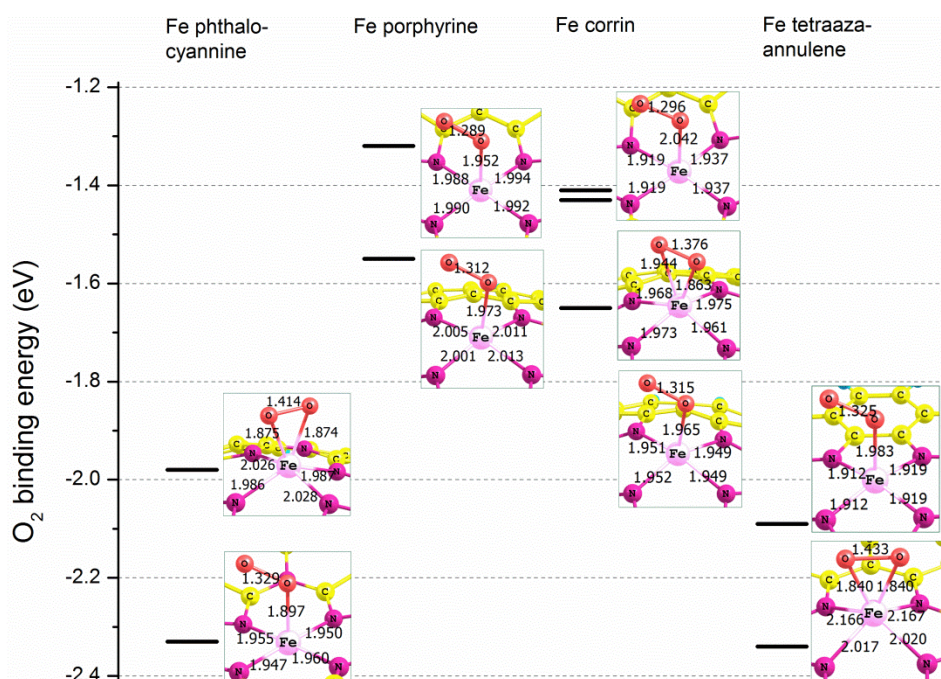


**Figure 4.4** Molecular oxygen binding to the four Fe macrocycles. The C, N, O and Fe atoms are designated by the yellow, purple, red and pink colours, respectively, and the interatomic distances are shown in Å.

The Co atom has one more electron in its external electron shell than an Fe atom, and the lowest spin multiplicity of the Co macrocycle model systems is two ( $M = 2$ ). Assigning a (-1) charge to the Co macrocycles results in  $M = 1$ . Molecular oxygen binding has been modelled both for the neutral and (-1) charged Co macrocycle systems, as shown in Figure 4.5. It can be observed that the oxygen molecule binds to the Co atom predominantly in the end-on configuration. Binding energies for the neutral systems vary from -0.1 to -0.8 eV, and for the (-1) charged systems from -0.9 to -1.6 eV, i.e. significantly more exothermic than for the neutral. In addition, calculated electron affinities of the four Co macrocycles are in the range of 2.1 to 3.3 eV, i.e. the Co macrocycle systems easily accept electrons. This indicates that the molecular oxygen preferentially binds to negatively charged Co macrocycles, rather than to the neutral ones.

Conversely to the Co macrocycle model systems, Mn has one electron less than Fe. The lowest multiplicity of the Mn macrocycles is two ( $M = 2$ ), and assigning a (-1) charge results in  $M = 1$ . Figure 4.6 illustrates the molecular oxygen binding to the neutral and charged Mn macrocycles. Molecular oxygen binds to the Mn centre predominantly in the side-on configuration. Binding energies of the (-1) charged systems vary from -2.4 to -3.4 eV, which is noticeably more exothermic than those of the neutral systems, varying from -0.7 to -2.5 eV. Calculated electron affinities of the Mn macrocycles are between 1.7 to 2.7 eV, which indicates that Mn macrocycles

accept an electron easily. Therefore, similar to Co, the negatively charged Mn macrocycles should bind the molecular oxygen more strongly than the neutral ones.

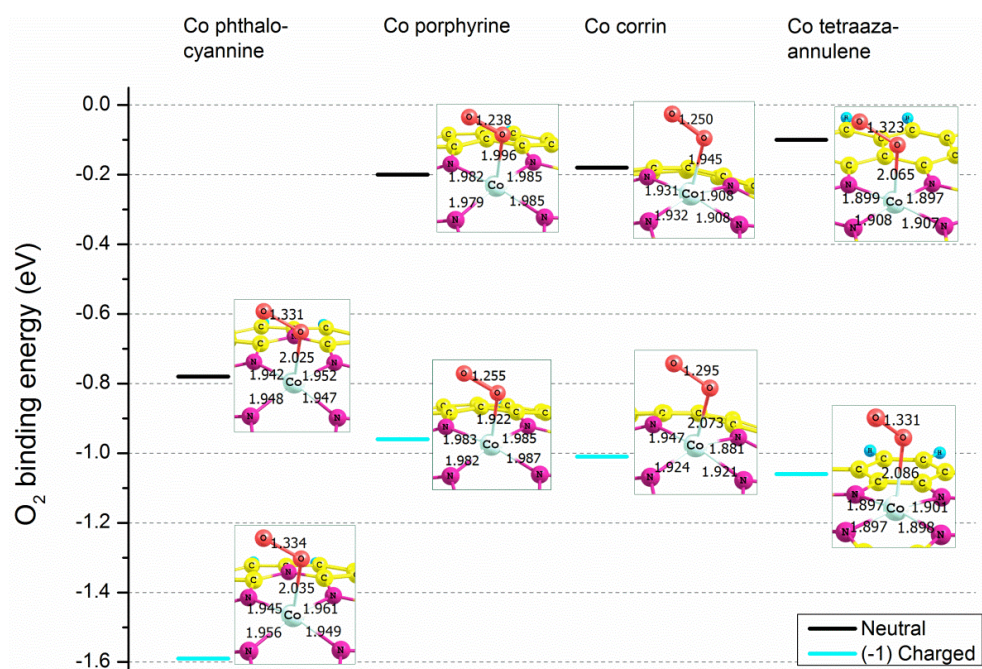


**Figure 4.5** Molecular oxygen binding to the four types of neutral and (-1) charged Co macrocycles. The C, N, O and Co atoms are designated by the yellow, purple, red and blue colours, respectively, and the interatomic distances are shown in Å.

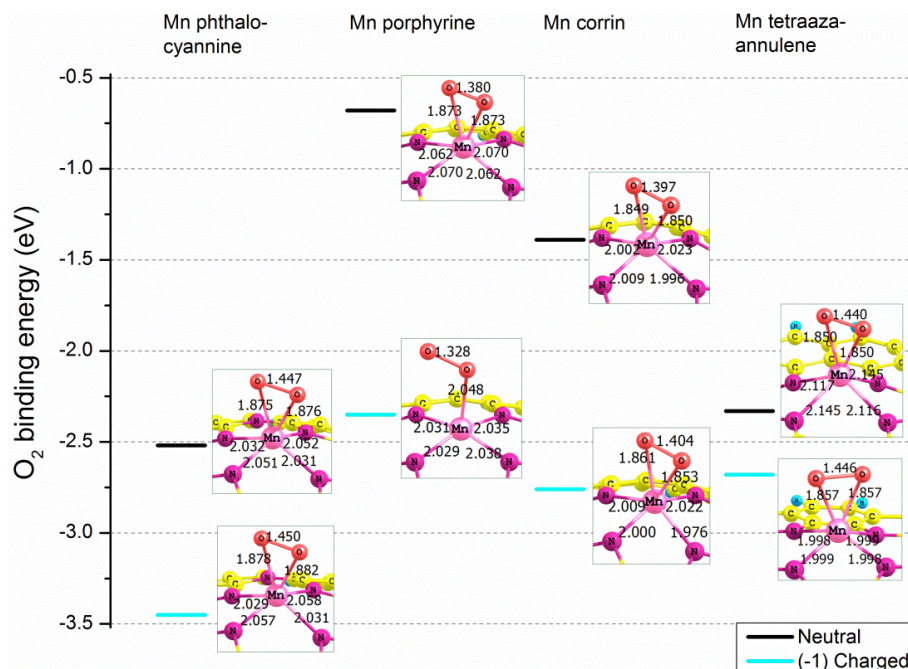


**Figure 4.6** Molecular oxygen binding to the four types of neutral and (-1) charged Mn macrocycles. The C, N, O and Mn atoms are designated by the yellow, purple, red and pink colours, respectively, and the interatomic distances are shown in Å.

Table 4.2 summarizes the calculated molecular oxygen binding energies illustrated in Figure 4.4 -Figure 4.6. The dependence of molecular oxygen binding strength has been evaluated with respect to the transition metal centre and the macrocycle structure. It has been observed that for all four macrocycle structures, the strength of molecular oxygen binding is in the following order: Mn > Fe > Co, i.e. the Mn centre accounts for the strongest binding of molecular oxygen, and the Co for the lowest. With respect to the macrocycle structure, the molecular oxygen binding strength decreases in the following order: phthalocyanines > tetraaza-annulenes > corrins > porphyrins. This correlation has been drawn based on a comparison of the binding energies for each of the four macrocycles and the transition metals both in the neutral and (-1) charged state. This illustrates that the strength of molecular oxygen binding is determined not only by the nature of the central transition metal atom, but also by the macrocycle structure, i.e. the local geometry of the macrocycle-based active site. This conclusion is in agreement with that derived by He et al. [107].

**Table 4.2** Energies (eV) of molecular oxygen binding to the four types of the Fe, Co and Mn macrocycles (neutral and negatively charged).

Macrocycle	Fe	Co <sup>0</sup>	Co <sup>-1</sup>	Mn <sup>0</sup>	Mn <sup>-1</sup>
Phthalocyanine	-2.21	-0.78	-1.59	-2.52	-3.45
Porphyrine	-1.44	-0.20	-0.96	-0.68	-2.35
Corrin	-1.50	-0.18	-1.01	-1.39	-2.76
Tetraaza-annulene	-2.22	-0.10	-1.06	-2.33	-2.68

#### 4.4.2 Thermodynamics of the ORR on Fe, Co and Mn Tetraaza-Annulene Model Systems

As mentioned in the previous section, the optimised structures of the transition metal phthalocyanines, corrins and porphyrins are semispherical, and this may cause differences in the calculated energies of the ORR steps on the convex and concave sides. The planar structure of the tetraaza-annulene system implies that both sides are equal with respect to the reaction modelling. Therefore, the tetraaza-annulene model system has been chosen to represent a base case of the catalyst active sites and model the entire ORR mechanism.

The calculated molecular oxygen binding energies reported in the previous section are highly exothermic. This indicates that the metal centres in the macrocycle systems bind molecular oxygen stronger than necessary for the ORR and thus can potentially impede it. In order to decrease the binding capacity of the transition metal macrocycle active sites, the metal centres should be terminated by a functional group at one side, e.g. hydroxyl (OH) group. Further modelling of the ORR mechanism has been performed using the Fe, Co or Mn tetraaza-annulene model systems with the

metal centres terminated by the OH group at one side. Figure 4.7 illustrates a schematic of the model system representing the transition metal macrocycle active site and the molecular oxygen binding as a first step of the ORR.

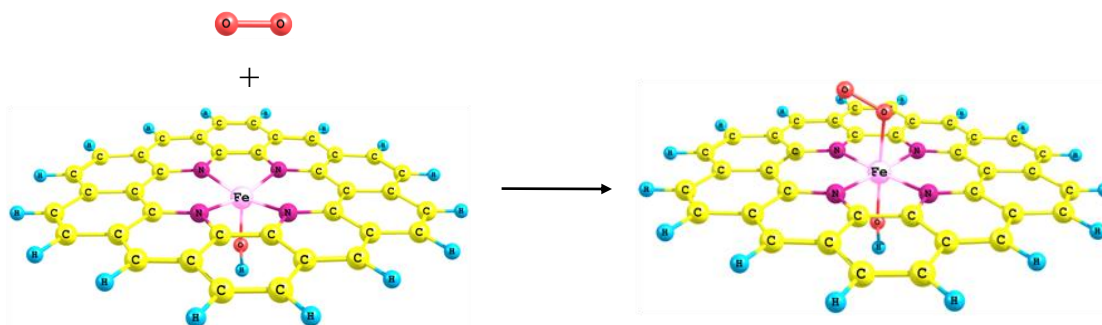


**Figure 4.7** Schematic of the molecular oxygen binding to the active site modelled by the OH-terminated Fe tetraaza-annulene system.

Figure 4.8 -Figure 4.10 illustrate thermodynamic pathways of the ORR on the OH-terminated Fe, Co and Mn tetraaza-annulene macrocycles, respectively. The horizontal bars designate the relative energy levels of the ORR intermediate steps, with the optimised structures of the ORR intermediates shown next to the corresponding energy levels.

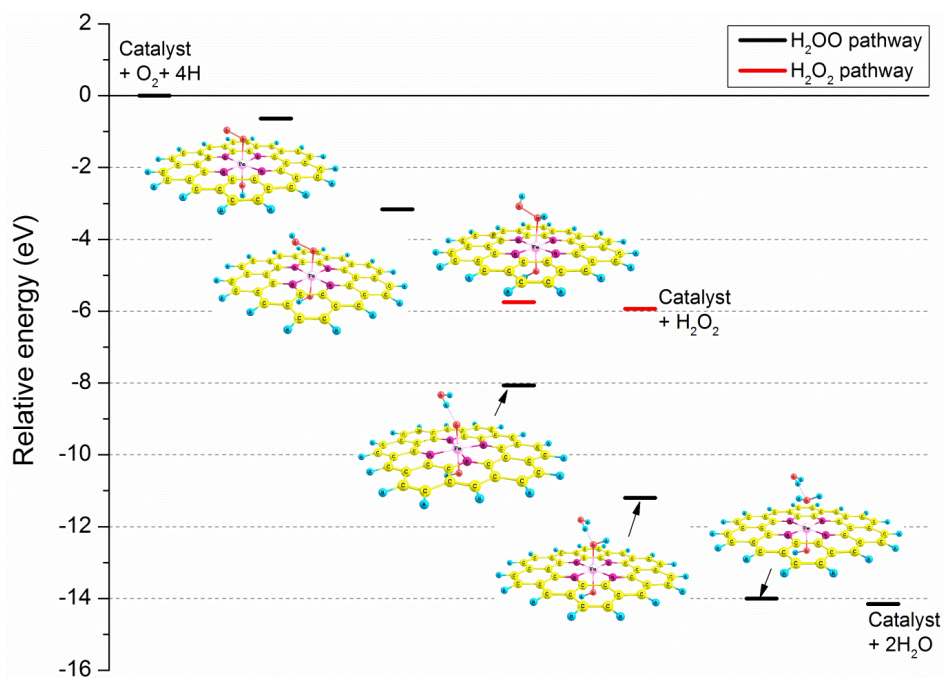


**Figure 4.8** Thermodynamics of the ORR pathways on the OH-terminated Fe tetraaza-annulene system.

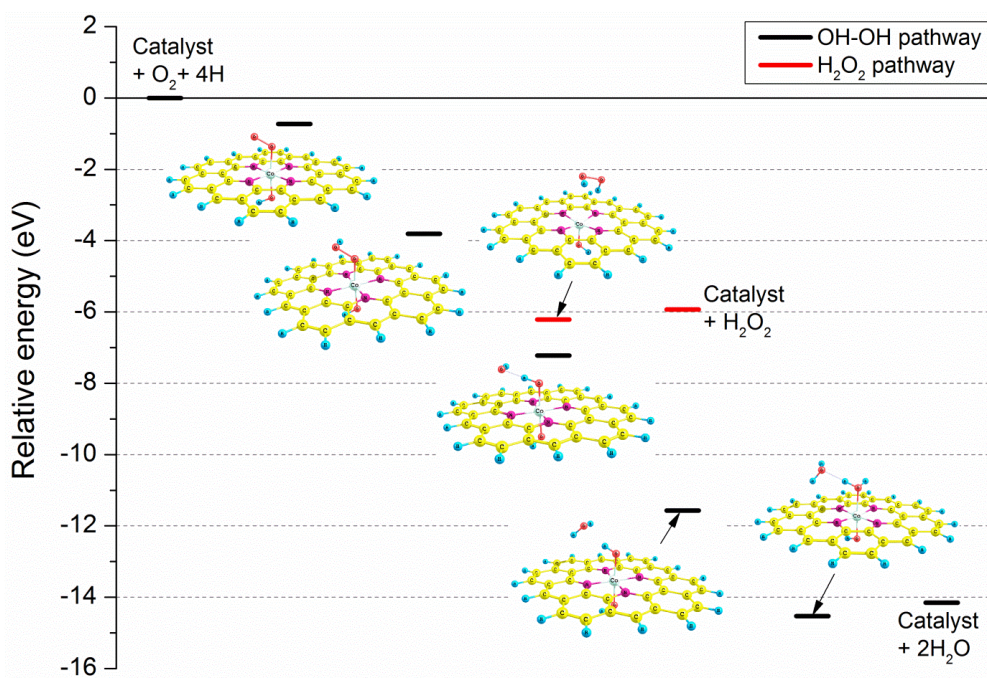


**Figure 4.9** Thermodynamics of the ORR pathways on the OH-terminated Co tetraaza-annulene system.

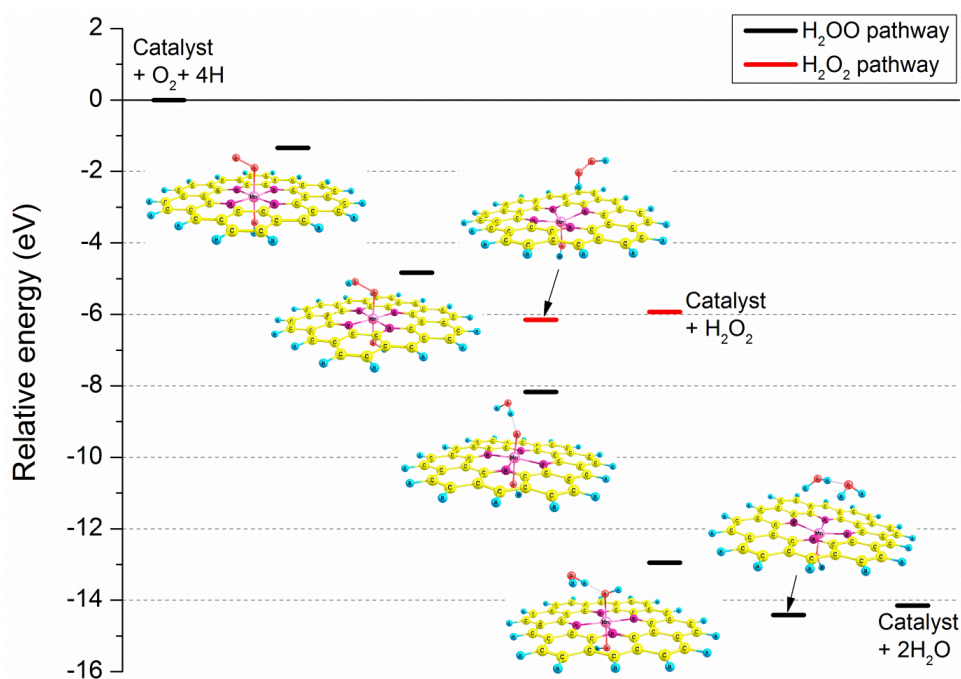


**Figure 4.10** Thermodynamics of the ORR pathways on the OH-terminated Mn tetraaza-annulene system.

Table 4.3 summarizes the calculated energies of the ORR elementary steps illustrated in Figure 4.8 - Figure 4.10. It can be observed that the calculated molecular oxygen binding energy is almost twice exothermic for the Mn centre compared to the

Fe and Co centres. This indicates that the Mn centre binds molecular oxygen too strongly and may impede the kinetics of the following steps.

**Table 4.3** Calculated reaction energies of the ORR elementary steps on the OH-blocked Fe, Co and Mn tetraaza-annulene model systems.

Elementary ORR step	Energy, eV		
	Fe	Co	Mn
Reactants	0	0	0
O <sub>2</sub> binding	-0.64	-0.73	-1.34
First H addition	-2.53	-3.08	-3.50
Second H addition (four-electron pathway)	-4.90	-3.41	-3.34
Second H addition (two-electron pathway)	-2.59	-2.40	-2.32
H <sub>2</sub> O <sub>2</sub> desorption	-0.18	0.28	0.22
Third H addition	-3.14	-4.35	-4.78
Fourth H addition	-2.80	-2.95	-1.46
2H <sub>2</sub> O desorption	-0.15	0.38	0.26

The first H addition leading to formation of the chemisorbed OOH group is found to be the least exothermic in the case of Fe centre. Introduction of the second H atom to each system in the H<sub>2</sub>O<sub>2</sub> mode (two-electron pathway) results in formation of the H<sub>2</sub>O<sub>2</sub> molecule in all three cases. The second H addition in the H<sub>2</sub>O-O mode (four-electron pathway) leads to the formation of the first water molecule and the oxidized metal centre in the case of Fe and Mn central atoms, and two hydroxyl groups in the case of the Co central atom. The second H addition in both the two- and four-electron pathways and H<sub>2</sub>O<sub>2</sub> desorption are more exothermic for the Fe centre than for the Co and Mn. This suggests that both the H<sub>2</sub>O<sub>2</sub> and the first water molecule are thermodynamically more favourable to form on the Fe centre than on the Co or Mn. The third H addition is more exothermic, and the fourth H addition is less exothermic on the Mn centre than on the Fe and Co. This indicates that the Mn centre terminated by the second OH group is very stable thermodynamically, and the OH group is more difficult to reduce to water on the Mn centre compared to the Fe or Co centres.

The calculated thermodynamics of the ORR steps on the OH-terminated Fe, Co and Mn tetraaza-annulene model systems enables us to conclude the following. (i) The ORR thermodynamics strongly depends on the nature of the central transition metal atom. (ii) Both the two- and four-electron ORR pathways are thermodynamically possible on all three metal centres. (iii) The four-electron ORR pathway is more exothermic in all cases and thus more thermodynamically favourable regardless of the nature of the transition metal centre. (iv) The relatively high energies of binding molecular oxygen and the OH group to the Mn centre suggest that Mn is likely to be blocked by a second OH group during the ORR.

### 4.4.3 Energetics of the ORR on the Fe, Co and Mn N-Coordinated Active Sites

In order to evaluate the kinetic aspects of the ORR on Fe, Co and Mn macrocycle active sites, it is necessary to obtain activation barriers for each elementary step of the ORR. Calculating activation barriers for the large tetraaza-annulene model systems is computationally expensive. In order to attain a reasonable computational time, the model system size has been reduced. Figure 4.11 illustrates the OH-terminated transition metal tetraaza-annulene model system, employed in the previous section, and the small-size system representing the transition metal macrocycle active sites. The small-size model system is further referred to as the M-4N, with the M being either Fe, Co or Mn. In the subsequent calculations, the M-4N model systems have been partially optimised, i.e. all the C-N and C-C bond lengths have been set constant and equal to those in the large optimized model system.

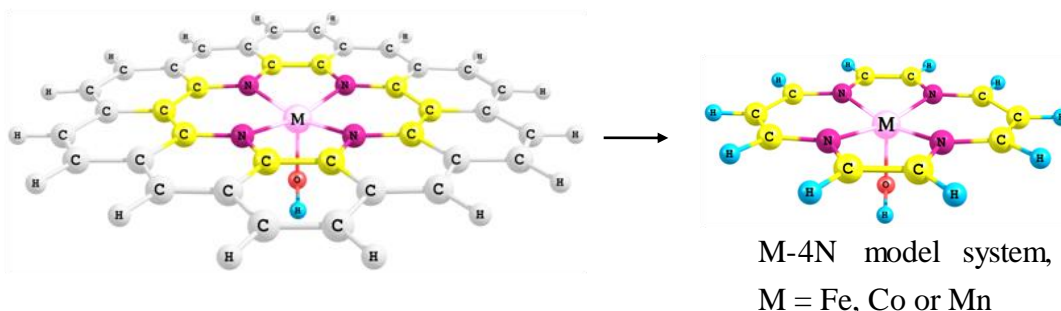


**Figure 4.11** Model systems representing transition metal macrocycle active sites: the large tetraaza-annulene and the small M-4N.

To evaluate the effect of model system truncation, molecular oxygen binding energies have been calculated for the large tetraaza-annulene and the small M-4N systems. In the M-4N, two cases have been considered: fully optimised and with C-N bonds frozen. The calculated binding energies are shown in Table 4.4. The energy differences between the large tetraaza-annulene and the M-4N systems are noticeable, but the effect of fully optimized and partially frozen M-4N geometries is not significant. However, the choice of the model system has been made in favour of the M-4N with frozen C-N bonds, since its structure is similar to that of the large tetraaza-annulene system.

Energies of the ORR elementary steps on the M-4N systems have been obtained in a similar way as on the OH-terminated transition metal tetraazaannulene systems. Table 4.5 lists the calculated energies of the ORR elementary steps on the M-4N and the tetraaza-annulene (large) systems. The M-4N and large tetraaza-annulene model systems have similar energies of the ORR elementary steps in most of the cases. This

reasonably justifies the use of the M-4N systems for calculating activation energies of the ORR steps.

**Table 4.4** Molecular oxygen binding energies for the large tetraaza-annulene and the small M-4N systems.

Metal centre	O <sub>2</sub> binding energy, eV		
	tetraazaannulene model system	M-4N model system	
		fully optimised	C-N bonds frozen
Fe	-0.33	-0.08	-0.12
Co	-0.42	-0.15	-0.19
Mn	-0.80	-0.85	-0.94

**Table 4.5** The calculated energies of the ORR elementary steps on the Fe, Co and Mn-4N model systems compared to the OH-terminated tetraaza-annulene (large) model systems.

Elementary reaction / state	Energies of the ORR elementary steps, eV					
	Fe-4N	Fe large	Co-4N	Co large	Mn-4N	Mn large
Reactants	<b>0</b>	0	<b>0</b>	0	<b>0</b>	0
O <sub>2</sub> binding	<b>-0.35</b>	-0.64	<b>-0.42</b>	-0.73	<b>-1.36</b>	-1.34
First H addition	<b>-2.48</b>	-2.53	<b>-3.07</b>	-3.08	<b>-3.17</b>	-3.50
Second H addition (two-electron pathway)	<b>-3.25</b>	-2.59	<b>-2.59</b>	-2.40	<b>-1.68</b>	-1.32
H <sub>2</sub> O <sub>2</sub> desorption	<b>0.15</b>	-0.18	<b>0.16</b>	0.28	<b>0.28</b>	0.22
Second H addition (four-electron pathway)	<b>-4.95</b>	-4.90	<b>-2.98</b>	-3.41	<b>-3.34</b>	-3.34
Third H addition	<b>-3.04</b>	-3.14	<b>-4.82</b>	-4.35	<b>-4.81</b>	-4.78
Fourth H addition	<b>-3.49</b>	-2.80	<b>-3.11</b>	-2.95	<b>-1.57</b>	-1.46
2H <sub>2</sub> O desorption	<b>0.11</b>	-0.15	<b>0.20</b>	0.38	<b>0.05</b>	0.26

As described in Section 4.3, activation barriers of the ORR elementary steps have been obtained using the technique of relaxed PES scan calculations, with the highest energy points being taken as transition states. Figure 4.12 illustrates the PES scan calculations of the ORR elementary steps on the Fe-4N system. Molecular oxygen binding to the Fe centre shown in Figure 4.12 a) is barrierless, i.e. this reaction does not have activation energy. In the first H addition step shown in Figure 4.12 b), the system's energy increases slightly until reaching the O-H distance of circa 1.55 Å, and then gradually decreases.

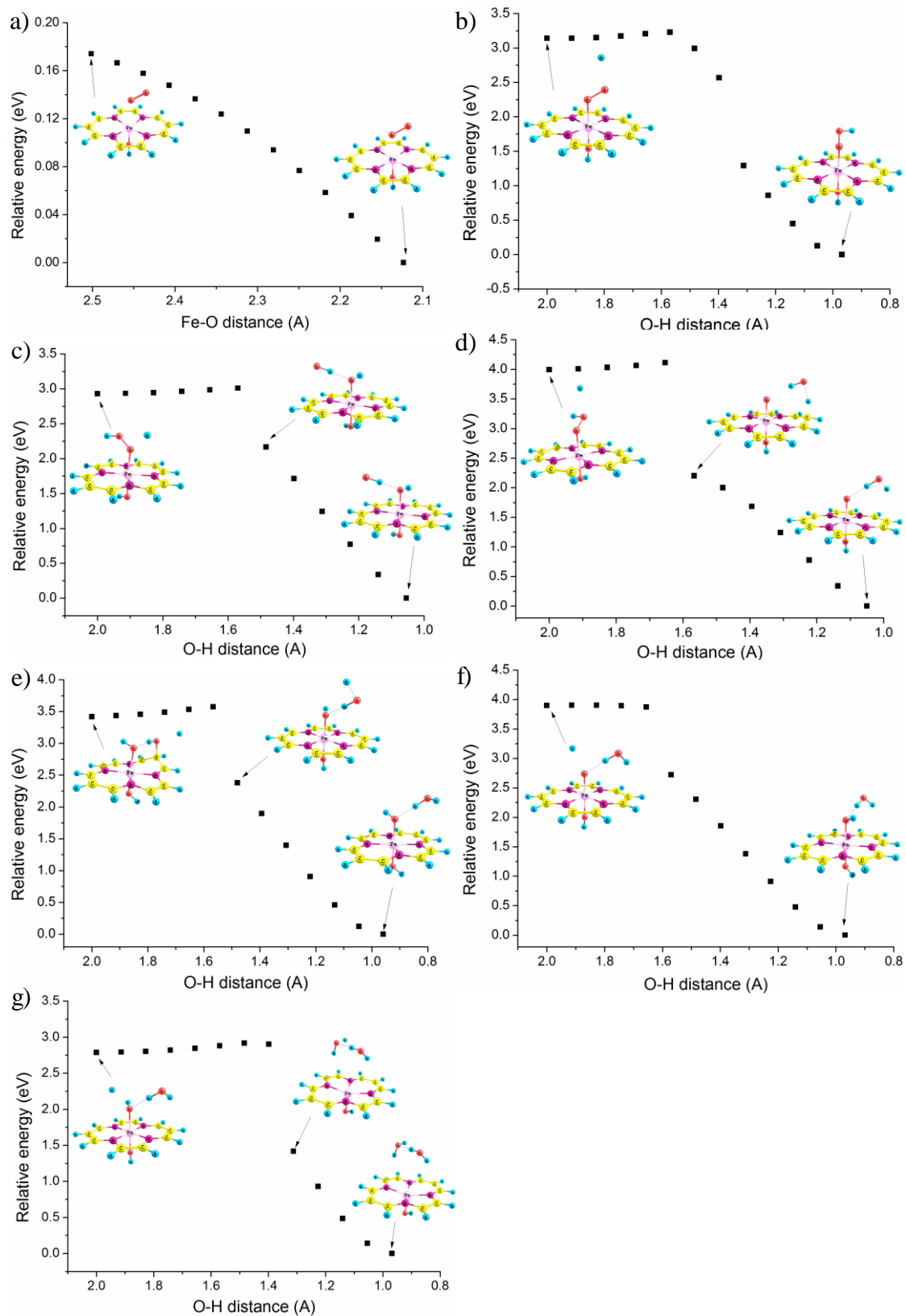


**Figure 4.12** Potential energy profiles of the ORR elementary steps on the Fe-4N model system: a) molecular oxygen binding; and H addition steps: b) first H; c) second H in the OH-OH pathway; d) second H in the H<sub>2</sub>OO pathway; e) third H in the OH-OH pathway; f) third H in the H<sub>2</sub>OO pathway; and g) fourth H.

The second H addition has been modelled by approaching the second H atom to either of the two O atoms of the OOH group, leading to the two four-electron pathways referred to as the OH-OH and H<sub>2</sub>OO. In the OH-OH pathway in Figure 4.12 c), the second H atom approaches the O atom connected to the metal centre. It is clear that hydrogen peroxide does not form, but the O-O bond dissociates at the O-H distance of circa 1.55 Å to form the two OH groups. Before the O-O bond cleavage, the system's energy virtually does not change and decreases sharply after the cleavage. It should be noted that the chemisorbed OH-OH structure obtained in the PES scan calculation is not a minimum energy one. Therefore, the final structure of the scan calculation has been used as an initial guess to find a local energy minimum by optimisation. In the H<sub>2</sub>OO pathway, the second H atom approaches the terminal O atom of the OOH group to form the first H<sub>2</sub>O molecule and the atomic O chemisorbed on the Fe centre, as shown in Figure 4.12 d). It can be observed that for the first five scan steps, the potential energy increases slightly and then drops sharply as a result of the O-O bond dissociation.

The third H addition has been modelled for the two ORR pathways. Figure 4.12 e) shows the scan calculation in the OH-OH pathway. It is observed that the system's potential energy increases slightly until reaching the maximum at the O-H distance of 1.55 Å and then drops sharply due to the O-C bond cleavage. Figure 4.12 f) shows the third H addition in the H<sub>2</sub>OO pathway, where the potential energy is constant for the five scan steps and then reduces significantly when the O-H bond forms. It is clear that the third H addition in both pathways results in the same intermediate product, namely OH chemisorbed on the Fe centre and the first H<sub>2</sub>O molecule weakly bound to it. The fourth H addition is shown in Figure 4.12 g). The potential energy increases slightly until the splitting of the Fe-O bond and then drops sharply with the formation of the second water molecule.

Figure 4.13 illustrates the obtained ORR pathways on the Fe-4N model system, including the relative energy levels of the ORR elementary steps and the corresponding transition states. The optimised structures of the intermediate products are shown adjacent to the corresponding energy levels. The dashed lines designate that the PES scan calculations did not reveal activation barriers and therefore the reactions are considered to be barrierless. It has been found that the ORR on the Fe-4N model system branches into two four-electron pathways, referred to as the H<sub>2</sub>OO and OH-OH pathways. All the intermediate steps in both pathways are barrierless except the third H addition. Interestingly, the two-electron pathway via hydrogen peroxide formation has not been found.

The calculated reaction and activation energies of the two ORR pathways on the Fe-4N model system are listed in Table 4.6. The second H addition steps in the two pathways have an energy difference of 0.45 eV. As observed in Figure 4.13, the non-

zero activation barriers have been obtained only for the third H addition steps, and these values are rather small: 0.01 eV in the H<sub>2</sub>OO pathway, and 0.16 eV in the OH-OH pathway. Given the lower activation energy in the H<sub>2</sub>OO pathway, it may have a faster kinetics than the OH-OH pathway. Overall, the non-activated potential energy profiles of the ORR indicate that the active sites modelled by the Fe-4N system may be potentially very effective in catalysing the oxygen reduction predominantly in the four-electron pathway via H<sub>2</sub>OO formation.

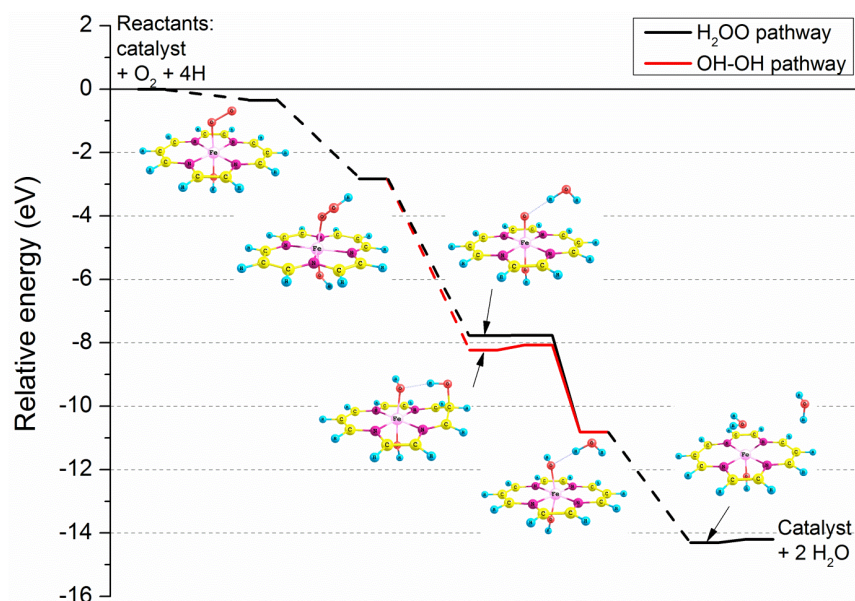


**Figure 4.13** The ORR pathways on the Fe-4N model system.

**Table 4.6** Reaction energies and activation energies of the ORR elementary steps on the Fe-4N model system.

Reaction/state	Elementary reaction / activation energy, eV	
	H <sub>2</sub> OO pathway	OH-OH pathway
Reactants	0	0
O <sub>2</sub> binding activation	none	none
O <sub>2</sub> binding	-0.35	-0.35
First H addition activation	none	none
First H addition	-2.48	-2.48
Second H addition activation	none	none
Second H addition	-4.95	-5.40
Third H addition activation	0.01	0.16
Third H addition	-3.04	-2.58
Fourth H addition activation	none	none
Fourth H addition	-3.49	-3.49
2H <sub>2</sub> O desorption	0.11	0.11

Figure 4.14 illustrates the PES scan calculations for the ORR elementary steps on the Co-4N system. In Figure 4.14 a) it is clear that the step of molecular oxygen binding is barrierless. During the first H addition shown in Figure 4.14 b), the system's energy increases till the O-H distance is circa 1.55 Å, and then drops sharply due to the C-H bond formation. After this, the energy increases, resulting in the second potential barrier which is attributed to cleavage of the C-H bond. This second potential barrier has been neglected since the C-H bond formation has been caused by the small size of the model system.

The second H addition has been modelled to simulate the two- and four-electron ORR pathways, i.e. with the second H atom approaching either of the two O atoms. Figure 4.14 c) depicts the pathway in which the second H atom approaches the O atom connected to the metal centre as in a hydrogen peroxide molecule. It is clear that the hydrogen peroxide does not form, but the O-O bond dissociates to produce the two OH groups. The sharp energy drop is due to formation of the first H<sub>2</sub>O molecule, and the further decrease in the O-H distance results in a gradual increase in the energy and the formation of the OH groups. It is clear that the final structure with the two OH groups is not a minimum energy state and has been used as an initial guess to find a local energy minimum by geometry optimisation. Figure 4.14 d) shows the second H atom approaching the terminal O atom of the OOH group in the H<sub>2</sub>OO pathway. The gradual increase and decrease of the potential energy clearly shows the position of the transition state.

The third H addition has been modelled for the two ORR pathways. Figure 4.14 e) shows the scan calculation for the OH-OH pathway, in which the potential energy increases until the O-H distance is 1.4 Å, and then sharply drops with the breaking of the C-O bond. Figure 4.14 f) shows the scan calculation of the third H addition in the H<sub>2</sub>OO pathway, in which the third H atom approaches the O atom bound to the metal centre. The potential energy steadily decreases, indicating the absence of activation barrier. The third H addition in both the ORR pathways results in the same products, namely the OH group chemisorbed on the metal centre and the H<sub>2</sub>O molecule weakly bound to it. The fourth H addition is shown in Figure 4.14 g). It has been observed that the potential energy increases linearly until the scanned O-H distance is circa 1.45 Å, and then reduces significantly due to the Co-O bond cleavage and formation of the second water molecule at a significant distance from the Co centre.

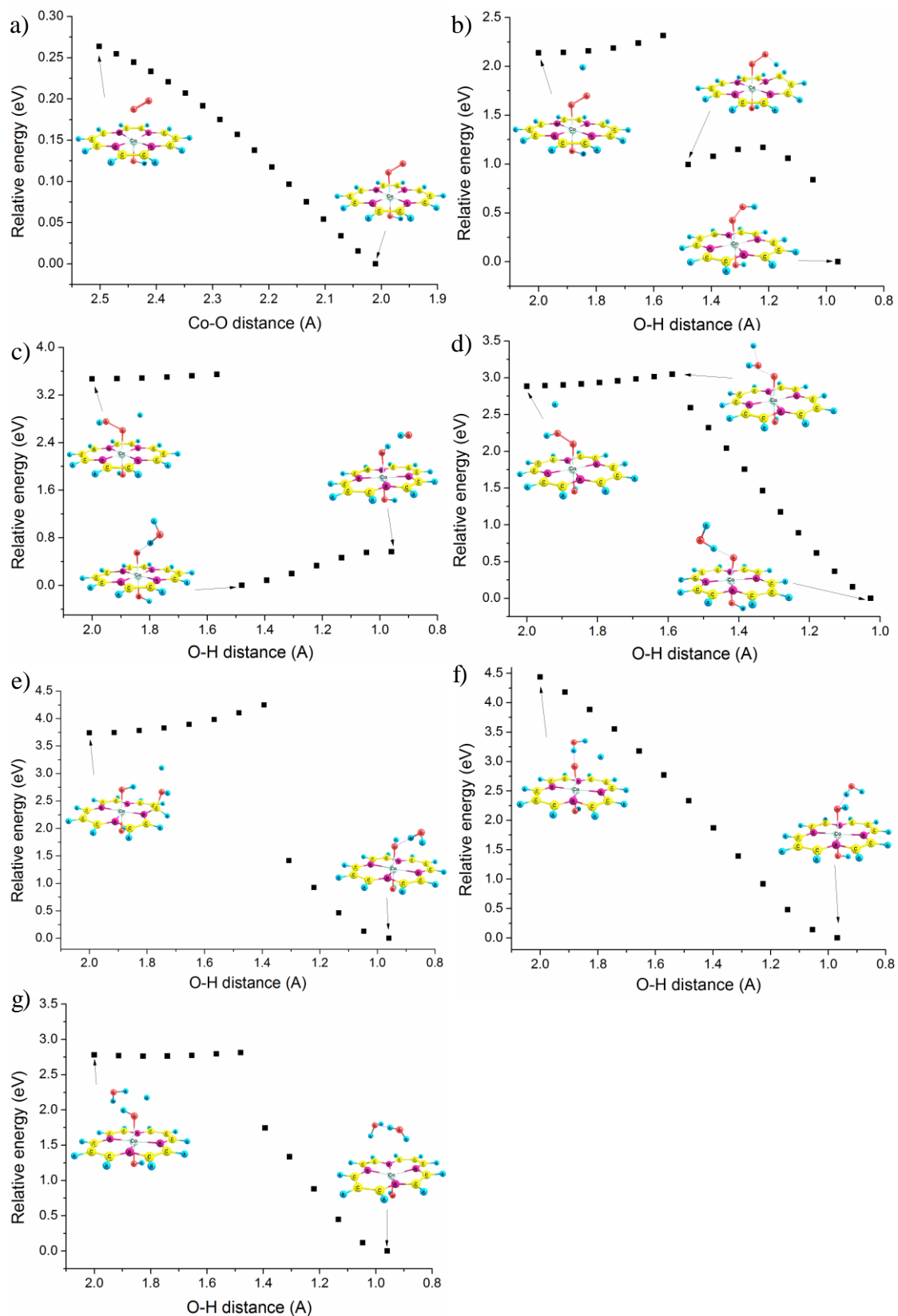


**Figure 4.14** Potential energy profiles of the ORR intermediate steps on the Co-4N model system: a) molecular oxygen binding; and H addition steps: b) first H; c) second H in the OH-OH pathway; d) second H in the H<sub>2</sub>OO pathway; e) third H in the OH-OH pathway; f) third H in the H<sub>2</sub>OO pathway, and g) fourth H.

Figure 4.15 illustrates the oxygen reduction mechanism on the Co-4N model system branching into two four-electron pathways, via the H<sub>2</sub>OO and OH-OH intermediates, and Table 4.7 lists the calculated elementary reaction energies and activation energies. It has been found that molecular oxygen binding to the Co-4N system does not have an activation barrier, similar to the Fe-4N system. However, the first H addition on the Co-4N system has activation energy of 0.07 eV.

As in the case of the Fe-4N system, the two-electron pathway via hydrogen peroxide has not been found. The second H addition in the OH-OH pathway is 1.12 eV more exothermic than in the H<sub>2</sub>OO pathway. Both pathways merge at the step of the third H addition, which is found to have no activation energy in the H<sub>2</sub>OO pathway, but has significant activation energy of 1.11 eV in the OH-OH pathway due to the cleavage of the C-H bond. This implies that the reaction may stop at this point of the OH-OH pathway, or its rate can be considerably slowed. Therefore, the ORR on the Co-4N model system can take a four-electron pathway via the H<sub>2</sub>OO formation only. The rate limiting step in this case is the second H addition, since it has the highest calculated activation energy of 0.14 eV.

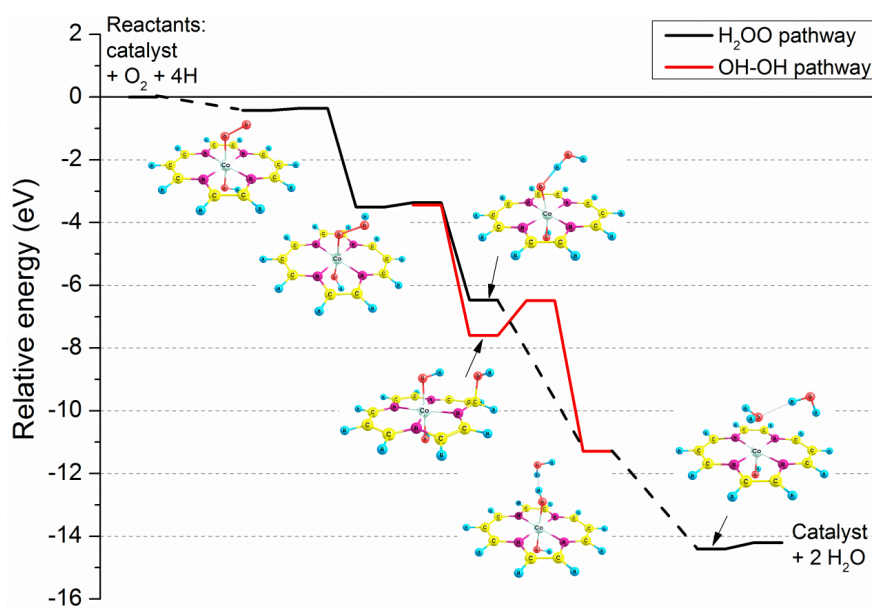


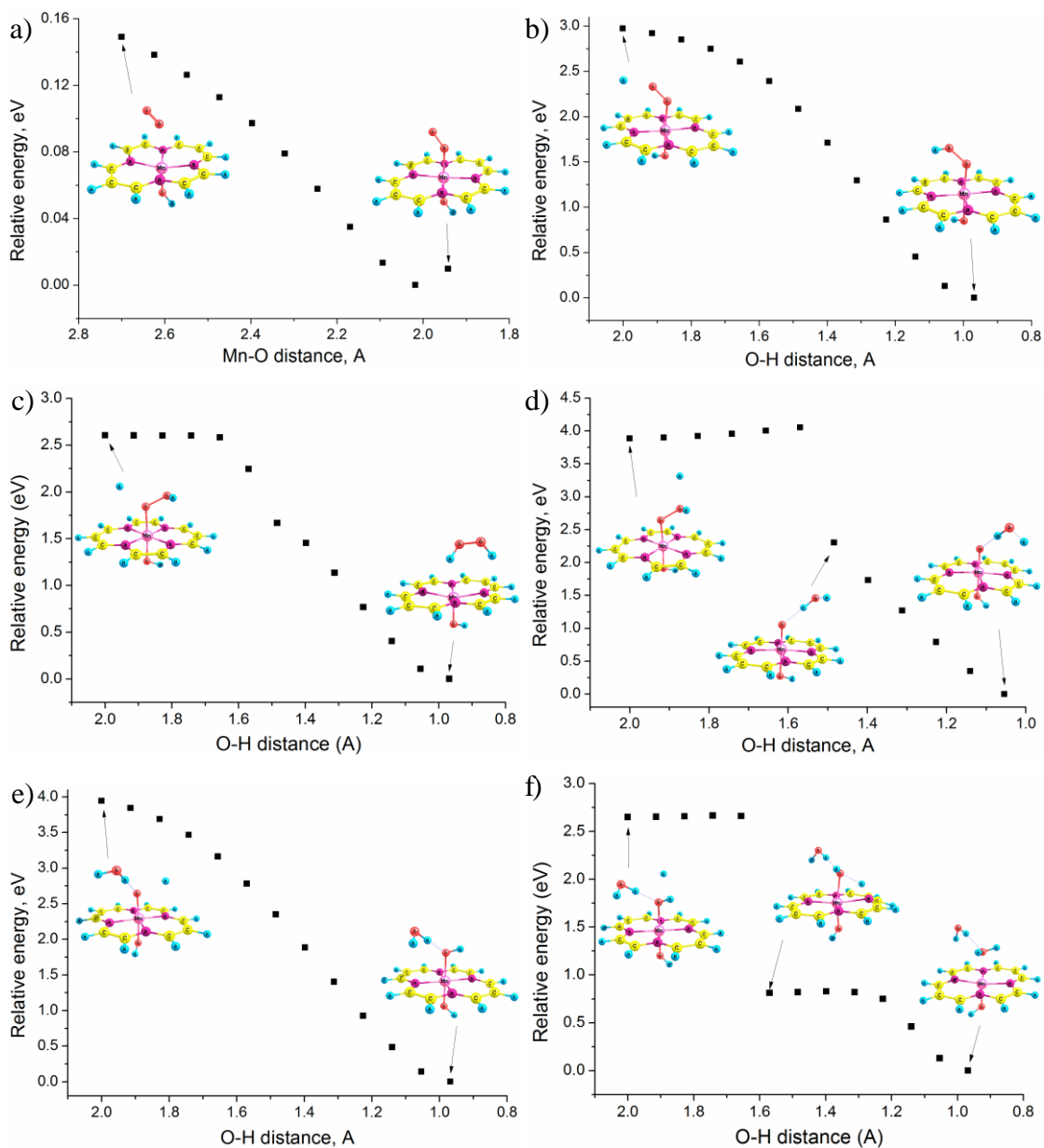
Figure 4.15 The ORR pathways on the Co-4N model system.

**Table 4.7** Elementary reaction energies and activation energies of the ORR steps on the Co-4N system.

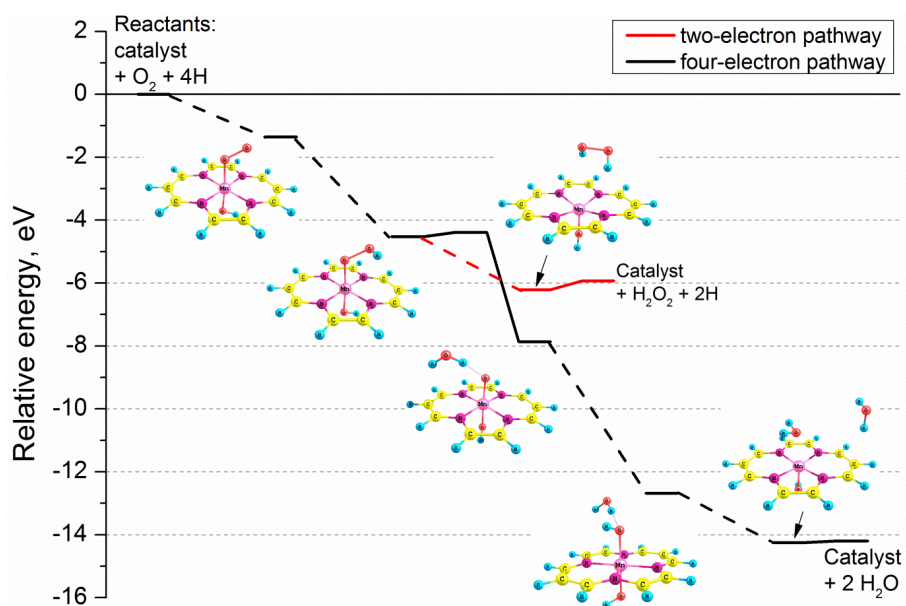
Reaction/state	Elementary reaction / activation energy, eV	
	H <sub>2</sub> OO pathway	OH-OH pathway
Reactants	0	0
O <sub>2</sub> binding activation	none	none
O <sub>2</sub> binding	-0.42	-0.42
First H addition activation	0.07	0.07
First H addition	-3.07	-3.07
Second H addition activation	0.14	none
Second H addition	-2.98	-4.10
Third H addition activation	none	1.11
Third H addition	-4.82	-4.82
Fourth H addition activation	none	none
Fourth H addition	-3.11	-3.11
2H <sub>2</sub> O desorption	0.20	0.20

Figure 4.16 shows the PES scan calculations of the ORR elementary steps on the Mn-4N model system. Figure 4.16 a) and b) illustrate that the molecular oxygen binding and the first H addition do not have activation barriers. The second H addition has been modelled in two ways, as previously, i.e. by the H atom approaching either of the two O atoms. Figure 4.16 c) illustrates the second H atom approaching the chemisorbed OOH in a hydrogen peroxide configuration (two-electron pathway), and this results in the formation of hydrogen peroxide molecule without activation energy. Figure 4.16 d) shows the second H addition in the H<sub>2</sub>OO configuration. In this case, the potential energy increases until the O-H distance is circa 1.55 Å, and then decreases sharply due to the O-O bond cleavage. The third and fourth H addition steps have been found to have no activation barriers, as illustrated in Figure 4.16 e) and f).

The ORR on the Mn-4N system is shown in Figure 4.17, and the elementary reaction energies and activation energies are summarized in Table 4.8. Figure 4.17 illustrates that the ORR branches into the two-electron pathway, terminating with the hydrogen peroxide formation, and the four-electron pathway. The second H addition step in the four-electron pathway is markedly more exothermic than that of the two-electron pathway. However, the two-electron pathway is found not to have activation barriers, whereas the second H addition in the four-electron pathway is the rate limiting step with the calculated activation energy of 0.14 eV. Thus, both the ORR pathways on the Mn-4N model system are thermodynamically possible, but the kinetics of the four-electron pathway should be somewhat slower than that of the two-electron pathway due to the non-zero activation energy of the rate limiting step. This suggests that during the ORR, the Mn-4N active sites can potentially yield hydrogen peroxide.



**Figure 4.16** Potential energy profiles of the ORR intermediate steps on the Mn-4N system: a) molecular oxygen binding; and H addition steps: b) first H; c) second H in the two-electron pathway; d) second H in the four-electron pathway; e) third H; f) fourth H.



**Figure 4.17** The ORR pathways on the Mn-4N model system.

**Table 4.8** Elementary reaction energies and activation energies of the ORR steps on the Mn-4N system.

Reaction/state	Elementary reaction / activation energy, eV	
	Two-electron pathway	Four-electron pathway
Reactants	0	0
O <sub>2</sub> binding activation	none	none
O <sub>2</sub> binding	-1.36	-1.36
First H addition activation	none	none
First H addition	-3.17	-3.17
Second H addition activation	none	0.14
Second H addition	-1.68	-3.34
H <sub>2</sub> O <sub>2</sub> desorption	0.28	-
Third H addition activation		none
Third H addition		-4.81
Fourth H addition activation		none
Fourth H addition		-1.57
2H <sub>2</sub> O desorption		0.05

## 4.5 Conclusion

In this chapter, the oxygen reduction reaction has been studied on model systems representing transition metal macrocycle active sites in order to identify potentially the most efficient ones. The effect of macrocycle structure has been studied by modelling molecular oxygen binding to phthalocyanine, porphyrin, corrin and tetraaza-annulene macrocycles either with iron, cobalt or manganese atoms in the centre. The effect of the central transition metal atom has been investigated by modelling the thermodynamics and kinetics of the oxygen reduction reaction.

The central transition metal atom is the reaction centre, and its strength of molecular oxygen binding depends primarily on the metal nature. It has been found that the binding strength increases in the order of  $\text{Co} < \text{Fe} < \text{Mn}$ . The structure of macrocycle also influences molecular oxygen binding and hence efficiency of the active sites, but its effect is not so pronounced as that of the metal nature.

The metal centre in macrocycle active sites should be terminated by a functional group on one side, e.g. hydroxyl group. This decreases the metal centre's binding capacity of the intermediate ORR species and therefore should facilitate the oxygen reduction on the other free side.

The iron macrocycle active sites demonstrate the highest catalytic activity towards the ORR, since the oxygen reaction proceeds through the four-electron pathway with negligible calculated activation energy of the rate limiting step (0.01 eV). The cobalt and manganese macrocycle active sites are predicted to have similar reaction rates and activities in the four-electron ORR pathway, since the calculated activation energies of the rate limiting steps are the same for the two metal centres (0.14 eV). The manganese macrocycle active sites may provide an accessible route to the two-electron ORR pathway producing undesirable hydrogen peroxide. Therefore, non-precious catalysts with high concentration of iron macrocycle active sites with the proposed structure are predicted to be the most promising for PEM fuel cells.

## **Chapter 5**

### **DFT Modelling of the Catalytic Active Sites on Heteroatom Doped Graphene**

#### **5.1 Introduction**

Carbon edges, studied in Chapter 3 of this thesis, are essentially defects in the ordered graphitic carbon phase and therefore only partially account for the catalytic activity of carbon catalysts. The bulk of the ordered carbon phase can consist of graphene basal planes or cylinder-like surfaces of carbon nanotubes. Therefore, this chapter is dedicated to a computational investigation of heteroatom doped graphene basal planes as the ORR catalysts for PEM fuel cells.

The effect of mono as well as binary doping of graphene with N, B, P and S heteroatom dopants is investigated. In order to identify catalytic active sites, the reaction of molecular oxygen chemisorption has been used as an indicator. The technique of potential energy surface scan calculations is used as a main tool of obtaining potential energy profiles of molecular oxygen chemisorption on various sites on doped graphene. Molecular oxygen binding energies and activation energies are calculated to obtain an insight into thermodynamic and kinetic favourability of the reaction and identify promising catalytic structures.

Atomic charge and spin density analysis is conducted for the doped graphene systems by analogy with the analyses of mono nitrogen doped carbon, as reported in the literature [69, 72]. Further, atomic charge and spin density distributions are obtained for the heteroatom doped graphene model systems in order to link their catalytic activity with electronic properties.

#### **5.2 Molecular Systems**

The mono and binary heteroatom doped graphene has been modelled by the systems consisting of ten conjugated benzene rings, as illustrated in Figure 5.1. The boundaries of the graphene model systems are terminated by the H atoms for simplicity, with no edge effects being considered. In the mono heteroatom doped graphene, one C atom has been substituted either by an N, P or B atom, and the model systems are referred to as N-G, P-G and B-G, respectively. Binary heteroatom doped graphene has been represented by two model systems. In the first system, the substituent N, B or P heteroatoms have been studied in the following combinations: (i) two N, (ii) two P, (iii) N and P, and (iv) N and B, further referred to as the 2N-G,

2P-G, NP-G and NB-G model systems, respectively. In the second binary doped system, one of the C atoms in the zigzag edge has been replaced by an S atom, and the second heteroatom, either N or P, has been placed in one of the positions designated as 1, 2 and 3. The three isomer model systems of (i) S and N, and (ii) S and P doped graphene are further referred to as the SN-G and SP-G systems, respectively.

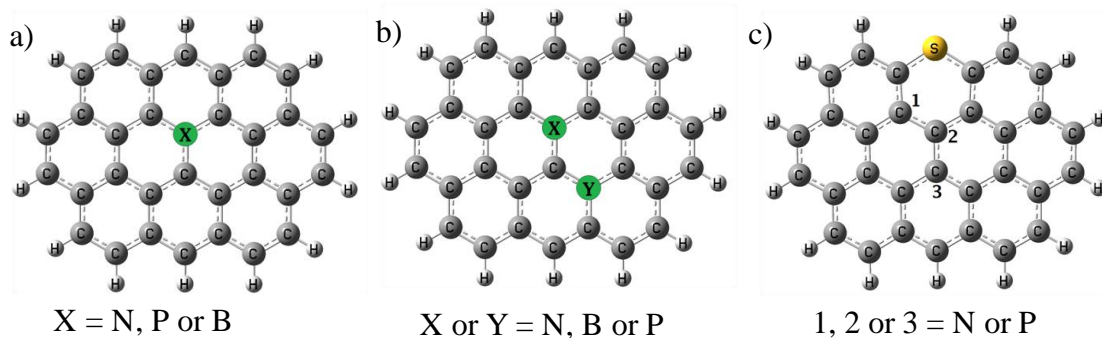


**Figure 5.1** Generic model systems of a) mono heteroatom doped graphene, b) binary doped graphene with the substituent N, B or P atoms, and c) binary doped graphene with the substituent S and N or P.

### 5.3 Theoretical Method

The DFT calculations have been performed using the B3LYP hybrid method in combination with a 6-31G(d) basis set in Gaussian09 [48]. To account for the aqueous ambience at the cathode catalyst in fuel cells, the polarized continuum model (PCM) of the self-consistent reaction-field (SCRF) method has been employed, in which water is simulated as a continuum of uniform dielectric constant [45]. The structures of the catalyst model systems have been fully optimized to the local minima on the potential energy surface. The spin multiplicities of the model systems have been allowed to relax, i.e. the electronic energy of each system has been obtained with two spin multiplicities: (i) the lowest,  $M = 1$  or  $2$ , and (ii) the next higher,  $M = 3$  or  $4$ , depending on the electronic structure. The ground state multiplicity was determined as having the lower electronic energy of the optimised structure.

Potential energy profiles of molecular oxygen binding to the model systems have been obtained using the technique of relaxed potential energy surface (PES) scan calculations [45]. The oxygen molecule was translated towards an atom on the surface of a model system, with the geometry being optimised at each step at a fixed value of the scanned coordinate. The initial distance between one of the oxygen molecule atoms and an atom of a model system was set to be equal to either  $3.5$  or  $4.0$  Å, and the final distance was set to be approximately equal to an average bond length between oxygen and the atom of a given element. Depending on the required fineness

of the scan calculations, the step size has been chosen to be between 0.1 and 0.15 Å. In order to account for the triplet spin state of the oxygen molecule in the scan calculations, the spin multiplicities have been set to be 3 or 4, depending on a system's electronic structure.

In the potential energy profiles, the maximum energy points have been taken as the transition states (TS). The starting points or minimum energy points preceding the maxima have been taken as reactant complexes, and the minimum energy points following the maxima have been taken as products. The relative energies for the potential energy profiles of molecular oxygen binding have been calculated as the difference between each scan point and the first energy point. Molecular oxygen binding energies  $\Delta E$  have been calculated as described in Section 3.3.

In order to investigate the charge and spin density distribution on the active sites in the doped graphene model systems, natural bond orbital (NBO) analyses have been performed [229]. The spin densities are observable and related to electron density, which determines a system's energy [230], whereas atomic charges are not quantum mechanical observable and the schemes of their assigning are ultimately arbitrary [45].

#### **5.4 Proposed Methodology of Modelling the ORR Mechanism in Acid and Alkaline Media**

As discussed in Chapter 4, in order to obtain the entire ORR mechanism, the four consequent steps of H atom (proton) addition should be modelled. The most accurate and realistic way of obtaining activation barriers of the H (proton) transfer reactions in the ORR is using the species acting as proton donors which are different in acid and alkaline media. In acid, the proton donor should be the hydronium cation  $\text{H}_3\text{O}^+$ , and in alkaline media it can be water molecule only. The principle of modelling the ORR in acid and alkaline media is described hereafter. In acid media, four hydronium ions can be used to represent the proton donors in the four proton transfer reactions of the ORR. The detailed schematic of modelling the four-electron ORR pathway is shown in Figure 5.3.

First, the oxygen molecule binds to a catalyst surface in the end-on configuration. Then, the first H atom is transferred from a hydronium molecule to the vicinity of the oxygen molecule to result in the OOH group chemisorbed on the catalyst surface. The second H atom is transferred from a second hydronium ion to the same oxygen atom to form the first separated water molecule. This first formed water molecule is not included in the following step of the third H transfer from a hydronium to the chemisorbed atomic oxygen to form the OH group. The fourth H transfer leads to the formation of the second separated water molecule.

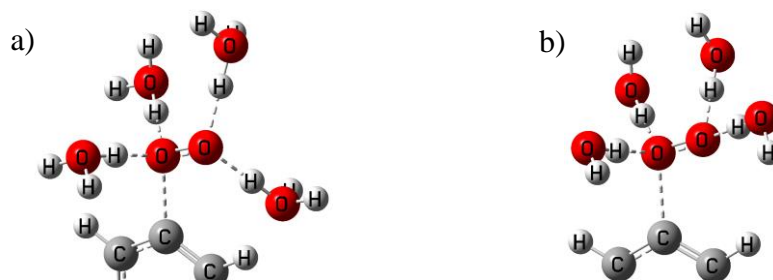


**Figure 5.2** Schematics of the ORR environment in a) acid, and b) alkaline media on a catalyst surface.

To account for the material balance, a hydronium molecule and a water molecule should be optimised separately and used in the calculations of reaction energies and activation energies as illustrated in Figure 5.3. Finding activation barriers of the intermediate protonation reactions implies obtaining the energy profiles of the proton transfer along the O-H...O hydrogen bonds. The transition state (TS) for a proton transfer reaction is the highest energy point, with the proton being approximately in the middle of a hydrogen bond (O...H...O). The most accurate technique of finding a TS in Gaussian 09 is QST2/QST3. However, it is frequently subject to convergence problems, as mentioned in Chapter 4. Therefore, the technique of “relaxed” PES scan calculations can be used as an alternative or supplement for finding the TS for the proton transfer reactions.

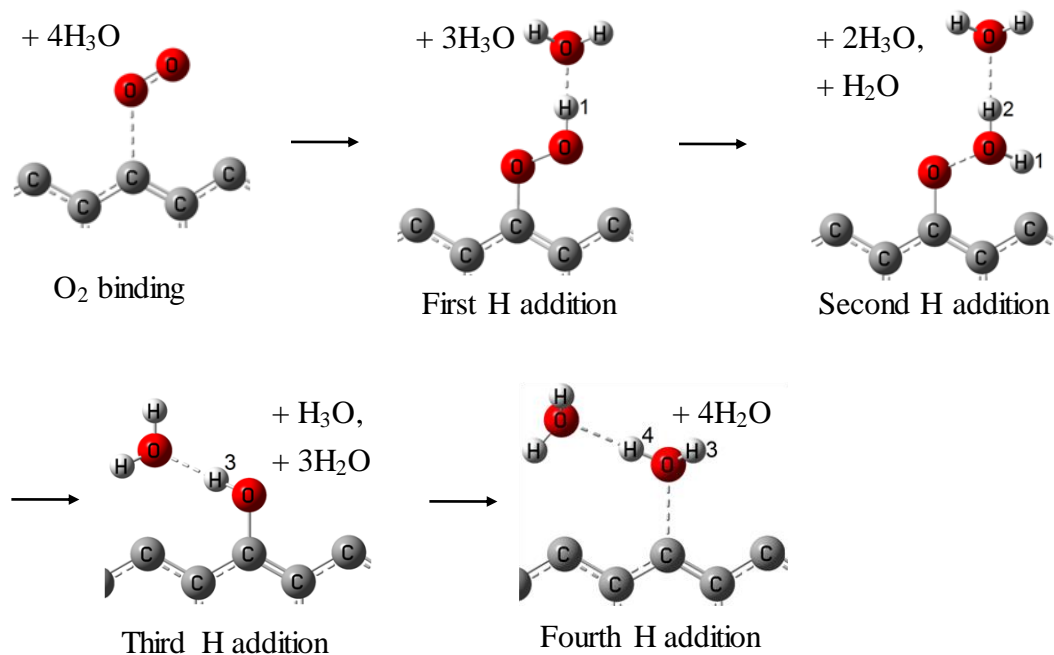


**Figure 5.3** Schematic of the four-electron ORR pathway in acid media on a catalyst surface. The transferred H atoms are designated by the numbers from 1 to 4.

The reaction energies of the ORR elementary steps have been calculated as shown in Table 4.3 which lists formulae used to calculate the full energies, relative energy levels and elementary reaction energies. Since each step of the ORR should contain the same number of atoms in a molecular system, the total energies, relative energy levels and elementary reaction energies are calculated as shown in Table 5.1. The activation barriers are calculated similarly using the energies of the TS corresponding to each elementary reaction.

**Table 5.1** The formulae for calculating the total energies, relative energy levels and elementary reaction energies of the four-electron ORR pathway accounting for the proton donors in acid media.

Reaction/state	Full energy formula	Relative energy level, eV	Elementary reaction energy, eV
Reactants	$E_0 = E_{\text{catalyst}} + E_{\text{O}_2} + 4 \cdot E_{\text{H}_3\text{O}}$	0	0
Molecular oxygen binding	$E_1 = E_{\text{O}_2\text{-catalyst}} + 4 \cdot E_{\text{H}_3\text{O}}$	$E_1 - E_0$	$E_1 - E_0$
First H transfer	$E_2 = E_{\text{OOH-catalyst}} + 3 \cdot E_{\text{H}_3\text{O}}$	$E_2 - E_0$	$E_2 - E_1$
Second H transfer	$E_3 = E_{\text{H}_2\text{OO-catalyst}} + 2 \cdot E_{\text{H}_3\text{O}} + E_{\text{H}_2\text{O}}$	$E_3 - E_0$	$E_3 - E_2$
Third H transfer	$E_4 = E_{\text{H}_3\text{O}_2\text{-catalyst}} + E_{\text{H}_3\text{O}} + 3 \cdot E_{\text{H}_2\text{O}}$	$E_4 - E_0$	$E_4 - E_3$
Fourth H transfer	$E_5 = E_{\text{2H}_2\text{O-catalyst}} + 4 \cdot E_{\text{H}_2\text{O}}$	$E_5 - E_0$	$E_5 - E_4$
2H <sub>2</sub> O desorption	$E_{\text{H}_2\text{O desorp.}} = E_{\text{catalyst}} + 6 E_{\text{H}_2\text{O}}$	$E_{\text{H}_2\text{O desorp.}} - E_0$	$E_{\text{H}_2\text{O desorp.}} - E_5$

The two-electron ORR pathway in acid media is illustrated in Figure 5.4. The steps of molecular oxygen binding and the first H addition are identical to those in the four-electron pathway shown in Figure 5.3. When the second H atom is transferred to the second O atom of the oxygen molecule, a hydrogen peroxide molecule is formed.

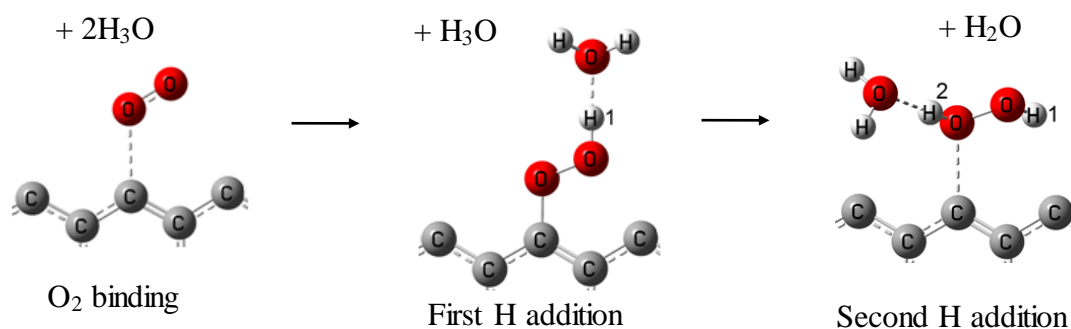


**Figure 5.4** Schematic of the two-electron ORR pathway in acid media on a catalyst surface. The transferred H atoms are designated by the numbers 1 and 2.

In the two-electron ORR pathway, two hydronium molecules participate as the H donors. In order to account for the material balance, a hydronium, water, and hydrogen peroxide molecules should be optimised separately and accounted for in the calculations of reaction energies and activation energies. The formulae of calculating the total energies, relative energy levels and elementary reaction energies as well as activation energies are shown in Table 5.2.

**Table 5.2** The formulae of calculating the total energies, relative energy levels and elementary reaction energies of the two-electron ORR pathway accounting for the proton donors in acid media.

Reaction/state	Full energy formula	Relative energy level, eV	Elementary reaction energy, eV
Reactants	$E_0 = E_{\text{catalyst}} + E_{\text{O}_2} + 2 \cdot E_{\text{H}_3\text{O}}$	0	0
O <sub>2</sub> binding	$E_1 = E_{\text{O}_2\text{-catalyst}} + 2 \cdot E_{\text{H}_3\text{O}}$	$E_1 - E_0$	$E_1 - E_0$
First H transfer	$E_2 = E_{\text{OOH-catalyst}} + E_{\text{H}_3\text{O}}$	$E_2 - E_0$	$E_2 - E_1$
Second H transfer	$E_3 = E_{\text{H}_2\text{O}_2\text{-catalyst}} + E_{\text{H}_2\text{O}}$	$E_3 - E_0$	$E_3 - E_2$
2H <sub>2</sub> O desorption	$E_{\text{H}_2\text{O desorp.}} = E_{\text{catalyst}} + E_{\text{H}_2\text{O}_2} + 2 E_{\text{H}_2\text{O}}$	$E_{\text{H}_2\text{O}_2 \text{ desorp.}} - E_0$	$E_{\text{H}_2\text{O}_2 \text{ desorp.}} - E_3$

In alkaline media, water molecules are the proton donors in the ORR, and the reaction mechanism is different from that in acid media, as illustrated in Figure 5.5. The first H is transferred from a water molecule to the chemisorbed oxygen molecule to form an OOH group on the catalyst surface. The next step is the dissociation of the O-OH bond results in releasing the first OH group. The second H is transferred from a water molecule to the remaining chemisorbed atomic oxygen to form the OH group chemisorbed on the catalyst surface. The final step is the desorption of the OH group from the surface. It should be noted that, according to the existing literature [149], the two-electron ORR pathway terminates with the desorption of the negatively charged HO<sub>2</sub><sup>-</sup> group, i.e. straight after the first H addition depicted in Figure 5.5. However, if

the HO<sub>2</sub> group dissociates as shown further in the schematic, the four-electron ORR pathway occurs. In order to preserve the material balance in the ORR in alkaline media, a water molecule, an OH group and an OOH group are optimised separately and accounted for as shown in Figure 5.5 and Table 5.3.

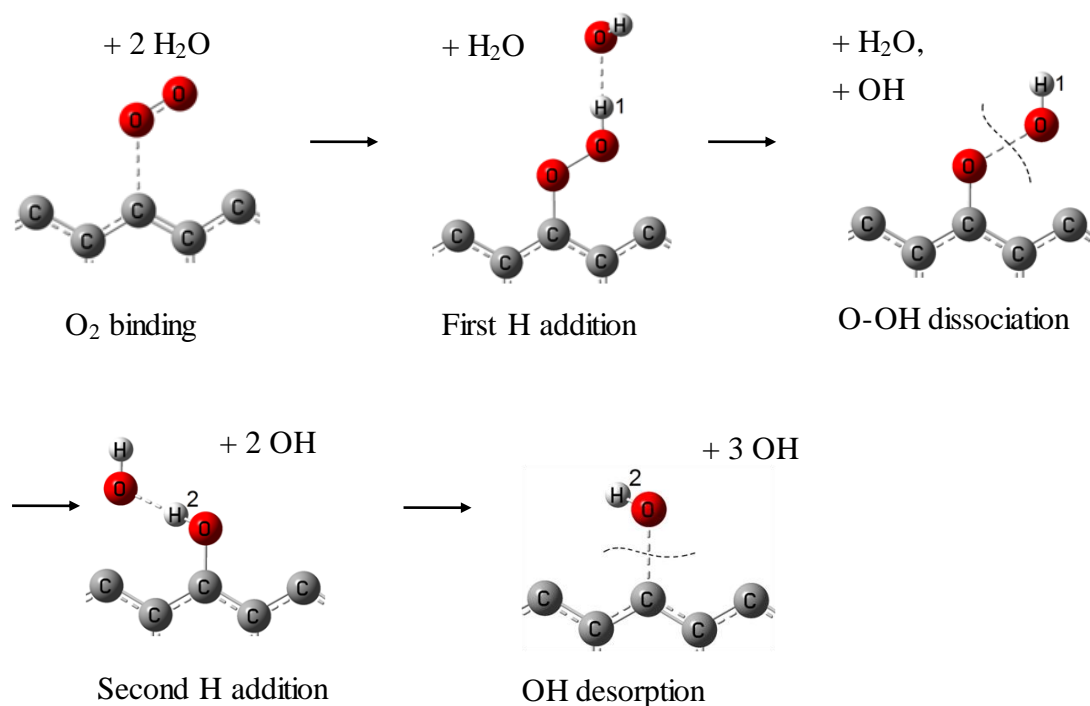


**Figure 5.5** Schematic of the four-electron ORR pathway in alkaline media on a catalyst surface. The transferred H atoms are designated by the numbers 1 and 2.

**Table 5.3** The formulae of calculating the total energies, relative energy levels and elementary reaction energies of the ORR pathways accounting for the proton donors in alkaline media.

Reaction/state	Full energy formula	Relative energy level, eV	Elementary reaction energy, eV
Reactants	$E_0 = E_{\text{catalyst}} + E_{\text{O}_2} + 2 \cdot E_{\text{H}_2\text{O}}$	0	0
O <sub>2</sub> binding	$E_1 = E_{\text{O}_2\text{-catalyst}} + 2 E_{\text{H}_2\text{O}}$	$E_1 - E_0$	$E_1 - E_0$
First H transfer	$E_2 = E_{\text{OOH-catalyst}} + E_{\text{H}_2\text{O}}$	$E_2 - E_0$	$E_2 - E_1$
OOH desorption (two-electron pathway)	$E_{\text{OOH desorp.}} = E_{\text{catalyst}} + E_{\text{OOH}} + E_{\text{H}_2\text{O}} + E_{\text{OH}}$	$E_{\text{OOH desorp.}} - E_0$	$E_{\text{OOH desorp.}} - E_2$
O-OH dissociation (four-electron pathway)	$E_3 = E_{\text{O-catalyst}} + E_{\text{H}_2\text{O}} + 2 E_{\text{OH}}$	$E_3 - E_0$	$E_3 - E_2$
Second H transfer	$E_4 = E_{\text{OH-catalyst}} + 2 E_{\text{OH}}$	$E_4 - E_0$	$E_4 - E_3$
OH desorption	$E_{\text{OH desorp.}} = E_{\text{catalyst}} + 4 E_{\text{OH}}$	$E_{\text{OH desorp.}} - E_0$	$E_{\text{OH desorp.}} - E_4$

Figure 5.6 illustrates the proposed method of the ORR simulation in acid media over a catalyst model system using Gaussian 09. In this schematic, the catalyst surface is represented by the graphene sheet doped with two nitrogen atoms. The molecular oxygen over the catalyst surface is connected to four hydronium ions. The presence of the hydronium ions implies that this part of the model system is positively charged, whereas the catalyst should be negatively charged since it is a reservoir of electrons. Thus, the electric field is directed along the Y axis of the Cartesian coordinates. As mentioned above, the initial distance between the catalyst surface and the nearest atom of the oxygen molecule in all calculations is set to the value of 3.5 Å. In PES scan calculations of the ORR intermediate steps, the distance between the oxygen molecule and the catalyst model system decreases to circa 1.4 Å. Nonetheless, the thickness of the electric double layer is assumed to be as reported in the study of Yeh et al. [34], namely, 3 Å.

The ORR mechanisms in acid and alkali media described above maintain the principle of mass conservation during the reaction, but do not account for the electric charges and their distribution that is present in the real catalytic system. Accounting for the electric charges is essential, since the ORR is an electrochemical reaction taking place in the presence of electric current.

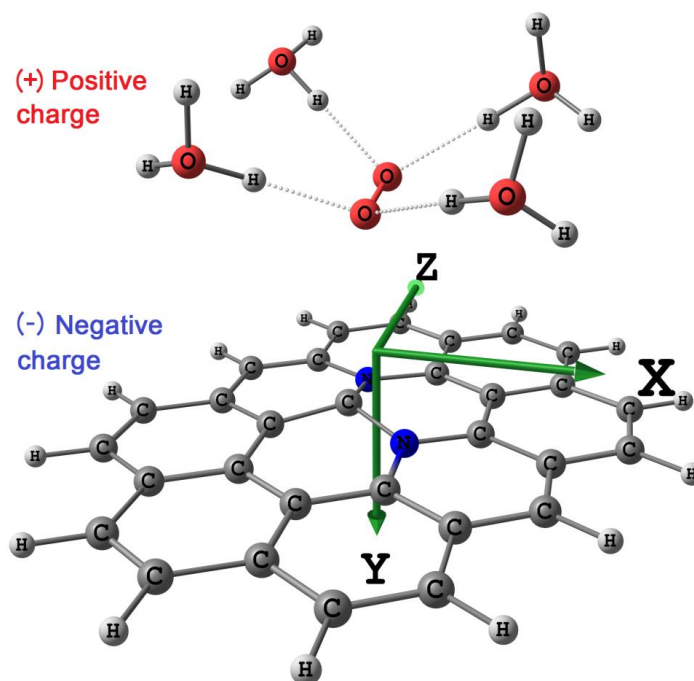


**Figure 5.6** Schematic of the ORR reactants over the catalyst model system. The electric field direction is along the Y axis.

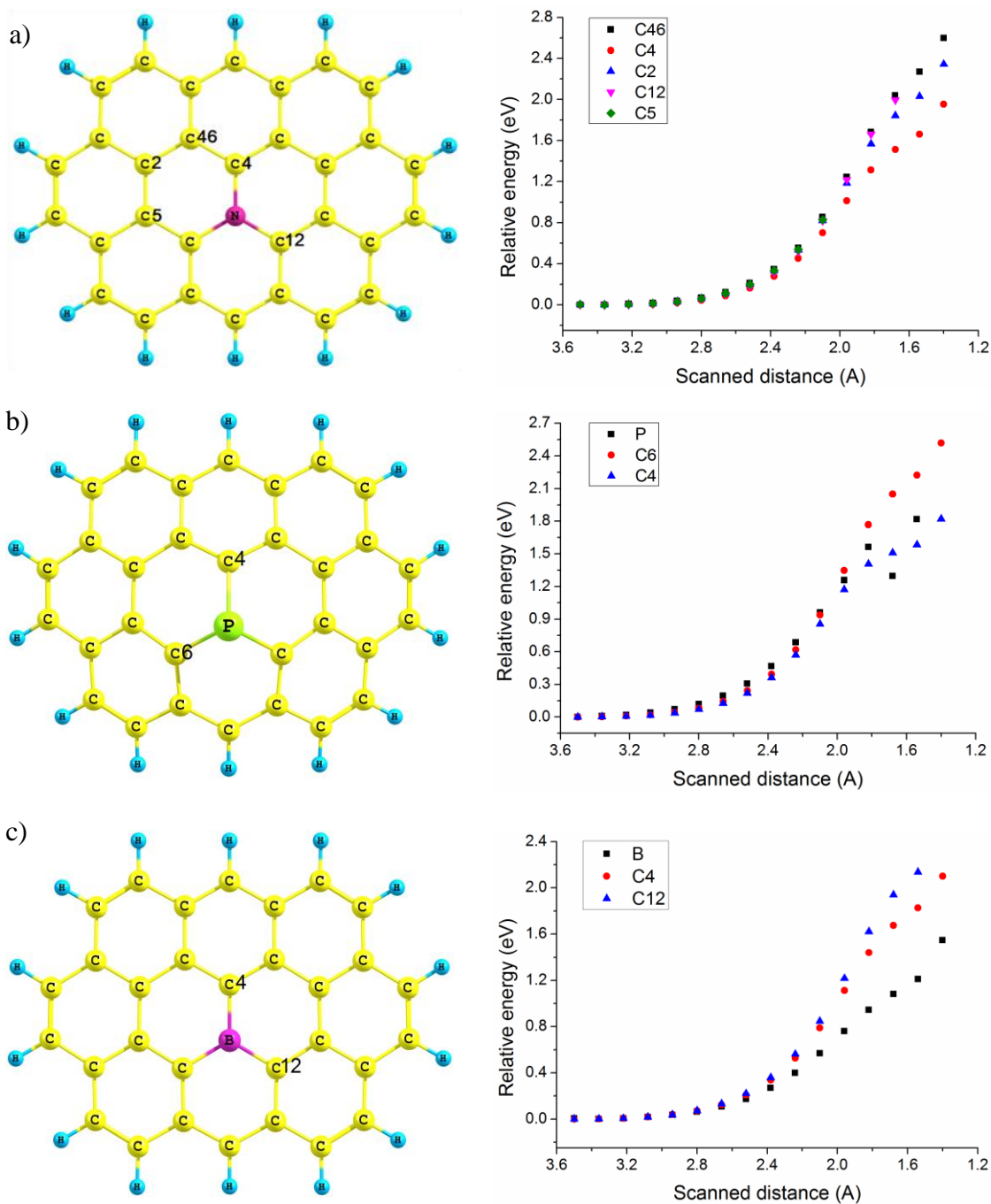
## 5.5 Results and Discussion

### 5.5.1 Potential Energy Profiles of the Molecular Oxygen Binding

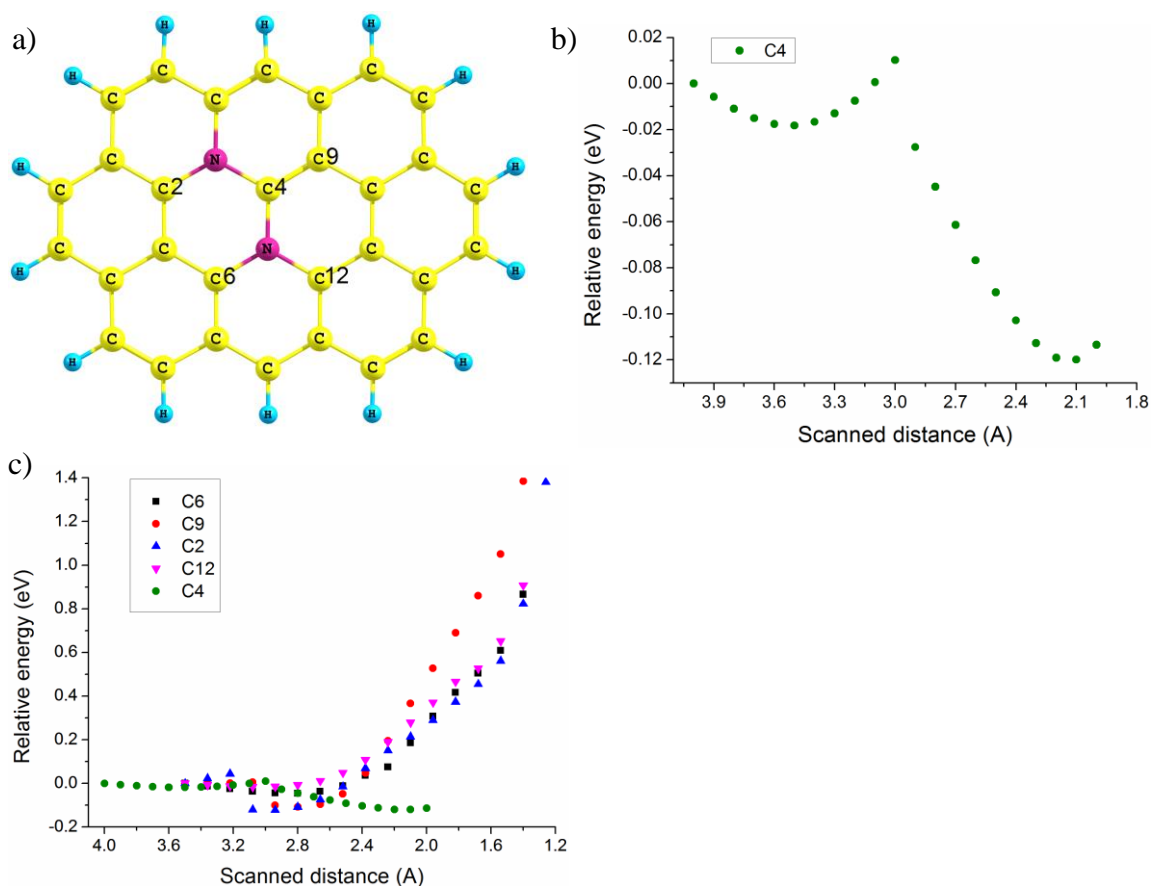
Initially, mono N, P and B doped graphene was studied. The optimised N-G and B-G model systems have a planar structure, and the P-G system has a non-planar structure due to the larger radius of the substituent P atom, inducing geometry defects in graphene. The ground state multiplicity of the three systems is two. As described in the Section 5.3, scan calculations have been performed for the distances between one of the atoms of the oxygen molecule and atoms in the model systems, namely between O and C, P or B atoms.

Figure 5.7 illustrates the structures of the N-G, P-G and B-G systems and the potential energy profiles of the molecular oxygen binding to the marked atoms. The C atoms are designated by their sequential numbers. It is clear that the energy increases gradually, starting from the scanned distance of circa 2.8 Å, and reaches as high as 1.6 to 2.8 eV with a further decrease in the scanned distance. This indicates that the oxygen molecule does not bind to either of the C atoms in the N-G system. Consequently, it is suggested that there are no active sites within N mono doped graphene to initiate the ORR. In addition, the energy increases with decreasing the O...P and O...B distances, and this indicates that the mono substituent P or B atoms do not bind molecular oxygen along with the adjacent C atoms. From these data, it is apparent that mono N, P or B doping of graphene is not sufficient to create active sites for molecular oxygen binding and hence for the ORR.

The effect of binary N doping to graphene has been investigated using the 2N-G model system, as shown in Figure 5.8. In contrast with the other C atoms, the potential energy along the O...C4 distance has two minima and a maximum. The first minimum at the O-C4 distance of 3.5 Å is the reactants complex, which has a lower total energy than that of the isolated reactants. The maximum at 3.0 Å and the second minimum at 2.1 Å are the TS and the product of molecular oxygen binding with the calculated activation and binding energies of 0.03 eV and -0.10 eV, respectively. The negligibly small activation energy and exothermic binding energy indicate that the C atom between the two substituent N atoms in graphene can serve as the site of molecular oxygen binding. The remaining marked C atoms do not bind molecular oxygen, since the energy starts to increase when the scanned distance is circa 2.8 Å and reaches a significant value of 0.9 to 1.4 eV at the scanned distances of 1.2 to 1.4 Å. The minima observed for the C2 and C9 atoms at 3.1 and 2.9 Å correspond to van der Waals coordination of molecular oxygen to the C4 atom. This suggests that the only site of molecular oxygen binding, and thus initiating of the ORR on the binary N doped graphene, is the C atom between the two substituent N atoms.



**Figure 5.7** Geometry-optimized a) N-G, b) P-G and c) B-G systems, and the corresponding potential energy profiles of molecular oxygen binding to the marked atoms (right side).



**Figure 5.8** a) The 2N-G system, and the potential energy profiles of the molecular oxygen binding to b) C4 atom, and c) all other marked atoms.

Molecular oxygen binding has been studied for the 2P-G model system, as illustrated in Figure 5.9. Unlike the 2N-G, the optimised structure of the 2P-G system is non-planar, with the two substituent P atoms protruding above the carbon framework to form pyramidal vertices. The second difference between the 2N-G and 2P-G systems is that the ground state multiplicity of the 2P-G is found to be three ( $M = 3$ ), whereas for the 2N-G it is one ( $M = 1$ ).

The potential energy profiles obtained for the C6, C2, and C12 atoms in the 2P-G show an increase in energies up to 0.5 – 1.2 eV with the scanned interatomic distances decreasing to circa 1.4 Å. The discontinuity in the potential energy for the O...C2 scanned distance can be explained by the spontaneous coordination of the oxygen molecule to the adjacent P1 atom, which decreases the systems energy. Overall, the increase of the energy, accompanying the approach of the oxygen molecule to the C atoms, indicates that the binding is not favourable both kinetically and thermodynamically. The potential energy profile for the C4 atom has a sharp maximum at about 2.2 Å followed by a minimum. The high calculated activation energy for the C4 atom, namely 0.70 eV, indicates that molecular oxygen binding to the C4 atom is unfavourable kinetically. The energy profiles obtained for the P1 and

P2 heteroatoms also have an energy maximum followed by a minimum. In contrast with the C4 atom, the calculated activation barriers for the P1 and P2 atoms are only 0.04 and 0.11 eV, and the binding energies are -0.68 and -0.40 eV, respectively. The different activation and binding energies correspond to the side-on and end-on products, the structures of which are shown in Figure 5.13. The relatively small values of the activation energies and exothermic binding energies indicate that the substituent P atoms in binary P doped graphene are the only sites of molecular oxygen chemisorption and hence the active sites for the ORR.

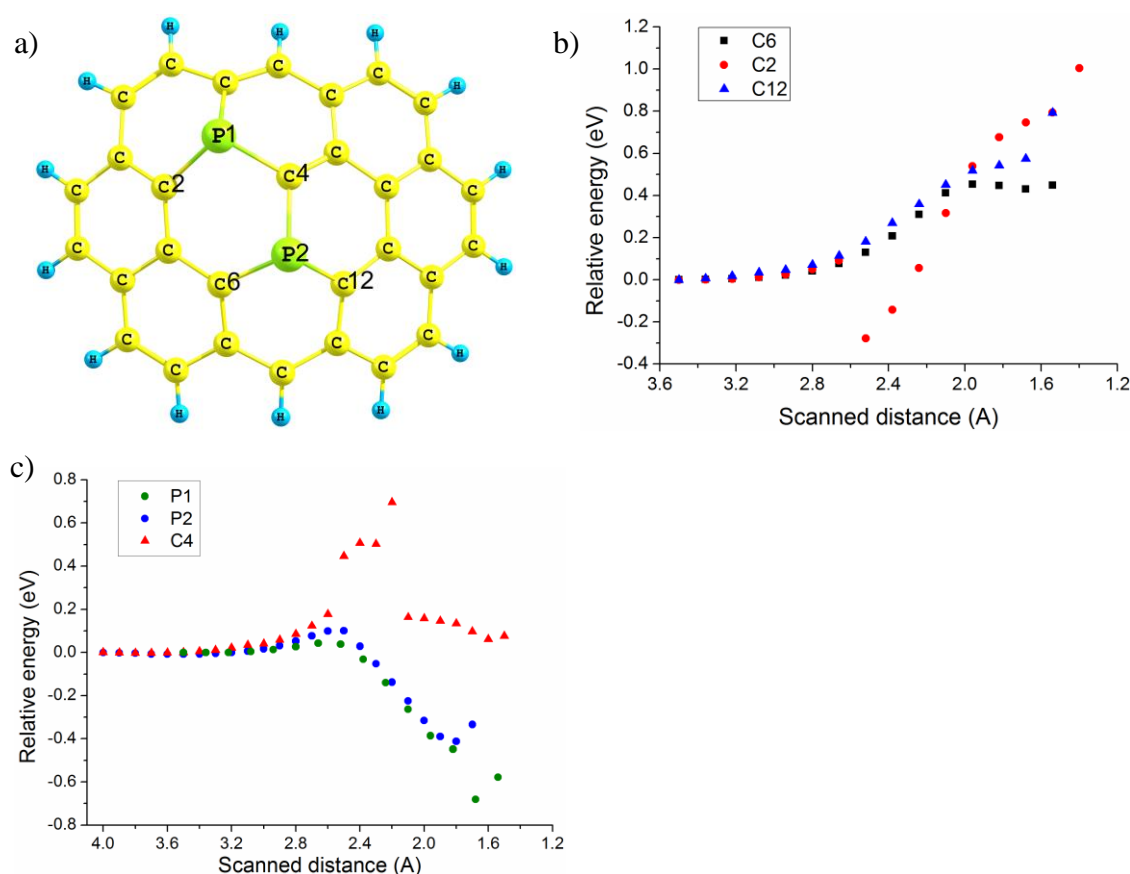


**Figure 5.9** a) The 2P-G system, and the potential energy profiles of molecular oxygen binding to b) the C6, C2, C12, and c) P1, P2 and C4 atoms.

The potential energy profiles of the molecular oxygen binding have been obtained for the NP-G, NB-G and SN-G model systems and are illustrated in Figure 5.10 and Figure 5.11. Using a similar evaluation approach, it has been concluded that molecular oxygen chemisorption on these systems is unfavourable. This suggests that the defects in graphene doped with neighbouring N and P, or N and B, or N and S heteroatoms are not sufficient to provide for molecular oxygen binding and serve as the ORR active sites.

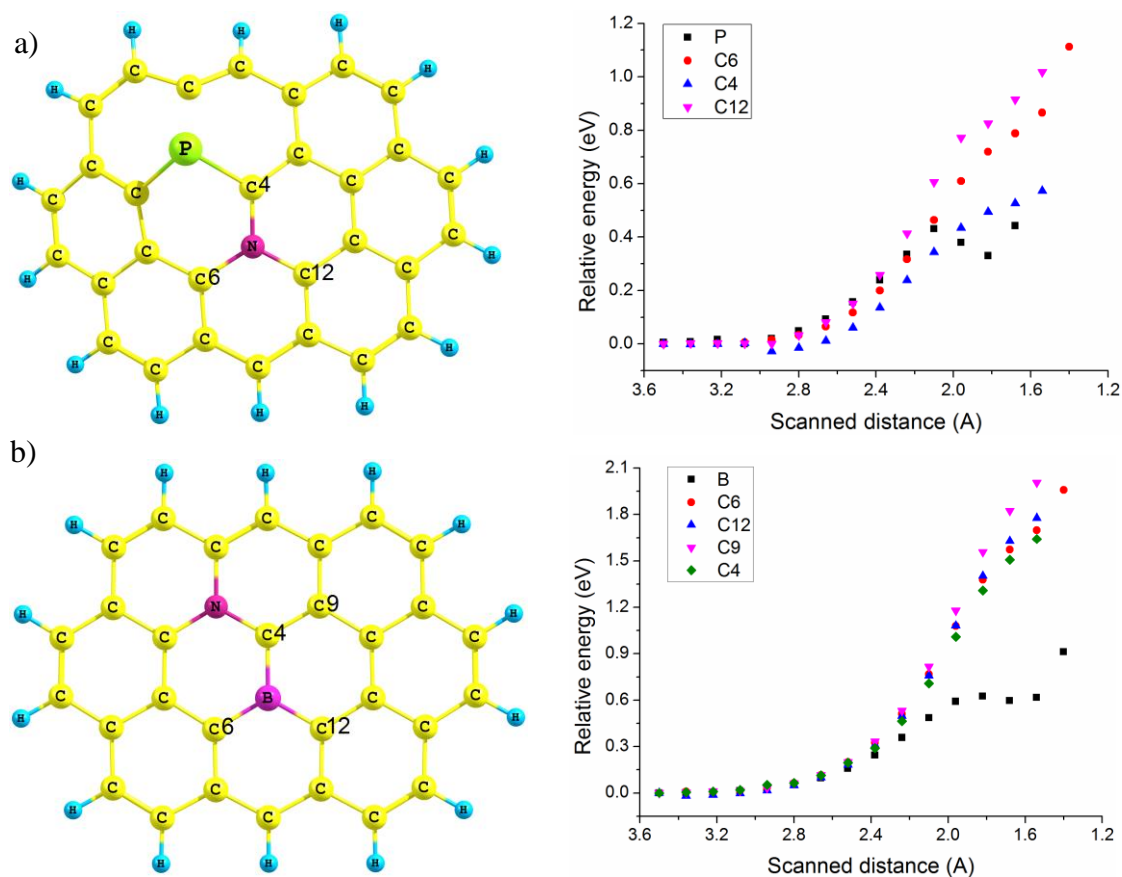


**Figure 5.10** a) NP-G and b) NB-G systems with the corresponding potential energy profiles of molecular oxygen binding to the marked atoms (right side).

Binary S and P doped graphene has been studied using three isomeric model systems, referred to as the SP1-G, SP2-G and SP3-G, as illustrated in Figure 5.12. The ground state multiplicities of the SP2-G and SP3-G have been found to be three ( $M = 3$ ), and that of the SP1-G is one ( $M = 1$ ). It is clear that the oxygen molecule does not bind to either the P or C atoms of the SP1-G system, since the energy increases with decreasing the scanned distance. In the case of the SP2-G, the potential energy profiles for the marked atoms have maxima followed by minima. In the case of the scan between the O and C atoms, the activation barriers are substantial, varying between 1.0 and 1.8 eV, while the minima are endothermic with reference to the starting point. However, the activation barrier of the molecular oxygen chemisorption to the substituent P atom is as low as 0.11 eV. Further, the potential energy profile for the  $O \cdots P$  distance has two minima at 1.8 and 1.6 Å. In the first minimum, the molecular oxygen chemisorbs in an end-on mode with an energy of -0.48 eV, then overcomes a small activation barrier of 0.08 eV and chemisorbs on the P atom in a side-on mode with a -0.59 eV binding energy. The structures of the end-on and side-on products are illustrated in Figure 5.13.

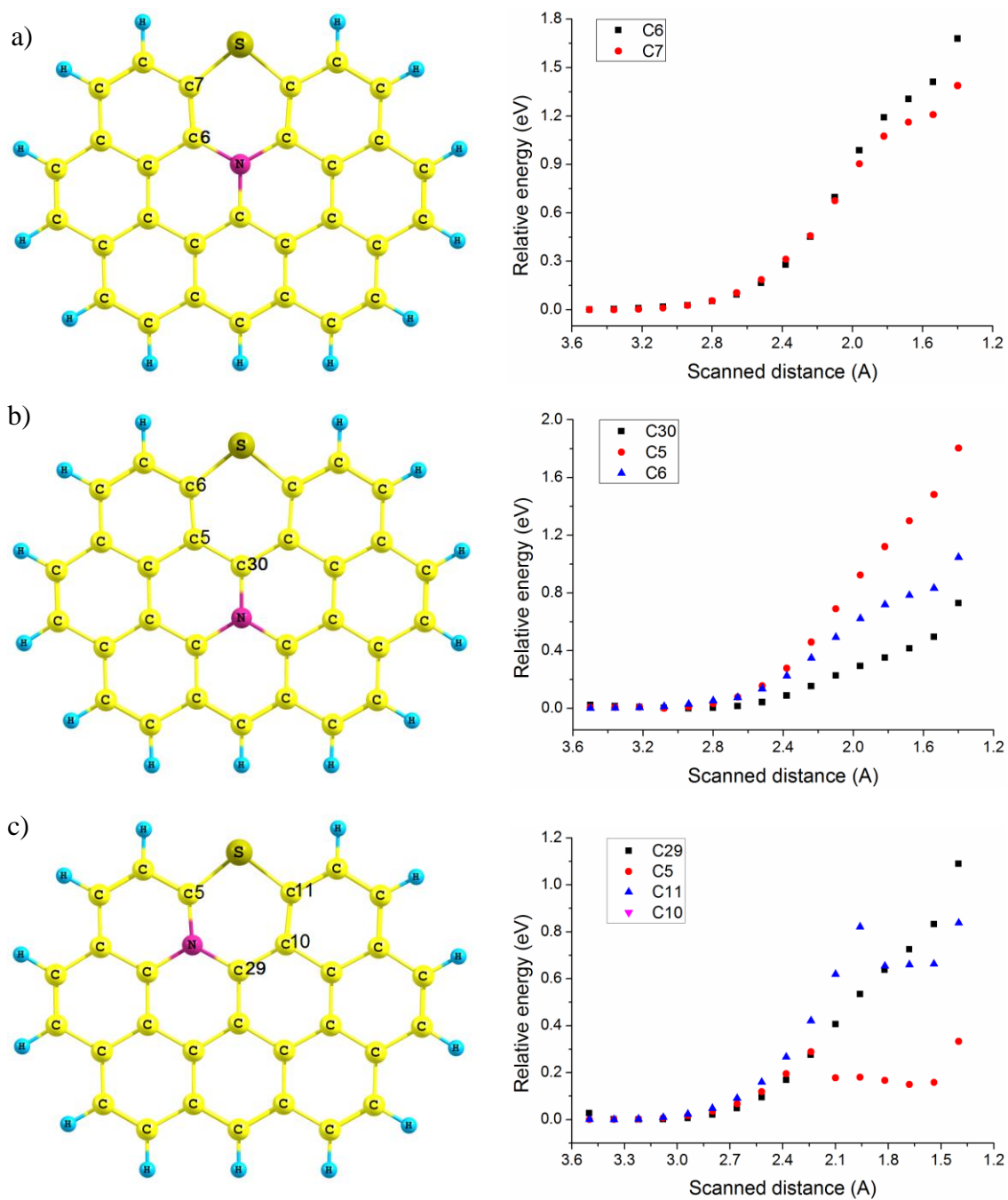


**Figure 5.11** Three isomeric SN-G model systems a), b), and c), and the corresponding potential energy profiles of molecular oxygen binding to the marked atoms (right side).

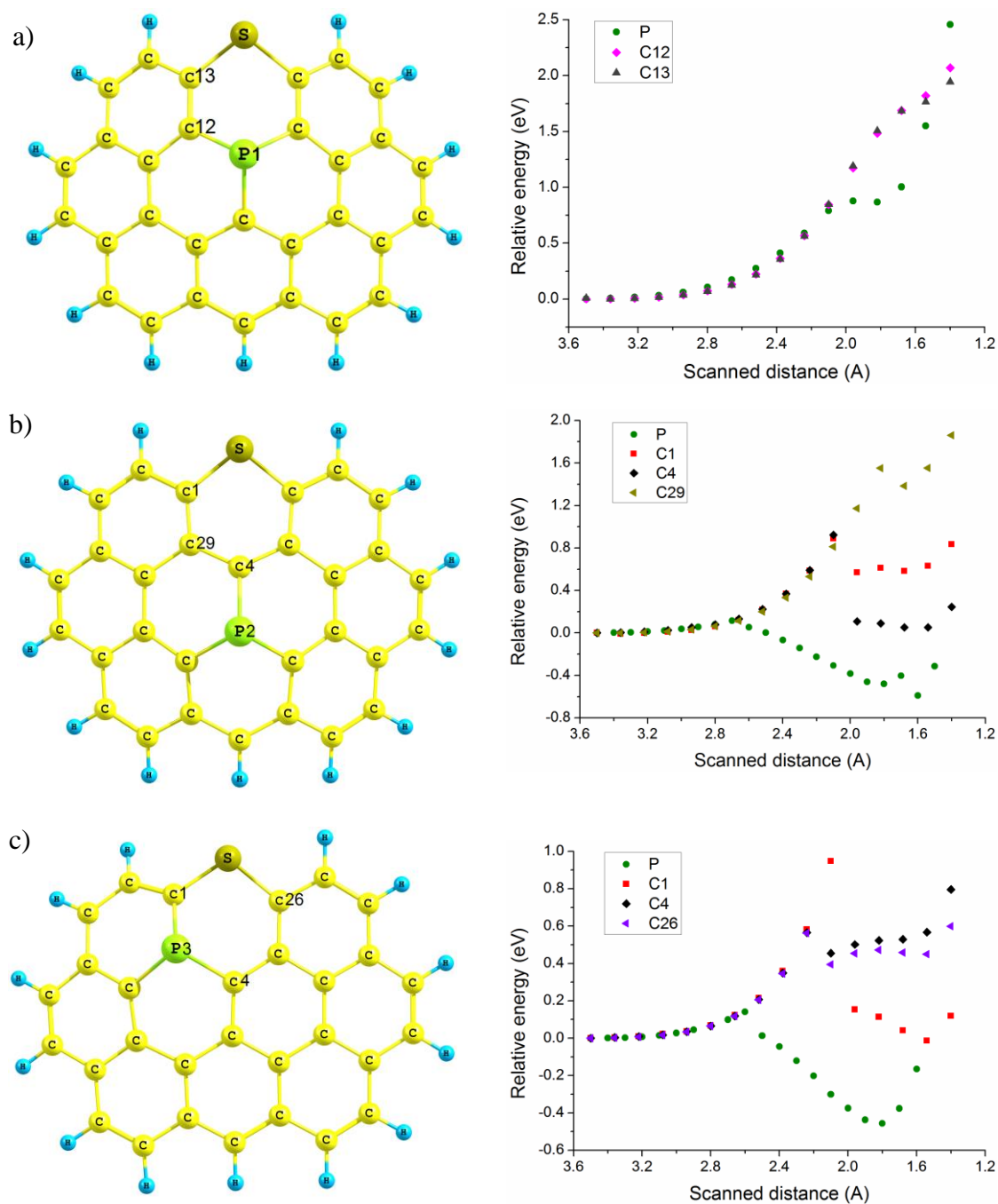


**Figure 5.12** a) SP1-G, b) SP2-G, and c) SP3-G isomeric model systems with the corresponding potential energy profiles of molecular oxygen binding to the marked atoms (right side).

The SP3-G model system shows similarities with the SP2-G. Binding to the C1, C4 and C26 carbon atoms in the SP3-G is unfavourable due to the relatively high activation energies of 0.6 to 1.0 eV. Molecular oxygen binds to the P atom in an end-on mode with the calculated activation barrier and binding energy of 0.14 and -0.46 eV, respectively. The small activation energies and exothermic binding energies for the P atoms suggest that that in S and P doped carbon materials, the substituent P atoms can serve as active sites for molecular oxygen chemisorption.

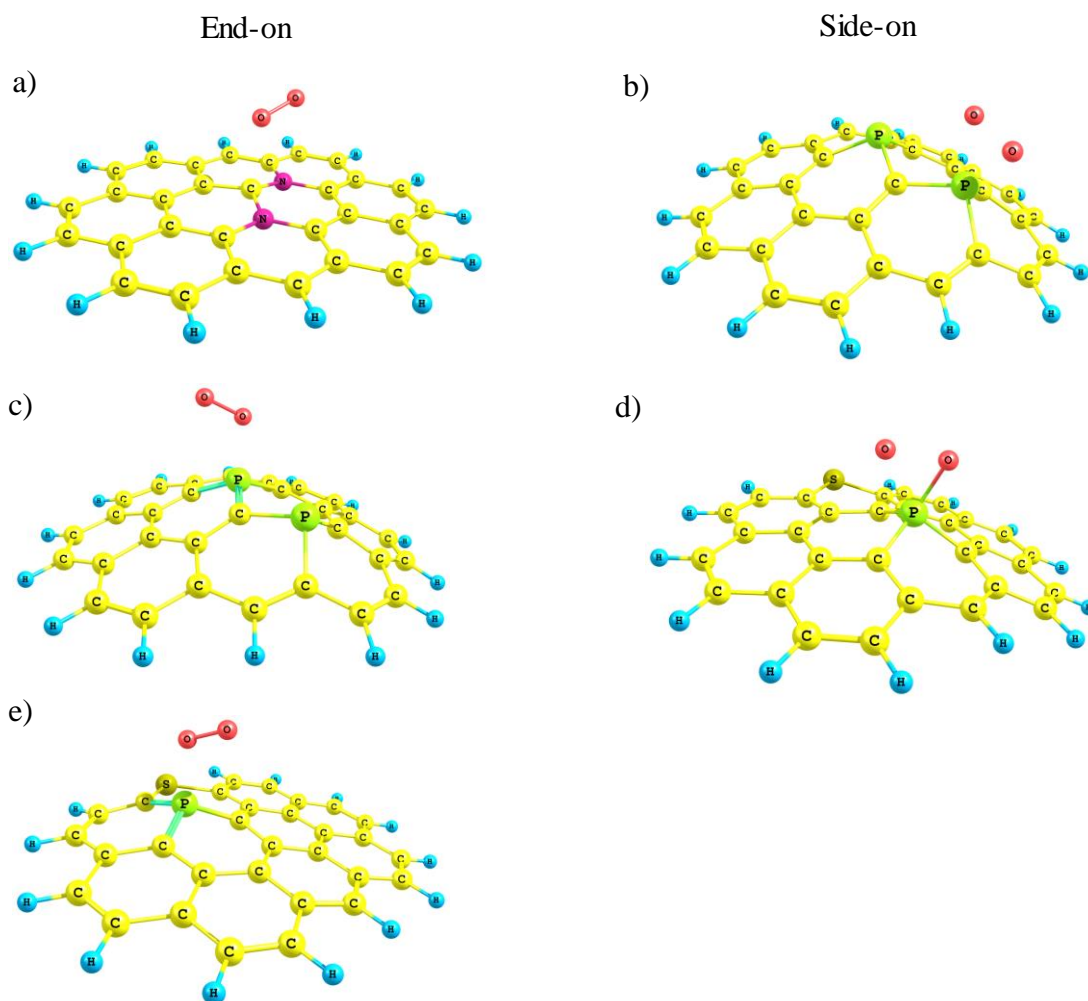


**Figure 5.13** Products of molecular oxygen end-on and side-on binding to the binary heteroatom doped model systems: a) 2N-G, b) and c) 2P-G, d) SP2-G, and e) SP3-G.

Table 5.4 summarizes the energies and corresponding activation barriers of molecular oxygen binding to the 2N-G, 2P-G, SP2-G and SP3-G model systems. The activation barriers are relatively small, and the slightly exothermic binding energies are comparable to those reported in the literature for platinum exothermic binding energies. This suggests that the proposed structures of doped graphene may provide active sites for the ORR in non-precious metal carbon-based catalysts for fuel cell cathodes. However, it can be noticed that in the case of the systems containing P, the absolute values of both activation and binding energies are higher than those of the N containing system, suggesting that molecular oxygen forms stronger bonds with the P atoms than with the C atoms of the N doped graphene.

**Table 5.4** Activation and binding energies of molecular oxygen chemisorption to the binary heteroatom doped model systems.

Doped graphene model system	2N-G	2P-G		SP2-G	SP3-G
Binding mode	End-on	End-on	Side-on	End-on	End-on
Activation energy, eV	0.03	0.11	0.04	0.11	0.14
Binding energy, eV	-0.10	-0.40	-0.68	-0.48	-0.46

### 5.5.2 Atomic Spin Density and Charge Analysis

In the four doped graphene structures, the sites of molecular oxygen binding are: (i) the C atom between the substituent N atoms in the 2N-G, (ii) the P atoms, interspaced by a C atom, in the 2P-G, and (iii) the P atom in the SP2-G and SP3-G model systems. In order to obtain an insight into the reactivity of these sites towards molecular oxygen binding, atomic spin density and charge distribution in the systems has been obtained.

Table 5.5 shows the atomic spin densities and natural charges on the C and N atoms of the N-G and 2N-G systems, the ground state multiplicities, which are two and one, respectively. The properties of the C4 atom are of major interest. At the ground state multiplicity, the spin densities of the C4 atom in both N-G and 2N-G are close or equal to zero. In addition, the spin densities of all other atoms in the 2N-G system are zero, since it has no unpaired electrons. In the higher multiplicity state, the spin density of C4 is lower in the 2N-G than in the N-G. The same is valid for the spin densities of the N atoms in both high and low spin states. This indicates that more of the spin density of the N atoms is distributed to the surrounding atoms. Conversely, the C4 atom's natural charge is higher in the 2N-G system than in the N-G in both low and high multiplicity states. Thus, in the 2N-G system, the C4 atom has lower spin density and at the same time higher natural charge than in the N-G system in the excited state.

Table 5.6 shows the atomic spin densities and natural charges obtained for the P-G and 2P-G systems, the ground state multiplicities of which are two and three, respectively. The calculated spin density of the P atoms is noticeably lower in the 2P-G system than in P-G, both in the low and high multiplicity states. However, the natural charges on the P atoms are similar, besides the relatively higher charge on the P1 atom in the 2P-G system.

Table 5.7 shows the calculated spin densities and natural charges on atoms of the three SP-G systems. The ground state spin multiplicity of the SP1-G is one, and of the other two systems is three. The spin density of the P atom is lower in the SP2-G and SP3-G than in the SP1-G at the higher multiplicity, and is approximately zero at the lower multiplicity. However, the spin density of the S atoms has an opposite trend. The natural charges of P atoms in SP2-G and SP3-G are noticeably higher than in

SP1-G in the singlet state, but similar in the triplet state. Thus, the insignificant deviation of the natural charge at ground state multiplicity is found in both P and S doped systems.

**Table 5.5** Spin densities and natural charges of the C4 and N atoms in the N-G and 2N-G systems in the two spin multiplicity states.

Atom	Spin density	Natural charge	Spin density	Natural charge	
		<u>N-G (doublet)</u>		<u>2N-G (singlet)</u>	
C4	-0.039	0.233	0.000	0.460	
N1	0.106	-0.326	0.000	-0.318	
N2			0.000	-0.374	
		N-G (quartet)		2N-G (triplet)	
C4	0.361	0.172	0.259	0.383	
N1	0.225	-0.348	0.142	-0.358	
N2			0.157	-0.360	

**Table 5.6** Spin densities and natural charges of the P atoms in the P-G and 2P-G systems in the two spin multiplicity states.

Atom	Spin density	Natural charge	Spin density	Natural charge	
		<u>P-G (doublet)</u>		<u>2P-G (singlet)</u>	
P1	0.100	1.055	0.000	1.419	
P2			0.000	0.943	
		P-G (quartet)		2P-G (triplet)	
P1	0.159	1.090	0.095	1.040	
P2			0.101	1.022	

**Table 5.7** Spin densities and natural charges of the P and S atoms in the three SP-G systems in the two spin multiplicity states.

Atom	Spin density	Natural charge	Spin density	Natural charge	Spin density	Natural charge	
		<u>SP1-G (singlet)</u>		<u>SP2-G (singlet)</u>		<u>SP3-G (singlet)</u>	
P	0.000	1.004	0.028	1.428	0.000	1.562	
S	0.000	0.319	-0.028	0.328	0.000	0.324	
		<u>SP1-G (triplet)</u>		<u>SP2-G (triplet)</u>		<u>SP3-G (triplet)</u>	
P	0.157	1.090	0.124	1.063	0.127	1.053	
S	0.011	0.326	0.097	0.397	0.080	0.407	

Overall, the natural charges on the potential chemisorption site are higher in the 2N-G than in the N-G system, but do not show any trend in the P and S doped graphene systems. However, spin densities of the atoms of interest are lower in the active systems than in the systems that do not bind molecular oxygen. The obtained results are in disagreement with results reported by Zhang and Xia [72], who found that in mono nitrogen doped graphene, the carbon atoms possessing highest spin density are the active sites for the ORR. Therefore, further calculations using more accurate methods should be performed to investigate the spin density and charge distribution on catalyst model systems.

To further investigate this, atomic spin densities have been examined for reactant and product structures in the potential energy profiles of molecular oxygen binding of the doped graphene systems, as illustrated in Figure 5.14. In the column of reactants, it can be observed that the oxygen molecule is at significant distances from the investigated chemisorption centres (3.5 – 4.0 Å) and the spin densities of both oxygen atoms are close to unity. At the same time, the spin densities on the atoms serving as the chemisorption centres are significantly lower than those in the bare systems. This is due to the fact that in all calculations, the total spin density is equal to a system's number of unpaired electrons and is redistributed between atoms differently for different systems with equal multiplicities, i.e. numbers of unpaired electrons. Therefore, the results of spin density distribution are not absolute and can be used only for qualitative description of the systems.

In the products illustrated in Figure 5.14, it is clear that the spin density of both the O atoms of the oxygen molecule decreases significantly, in particular that of the O atoms nearest to the chemisorption sites. This indicates that the spin density of the oxygen molecule decreases when it binds to an active site. Consequently, a lower spin density of an active site facilitates the transfer of spin density from molecular oxygen to a catalyst surface. In addition, it should be noted that the spin density of the chemisorption centre in most of the cases decreases slightly and increases also insignificantly in the SP2-G system. Thus, the spin density decreases on the chemisorbed oxygen molecule and increases on the surface of the model systems. The lower spin density of chemisorption sites may facilitate the transfer of spin density from molecular oxygen to the catalyst surface.

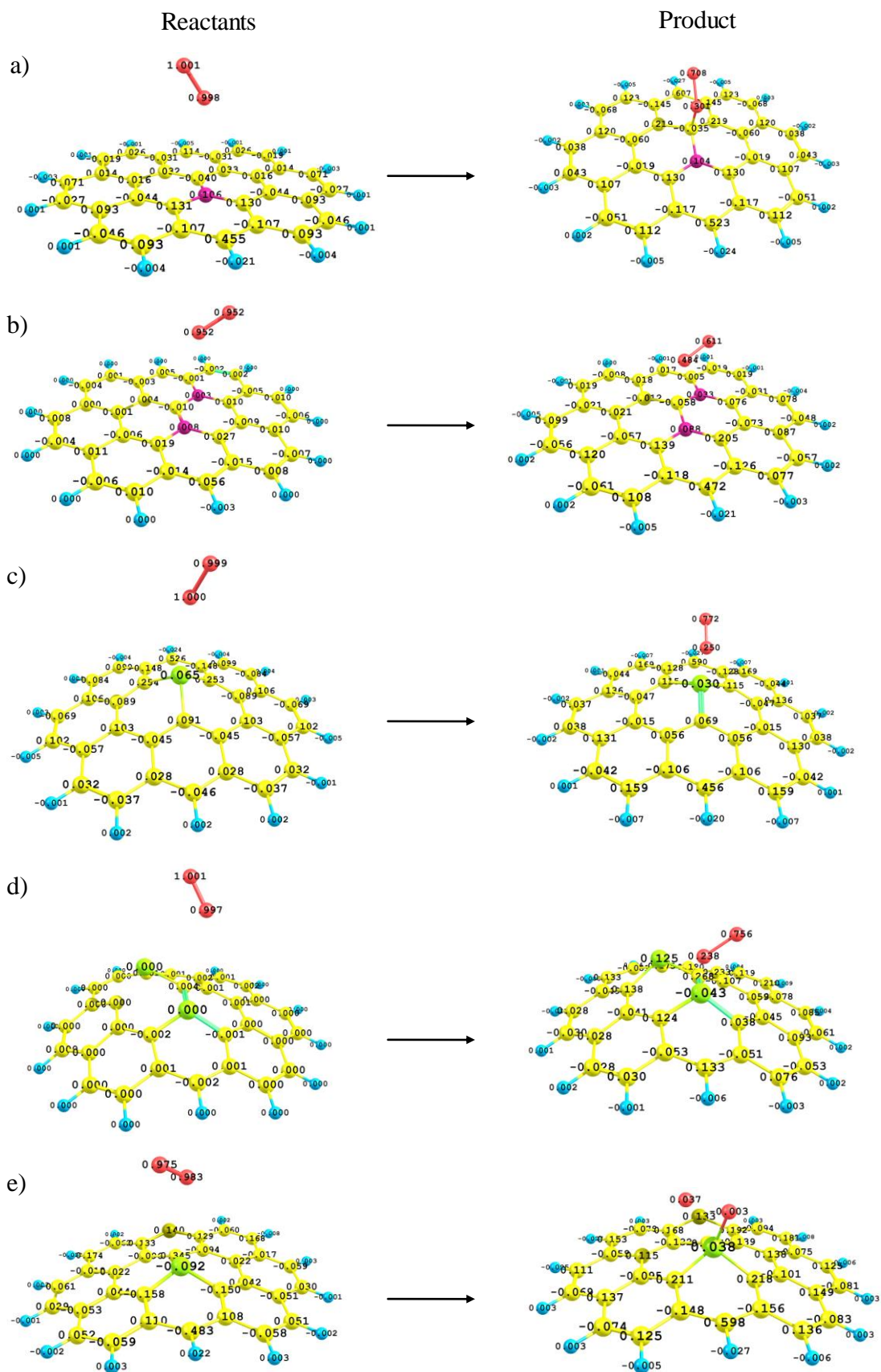


**Figure 5.14** Atomic spin densities of the starting and end structures of potential energy profiles of molecular oxygen binding to a) N-G, b) 2N-G, c) P-G, d) 2P-G, and e) SP-G model systems.

## 5.6 Conclusion

In order to predict the catalytic activity of non-metal heteroatom doped graphene towards the oxygen reduction, molecular oxygen chemisorption has been studied on graphene model systems doped with nitrogen, phosphorus, boron and sulphur by means of DFT simulations. Further, the effect of mono and binary doping of graphene has been investigated. Atomic spin density and charge analysis has been performed in order to explain the origin of reactivity towards molecular oxygen binding.

The obtained potential energy profiles show that mono nitrogen, phosphorus or boron doped graphene sheets do not provide active sites for molecular oxygen binding. Similarly, graphene co-doped with nitrogen and either phosphorus, or boron or sulphur is also inactive towards molecular oxygen chemisorption.

Binary nitrogen doped graphene sheet provides one site for molecular oxygen binding, and this is a carbon atom between two substituent nitrogen atoms. In binary phosphorus and phosphorus plus sulphur doped graphene sheets, the substituent phosphorus atoms are potential molecular oxygen chemisorption sites.

The calculated binding energies and the corresponding activation barriers of molecular oxygen chemisorption on these doped graphene systems vary from -0.10 to -0.70 eV, and 0.03 to 0.14 eV, respectively. This is comparable to the values reported for platinum in the literature.

The spin density on atoms participating in the molecular oxygen chemisorption is proposed to be a determining factor in the catalytic activity. It has been found that the chemisorption sites have a lower spin density than inactive sites and therefore may facilitate spin density transfer from molecular oxygen to the catalyst surface.

## **Chapter 6**

### **Experimental Methods of Catalyst Synthesis and Characterisation**

#### **6.1 Introduction**

This chapter introduces the most common techniques employed in the characterisation of cathode catalysts for PEM fuel cells. These fall broadly into two types of analysis techniques, namely electrochemical characterisation of the catalytic performance in the ORR and physicochemical methods characterising the chemical state, surface composition and morphology of the compound.

Electrochemical characterisation has become a standardised technique for catalysts characterisation as it provides an objective evaluation of its catalytic activity in the ORR. Therefore, this chapter describes the theoretical background and employment of the most common electrochemical techniques, namely, cyclic voltammetry and linear sweep voltammetry using a rotating ring-disk electrode (RRDE). In addition, the most common physicochemical methods are discussed, which have been used to further characterize the catalysts in this thesis.

The final step in characterising a catalyst is its test in a small scale PEM fuel cell, enabling the evaluation of catalyst performance and durability under fuel cell operating conditions. Thus, this chapter describes the most common fuel cell performance evaluations and the experimental setup employed in this thesis.

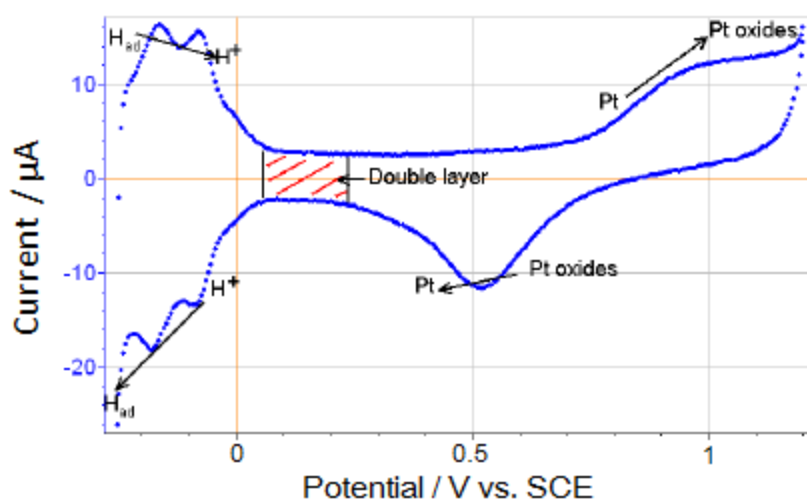
#### **6.2 Electrochemical Characterisation Using a Rotating Ring Disk Electrode**

##### **6.2.1 Cyclic Voltammetry**

Cyclic voltammetry (CV) is a good technique for obtaining qualitative information on catalytic activity towards an electrochemical reaction and is a first step of electrochemical characterisation of catalytic activity towards the ORR. It can help evaluate either the relative activities of a series of catalysts towards the same reaction, or the activity of one catalyst towards a few different reactions. The CV method using a rotating disk electrode (RDE) consists of cycling the potential between chosen low and high points and recording the current in the potential cycling region. The range of potential sweeping is often chosen to comprise the thermodynamic potential of the reaction of interest. The resulting potential versus current plot is called a

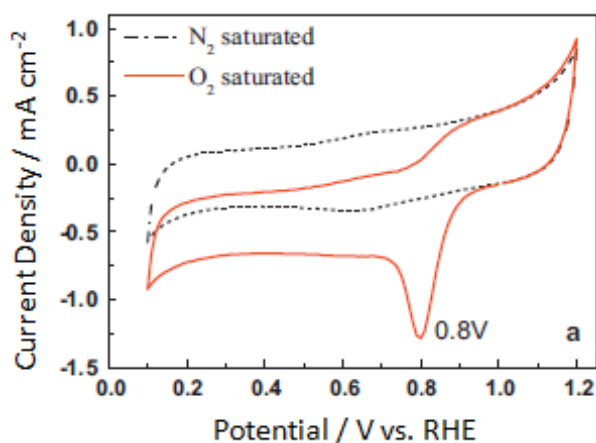
voltammogram. The activity of a catalyst can be measured by both the peak potential and the peak current [2].

Figure 6.1 illustrates a typical cyclic voltammogram of the ORR on a commercial platinum catalyst, where the potential is cycled between -0.3 and 1.2 V. The direction of increasing potential corresponds to oxidation, and the direction of decreasing potential to reduction. During the oxidation, hydrogen atoms, adsorbed on the platinum catalyst surface, desorb and transit to the electrolyte solution as protons. Further increase in the potential causes the formation of platinum oxides. When the potential is reversed and starts to decrease, the oxidized platinum is reduced, and this is evidenced by the clear reduction peak. With a further potential decrease, protons from the electrolyte solution adsorb and become reduced on the surface of the platinum electrode [231]. The reduction peak of platinum catalyst corresponds to the ORR. The activity towards the ORR of any cathode catalyst can be gauged by the potential and current of the reduction peak. A high peak potential and high absolute peak current indicate high catalytic activity.



**Figure 6.1** Cyclic voltammogram of a platinum catalyst in an acid electrolyte [232].

Figure 6.2 illustrates CVs for a nitrogen doped carbon catalyst [233], obtained in nitrogen and an air saturated acid electrolyte solution. CVs in nitrogen or another inert gas are used to identify changes in oxidation state in an inert environment and also to clean the catalyst surface electrochemically. CVs in air or oxygen indicate the ORR activity of a catalyst by the position and current of the reduction peak. The closer the peak potential to the thermodynamic limit of 1.23 V and the more pronounced the peak, the more active is the catalyst.



**Figure 6.2** Cyclic voltammogram of a nitrogen doped carbon catalyst in acid electrolyte [233].

### 6.2.2 Linear Sweep Voltammetry

In linear sweep voltammetry (LSV), the cell potential is swept only in one direction, so is equivalent to half of a cyclic voltammogram. LSV is performed at a relatively slow sweep rate to provide for the emergence of the diffusion limiting current which is current proportional to the concentration of the reactants at the electrode surface and independent on the potential [231].

The rotating ring disk electrode (RRDE) technique is a variation of the RDE method and is implemented when a concentric ring electrode outside the circular disk electrode is operated. A linear sweep voltammogram obtained using the RRDE contains currents measured both at the disk and ring electrodes. The disk current accounts for the reaction of interest, and ring current reflects the process of oxidation of hydrogen peroxide formed on the disk. The catalytic activity towards the ORR in LSV is determined by the onset potential and the diffusion limiting current. The onset potential is the potential at which the ORR initiates and can be defined as the potential at which the current is larger than a certain small value, e.g. 1  $\mu\text{A}$ . High onset potential and diffusion limiting current indicate high activity towards the ORR [133].

Figure 6.3 illustrates LSVs of the ORR for a few non-precious metal catalysts [126], measured on the disk and ring of the RRDE. The potential of the disk electrode is normally swept from circa 1.2 to 0.1 V and the ring potential is kept constant at a high potential from 1.2 to 1.4 V, at which hydrogen peroxide can be oxidized. The most active catalyst demonstrates the highest onset potential and diffusion limiting current on the disk LSV, and the lowest ring current on the ring LSV. The ring current is directly related to the amount of hydrogen peroxide formed on the catalyst. Further, the formation of hydrogen peroxide should be avoided, since it reduces the energy efficiency of a fuel cell and damages both its membrane and catalyst [133].

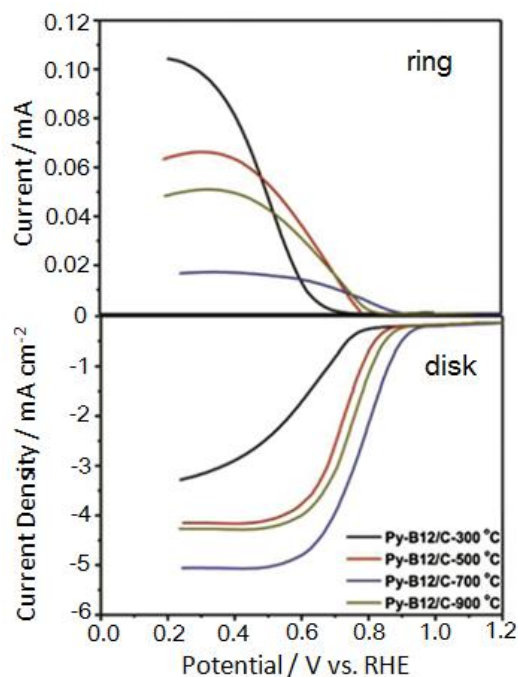


**Figure 6.3** LSVs of an alternative carbon based catalysts measured using RRDE [126].

### 6.2.3 RRDE Principle

The RRDE three-electrode cell setup, in which the catalyst is placed in an oxygen-saturated electrolyte, acts as a model of a fuel cell environment. The electrolyte (usually diluted solutions of perchloric or sulphuric acid) provides protons for the catalytic reaction similar to a Nafion<sup>®</sup> membrane transporting incoming protons from the anode to the cathode in an actual PEM fuel cell [2].

The three electrodes used in the RRDE cell are referred to as the working, reference and counter electrodes. A catalyst or electrode under investigation is used as the working electrode. The electrical potential of the working electrode is controlled by a potentiostat with respect to the reference electrode. The potentiostat simultaneously measures the current flowing between the working electrode and the counter electrode which serves as a source or sink of electrons [231]. The reference electrode has a well-known standard potential, with the potential of the standard hydrogen electrode (SHE) conventionally taken as zero. There are a number of other standard electrodes, the most common of which are the saturated calomel (SCE) and saturated silver chloride (Ag/AgCl) electrodes. For instance, the electrode potential of the saturated calomel electrode is 0.241 V versus the SHE at 25 °C. When experimental measurements of potential are made against these alternative reference electrodes, the potentials are shifted relative to the SHE. In this thesis, all

electrochemical measurements have been performed using the standard hydrogen electrode.

The oxygen reduction reaction occurs on the interface of the solution and the working electrode, which is the rotating ring-disk electrode (RRDE), and is illustrated in Figure 6.4. In the cylindrical RRDE, the disk electrode is insulated from the ring electrode. Both disk and ring electrodes are independently controlled by separate potentiostats via common reference and counter electrodes, and a catalyst is applied on the surface of the disk electrode.

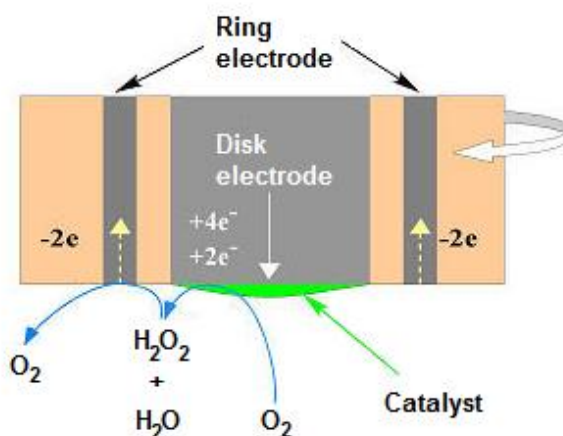


**Figure 6.4** Oxygen reduction reaction on the rotating ring disk electrode [234].

When the working electrode is rotated, convection occurs near the electrode surface. Oxygen within the solution diffuses to the surface of the negatively charged disk electrode and reacts to form water or hydrogen peroxide, depending on the catalytic activity and the ORR pathway on a specific catalyst. The product of a two-electron ORR, hydrogen peroxide, is transported to the ring electrode by the centrifugal force and is oxidized to molecular oxygen on the positively charged ring electrode, producing the ring current [234].

### 6.2.4 Analysis of Catalytic Activity towards the ORR using RRDE Data

The RRDE is widely used to determine the activity of catalysts towards the ORR. By rotating the electrode at different rates, the mass transfer effects of oxygen diffusion through the electrolyte solution can be accounted for, and the kinetic current, i.e. the measure of catalytic performance can be calculated at specific potentials. In addition, if the surface area of the cathode is known, the number of electrons transferred per mole of the reacting oxygen can be calculated, providing a measure of the catalyst selectivity. For complete reduction to water, the number of electrons is four [61].

In the entire range of potential sweeping, the overall current density  $j$  is related to the kinetic current density  $j_k$  and diffusion controlled, or limited, current density  $j_d$  according to the Koutecky-Levich equation [2]:

$$\frac{1}{j} = \frac{1}{j_k} + \frac{1}{j_d} \quad (6.1)$$

The kinetic current density and diffusion controlled current density are expressed as follows:

$$j_k = nFk_fC \quad (6.2)$$

$$j_d = 0.62 nFAD^{2/3} \omega^{1/2} \nu^{-1/6} C \quad (6.3)$$

where  $n$  is the number of electrons per reactant molecule,  $F$  is the Faraday constant,  $A$  is the surface area,  $k_f$  is the rate constant,  $C$  is the concentration of the reacting species,  $D$  is the diffusion coefficient,  $\omega$  is the angular velocity of the electrode,  $\nu = \eta/d$  is the kinetic viscosity, where  $\eta$  and  $d$  are the viscosity and density of the electrolyte solution, respectively.

Using linear sweep voltammograms measured with a rotating disk electrode, a plot of  $j^{-1}$  versus  $\omega^{-1}$  can be obtained, which is normally a straight line and called the Koutecky-Levich plot. The slope of the line is inversely proportional to the number of transferred electrons  $n$ , and the intercept is inversely proportional to the reaction rate constant  $k_f$ . When the experimental Koutecky-Levich plots are linear, values of  $n$ ,  $D$  and  $k_f$  can be determined from the line slope and intercept with the X axis [2].

In the RRDE technique, the presence of the ring electrode allows a measurement to be made of the extent of hydrogen peroxide, which forms during the two-electron ORR mechanism [2]:



The number of electrons  $n$ , transferred during the ORR, and the amount of hydrogen peroxide formed from one  $\text{O}_2$  molecule,  $X_{\text{H}_2\text{O}_2}$ , can be calculated as follows:

$$n = 4 \frac{j_D}{j_D + j_R/N} \quad (6.5)$$

$$X_{\text{H}_2\text{O}_2} = \frac{2j_R/N}{j_D + j_R/N} \quad (6.6)$$

where  $j_D$  and  $j_R$  are the disk and ring currents, respectively, and  $N = -j_R/j_D$  is the collection efficiency [2].

The potential and current during an electrochemical reaction are linked by a dependence named after Tafel. The potential drop occurring on the electrode is known as the overpotential (over-voltage) and reflects the fact that some energy is needed to generate a reaction product. The dependence is expressed as follows [235]:

$$\Delta E_{OV} = \frac{2.3RT}{\alpha nF} \ln \frac{j}{j_0} \quad (6.7)$$

where  $\Delta E_{OV}$  is the overpotential,  $R$  is the universal gas constant,  $T$  is the temperature,  $\alpha$  is the symmetry coefficient (usually circa 0.5),  $n$  is the number of exchanged electrons,  $F$  is the Faraday constant  $j$  is the measured current,  $j_0$  is the exchange current which is dependent on the materials involved, temperature and material active area.

The exchange current can be explained as the rate at which an electrode reaction proceeds at equilibrium when the net current  $j$  is zero [2, 235]. Both the exchange current and the overpotential are directly linked to the reaction kinetics. The value of the exchange current depends on the inherent speed of the electrode reaction. A slow reaction, i.e. with a small exchange current, will require a larger overpotential for a given current density than a fast reaction (with a large exchange current). Therefore, a large overpotential of the ORR on a given catalyst is undesirable and implies a low reaction rate. The dependence of the overpotential on the logarithm of current is linear and known as the Tafel plot. The slope of this line is called the Tafel slope, and a high Tafel slope indicates slow reaction kinetics [2].

### 6.3 Physicochemical Characterisation

There are several methods of physicochemical characterisation of catalysts for the ORR reported in the literature. These include X-ray diffraction (XRD) [20], X-ray photoelectron spectroscopy (XPS) [127], scanning electron microscopy (SEM) [24] transmission electron microscopy (TEM) [171], Raman spectroscopy [175], Mossbauer spectroscopy [213], etc. In this thesis, catalyst materials have been characterized by the XRD, XPS and SEM methods, and the principles of which are briefly described hereafter.

### 6.3.1 X-Ray Diffraction

X-ray diffraction (XRD) reveals the chemical composition and crystallographic structure of materials. The principle of the method is as follows: X-rays interact with electrons in matter and are scattered in various directions. Crystalline materials have a particular ordered arrangement of atoms (crystal structure) which diffracts the X-rays in a unique pattern. The wavelength of the X-rays is selected to be comparable to interatomic distances in crystals, so that interference between the reflected X-rays can occur [2].

The interference of the X-rays reflected from the crystalline material occurs according to the Bragg's law:

$$n\lambda = 2d \sin\theta \quad (6.8)$$

where  $\lambda$  is the wavelength of the X-rays,  $d$  is the spacing between layers of atoms,  $\theta$  is a half-value of the diffraction angle,  $n=1,2,3,\dots$  is the order of the reflection [2].

The XRD patterns with certain peak spacing and intensities are obtained for materials by scanning them in a range of the diffraction angle, as Figure 6.5 illustrates for a Fe/N/C catalyst [20]. The peaks are assigned to different planes of crystalline substances present on the material: the broad peaks correspond to amorphous carbon, and the smaller sharp peaks correspond to various crystalline compounds of iron.

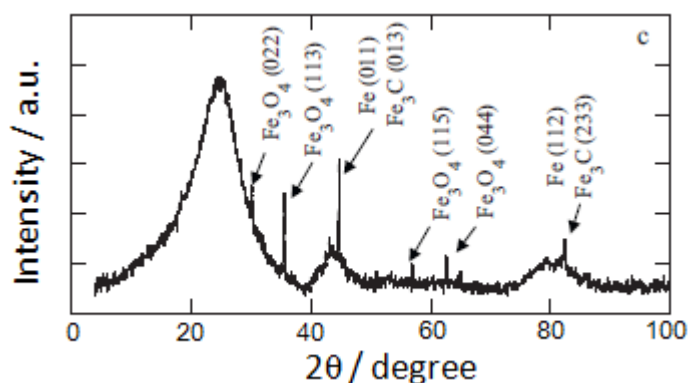


**Figure 6.5** The XRD spectrum of a Fe/N/C catalyst [20].

In this thesis, XRD measurements were performed with an automated Bruker D8 powder diffractometer, using Cu radiation ( $K_{\alpha 1} = 1.5406 \text{ \AA}$ ). The data were collected over a range in the  $2\theta$  range of  $10$  to  $70^\circ$  with an increment step size of  $0.05^\circ$  and at a speed of  $0.1 \text{ sec/step}$ .

### 6.3.2 X-Ray Photoelectron Spectroscopy

X-ray photoelectron spectroscopy (XPS) is a tool of surface analysis that allows the determination of the elemental composition on the surface, chemical state of elements and valence band structure. XPS is based on irradiating a material with monochromatic X-rays, named also photons. An X-ray photon absorbed by an atom of the analysed material leads to emission of an electron from the core (inner) shell of the atom. The number of the emitted electrons, named photoelectrons, is measured as a function of their kinetic energy. The correlation between the photon energy and photoelectron kinetic energy is described by the Einstein relation [2]:

$$h\nu = E_K + E_B + \varphi \quad (6.9)$$

where  $h\nu$  is a photon energy,  $E_K$  is the kinetic energy of a photoelectron,  $E_B$  is the binding energy of the electron, i.e. the difference in energy between the ionized and neutral atom, and  $\varphi$  is the work function of the solid material.

In the XPS method, the number of electrons emitted from the material is counted over the range of their kinetic energies. The photon energy and work function are always known, and the kinetic energy is measured, thus XPS spectra are plotted against the binding energy. The lines in the spectra designate electron transitions from the core levels of different atoms, i.e. from the 1s, 2p, 3d, etc. levels. Figure 6.6 illustrates the XPS spectra obtained for an alternative carbon based catalyst [236], including the whole survey over the wide range of binding energies and high resolution spectrum of the N 1s region.

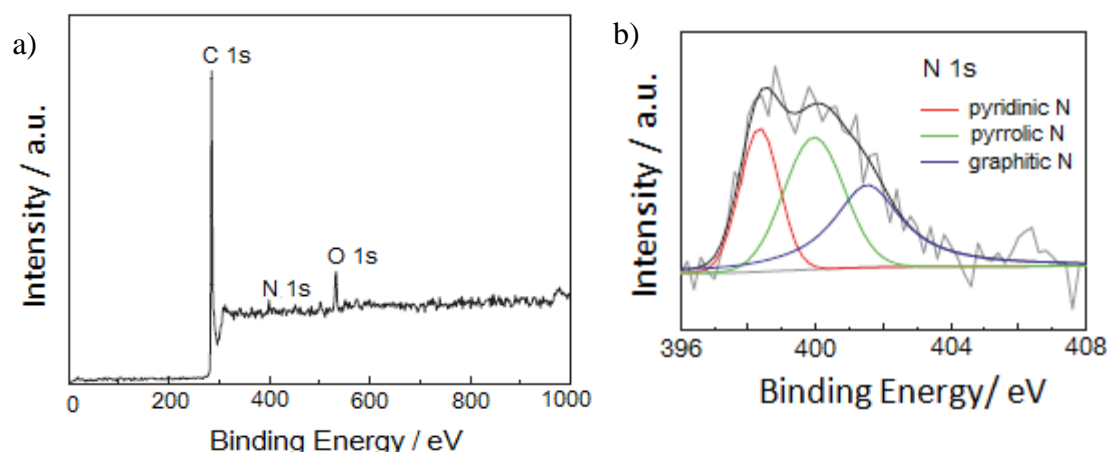


**Figure 6.6** The XPS spectra of the non-precious FeCo/N/C catalyst: a) survey and b) high resolution of N 1s region [236].

Binding energies of electrons in atoms depend on the chemical state of the atoms, i.e. the oxidation state and the chemical and physical environment. Changes in

the chemical state induce small shifts in peak positions in spectra, named chemical shifts. Atoms in a higher oxidation state exhibit a higher binding energy due to the additional Coulombic interaction between the photoelectron and the ion core [237]. Therefore, the XPS method allows the determination of the oxidation states and the chemical environments of elements in a material. However, observation of the peaks of atoms with slightly different chemical shifts is limited by the resolution, which depends on certain experimental factors. For example, Figure 6.6 b) illustrates the overlapping peaks of N atoms present in three different chemical states.

XPS allows a quantitative analysis of a material's elemental composition using the peak intensities and positions. The peak positions show the elemental and chemical composition of a material, and the peak intensities are proportional to the amount of elements on the surface, since the number of detected photoelectrons is proportional to the number of atoms in a given chemical state. The XPS spectra may contain elements with interfering and overlapping peaks, as well as in the case of different chemical states of one element. Fitting the convoluted peaks to the observed signal is complex, and peak models are constructed using a set of Gaussian or Lorentzian shapes [90].

All XPS measurements for the present thesis were performed using a VG Escalab 250 X-ray photoelectron spectrometer with a monochromated aluminium  $K_{\alpha}$  X-ray source. The spot size was 500  $\mu\text{m}$  with a power of 150 W. Detailed spectra of individual peaks were taken at an energy of 20 eV with a step size of 0.1 eV. Binding energy was calibrated by setting the carbon 1s peak to 285 eV. Detailed spectra had a Shirley or linear background fitted to them, and peaks were fitted using mixed Gaussian-Lorentzian fits (using CASAXPS software).

### **6.3.3 Scanning Electron Microscopy and Energy Dispersive Spectroscopy**

Scanning electron microscopy (SEM) is widely used for investigating surface morphology of catalyst materials and obtaining high magnification images of catalyst surfaces [24, 29, 67, 175, 219]. SEM can be used in conjunction with the closely-related technique of energy dispersive spectroscopy (EDS), and this allows the determination of the elemental composition of the investigated materials [164, 179].

The principle of scanning electron microscope is the irradiation of a material with a focused beam of electrons, accelerated by a high voltage of a few kV. The beam of electrons scans the material surface and interacts with its nuclei and electrons. These interactions induce several types of signals, including backscattered electrons, secondary electrons, X-rays, Auger electrons, cathodoluminescence, etc. In SEM, the signals of secondary and backscattered electrons are registered by a detector and processed to produce an image.

Images generated in SEM by backscattered electrons show compositional contrasts, which result from different atomic numbers of elements and their distribution. EDS identifies the elements and evaluates their distribution [238, 239], as illustrated in Figure 6.7. In EDS, the detected signal is the X-rays, emitted from inner shells of atoms of investigated material by the microscope's electron beam, and named characteristic X-rays. The energy of characteristic X-rays is unique for different elements. An EDS spectrum is plotted with the X axis representing the X-ray energy, and the Y axis representing the number of counts, i.e. number of X-rays received and processed by the detector. An X-ray line is broadened by the response of the system, producing a Gaussian shape [239, 240].

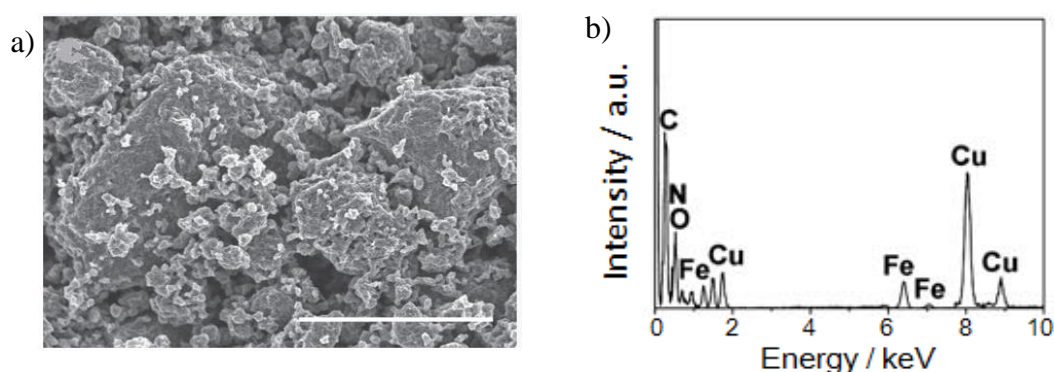


**Figure 6.7** a) SEM image [67], and b) EDS spectrum [179] of alternative carbon-based catalysts.

The SEM measurements in this thesis were performed on a Zeiss EVO MA15 scanning electron microscope with a tungsten electron source, and the EDS measurements were performed using the Oxford Instruments XMax 80 mm<sup>2</sup> detector system. The operational conditions were 5 kV of acceleration voltage, and  $K_{\alpha} = 2.0134 \text{ \AA}$ .

## 6.4 PEM Fuel Cell Tests

### 6.4.1 Polarisation Curves

A PEM fuel cell test is one of the direct and effective methods of evaluation of the catalytic activity towards the ORR. A correlation between the cell potential (voltage) and current density in PEM fuel cell tests is named the polarisation curve. A polarization curve shows the actual output from the cell and is the best way to illustrate the performance of the cell [1]. There are two modes of data collection in obtaining the polarization curves. One is to adjust the current density and record the cell potential, the other mode is to adjust the cell potential and record the current density. The former is the most common technique of fuel cell performance data

collection. The cathode and anode reactions in PEM fuel cells are reversible electrochemical reactions, the relationship between current and potential in which is described by the Butler-Volmer equation [2]:

$$I = I_0 \left[ \frac{C_{Ox}}{C_{Ox}^b} \exp\left(\frac{-\alpha n F \eta}{RT}\right) - \frac{C_{Rd}}{C_{Rd}^b} \exp\left(\frac{(1-\alpha) n F \eta}{RT}\right) \right] \quad (6.10)$$

where  $I$  is the current density,  $I_0$  is the exchange current density,  $C_{Ox}$ ,  $C_{Rd}$  are the surface concentrations of reacting species,  $C_{Ox}^b$ ,  $C_{Rd}^b$  are the bulk concentrations of reacting species,  $\alpha$  is the transfer coefficient (between 0 and 1, typically around 0.5),  $n$  is the number of transferred electrons in the rate-limiting step,  $F$  is the Faraday constant,  $R$  is the universal gas constant,  $T$  is the temperature,  $\eta = E - E_{eq}$  is the overpotential.  $E_{eq}$  is the reversible, or equilibrium, potential at a PEM fuel cell anode or cathode at 25 °C and equals 0 or 1.229 V, respectively.  $E$  is the actual potential of the cell's anode or cathode [2].

When a PEM fuel cell operates, the actual cell potential is less than the value of the open circuit potential (OCP). The flowing current in the cell causes the electrodes to be polarized, so that the anode potential moves to a more positive value, and the cathode potential moves to a more negative value, resulting in a decrease in the cell potential. This phenomenon is known as overpotential or voltage losses. The voltage losses are classified into three types: (i) activation losses, (ii) ohmic losses, and (iii) concentration losses. Figure 6.8 shows potential drops caused by each type of the losses. At low current densities, the activation losses are caused by the sluggish reaction kinetics of the ORR. At intermediate current densities, the additional potential drop is caused by the ohmic resistance of the electrolyte membrane to protons and the electrodes to the flow of electrons. At high current densities, the concentration polarization losses become significant as a result of the limited rate of mass transport of the reactants to the electrode surface [2].

When more than one polarization curve is plotted on the same graph, the higher lying curves mean a higher cell performance, as illustrated in Figure 6.9 a). The current density at about the cell potential of 0.6 V (or 0.7 V) is often used to present the activity of a cathode catalyst. PEM fuel cells with a commercial Pt/C cathode catalyst show a current density of approximately 1 A·cm<sup>-2</sup> at 0.6 V [1, 7]. Very often, polarization curves are converted to power density versus current density by multiplying the measured cell potential by the current density and plotted together with polarization curves on the same diagram, as illustrated in Figure 6.9 b) [2]. A fuel cell can reach a maximum power density at a certain current density. The combined graph shows a relationship between the cell efficiency, which is proportional to potential, and maximum power density [1]. In addition, the current density divided by total mass of a catalyst is called mass specific activity, and current density divided by

total surface area of the catalyst is called area specific activity. A higher area specific activity indicates that the catalyst surface is more effectively used [7].

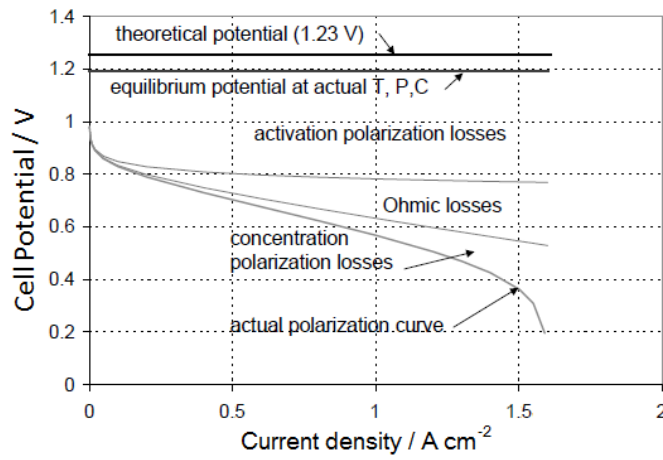


Figure 6.8 Potential losses and resulting polarization curve in PEM fuel cells [1].

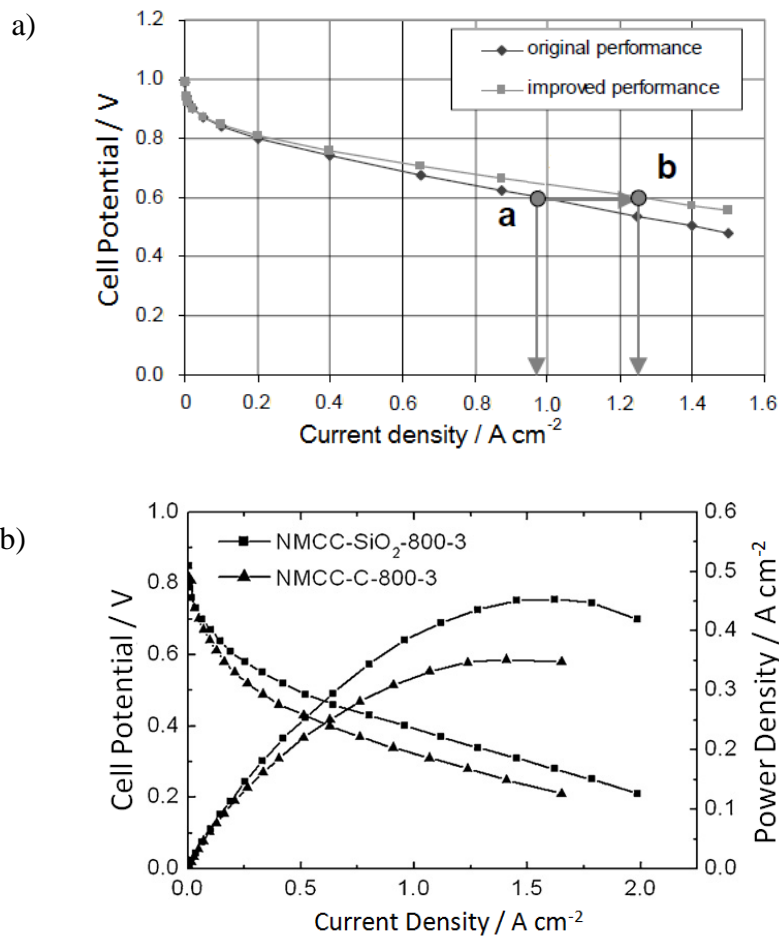


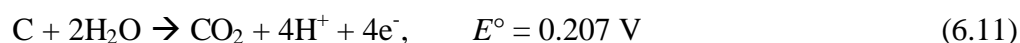
Figure 6.9 a) Evaluation of PEM fuel cell performance using polarization curves [1], and b) polarization and power density curves in PEM fuel cell tests with two alternative catalysts [137].

Importantly, a PEM fuel cell performance, and hence polarization curve, strongly depend on the operating conditions, such as cell internal electrical resistance, temperature, pressure, oxygen concentration, relative humidity, gas flow rates, etc. Normally, the performance increases with increasing temperature, pressure, relative humidity, oxygen concentration and gas flow rate and decreasing the cell electrical resistance [1]. Consequently, measurements of a PEM fuel cell performance with different cathode catalysts should be performed at the same operating conditions.

#### 6.4.2 Catalyst Durability Evaluation

As mentioned in Chapter 1, PEM fuel cells should sustain 5,000 hours of operation for mobile or transportation applications and 40,000 hours for stationary applications. However, PEM fuel cells at present cannot achieve such long lifetimes. Fuel cell durability is the ability of a cell to resist permanent change in performance over time, which is strictly related to the lifetime. A good durability is a key requirement for the commercialization of PEM fuel cells.

Fuel cell durability is determined by its decay rate. The decay is related to the degradation of different fuel cell components, especially the membrane electrolyte, the catalysts and catalyst supports [2]. The decay of the conventional carbon-supported platinum catalyst is caused by the degradation of both the structure of platinum particles and their carbon support. Platinum particles are affected by two processes. On one hand, highly dispersed platinum particles have high surface energy, and their size can increase with fuel cell operation. This process is known as sintering. Sintering of platinum particles can lead to a decrease in the electrochemical platinum surface area, resulting in a degraded fuel cell performance as well as decreased durability. On the other hand, platinum is oxidized by water or oxygen at high cathodic potentials and can be dissolved in the catalyst layer. Migration of the dissolved platinum particles can result in their undesired distribution within the ionomer membrane. Platinum oxide formation also decreases the catalyst's active surface area and the fuel cell open circuit potential [2, 241]. The carbon catalyst support is degraded by the corrosion of amorphous carbon, which results in the loss of the catalyst three-phase sites [3]. Carbon corrosion is described by the following reaction:



The rate of carbon corrosion depends on the operating temperature and cell potential. Rapid carbon corrosion occurs at typical values of the cell potential and temperatures [2].

Durability testing takes long time and is difficult to implement, since several thousand hours are necessary to obtain a meaningful conclusion. Durability testing employs the same methods and techniques as for catalyst evaluation: scanning electron microscopy (SEM), transmission electron microscopy (TEM), X-ray diffraction (XRD), cyclic voltammetry (CV) [2].

The best and simplest reliable method to test fuel cell durability is to operate the fuel cell directly, hour by hour, at the desired conditions. However, the direct method is costly in time and materials, and therefore accelerated durability test (ADT) methods are used. Normally, ADTs are performed under more “stressful” conditions compared to actual operation conditions in order to accelerate fuel cell failure. Among the ADT methods are potential cycling, load and temperature cycling, high-temperature operation, and low/no humidity operation. A correlation between the accelerated and the actual tests must be established in order to confidently predict fuel cell durability [2].

The target for the durability of cathode catalysts in PEM fuel cells using the technique of potential cycling are as follows: 5,000 hours at temperatures below 80°C and 2,000 hours at temperatures above 80°C with less than 40% loss of initial catalytic mass activity, and less than 30 mV loss at 0.8 A·cm<sup>-2</sup> [242]. For PEM fuel cells operated in steady state, without cycling of open circuit potential, at a temperature of 70–75 °C and 100% relative humidity of the reactant gases, the overall potential decay rate is generally in an acceptable range, i.e. less than 6 μV·h<sup>-1</sup>. However, as the potential decay rate can increase sharply when either the temperature is above 75 °C, or the gases are not fully humidified, or there exists a cycling of the load or potential (especially open circuit potential), state-of-the-art platinum and carbon-black support materials do not meet the requirements [241].

### 6.4.3 Electrochemical Impedance Spectroscopy

EIS is used for PEM fuel cell diagnostics and allows studying processes occurring with different time scales, such as double layer charging, charge transfer, ion conduction, and mass transport. Basically, impedance is a measure of a system’s ability to impede electrical current. In EIS, a small alternating voltage or current signal of known amplitude and frequency is applied to the cell, and the amplitude and frequency of resulting signal are measured. In order to deconvolute the resulting impedance spectra and extract parameters of interest, physical analogues of the processes are needed, and these are called equivalent circuit models. Equivalent circuit models can include resistor(s), capacitor(s), inductor(s), etc. Resistors represent electronic and ionic resistances when electrons and ions move during electrochemical processes. Capacitors represent charge accumulation that occurs at the electrode-

electrolyte surfaces. Thus, these elements in equivalent circuits are used to simulate different reaction processes. Importantly, impedance spectra obtained experimentally can be represented by more than one equivalent circuit, and understanding of the electrochemical processes is necessary in order to build correct equivalent circuit models [1, 2].

In PEM fuel cells, equivalent circuits commonly include electronic, ionic, and contact resistance, charge transfer resistance accounting for activation polarization, resistance of double-layer capacitor and Warburg impedance accounting for mass transport (concentration polarization), as shown in Figure 6.10. It should be noted that the mathematical expression for the capacitor resistance contains unit imaginary number. Therefore, when an alternating current perturbation is applied to an equivalent circuit, in which elements are connected in various combinations, the overall impedance can be expressed as follows [1, 2]:

$$Z = Z_R - jZ_C \quad (6.12)$$

where  $Z_R$  is real part of impedance,  $Z_C$  is imaginary part, and  $j = \sqrt{-1}$ .

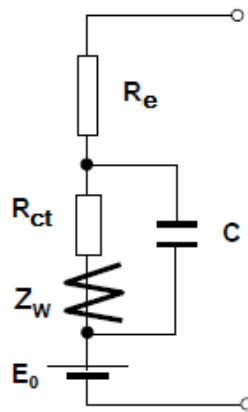


**Figure 6.10** Equivalent circuit representing a fuel cell, where  $R_e$  is both electronic and ionic resistance,  $R_{ct}$  is charge transfer resistance,  $Z_w$  is Warburg impedance,  $C$  is capacitive resistance [1].

In impedance spectra in the Nyquist form, the imaginary part of the impedance is plotted as a function of the real impedance, as illustrated in Figure 6.11. Nyquist plots show the response to alternating current perturbations of a wide range of frequencies [2]. Typically, electronic (ohmic) resistance appears on the x-axis of Nyquist plots as a single point at high frequencies, i.e. the beginning of the arc. The charge transfer resistance is determined as the diameter of the arc. Since it is related to the reaction kinetics, a small charge transfer resistance implies fast reaction kinetics. The extended

straight line following the semi-circle is detected at low frequencies and is related to the mass transport of the reacting species [1].

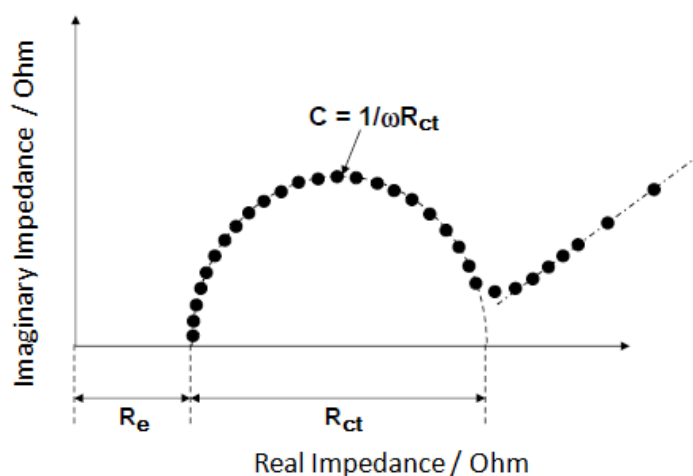


**Figure 6.11** The EIS spectrum at various frequencies of the fuel cell equivalent circuit in the Nyquist form. The frequencies  $\omega$  increase from right to left [1].

## 6.5 Experimental Setup

This section describes the experimental equipment used for catalyst syntheses, electrochemical characterisation and PEM fuel cell testing.

### 6.5.1 Equipment for Catalyst Synthesis

Basic equipment for catalyst syntheses include:

- Ultrasonic bath for dispersing solid powder materials in solvents;
- Buchner set for filtering and washing materials to remove dissolved species;
- Vacuum rotary evaporator for vacuum drying;
- Reflux condenser for acid leaching, i.e. treating materials with diluted sulphuric acid solution to remove impurities or ions;
- Tube furnace for heat treatment.

The reflux condenser, shown in Figure 6.12, has been assembled from a three-neck round bottom flask, water-cooled reflux condensing column, thermometer and ancillary glassware, e.g. dropping funnel or stopper. The flask was held in a heated magnetic stirrer. A magnetic stirrer with a flat plate was used to conduct reactions at lower than ambient temperatures. The tube furnace was used to pyrolyse materials in an inert atmosphere, i.e. flowing nitrogen gas, in order to avoid interaction with the

oxygen from the air and the combustion of the material. The nitrogen gas flow rate was controlled by a gas flow-meter with a digital control panel, illustrated in Figure 6.13. The flow-meter has been calibrated to match the actual nitrogen flow rate measured in the units of ml/min to settings of the digital control panel. The obtained calibration line, illustrated in Figure 6.14, has been used to set the accurate values of the nitrogen gas flow rate.



**Figure 6.12** Photograph of the reflux condenser.

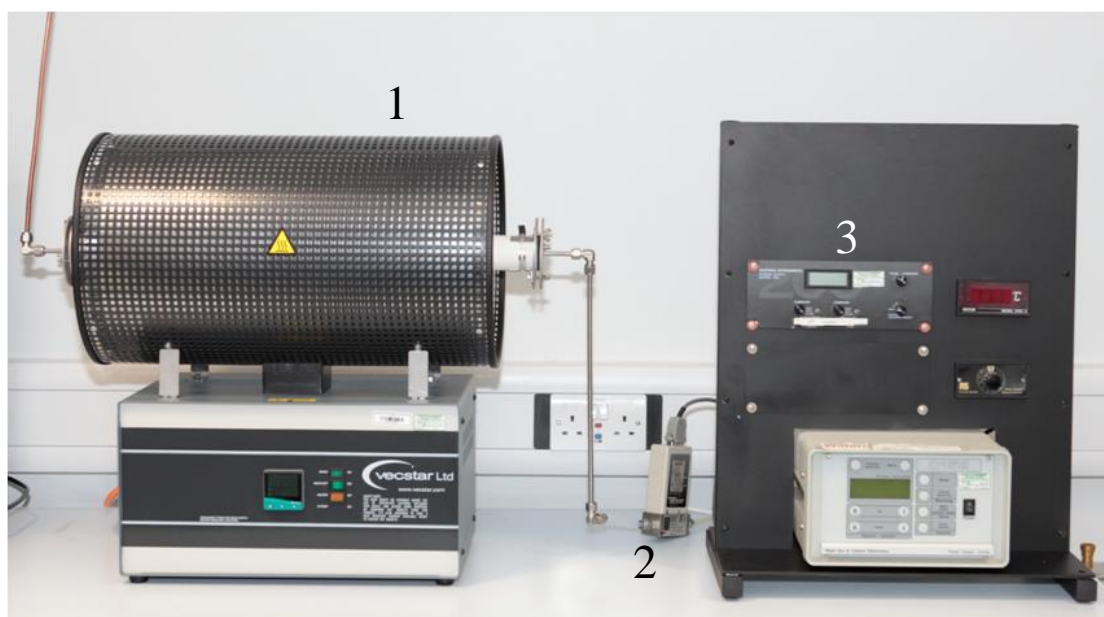


**Figure 6.13** Photograph of the tube furnace (1) with gas flow-meter (2), and digital control panel (3).

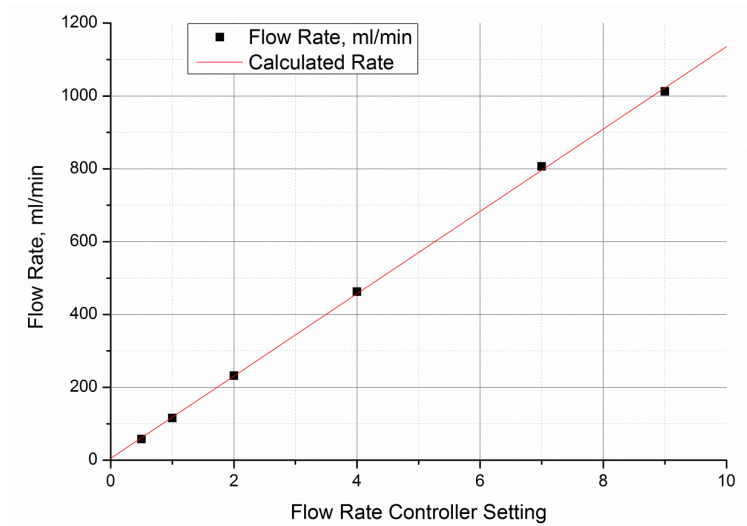


**Figure 6.14** Gas flow-meter calibration.

### 6.5.2 Equipment for Electrochemical Characterisation

State-of-the-art electrochemical equipment (Gamry, Figure 6.15) was purchased for electrochemical characterisation of the ORR catalysts. The main functional components are as follows:

- Potentiostat(s);
- Rotating ring disc electrode (RRDE);
- Counter electrode;
- Reference electrode;
- Test cell;
- Electrode rotator;
- Computer.

The RRDE working electrode has a cylindrical shape and is composed of ring and disk electrodes. The disk electrode is made of glassy carbon with an area of 0.196 cm<sup>2</sup>, and the ring electrode is made of platinum. The counter electrode is platinum wire, and the reference electrode is the standard hydrogen electrode (SHE). The RRDE, counter and reference electrodes were submerged into the glass test cell filled with 0.5 M H<sub>2</sub>SO<sub>4</sub> electrolyte solution. Bubbling with nitrogen gas for 30-40 minutes was used to remove dissolved oxygen from the solution, and bubbling with air was used to saturate it with oxygen. The RRDE rotation is controlled by the electrode rotator, and the potentials from the disk and ring electrodes ( $E_D$  and  $E_R$ ) are independently controlled by two potentiostats using common reference and counter electrodes [234]. The disk and ring currents ( $I_D$  and  $I_R$ ) are recorded by the potentiostats, and the data are collected and analysed by the software for electrochemical characterisation.



**Figure 6.15** Photograph of the RRDE equipment: (1) potentiostat, (2) rotating ring disk electrode, (3) test cell, (4) electrode rotator, and (5) computer.

### 6.5.3 In-house PEM Fuel Cell Test Station

The in-house PEM fuel cell test station is illustrated in Figure 6.16. The principal part of the station is the air-breathing PEM fuel cell, consisting of a membrane electrode assembly (MEA) with an area of  $3.4 \times 3.4 \text{ cm}^2$ , interlaid between two graphite composite current collectors. The cell potentials were controlled and corresponding electric currents were registered by the potentiostat. The reactant gases, hydrogen (99.995% purity) and air, were supplied from compressed cylinders. Nitrogen and helium gases were used to (i) detect air and hydrogen leaks, and (ii) to purge the unused gases at the cathode and anode before turning off the test station. Mass flow controllers were used to control and monitor flow rates of the reactant gases; the flow rates of gases at the anode and cathode were set at 1000 and 5000 sccm, respectively. The reactant gases were humidified by passing through bubble-type humidifiers. The pressure of the inlet and outlet gases was controlled by back pressure regulators. Temperature of the fuel cell and reactant gases at the inlet were set by a temperature controller. The humidifiers and the fuel cell were at room temperature, about  $20 \text{ }^\circ\text{C}$ . Flow rates of air and hydrogen were 100 and 200 sccm, respectively, and the gauge pressure was set to 1 bar for the inlets of both gases.

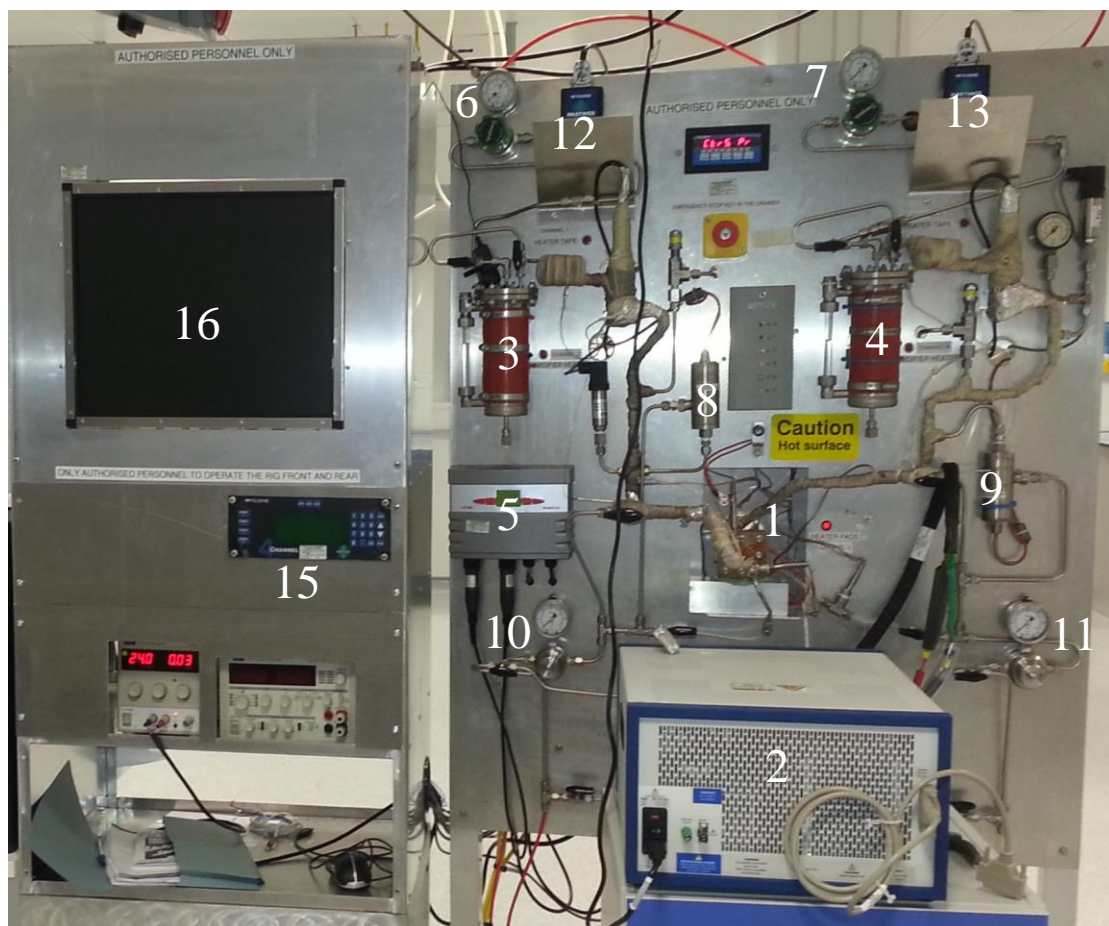


**Figure 6.16** Photograph of the in-house PEM fuel cell test station: 1) air-breathing PEM fuel cell, 2) potentiostat, 3) and 4) bubbler-type hydrogen and air humidifiers, 5) humidity sensor and reader, 6) and 7) hydrogen and air pressure regulators, 8) and 9) hydrogen and air pressure differential transducers, 10) and 11) hydrogen and air back pressure regulators, 12) and 13) mass flow controllers, 15) flow rates control display, and 16) gas leak control monitor.

## 6.6 Experimental Research Outline

The experimental part of this thesis focuses on the research and development of alternative cathode catalysts for PEM fuel cells. Chapters 3 - 5 have discussed the predictions for a multitude of doped carbon based catalysts based on theoretical modelling by means of computational chemistry. It was predicted that N, P, Fe and Co doping may produce highly active catalysts, while a combined N and P doping of carbon results in a reduction of catalytic activity. These predictions are investigated experimentally by synthesizing N and P doped carbon catalysts in the presence of Fe and Co. A novel technique of synthesis of phosphorus doped carbon catalyst is proposed, which consists of applying the catalyst coating directly onto the gas diffusion layer for PEM fuel cells.

The experimental research is also dedicated to investigation of the effect of alternative support materials on which the carbon based catalytic active sites are mounted. Since an efficient support material for PEM fuel cell catalysts should provide a large surface area and good electrical conductivity, conductive, non-conductive and high surface area non-carbon catalyst supports are investigated in this thesis. The chosen conductive catalyst supports are titanium nitride, tungsten carbide, indium tin oxide and multiwall carbon nanotubes, while the non-conductive catalyst supports are silica, titanium dioxide, molecular sieves and zeolites.

The effectiveness of synthesized catalysts in the oxygen reduction reaction is assessed by electrochemical characterisation using the RRDE techniques of cyclic voltammetry and linear sweep voltammetry. The catalysts are then investigated by physicochemical methods, namely, XRD, XPS, or SEM. Catalyst candidates that showed a promising electrochemical performance are finally tested in a small scale PEM fuel cell.

## **Chapter 7**

### **Experimental Investigation of Heteroatom Doped Carbon Catalysts for PEM Fuel Cells**

#### **7.1 Introduction**

The computational studies in the present thesis suggest that N or P doped carbon as well as Fe and Co macrocycles may be promising carbon based catalysts for the ORR. Therefore, this experimental chapter focuses on the development of synthesis techniques of N and P doped carbon in the presence of Fe and Co. The N doped carbon catalysts have been synthesized based on the technique developed by the Los Alamos National Laboratory [24, 243], since their carbon based catalyst is one of the most active and durable cathode materials for PEM fuel cells so far [22].

Synthesis of P doped as well as N and P co-doped carbon based catalyst has been undertaken. A few research groups have reported P doped carbon as a catalyst for the ORR. In these studies, P doped carbon catalysts were synthesized using either triphenylphosphine [96, 97] or phosphoric acid [92, 93, 98] as a source of P. In this thesis, novel P and N,P precursors have been utilized in the catalyst syntheses.

The synthesis techniques reported in the literature do not exclude uncontrolled incorporation of O into carbon and formation of various C-O and P-O bonds, revealed by XPS analyses. The XPS data in the literature indicate the presence of significant amount of O and negligible amount of P in carbon, with a significant portion of P existing in the catalytically inactive phosphate state. In an attempt to find ways of more efficient P doping of carbon, catalysts were manufactured using the common chemical synthesis techniques and also a novel glow discharge method.

#### **7.2 Catalyst Ink Preparation for the RRDE Measurements**

In the electrochemical experiments, catalysts are applied on the glassy carbon disk (GCD) of the working RRDE electrode. The catalyst inks for the RRDE measurements in the present thesis were prepared as follows.

The GCD was polished with 0.3 and then 0.05  $\mu\text{m}$  alumina slurry, rinsed with de-ionized water and ethanol, and wiped with a lint-free cloth. 5 mg of a catalyst were mixed with 1 ml of ethanol and 50  $\mu\text{l}$  of 5% Nafion<sup>®</sup> solution, and then ultrasonicated for 30 minutes. A 20  $\mu\text{l}$  aliquote of the catalyst ink was cast onto the polished GCD and dried under an infra-red lamp.

Cyclic voltammograms (CVs) were obtained in nitrogen and air. Firstly, nitrogen gas was purged for 30 minutes through 0.5 M H<sub>2</sub>SO<sub>4</sub> to remove oxygen from it. During the measurement, the potential was cycled between 0 and 1.1 V at a scan rate 50 mV s<sup>-1</sup> until reproducible CVs were obtained (20 times). The non-changing shape of the voltammogram showed the electrochemical stability in the given potential range. Secondly, compressed air was bubbled into the solution for 30 minutes to saturate it with oxygen. The potential of the air-saturated cell was cycled 20 times between 0 and 1.1 V with 50 mV s<sup>-1</sup> scan rate.

Linear sweep voltammograms (LSVs) were obtained in air-saturated electrolyte after the CV measurements. The potential of working electrode was changed from 1.1 to 0.05 V with 3 mV s<sup>-1</sup> scan rate and 1 mV step size. The series of the RRDE measurements were performed at a speed of 0 – 2400 RPM and with 300 RPM step size. The ORR onset potential was defined as the electrode potential at the current density 0.2 μA cm<sup>-2</sup>. To compare the LSV performance of different catalysts, the curves obtained at 1200 RPM were overlaid.

### 7.3 Catalyst Ink Preparation for PEM Fuel Cell Tests

Catalysts were applied onto GDLs by spraying a catalyst ink. Normally, there is a considerable amount of the catalyst lost when spraying its ink to the GDL: only 1/3 to 1/4 of the prepared catalyst is attached to the GDL, and the rest of the catalyst is lost to the environment and the area surrounding the GDL. Therefore, the calculated amount of the catalyst is normally multiplied by factor to compensate for this loss, ensuring that the target catalyst loading is achieved. From experience, it was found that this loss factor is between 3 and 4. Thus, the weight of a catalyst required for the ink preparation has been calculated using the following equation:

$$m_{\text{weight}} = l_{\text{cat}} \cdot A_{\text{GDL}} \cdot f \quad (7.1)$$

where  $m_{\text{weight}}$  is the weight of catalyst for the catalyst ink preparation,  $l_{\text{cat}}$  is the catalyst loading,  $A_{\text{GDL}}$  is the GDL area, and  $f$  is the loss factor.

The weighed amount of catalyst was mixed with a few drops of de-ionized water and ultrasonicated for a few minutes. The amount of 50% ethanol required for the catalyst ink preparation was calculated using the proportion of 15 ml of 50% ethanol per 50 mg of the catalyst:

$$V_{50\% \text{ethanol}} = \frac{15}{50} \cdot m_{\text{weight}} \quad (7.2)$$

The amount of 5% Nafion<sup>®</sup> solution was calculated based on the proportion of 85 mg of catalyst per 15 mg of solid Nafion<sup>®</sup>:

$$m_{5\%Nafion} = \frac{15}{85} \cdot \frac{100\%}{\omega_{Nafion}} \cdot m_{weight} \quad (7.3)$$

where  $m_{5\%Nafion}$  is the required amount of 5% Nafion<sup>®</sup> solution,  $\omega_{Nafion}$  is the mass percentage of solid Nafion<sup>®</sup> in a required solution.

The calculated amount of 5% Nafion<sup>®</sup> solution was added to the catalyst slurry in water and ultrasonicated for 30 minutes. The catalyst ink was sprayed onto a GDL, mounted vertically on a plate heated at 80 °C. The required amount of catalyst on the coated GDL should be:

$$m_{cat} = l_{cat} \cdot A_{GDL} \quad (7.4)$$

The amount of dry Nafion<sup>®</sup> on the coated GDL should be was calculated using the 15:85 ratio of dry Nafion<sup>®</sup> to the catalyst:

$$m_{Nafion} = m_{cat} \cdot \frac{15}{85} \quad (7.5)$$

After coating with the catalyst ink, the GDL was coated with 5% Nafion<sup>®</sup> solution. The amount of the 5% Nafion<sup>®</sup> was calculated as follows:

$$m_{5\%Nafion} = l_{Naf} \cdot A_{GDL} \cdot \frac{100\%}{\omega_{Nafion}} \quad (7.6)$$

where  $m_{5\%Nafion}$  is the amount of 5% Nafion<sup>®</sup> solution required, and  $l_{Naf}$  is the loading of solid Nafion<sup>®</sup>.

The calculated amount of 5% Nafion<sup>®</sup> was mixed with 3-5 ml of pure acetone, and sprayed onto the coated GDL.

## 7.4 Preparation of the Membrane Electrode Assembly

The membrane electrode assembly (MEA) for PEM fuel cell testing were prepared using alternative catalysts and 20%Pt/C catalyst. The alternative catalysts were applied on a GDL at the cathode side, and the commercial 20% Pt/C on a GDL at the anode side. The alternative catalyst loading was 4 mg/cm<sup>2</sup>, and that of platinum in the 20%Pt/C was 0.25 mg/cm<sup>2</sup>. Procedures of the cathode and anode catalyst ink preparation are described in the following sections. The MEA was prepared by placing a Nafion<sup>®</sup> membrane between the catalyst-coated cathode and anode GDLs and

pressed by 100 kg, then heated to 130 °C and pressed 600 kg for 3 minutes. After pressing, the MEA was cooled down to room temperature with a fan.

## 7.5 RRDE Collection Efficiency Measurement

As mentioned in Section 6.2.4, collection efficiency is a parameter necessary for calculating the number of electrons transferred in the ORR and the percentage of generated hydrogen peroxide.

Collection efficiency ( $N$ ) is defined as the fraction of material flowing from the disk past the ring electrode [244]. The theoretical collection efficiency can be calculated analytically based on the disk diameter and inner and outer ring diameters, and for the employed RRDE system  $N = 0.256$  (25.6%) [245]. However, in practice, the actual disk and ring diameters may not be known due to uncertainties in their machining process. Therefore, the collection efficiency is also measured empirically and determined as follows [244]:

$$N_{\text{empirical}} = \frac{j_{\text{limiting,ring}}}{j_{\text{limiting,disk}}} \quad (7.7)$$

where  $j_{\text{limiting,ring}}$  and  $j_{\text{limiting,disk}}$  are the ring and disk diffusion limiting currents, respectively.

Usually, in order to measure collection efficiency, a well-known ferrocyanide/ferricyanide redox system is used, since it is a simple, single-electron, reversible reaction [244]:



The RRDE is placed in the electrolyte solution containing a small concentration of potassium ferricyanide,  $\text{K}_3\text{Fe}(\text{CN})_6$ , and another suitable electrolyte, e.g. potassium nitrate,  $\text{KNO}_3$  [244]. Figure 7.1 illustrates the technique of measurement of the empirical collection efficiency. The RRDE experiment is conducted at a few different rotation speeds, and the obtained collection efficiencies are plotted against the rotation speeds at which they were calculated. The measured ring and disk current ratios should be almost constant under various rotation speeds and the average should be the empirical collection efficiency [234].

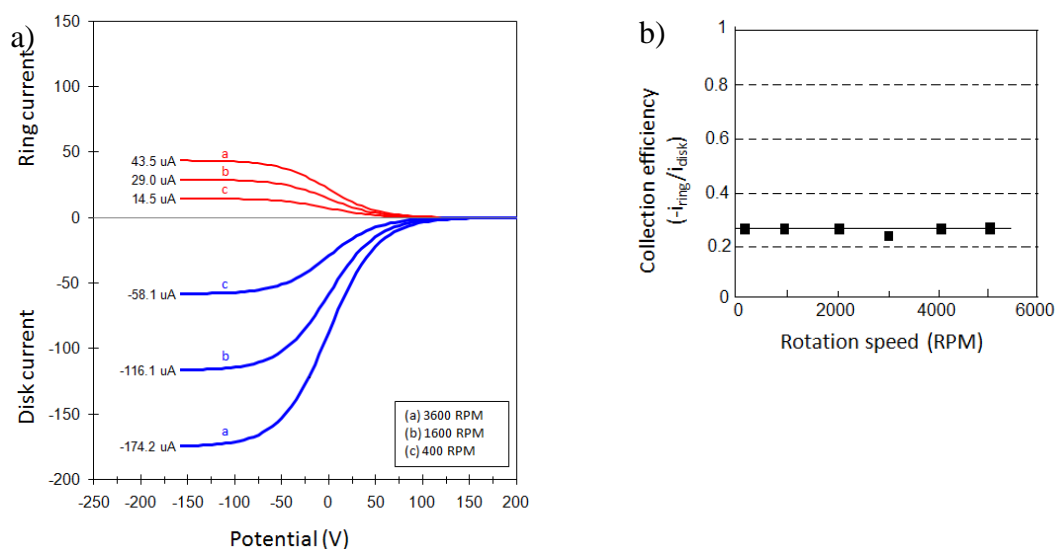


**Figure 7.1** Principle of measurement of the empirical collection efficiency: a) LSVs at different electrode rotation speeds [244], and b) calculated collection efficiency as a function of electrode rotation speed [234].

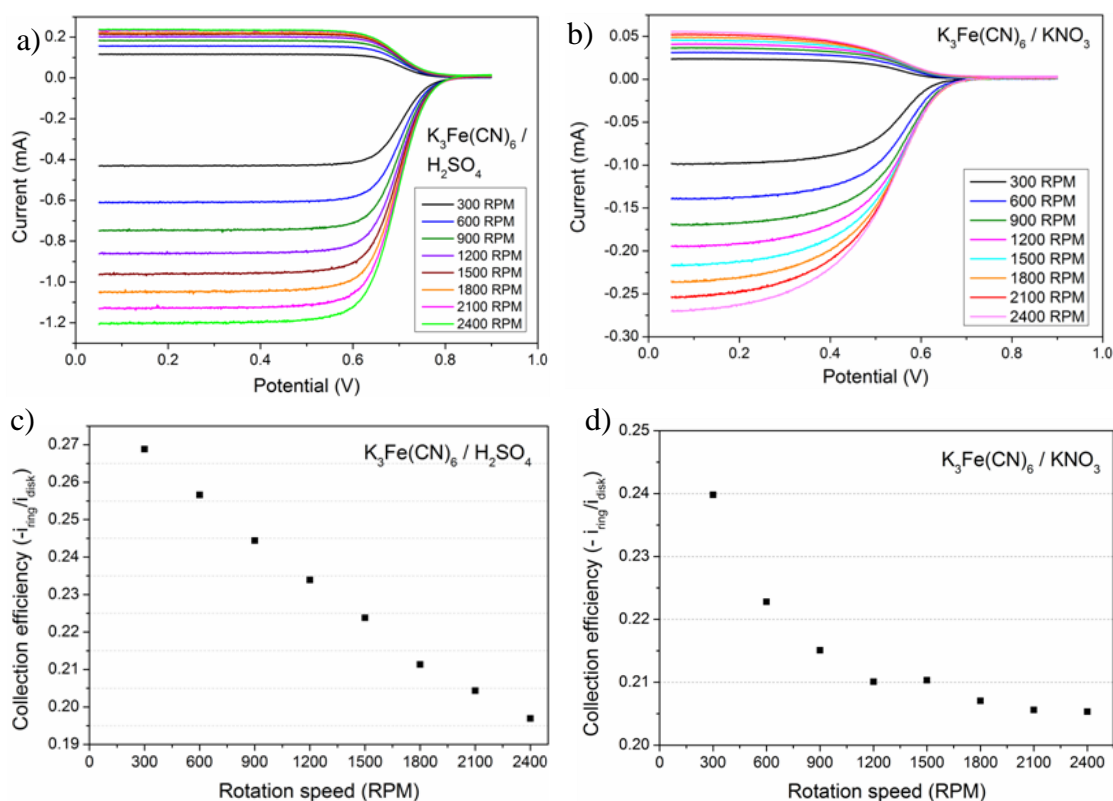


**Figure 7.2** Measurement of the empirical collection efficiency on glassy carbon disk and platinum ring electrode in 3 mM  $K_3Fe(CN)_6$  solution: a) and b) LSVs at different rotation speeds in 0.5 M  $H_2SO_4$  and 1 M  $KNO_3$ , respectively; c) and d) empirical collection efficiency as a function of electrode rotation speed in 0.5 M  $H_2SO_4$  and 1 M  $KNO_3$ , respectively.

In this thesis, several measurements of the empirical collection efficiency have been performed both on glassy carbon disk (GCD) and on the commercial 20%Pt/C catalyst applied onto it. The electrolyte solution was 3 mM  $\text{K}_3\text{Fe}(\text{CN})_6$  in either 0.5 M  $\text{H}_2\text{SO}_4$  or 1 M  $\text{KNO}_3$ . The best results have been achieved on the GCD in 3 mM  $\text{K}_3\text{Fe}(\text{CN})_6$  prepared either in 0.5 M  $\text{H}_2\text{SO}_4$  or 1 M  $\text{KNO}_3$  and are illustrated in Figure 7.2. It is clear that measurements in 0.5 M  $\text{H}_2\text{SO}_4$  show better defined diffusion limited currents and have a few times higher current values than in 1 M  $\text{KNO}_3$ . Interestingly, the calculated collection efficiencies decrease with increasing electrode rotation speed. This result can be explained by an increase in centrifugal flux of the reacting species at higher rotation speeds, which decreases the probability of oxidation at the ring. After averaging, the empirical collection efficiencies are 0.23 in  $\text{K}_3\text{Fe}(\text{CN})_6 / \text{H}_2\text{SO}_4$  and 0.21 in  $\text{K}_3\text{Fe}(\text{CN})_6 / 1 \text{ M } \text{KNO}_3$ .

## 7.6 RRDE Characterisation of the Commercial Platinum Catalyst

Figure 7.3 shows the results of the RRDE characterisation for the commercial 20%Pt/C catalyst. The cyclic voltammetry in air saturated electrolyte has been performed in the potential range of 0.2 - 1.1 V. The reduction peak potential is observed at 0.83 V, and the peak current is  $2.36 \text{ mA}\cdot\text{cm}^{-2}$ . The LSVs obtained at different rotation speeds show the ORR onset potential of 0.95 V. For a more quantitative analysis of the ORR on the 20%Pt/C catalyst, the LSV curves were analysed using the Koutecky-Levich theory mentioned in Section 6.2.4. The Koutecky-Levich plot was created as a function of the reciprocal disk current density  $(j_D)^{-1}$  from the reciprocal square root of the electrode rotation speed  $(\omega^{-1/2})$  using the at 0.4 V vs. SHE. The number of electrons  $n$  was obtained from the slope of the line using the following values of the parameters in Equation 6.3:

$$F = 96487 \text{ C/mole (Faraday constant),}$$

$$C = 1.30 \cdot 10^{-6} \text{ mol}\cdot\text{cm}^{-3} \text{ (concentration of molecular oxygen in the electrolyte),}$$

$$D = 1.97 \cdot 10^{-5} \text{ cm}^2\cdot\text{s}^{-1} \text{ (diffusion coefficient),}$$

$$\nu = 0.01 \text{ cm}^2\cdot\text{s}^{-1} \text{ (kinetic viscosity) [20].}$$

According to the obtained slope of the Koutecky-Levich plot, the electron transfer number of the overall reduction process was calculated to be 3.8. This result suggests a four-electron mechanism of the ORR. In order to validate the electron transfer number obtained from the Koutecky-Levich plot, it was calculated using the RRDE data and Equation 6.5. The electron transfer number was plotted as a function of either electrode rotation speed or electrode potential, as shown in Figure 7.4. This technique

suggests that the electron transfer number tends to increase with the rotation speed, although the curves have minima at 1200 RPM. The average electron transfer number steadily increases with increasing the rotation speed, and the highest value of 3 – 3.2 is achieved at the highest electrode rotation speed (2400 RPM).

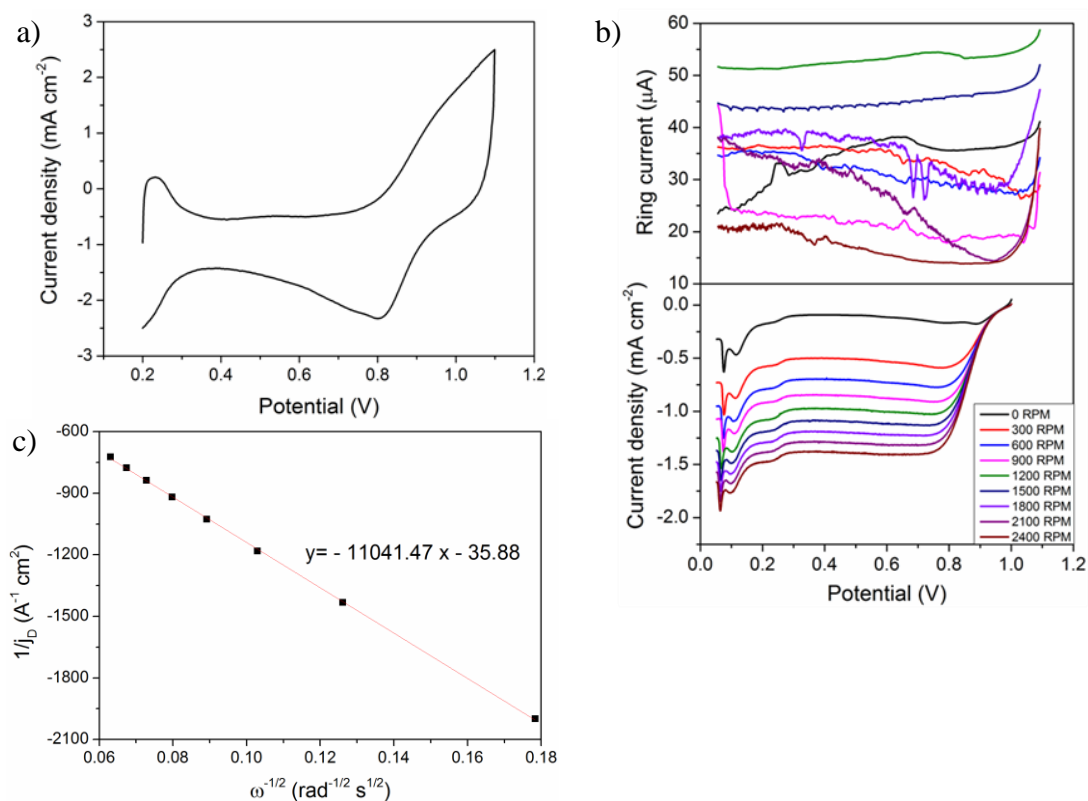


**Figure 7.3** RRDE characterisation of the 20% Pt/C catalyst: a) CV in air, b) LSVs at different electrode rotation speeds, and c) Koutecky-Levich plot (the current density data were taken at 0.4 V vs. SHE).

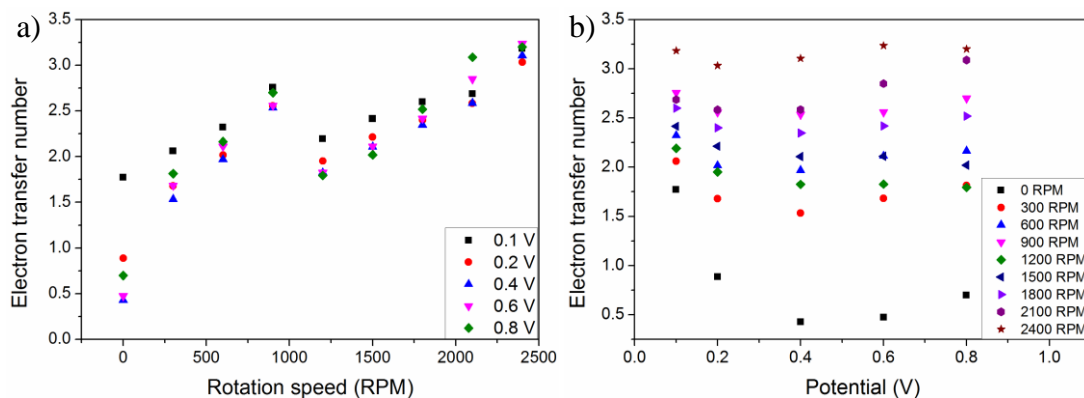


**Figure 7.4** Electron transfer numbers for the ORR on the 20% Pt/C catalyst plotted versus a) electrode rotation speed, and b) potential.

## 7.7 N doped Carbon Catalysts

### 7.7.1 LANL1 Catalysts

#### 7.7.1.1 Synthesis

The N doped carbon catalysts have been synthesised according to the techniques reported by the Los Alamos National Laboratory (LANL). The synthesis technique described in the research article [24] is different from the technique described in the patent [243]. The catalysts synthesized according to the paper and patent techniques are further designated as the LANL1 and LANL2, respectively. The schematic procedure of the LANL1 catalyst synthesis is presented in Figure 7.5.

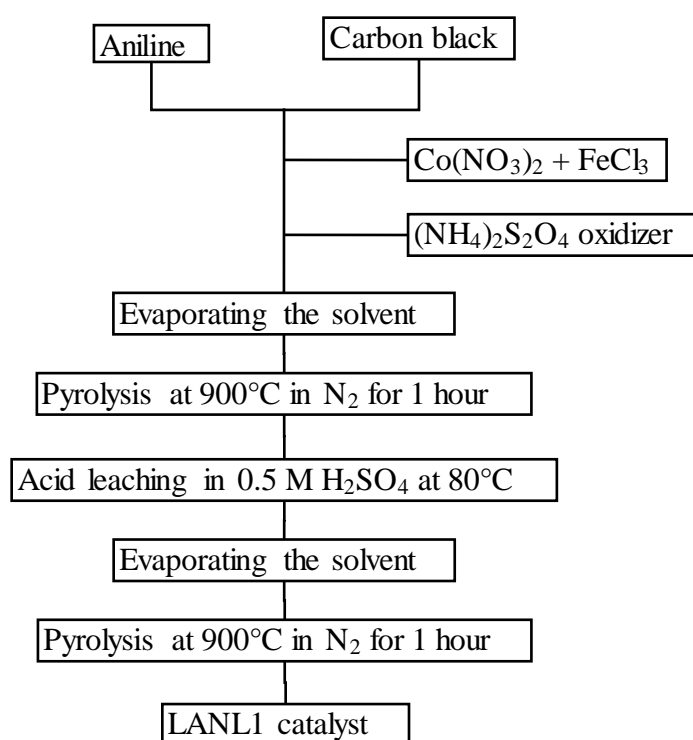


**Figure 7.5** Schematic of the LANL1 catalyst synthesis.

The LANL1 catalyst has been synthesized according to the technique described in the research article of Wu et al. [24] as follows. Approximately 2 g of Ketjen Black EC 300J was dispersed in 0.5 M HCl ultrasonically for 24 hours to remove any metal impurities. The Ketjen Black suspension was filtered and then dried in the vacuum rotary evaporator. 0.4 g of the purified Ketjen Black was mixed with 3 ml of aniline and 400 ml 0.5 M HCl in a three-neck round-bottom flask, and then cooled down to a temperature of circa 8 °C. 0.5 g Co(NO<sub>3</sub>)<sub>2</sub>·6H<sub>2</sub>O and 3 g of FeCl<sub>3</sub>·6H<sub>2</sub>O were dissolved in 0.5 M HCl and added dropwise to the flask while stirring. 5 g of ammonium persulfate (NH<sub>4</sub>)<sub>2</sub>S<sub>2</sub>O<sub>4</sub> was dissolved in 0.5 M HCl and also added to the

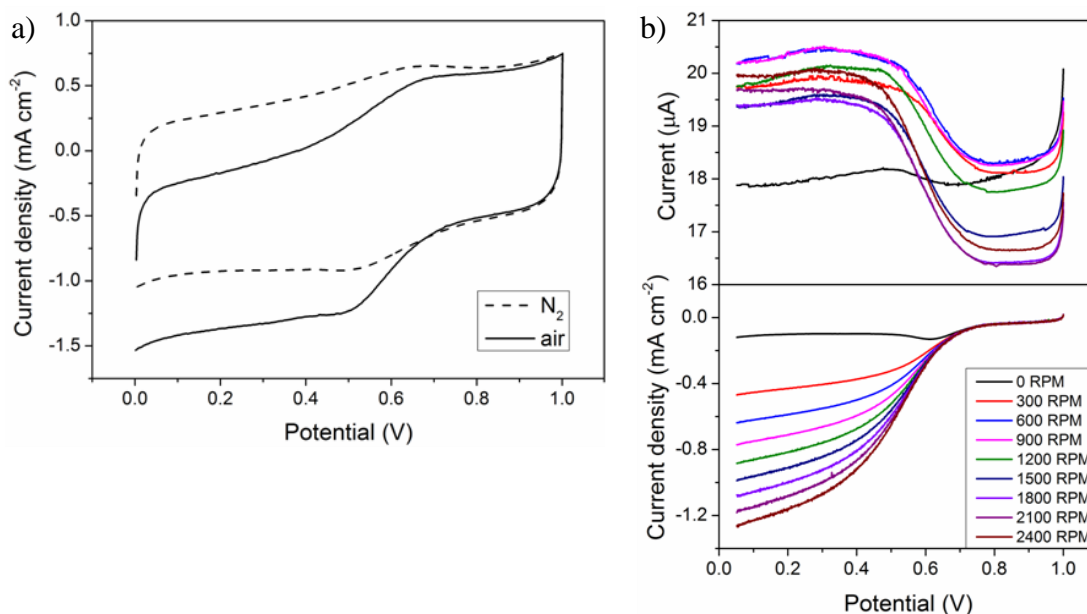
flask dropwise while stirring for 12-24 hours. The resulting suspension was filtered, washed with de-ionized water, dried in the vacuum rotary evaporator, and then pyrolysed at 900 °C for 1 hour in the tube furnace in an inert atmosphere of N<sub>2</sub> gas flowing with circa 200 ml/s rate. After the pyrolysis, the powder was leached in 0.5 M H<sub>2</sub>SO<sub>4</sub> in the reflux condenser for 8 hours at 80 °C with constant stirring. After the acid leaching, the suspension was washed with de-ionized water and dried in the vacuum rotary evaporator. The solid was then pyrolysed at 900 °C for 3 hours in the N<sub>2</sub> flow.

In order to evaluate the effect of the catalyst texture, the obtained material was divided into two parts, the first of which has been sieved through a sieve with a cell diameter of 40 µm, and the other part remained as synthesised. The sieved and non-sieved LANL1 catalysts are further referred to as the LANL1-s and LANL1-ns, respectively.

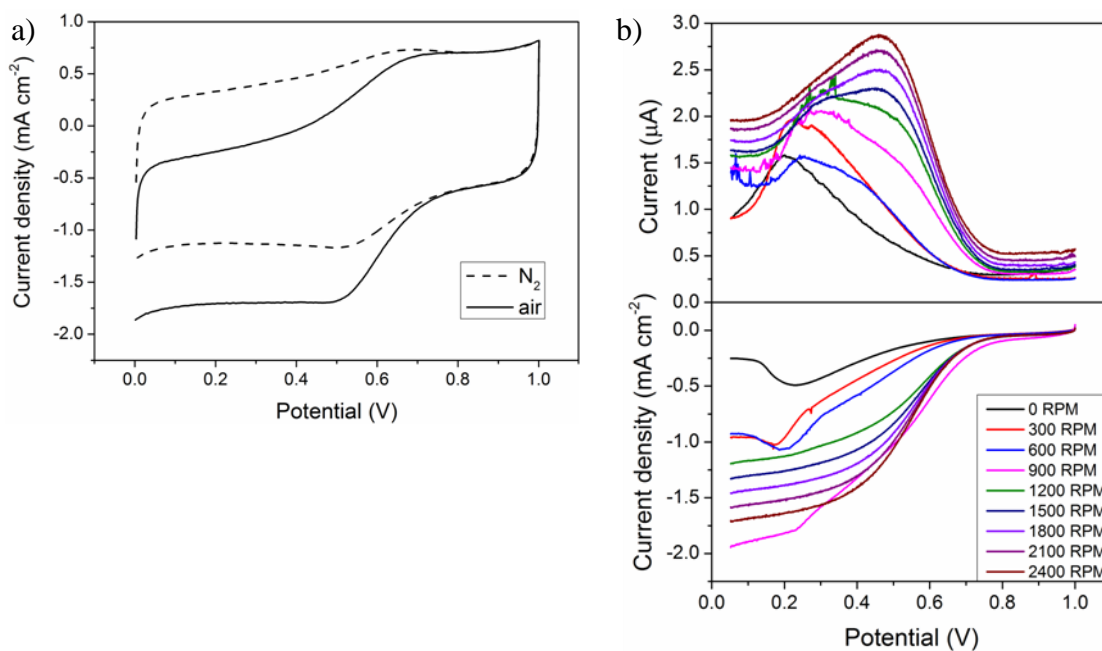
#### **7.7.1.2 RRDE Characterisation and the Effect of Sieving**

Figure 7.6 shows the results of electrochemical characterisation of the LANL1-ns. Cyclic voltammetry in the electrolyte bubbled with nitrogen gas was performed 20 times to clean the catalyst surface electrochemically, and then CVs in air saturated electrolyte were measured to locate the oxygen reduction peak. As can be observed in the CVs, the peak is not well defined but transformed to a wave with the ridge at the potential of about 0.5 V. Linear sweep voltammetry (LSV) at different rotation speeds has been performed including measurements on the ring electrode. The potential of the ring was held at 1.2 V to ensure oxidation of hydrogen peroxide formed on the disk. In the LSVs, the ring currents are proportional to the hydrogen peroxide yield at different electrode rotation speeds. The disk currents indicate the onset potential of the ORR to be circa 0.75 V, and the diffusion limiting current densities increase with increasing rotation rate due to the accelerated mass transport of the molecular oxygen.

Figure 7.7 shows the CVs in nitrogen and air saturated electrolyte and LSVs at different rotation speeds for the sieved LANL1-s catalyst. The reduction peak in the CV in air is located at 0.5 V, and this is similar to that of the LANL1-ns. The LSVs show circa 0.70 V onset potential for both the sieved and non-sieved catalysts, and the disk current densities and ring currents increase with increasing electrode rotation speed. The diffusion limiting disk current densities are well defined starting from circa 0.75 V and increase with the increasing the electrode rotation speed. However, there is no trend in the ring currents with respect to increasing rotation speed.



**Figure 7.6** RRDE characterisation of LANL1-ns catalyst: a) CVs in  $N_2$  and air, and b) LSVs at different electrode rotation speeds, shown in the legend.



**Figure 7.7** RRDE characterisation of LANL1-s catalyst: a) CVs in  $N_2$  and air, and b) LSVs at different electrode rotation speeds, shown in the legend.

The LSVs show that the ORR onset potentials of the 20%Pt/C and LANL2 catalysts are 0.96 and 0.80 V, respectively. The onset potentials for the LANL1-s and carbon black are significantly lower, circa 0.76 V. The 20%Pt/C catalyst shows a well defined diffusion limited disk current density, which is 1.5 times higher than that of the LANL2 catalyst and carbon black. Interestingly, the diffusion limiting current densities for the LANL2 and carbon black are lower than that of the LANL1-s

catalyst. The ring current is highest for the 20%Pt/C catalyst followed by the LANL2, carbon black and the LANL1-s. These data indicate that although platinum based catalyst demonstrates outstanding catalytic activity, the alternative catalysts are potentially more selective towards the four-electron oxygen reduction than platinum based catalysts.

In order to compare the ORR performance of the synthesised sieved and non-sieved LANL1 catalysts with the commercial 20%Pt/C catalyst, the corresponding CVs and LSVs at the rotation speed of 1200 RPM have been overlaid, as shown in Figure 7.8. Both the CVs and LSVs show that the 20%Pt/C substantially outperforms the LANL1 catalysts. The difference in the peak potentials of the 20%Pt/C and the LANL1 catalysts is about 0.30 V, and the difference in the onset potentials is 0.20 V. This indicates that the LANL1 has a substantially higher overpotential for the ORR than a platinum-based catalyst. For the LANL1 catalyst, the positive effect of sieving can be observed. The sieved LANL1-s catalyst has a greater CV area and diffusion limiting current and a considerably lower ring current than the non-sieved LANL1-ns catalyst.

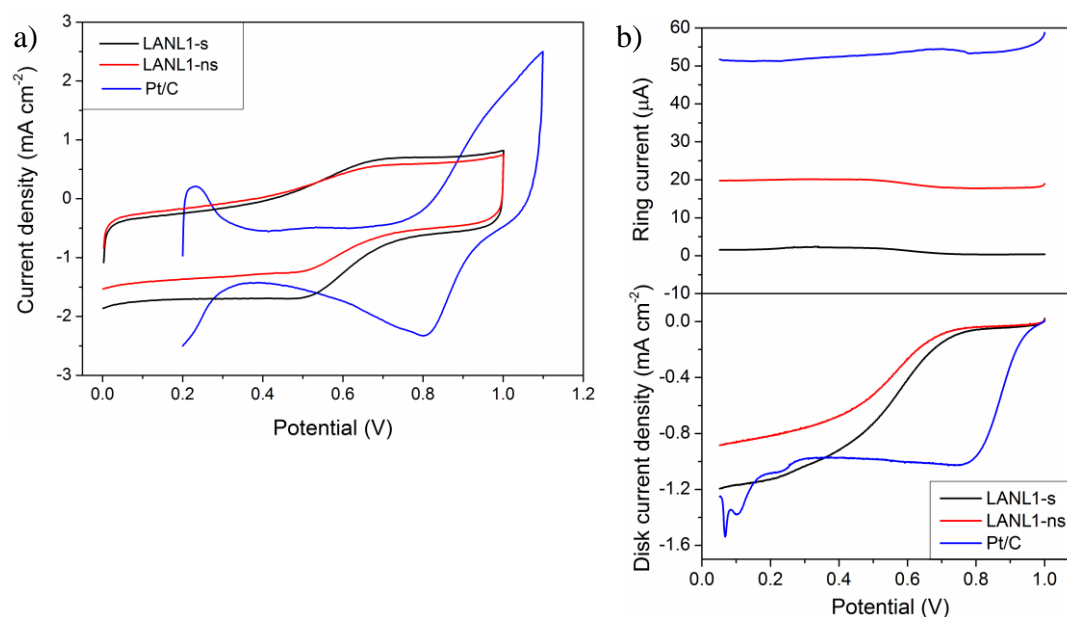


**Figure 7.8** Overlaid RRDE results for the LANL1-s, LANL1-ns and the commercial 20% Pt/C catalysts: a) CVs in air, and b) LSVs at 1200 RPM.

Interestingly, the 20%Pt/C catalyst displays the highest ring current and thus the highest amount of hydrogen peroxide. The larger CV area of the LANL1-s than LANL1-ns is evidence of a larger catalyst surface area [98]. The onset potential and disk current density in the LSV for the LANL1-s is noticeably higher than those for the LANL1-ns catalyst, while the ring current for the LANL1-s is lower than for the LANL1-ns. This indicates a better selectivity of the sieved LANL1-s towards the four-

electron ORR than the non-sieved catalyst. The observed effect of sieving can be explained by an increase in the catalyst surface area and a more uniform particle size distribution. This suggests that sieved catalysts are more effective than non-sieved for the ORR, and therefore sieving will be performed on the final stage of synthesis of all the subsequent alternative catalysts.

### 7.7.1.3 Deactivation of the LANL1 Catalyst

In order to evaluate the performance stability and resistance to ageing, RRDE measurements were repeated for the LANL1-s catalyst after a period of two months in order to evaluate. Figure 7.9 illustrates the overlaid CVs in air for the same LANL1-s catalyst freshly prepared and two months later. It is clear that a significant drop in the activity occurred, since the CV area of the two-month old catalyst is substantially less than that of the fresh catalyst, and the reduction peak current density is negligibly low. The LSVs of the deactivated LANL1-s catalyst confirm the loss of its activity towards the ORR, since the onset potential is circa 0.30 V and no diffusion limiting current is observed. In addition, the measured ring currents are several times higher than those of the freshly prepared LANL1-s catalyst. These results suggest that the LANL1 catalyst synthesized according to the technique [24] is insufficiently active and unstable to be utilized for the ORR.

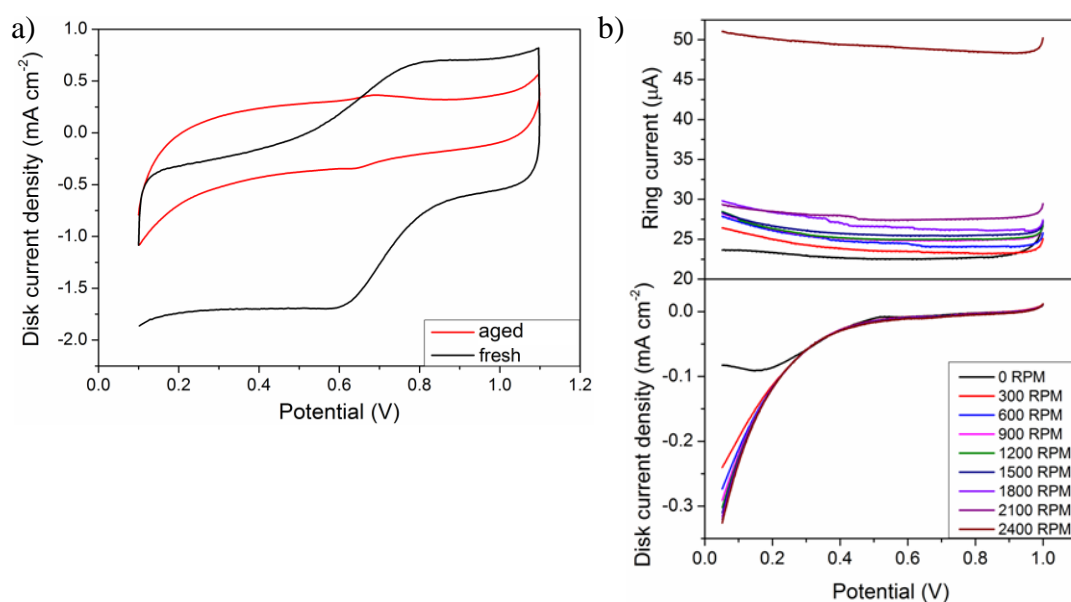


**Figure 7.9** The RRDE characterisation of the aged LANL1-s catalyst: a) the overlaid CVs in air for the aged and fresh catalyst, and b) LSVs for the aged catalyst at different electrode rotation speeds.

## 7.7.2 LANL2 Catalyst

### 7.7.2.1 Synthesis

Further, a nitrogen doped carbon catalyst has been manufactured according to the patent of the LANL group [243] and further referred to as the LANL2. All materials utilized in the catalyst synthesis are the same as in Section 7.7.1.1, but the synthesis procedure is different. Figure 7.10 shows the schematic of the catalyst synthesis technique. The LANL2 synthesis consists of two stages, the first of which is fabrication of the catalyst support containing cobalt (Co), and the second includes incorporation of iron (Fe) into the final product.

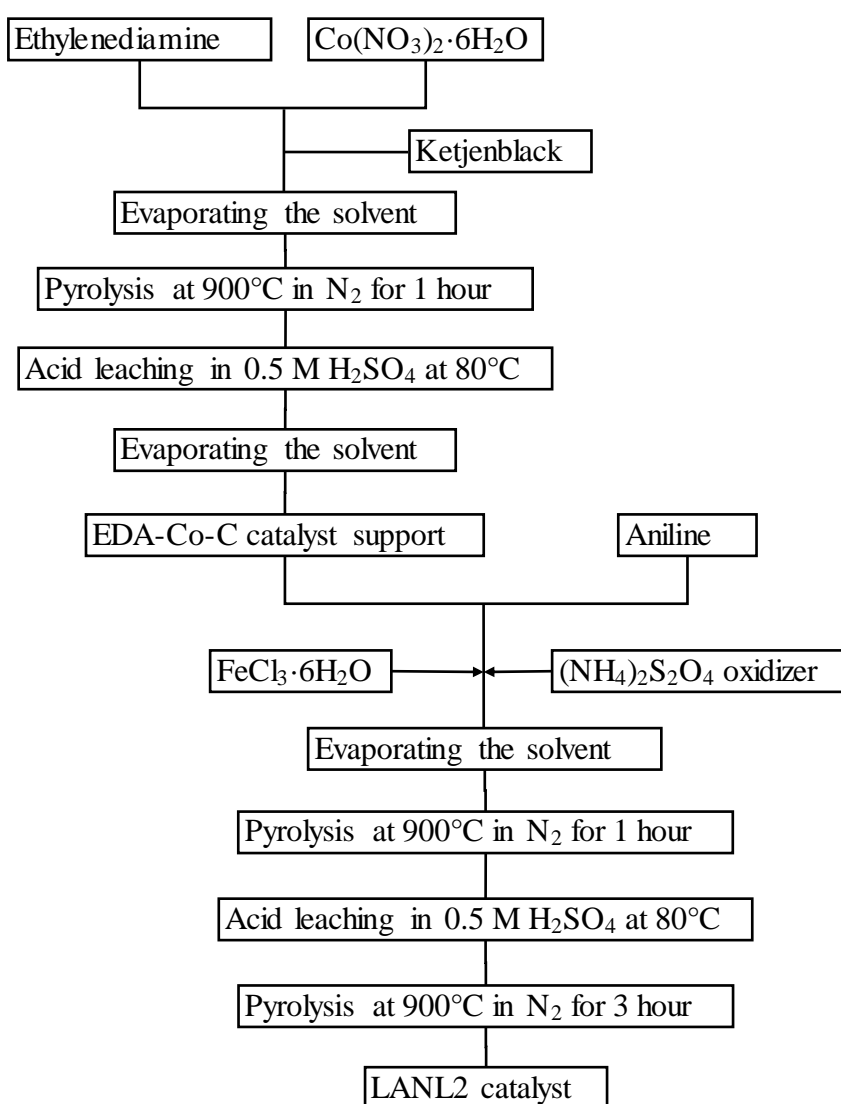


**Figure 7.10** Schematic of the LANL2 catalyst synthesis.

The synthesis was implemented as follows. 0.5 g of  $\text{Co}(\text{NO}_3)_2 \cdot 6\text{H}_2\text{O}$  was dissolved in 400 ml of ethanol and mixed with 2.0 ml of ethylenediamine (EDA) to

form a Co chelate complex. The chelate complex was added to 0.4 g of purified Ketjen Black EC 300J and dispersed ultrasonically for a few hours. The suspension was dried in the vacuum rotary evaporator and then pyrolysed at 900 °C for 1 hour in the flow of N<sub>2</sub>. After the pyrolysis, the solid was mixed with 0.5 M H<sub>2</sub>SO<sub>4</sub> in a three-neck round-bottom flask with a reflux condenser and leached at 80 °C for 8 hours. After the acid leaching, the suspension was filtered, washed with de-ionized water and vacuum-dried to obtain the EDA-Co-C catalyst support. 3 ml of aniline was dispersed in 400 ml of 0.5 M HCl in a three-neck round-bottom flask and mixed with 0.4 g of the EDA-Co-C catalyst support. The suspension in the flask was cooled down to a temperature slightly below 10°C. 3.0 g of FeCl<sub>3</sub>·6H<sub>2</sub>O and 5.0 g of (NH<sub>4</sub>)<sub>2</sub>S<sub>2</sub>O<sub>4</sub> were dissolved in 0.5 M HCl and added to the flask dropwise for 24 hours while stirring. The suspension was dried in the vacuum rotary evaporator and then pyrolysed at 900 °C for 1 hour in a N<sub>2</sub> atmosphere. The solid was mixed with 0.5 M H<sub>2</sub>SO<sub>4</sub> in a three-neck round-bottom flask with a reflux condenser and leached for 8 hours at 80 °C. The suspension was filtered, washed with de-ionized water and vacuum-dried. The solid was pyrolysed at 900 °C for 3 hours in N<sub>2</sub> flow.

#### 7.7.2.2 RRDE Characterisation

The LANL2 catalyst was characterised electrochemically using the RRDE methods in order to evaluate its activity towards the ORR. Figure 7.11 shows CVs measured in nitrogen gas and air saturated electrolyte, and LSVs at different rotation speeds. The CV in air shows the oxygen reduction peak potential of 0.63 V and the peak current of 1.82 mA cm<sup>-2</sup>. In the LSVs, the onset potential is circa 0.80 V, and the diffusion limited disk current densities and ring currents are well defined and increase with the electrode rotation speed. The highest diffusion limited disk current density at 2400 RPM is 0.94 mA·cm<sup>-2</sup>. The Koutecky-Levich analysis was performed for the current densities at 0.1 V vs. SHE. The electron transfer number *n* calculated using Equation 6.3 and the slope of the line is 3.8. This result suggests that the LANL2 catalyst catalyses predominantly a four-electron mechanism of the ORR.

The electron transfer number derived from the Koutecky-Levich plot was also calculated using the RRDE data and Equation 6.5. Figure 7.12 shows the electron transfer number plotted as a function of either electrode rotation speed or potential. It is clear that *n* increases monotonously with increasing electrode rotation speed reaching the maximum limit of 2.1, and decreases with increasing potential. Thus, this technique suggests a two-electron mechanism of the ORR. This discrepancy between the obtained electron transfer numbers may be caused by a problem in the ring current measurements.

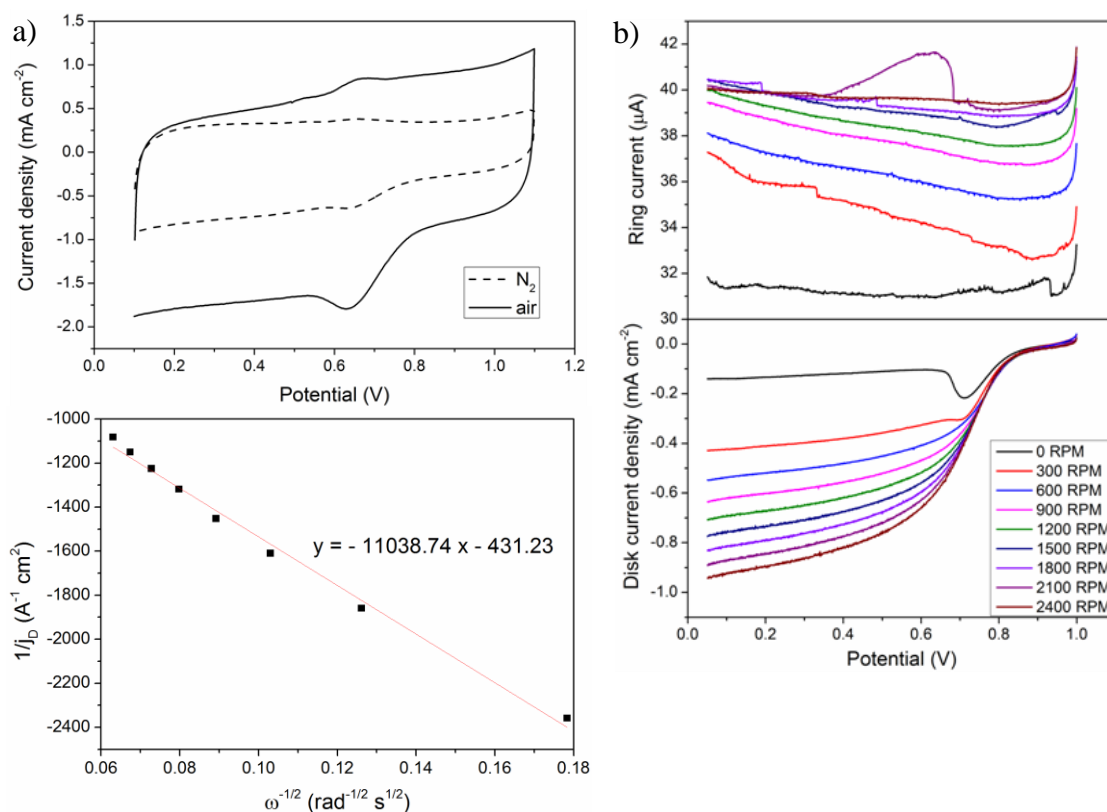


**Figure 7.11** RRDE characterisation of the LANL2 catalyst: a) CVs in  $N_2$  and air, b) LSVs at different electrode rotation speeds, shown in the legend, and c) Koutecky-Levich plot (the current density data were taken at 0.1 V vs. SHE).

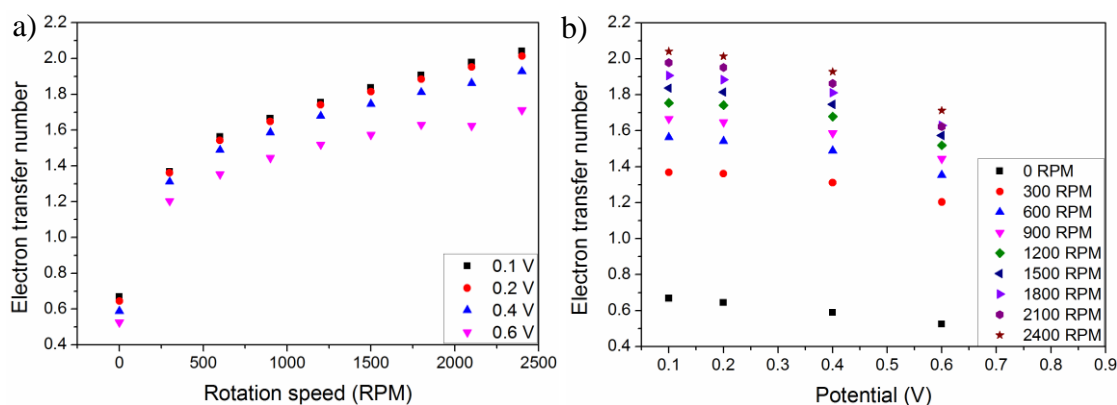


**Figure 7.12** Electron transfer numbers for the ORR on the LANL2 catalyst plotted versus a) electrode rotation speed, and b) potential.

CV and LSV using the RRDE have been performed also for Ketjen Black EC 300J in order to evaluate the ORR activity of pure carbon black. Further, the ORR activities of 20%Pt/C, carbon black and fresh LANL1-s and LANL2 catalysts have been compared by overlaying the CVs in air and the LSVs at 1200 RPM, as illustrated in Figure 7.13. In the CVs, it is clear that the commercial 20%Pt/C catalyst demonstrates the most positive peak potential of 0.81 V and the highest peak current

density of  $2.35 \text{ mA cm}^{-2}$ , followed by the LANL2 and LANL1-s catalysts with the peak potentials of circa  $0.6 \text{ V}$  and the peak current density being 1.3 times lower than that of the 20%Pt/C catalyst. The activity of carbon black is clearly far lower than those of the LANL2 and LANL1-s catalysts, and this is evidenced by the small voltammogram area as well as by the absence of well defined reduction peak.

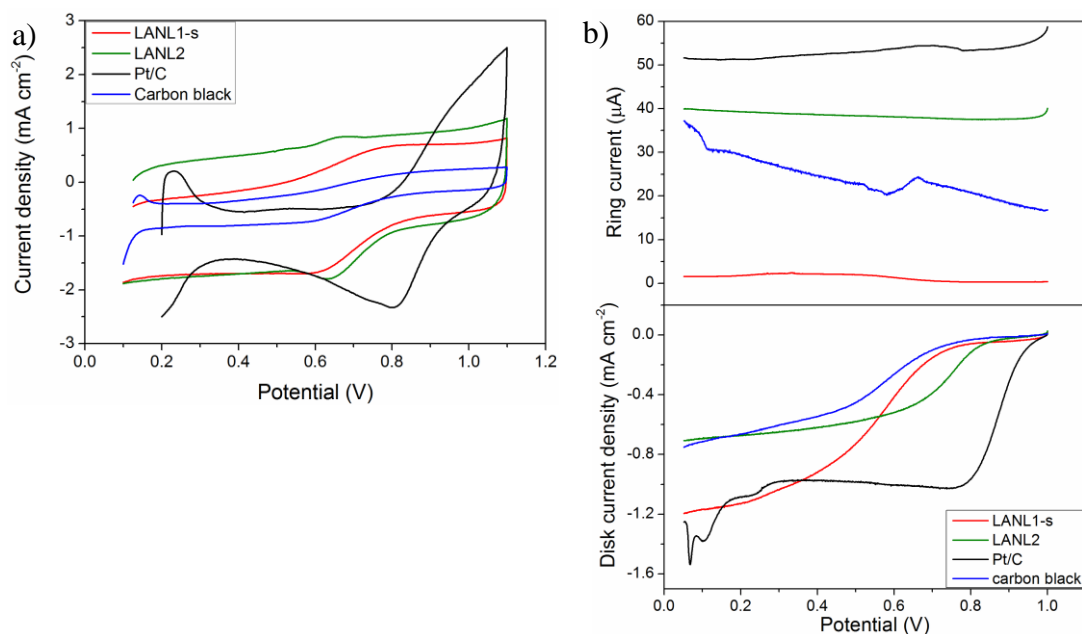


**Figure 7.13** Comparison of the RRDE results for the LANL1-s, LANL2 catalysts, commercial 20%Pt/C and carbon black: a) CVs in air, and b) LSVs at 1200 RPM.

The LSVs show that the ORR onset potentials of the 20%Pt/C and LANL2 catalysts are  $0.96$  and  $0.80 \text{ V}$ , respectively. The onset potentials for the LANL1-s and carbon black are significantly lower, circa  $0.76 \text{ V}$ . The 20%Pt/C catalyst shows a well defined diffusion limited disk current density, which is 1.5 times higher than that of the LANL2 catalyst and carbon black. Interestingly, the diffusion limiting current densities for the LANL2 and carbon black are lower than that of the LANL1-s catalyst. The ring current is highest for the 20%Pt/C catalyst followed by the LANL2, carbon black and the LANL1-s. These data indicate that although platinum based catalyst demonstrates outstanding catalytic activity, the alternative catalysts are potentially more selective towards the four-electron oxygen reduction than platinum based catalysts.

### 7.7.2.3 Reproducibility

In order to test reproducibility of the LANL2 catalyst and its electrochemical properties, the LANL2 catalyst synthesis has been repeated. The catalyst is further

referred to as the LANL-p. The results of RRDE characterisation for the LANL-p are presented in Figure 7.14. The CV shows that the ORR peak potential is about 0.59 V and the peak current is 1.59 mA cm<sup>-2</sup>. The disk current in the LSVs increases with the electrode rotation speed, however, the diffusion limited current is not defined well. Figure 7.14 c) presents the overlaid CVs in air for the LANL2 and LANL-p catalysts. It is clear that the shape of the curves is similar, however, the activity of the LANL-p is lower than that of LANL2 since both the peak potential and current are slightly lower for the LANL-p.

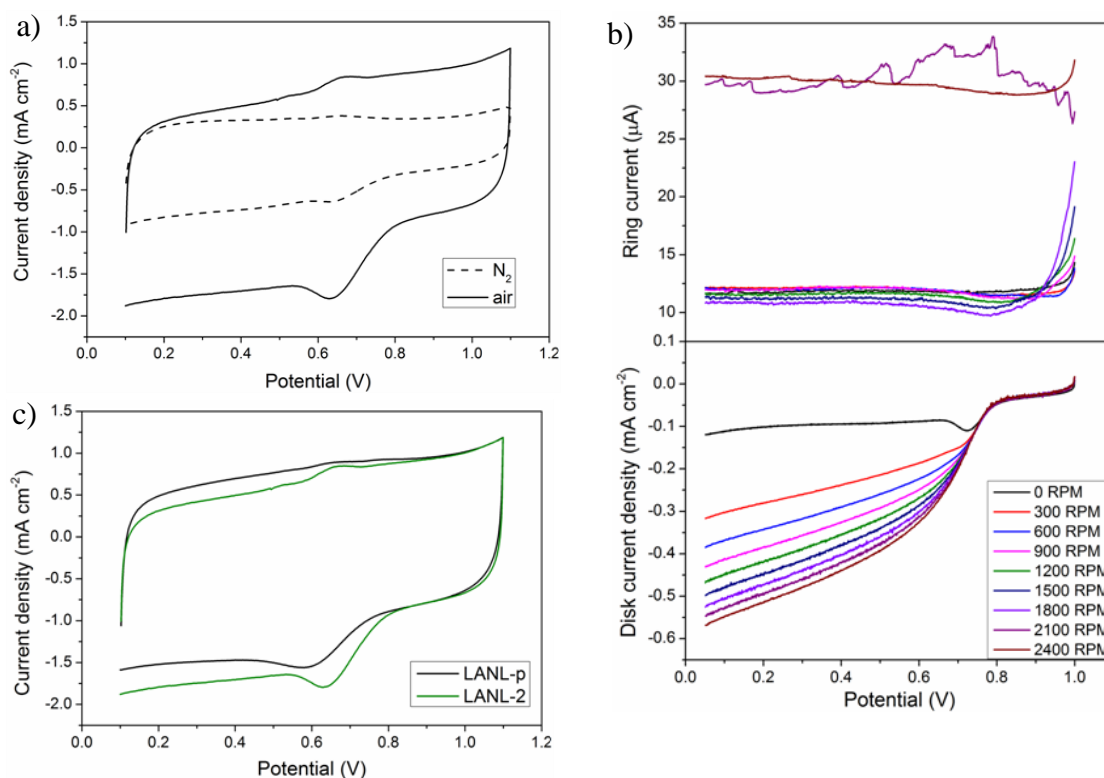


**Figure 7.14** RRDE results of the LANL-p catalyst: a) CVs in N<sub>2</sub> and air, b) LSVs at different rotation speeds, and c) CVs in air for the LANL-p and LANL2.

#### 7.7.2.4 Deactivation

To evaluate the stability of the LANL2 catalyst, the RRDE measurements have been repeated in the period of two months after the synthesis. As can be observed in Figure 7.15, the CV area of the LANL2 catalyst, measured in two months after the synthesis, has decreased compared to that measured immediately upon synthesis. This may be due to an aggregation of particles in the LANL2 catalyst, which decreases the catalyst's capacitance and surface area. The peak current density of the LANL2 catalyst after two months decreased from 1.8 to 1.1 mA·cm<sup>-2</sup> (1.6 times), but the peak potential of 0.65 V remained. This suggests that the intrinsic activity of the catalyst's

active sites has not changed, but their number has reduced due to the decreased surface area.

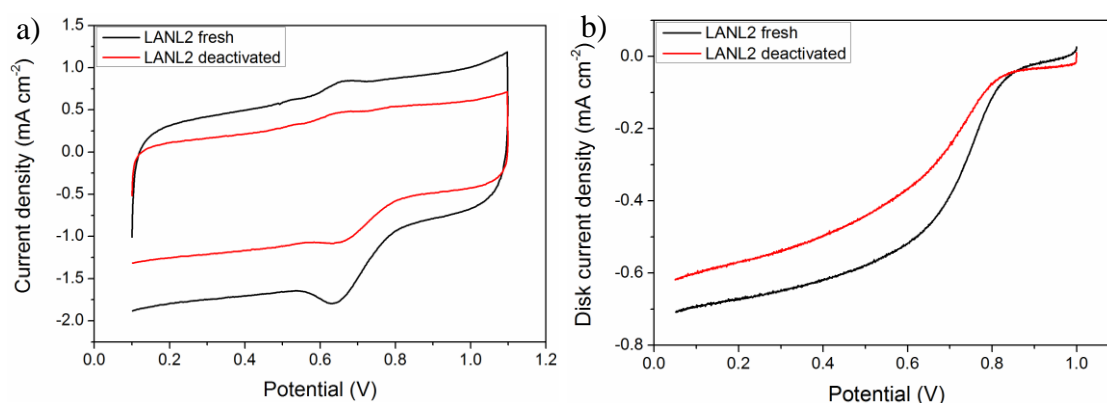


**Figure 7.15** Deactivation of the LANL2 catalyst in the period of two months a) CVs in air, and b) LSVs at 1200 RPM.

### 7.7.2.5 Physicochemical Characterisation

The LANL1-s, LANL2 and LANL1-p catalysts have been characterised using the XRD method. The XRD measurements performed over the  $2\theta$  angle range of  $10 - 70^\circ$  are shown in Figure 7.16. In both materials, two broad diffraction peaks are observed: the large peak at  $2\theta = 25^\circ$  (graphite 002) and the smaller peak at  $2\theta = 44^\circ$  (graphite 101). These peaks are associated with amorphous carbon which is the dominant phase in the two catalysts. In the LANL1-s, the remaining smaller peaks are attributed to magnetite  $\text{Fe}_3\text{O}_4$  and iron cobalt oxide  $\text{CoFe}_2\text{O}_4$ . In the LANL2 catalyst, iron and cobalt sulfides and iron-cobalt alloy have been detected. The absence of small sharp peaks in the LANL-p XRD pattern indicates that non-carbon crystalline species have been effectively removed from the surface by acid-leaching. Therefore, the transition metal sulphides on the LANL2 catalyst do not account for its relatively high catalytic activity.

XPS analysis has been performed for the LANL2 catalyst to identify the chemical state of elements on the surface. The elemental surface composition, derived from the XPS measurements, is presented in Table 7.1. The N atomic ratio of 2.52% evidences that N doping to carbon has been successful. Also, a relatively significant amount of O and trace amounts of S, Si, Fe and Co have been identified. The XPS survey and high resolution spectra of the C1s and N1s peaks are presented in Figure 7.17. The XPS survey reveals that the LANL2 catalyst is composed mainly of carbon (C1s = 284.5 eV), oxygen (O1s = 532.0 eV) and nitrogen (N1s = 400.5 eV) as well as a small amount of sulphur (S2p = 165.1 eV). The amounts of other elements are too small to be observed and do not reveal clear peaks.

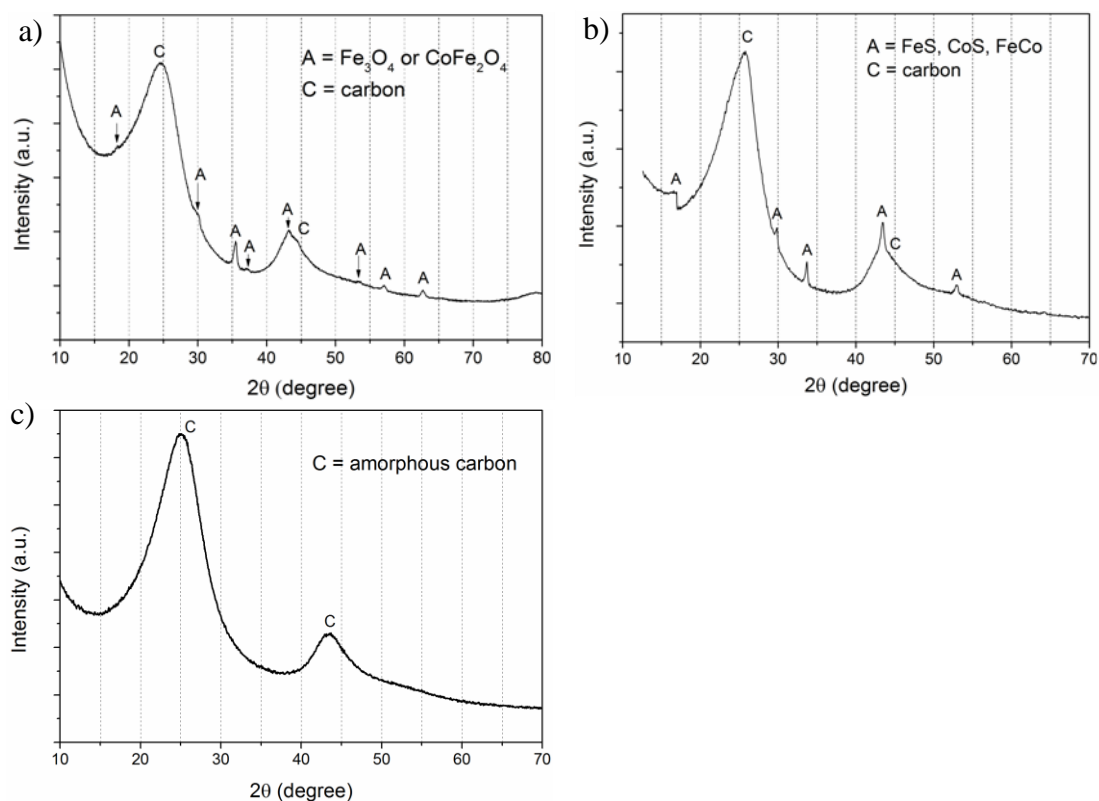


**Figure 7.16** The XRD patterns of a) LANL1-s, b) LANL2, and c) LANL1-p catalysts.

**Table 7.1** Elemental composition of the LANL2 catalyst from the XPS analysis.

Element	C	O	N	S	Si	Fe	Co
Content, at. %	93.09	3.15	2.52	0.77	0.40	0.05	0.02

The high resolution C1s and N1s spectra have been deconvoluted by fitting them with the Lorentzian-Gaussian multi-peak technique [90]. The C1s spectrum indicates the presence of four forms of carbon:  $sp^2$  hybridised carbon of graphitic planes with a binding energy of 284.6 eV,  $sp^2$  carbon bound to N at 285.4 eV,  $sp^3$  hybridised carbon bound either to N or O at 287.8 eV, and carboxyl carbon at 289.9 eV [246]. It is clear that most of the carbon exists in the graphitic state. The N1s spectrum indicates the existence of three types of N: graphitic N with the main central peak at 401.0 eV, pyridinic N at 398.5 eV, and oxidized pyridinic N at 403.3 eV [233, 246].

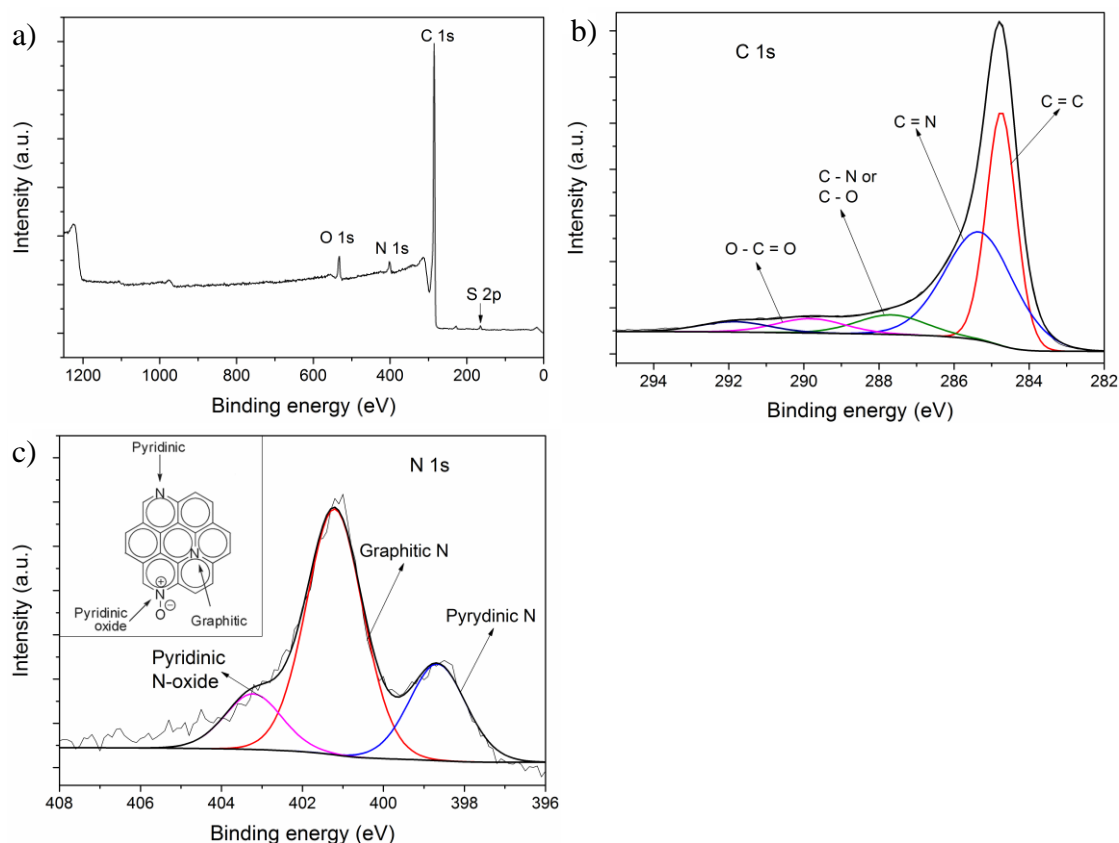


**Figure 7.17** XPS analysis of the LANL2 catalyst: a) survey, and the deconvoluted high resolution b) C1s, and c) N1s spectra.

### 7.7.2.6 PEM Fuel Cell Test

The PEM fuel cell tests were performed as follows. First, the open circuit potential (OCP) was measured for about 5 minutes until stabilization. After the OCP measurement, cyclic voltammetry was performed by scanning the cell potential between the OCP and 50 to 80 mV at a scan rate of 5 mV/s. The electrochemical impedance spectroscopy (EIS) measurements were taken at the cell potential of circa 750 mV with frequencies in the range of 10 kHz – 0.1 Hz.

The LANL2 catalyst has shown superior catalytic performance in RRDE tests and therefore has been tested in the in-house PEM fuel cell. The membrane electrode assembly (MEA) was fabricated with the LANL2 catalyst loading of 4 mg/cm<sup>2</sup> at the cathode side, and platinum loading of 0.25 mg<sub>Pt</sub>/cm<sup>2</sup> of the commercial 20% Pt/C catalyst at the anode side.

Briefly, the cathode catalyst ink has been prepared as follows. 161.84 mg of the LANL2 catalyst was mixed with a few drops of de-ionized water and ultrasonicated for a few minutes. 48.6 ml of 50% ethanol and 571.2 mg of 5% Nafion<sup>®</sup> were added to the LANL2 and ultrasonicated for 30 minutes. The obtained catalyst ink was sprayed onto the 3.4×3.4 cm<sup>2</sup> MPL-coated GDL with 11.56 cm<sup>2</sup> active area until the mass of

the dry catalyst and Nafion<sup>®</sup> mixture was 54.4 mg. After depositing the catalyst ink, 115.6 mg of 5% Nafion<sup>®</sup> was sprayed on the coated GDL.

The anode catalyst ink was prepared as follows. 50.58 mg of the 20%Pt/C catalyst has been ultrasonicated with a few drops of DI water for a few seconds. 15 ml of 50% ethanol and 178.5 mg of 5% Nafion<sup>®</sup> were added to the catalyst and ultrasonicated for 30 minutes. The catalyst ink was deposited onto the 3.4×3.4 cm<sup>2</sup> GDL with 11.56 cm<sup>2</sup> active area until the mass of the dry catalyst and Nafion<sup>®</sup> was 17 mg. After depositing the catalyst ink on the GDL, 115.6 mg of 5% Nafion<sup>®</sup> was sprayed onto the coated GDL.

The MEA was fabricated by hot-pressing the coated anode and cathode GDLs with a polymer electrolyte membrane between them at 130 °C and 0.6 tonnes (600 kg) for 3 minutes, with subsequent forced cooling to 60 °C. In the fuel cell test, hydrogen flow at the anode has been set at 0.1 ml/min, and air flow at the cathode at 0.2 ml/min. The polarisation curve, impedance spectrum and performance durability have then been measured.

Figure 7.18 shows the polarisation and power density curves obtained for two MEAs, in which the cathode catalyst is the LANL2 and commercial 20%Pt/C, respectively. It is clear that the performance of the LANL2 catalyst is substantially lower than that of 20%Pt/C. For the MEA with the LANL2 cathode, current density at 0.6 V is 10.0 mA cm<sup>-2</sup>, and this is 88.5% lower than for the MEA with 20%Pt/C (87.0 mA cm<sup>-2</sup>). The peak power density for the LANL2 MEA is 14.0 mW cm<sup>-2</sup>, which is 78.1% lower than 64.4 mW cm<sup>-2</sup> delivered by the 20%Pt/C MEA.

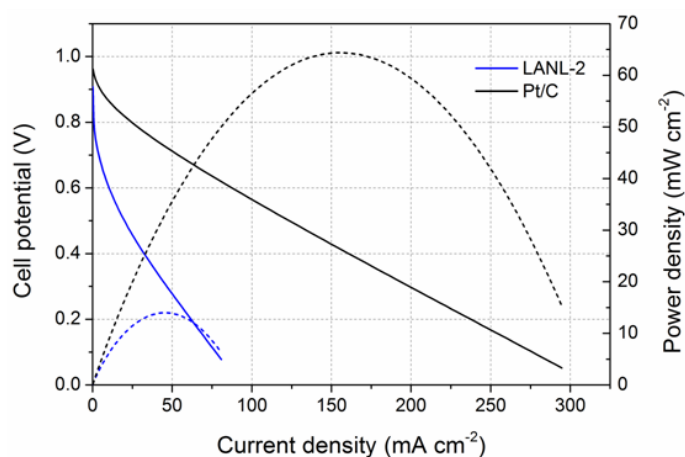


**Figure 7.18** Polarisation (solid line) and power density (dashed line) of the MEAs with LANL2 (blue) and commercial 20%Pt/C (black) in the in-house PEM fuel cell test.

The results of electrochemical impedance spectroscopy (EIS) for the MEAs with the LANL2 and 20%Pt/C at the cathode are presented in Figure 7.19. It is clear that

both ohmic and kinetic (charge transport) resistance of the LANL2 catalyst is significantly larger than those of the 20%Pt/C. Ohmic resistance of the LANL2 is 0.25 Ohm, which is 1.47 times higher than that of the 20%Pt/C catalyst (0.17 Ohm). The kinetic resistance, measured as the diameter of the EIS arc, is 0.18 Ohm for the 20%Pt/C catalyst. The arc of kinetic resistance of the LANL2 catalyst is not complete and spans outside of the measurement range. This indicates that the kinetic resistance of the LANL2 catalyst is considerable, and the ORR kinetics on the LANL2 cathode catalyst is significantly slower than on the 20%Pt/C catalyst.

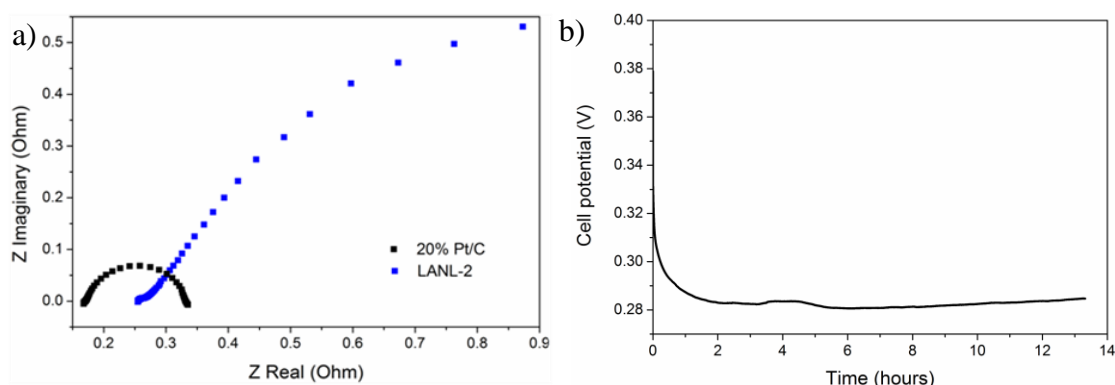


**Figure 7.19** a) The EIS spectra of the MEAs with the LANL2 and commercial 20%Pt/C catalysts, and b) performance stability of the MEA with the LANL2 catalyst in the PEM fuel cell test.

In measurement of performance stability of the PEM fuel cell with the LANL2 catalyst at the cathode, current has been held constant while the cell potential was monitored. After an initial drop from 0.38 to 0.29 V, the potential reaches a steady state and remains constant for more than 10 hours. Although this measurement is not a conventional durability test, it indicates that the carbon based catalyst can provide initial stability of PEM fuel cell operation.

## 7.8 P doped Carbon Catalysts

### 7.8.1 Synthesis

The following organic P precursors were employed for the synthesis of the P doped carbon catalyst:

- triphenylphosphine oxide (TPPO),
- 1,2-Bis[(2S,5S)-2,5-dimethylphospholano]benzene mono-oxide Met-BozPhos, and
- (+)-1,2-Bis[(2S,5S)-2,5-dimethylphospholano]benzene (Met-Duphos).

Chemical structures of the three P organic compounds are shown in Figure 7.20. The P precursors were used as ligands in chelating reactions with transition metals (Fe and Co) in the catalyst syntheses. The aim is to anchor efficiently the chelate compounds to the carbon support and thus ensure that P is deposited on the carbon in sufficient amount. At the same time, coordination of the P atoms to three C atoms in these compounds provides a prototype of P doped carbon framework.

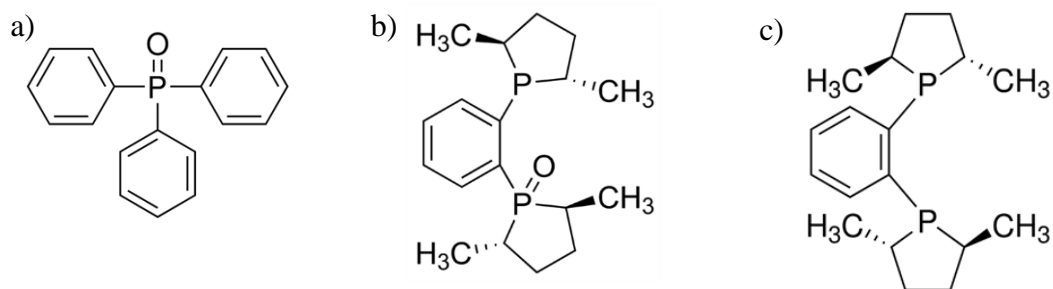
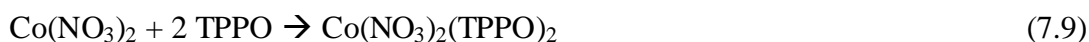


**Figure 7.20** Chemical structures of a) triphenylphosphine oxide, b) Met-BozPhos, and c) Met-DuPhos molecules.

The technique of P doped carbon catalyst synthesis shown in Figure 7.21 has similar steps with the LANL2 synthesis. It also includes two stages: (i) synthesis of the Co-P catalyst support using a cobalt salt and TPPO, and (ii) synthesis of the supported catalyst using an iron salt and a second P precursor, either Met-BozPhos or Met-DuPhos. The effect of pyrolysis temperature has also been studied, namely, the catalysts synthesised using Met-BozPhos and Met-DuPhos have been heat treated at 700 and 800 °C, respectively. These catalysts are hereafter referred to as the LP1-700 and LP1-800.

The Co-P support was synthesised as follows. 1.43 g of TPPO and 0.75 g of  $\text{Co}(\text{NO}_3)_2 \cdot 6\text{H}_2\text{O}$  were dissolved in 5-7 ml of ethanol in separate vessels. The two solutions were mixed and heated to approximately 80 °C to form a chelate complex. The required amounts of the cobalt salt and TPPO were calculated based on the stoichiometry of the chelating reaction:



0.6 g of purified Ketjen-black EC 300J was added to the chelate complex and dispersed ultrasonically for a few hours. The suspension was filtered, washed with DI water and vacuum-dried. To study the effect of different pyrolysis temperature, the solid was divided into three parts, each weighing approximately 0.67 g. The three parts were pyrolysed at 700, 800 and 900 °C for 1 hour in flowing  $\text{N}_2$  gas and then

ground to powder using a mortar and pestle. The masses of the pyrolysed solids were  $m_{700^{\circ}\text{C}} = 0.28$  g,  $m_{800^{\circ}\text{C}} = 0.31$  g, and  $m_{900^{\circ}\text{C}} = 0.31$  g.

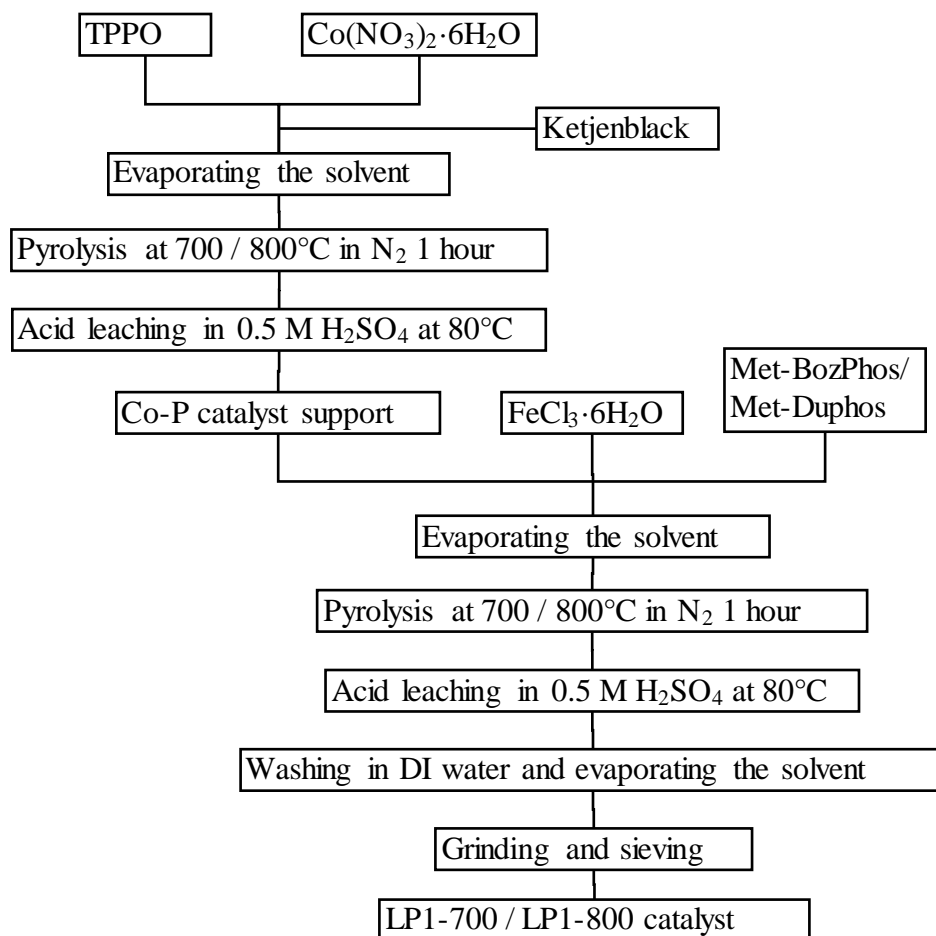


**Figure 7.21** Schematic of syntheses of the P doped carbon catalysts.

To the author's knowledge, chelating reactions of Met-BozPhos and Met-Duphos have not been reported in the scientific literature. In order to study the reactivity of Met-BozPhos in the chelating reactions with iron both in Fe(III) and Fe(II) oxidation states,  $\text{FeCl}_3 \cdot 6\text{H}_2\text{O}$  and  $\text{FeCl}_2 \cdot 4\text{H}_2\text{O}$  salts have been utilised, respectively. Fe may be coordinated with either two P atoms or P and O atoms of one Met-BozPhos or Met-Duphos molecule, i.e. the metal to ligand ratio is 1:1. This coordination ratio is proposed due to the large size of both P precursors and thus their steric restrictions.

First, the reactivity of Met-BozPhos with Fe(III) has been investigated by dissolving 0.1 g of Met-BozPhos and 0.05 g of  $\text{FeCl}_3 \cdot 6\text{H}_2\text{O}$  in 5-7 ml of ethanol in separate beakers at slightly elevated temperature. The compounds have formed transparent and yellow solutions, respectively, and have been mixed together. A dark brown precipitate has formed, evidencing a successful chelating reaction. The reaction can be expressed as follows:



Chelating of Met-BozPhos with Fe(II) was performed by dissolving 0.1 g of Met-BozPhos and 0.06 g of  $\text{FeCl}_2 \cdot 4\text{H}_2\text{O}$  separately in ethanol at elevated temperature. The compounds formed transparent and light-green solutions, respectively. After mixing together, a transparent brown solution has formed. An oxidizing agent ammonium persulfate,  $(\text{NH}_4)_2\text{S}_2\text{O}_8$ , has been added to oxidize Fe(II) to Fe(III), and the solution turned opaque brown. This colour change can be explained by formation of  $\text{Fe}(\text{OH})_3$  instead of the chelate complex.

The two suspensions of Met-BozPhos chelate compounds were mixed together, and 0.28 g of the Co-Pcatalyst support (700 °C pyrolysed) was added and ultrasonicated for several hours. The resulting suspension was filtered and vacuum-dried in the vacuum rotary evaporator. The solid was ground in a mortar with a pestle and then pyrolysed at 700 °C for 1 hour in flowing  $\text{N}_2$  gas. After the pyrolysis, the solid was ground and then acid-leached in 0.5 M  $\text{H}_2\text{SO}_4$  for 8 hours at 80 °C under reflux conditions. The suspension was filtered, washed with DI water, dried in the vacuum rotary evaporator, ground in a mortar with pestle and sieved. The obtained material is referred to as the LP1-700 catalyst.

Met-Duphos as a P precursor has been utilised to synthesise the LP1-800 catalyst. 0.1 g of Met-Duphos and 0.05 g of  $\text{FeCl}_3 \cdot 6\text{H}_2\text{O}$  were dissolved in ethanol separately at a slightly elevated temperature, forming transparent and yellow solutions, respectively. After mixing the solutions together, a green precipitate of a chelate appeared. The chelating reaction can be expressed as follows:



The chelate complex was mixed with 0.31 g of the Co-P catalyst support pyrolysed at 800 °C and then ultrasonicated for several hours. The suspension was filtered and vacuum-dried. The obtained solid was ground in a mortar with a pestle and pyrolysed at 800 °C for 1 hour in flowing  $\text{N}_2$  gas. After the pyrolysis, the solid was ground and leached in 0.5 M  $\text{H}_2\text{SO}_4$  for 8 hours at 80 °C at reflux conditions. The suspension was filtered, washed with de-ionized water, dried in the vacuum rotary evaporator, ground in a mortar with a pestle and sieved.

## 7.8.2 RRDE Characterisation

The LP1-700 and LP1-800 catalysts were characterised electrochemically using the RRDE methods, and the results are shown in Figure 7.22. The CVs of both

catalysts in nitrogen and air bubbled electrolyte almost coincide in shape, and the reduction peak at circa 0.6 V is negligible. This evidences that the ORR activity of both catalysts is very low.

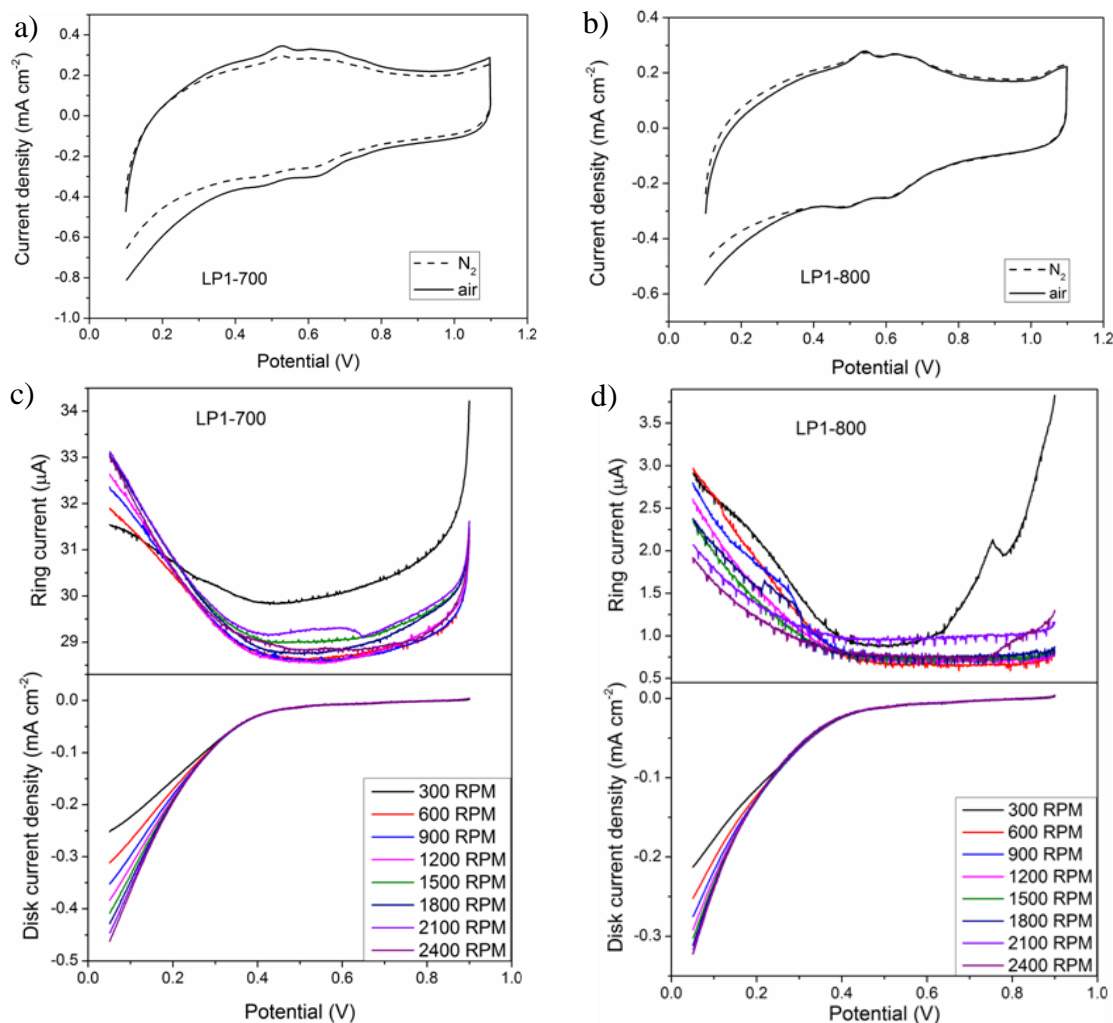


**Figure 7.22** RRDE characterisation of the synthesized P doped carbon catalysts: CVs in N<sub>2</sub> and air of the a) LP1-700, and b) LP1-800 b) catalysts; and LSVs of c) LP1-700, and d) LP1-800 catalysts at different electrode rotation speeds.

In the LSVs, the disk current densities of both catalysts increase with the rotation speed increase, however, there is no diffusion limiting current observed. The onset potential of the oxygen reduction is circa 0.40 V for both catalysts, i.e. very low compared to that of the LANL2 catalyst (0.80 V). Thus, the overpotential of the ORR on the synthesized P doped catalysts is  $1.23 - 0.40 = 0.83$  V, i.e. significant and unacceptable for practical application. The ring currents in the LSVs of both catalysts show a synchronous increase after reaching the onset potential and grow proportionally to the disk current densities. This suggests that the ORR on the catalysts takes predominantly a two-electron pathway leading to hydrogen peroxide

formation rather than water. The significant overpotential and an ORR mechanism yielding hydrogen peroxide on the synthesised P doped catalysts indicate low efficiency.

### 7.8.3 The Effect of Final Pyrolysis

To improve the catalytic performance of the as-synthesised LP1-700, it has been additionally pyrolysed at 700 °C for 1 hour in flowing N<sub>2</sub> gas, in total having undergone three pyrolyses. The pyrolysed catalyst is further referred to as the LP1-700-3-pyr. The results of the LP1-700-3-pyr electrochemical characterisation are presented in Figure 7.23.

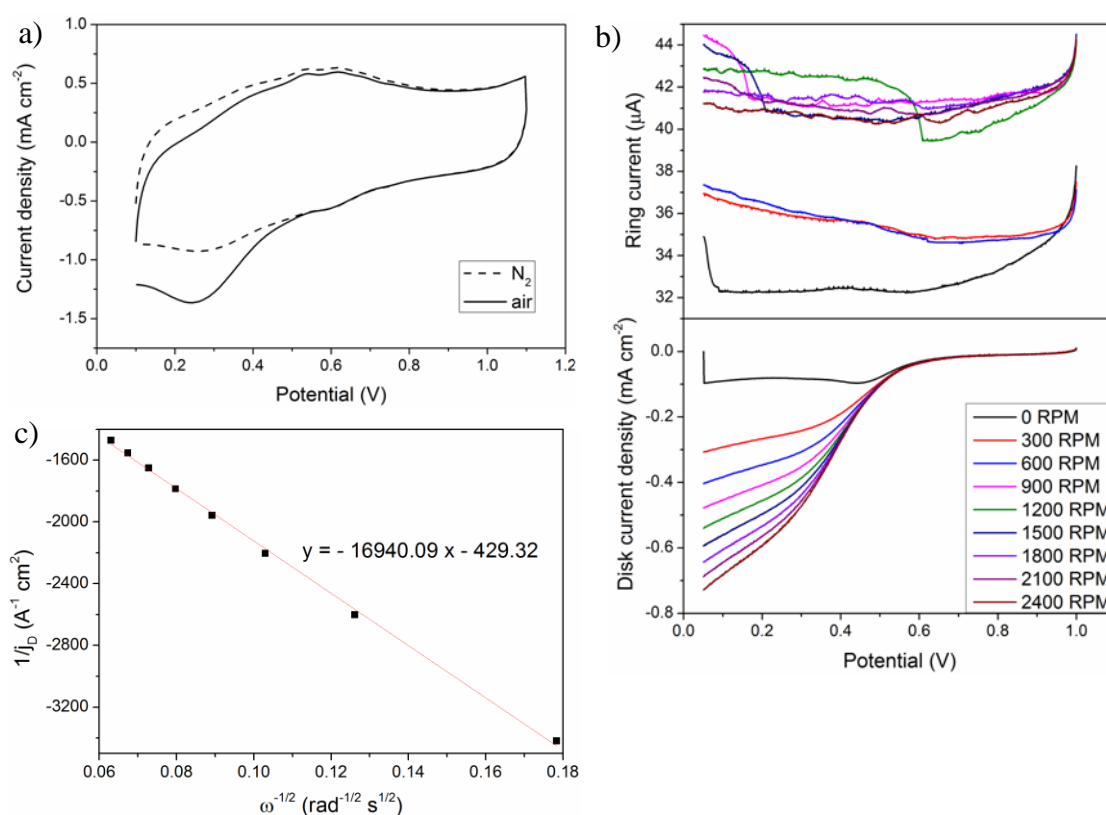


**Figure 7.23** RRDE characterisation of the LP1-700-3-pyr catalyst: a) CVs in N<sub>2</sub> and air, b) LSVs at different electrode rotation speeds, and c) Koutecky-Levich plot (the current density data were taken at 0.1 V vs. SHE).

The CVs in nitrogen and air saturated electrolyte show the oxygen reduction peak potential at 0.25 V and the peak current density of 1.4 mA·cm<sup>-2</sup>. The disk current densities of the LP1-700-3-pyr in the LSVs increase with increasing electrode rotation speed, however, the diffusion limiting current is clearly observed only at zero RPM. The onset potential of the ORR is circa 0.50 V, which is 0.10 V higher than that of the as-synthesised catalyst. The ring currents show a trend to increase with the rotation

speed but remain relatively constant over the swept potential range, thus indicating a possibility of a four-electron ORR pathway. Thus, the final heat treatment noticeably improved the ORR activity of the P doped carbon catalyst, and this final pyrolysis procedure is performed in the following catalyst syntheses.

The Koutecky-Levich analysis was performed for the current densities at 0.1 V to calculate the electron transfer number  $n$ . Using the obtained slope of the Koutecky-Levich plot,  $n$  is found to be 2.5, i.e. a two-electron mechanism of the ORR is likely to take place on the LP1-700-3-pyr catalyst. The electron transfer number was also calculated using the ring currents data and Equation 6.5 for different electrode rotation speeds and potentials, as shown in Figure 7.24. The electron transfer number increases with increasing electrode rotation speed and decreases with increasing potential. The highest electron transfer number obtained using this technique is 1.9. These values are noticeably lower compared to those obtained for the 20%Pt/C and LANL2 catalyst and indicate that the ORR proceeds through a two-electron mechanism on the synthesised LP1-700-3-pyr catalyst.

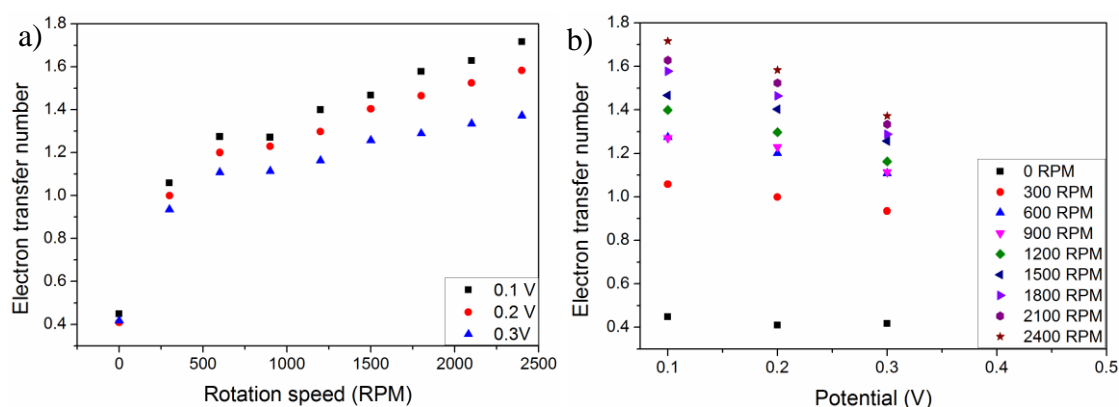


**Figure 7.24** Electron transfer numbers for the ORR on the LP1-700-3-pyr catalyst plotted versus a) electrode rotation speed, and b) potential.

The positive effect of final pyrolysis on catalytic activity is illustrated in Figure 7.25, where the CVs in air and LSVs at 1200 RPM are overlaid for the LP1-700, LP1-800, and LP1-700-3-pyr catalysts. The CV area of the LP1-700-3-pyr catalyst is substantially larger than that of the other two materials. This indicates that final pyrolysis increases a catalyst's surface area and capacitance in the electrochemical measurements.

In addition, a pronounced reduction peak is observed for the pyrolysed catalyst, but not for the as-synthesised catalysts. The disk current density of the LP1-700-3-pyr LSV shows both higher onset potential and diffusion limited current compared to the other two catalysts. The LSV ring current of the LP1-700-3-pyr is the highest, followed by the LP1-700 and the LP1-800 catalysts. This indicates that the

LP1-700-3-pyr generates somewhat larger amount of hydrogen peroxide than the other two catalysts.

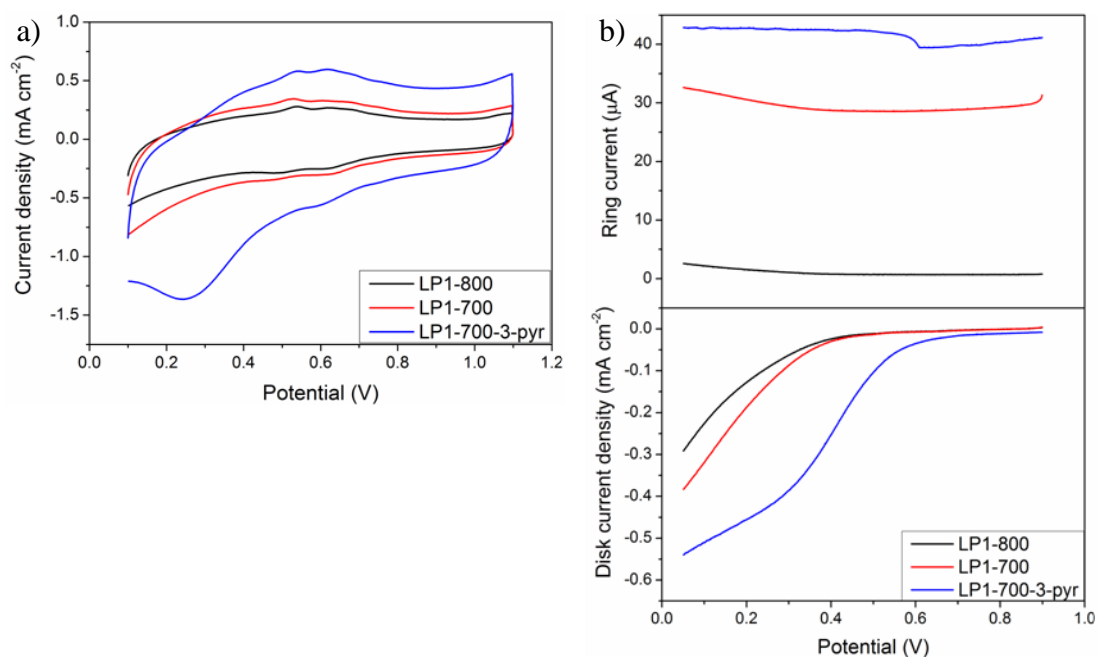


**Figure 7.25** Comparison of the RRDE results for the LP1-800, LP1-700 and LP1-700-3-pyr catalysts: a) CVs in air, and b) LSVs at 1200 RPM.

#### 7.8.4 Physicochemical Characterisation

The LP1-700-3-pyr has been investigated by XRD as Figure 7.26 illustrates. The XRD pattern featuring the two broad peaks at  $2\theta = 25$  and  $44^\circ$  confirms the amorphous structure of carbon in the catalyst. The multiple sharp peaks observed in the  $10$  to  $45^\circ$   $2\theta$  angle range are assigned to iron or cobalt metaphosphates  $\text{Fe}(\text{PO}_3)_2$  and  $\text{Co}(\text{PO}_3)_2$ .

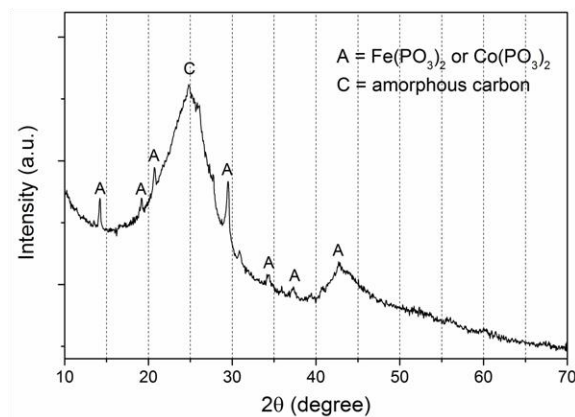


**Figure 7.26** The XRD pattern of the LP1-700-3-pyr catalyst.

An XPS analysis of the LP1-700 catalyst has provided information on the chemical composition of its surface. The elemental composition of the catalyst surface derived from the XPS survey is shown in Table 7.2. The amount of O (3%) in carbon is significantly higher than the amounts of the other elements and, most importantly, than that of P (0.3%). Notably, there has been identified 0.3% of N and S and 0.4% of Si. N and S may originate from  $\text{Co}(\text{NO}_3)_2$  and  $\text{H}_2\text{SO}_4$ , and the Si from the glass walls of chemical glassware used.

**Table 7.2** Elemental composition of the LP1-700 catalyst derived from the XPS analysis.

<b>Element</b>	<b>C</b>	<b>O</b>	<b>N</b>	<b>P</b>	<b>S</b>	<b>Si</b>
Content, at. %	95.6	3.0	0.3	0.3	0.3	0.4

The XPS survey and the deconvoluted high resolution C 1s and P 2p spectra of the LP1-700 are illustrated in Figure 7.27. The survey demonstrates that the catalyst's surface is composed predominantly of C and O, while the peaks of the other identified elements present in trace amounts are not clearly observed. The significant O 1s peak may appear due to the exposure of the material to the air during the LP1-700 catalyst fabrication process.

The high resolution C 1s XPS spectrum has four deconvoluted contributions. The main peak centred at 284.6 eV corresponds to  $\text{sp}^2$  carbon, which is predominant state of carbon in the catalyst. The smaller peak at 285.7 eV suggests the existence of  $\text{O}=\text{C}(\text{sp}^2)$  bonds, since O is present on the surface in an abundant amount compared to the trace amounts of P and other elements. The other two flat peaks are ascribed to  $\text{O}-\text{C}(\text{sp}^3)$  and carbonates.

The nature of P bonding is illustrated in the high resolution P 2p spectrum. The deconvoluted contributions appearing at 135.3, 134.1 and 133.0 eV are assigned to high oxidation states of P, namely, phosphorus oxide (V), metaphosphate and pyrophosphate, respectively. The contribution at 131.9 eV is assigned to the P-C bonding of triphenylphosphine-type [247] and indicates that P atoms have been partially incorporated into the carbon structure. According to the results of the ORR modelling, this P doped carbon should be responsible for the catalytic activity. However, the XPS results show as little as 0.3% of P on the surface, more than half of which is ascribed to high oxidation states. Therefore, a method of more efficient incorporation of P into carbon should be developed.

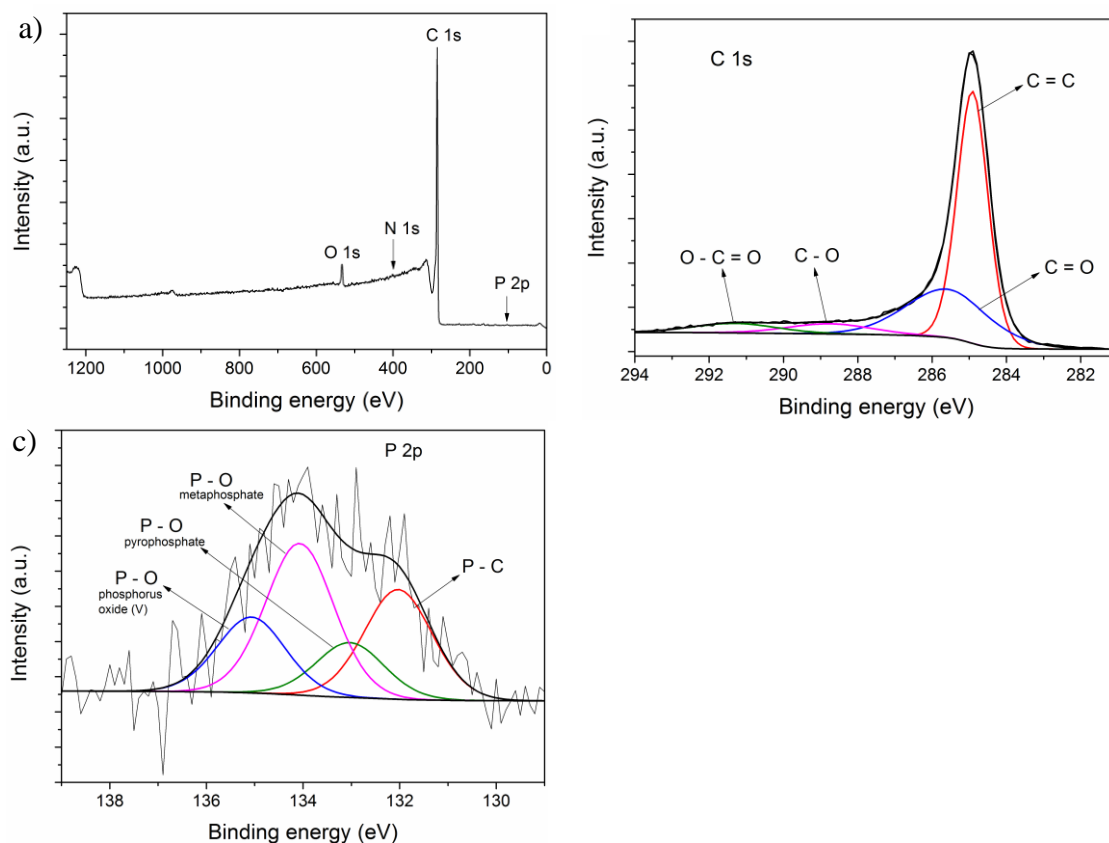


**Figure 7.27** XPS analysis of the LP1-700 catalyst: a) XPS survey; deconvoluted high resolution b) C 1s, and c) P 2p spectra.

## 7.9 N and P Co-doped Carbon Catalyst

### 7.9.1 Synthesis

A novel N and P precursor has been tested in order to synthesise N and P co-doped carbon catalyst, which is diphenyl-2-pyridylphosphine ( $\text{Ph}_2\text{PPy}$ ), shown in Figure 7.28. Since  $\text{Ph}_2\text{PPy}$  can form chelate complexes with transition metals [248], it has been used as a ligand in chelating reactions with transition metals in order to efficiently deposit the N,P chelate compounds on carbon particles.

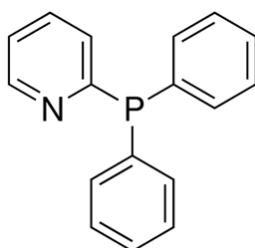
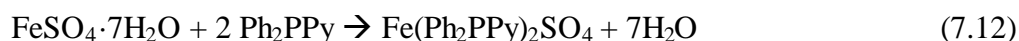


**Figure 7.28** Chemical structure of diphenyl-2-pyridylphosphine.

The catalyst synthesis technique is similar to that in Figure 7.21. The difference is the utilizing Ph<sub>2</sub>PPy instead of the second P precursor and pyrolysis at 800 °C after the last step of solvent evaporation. The Co-P catalyst support was synthesized using triphenylphosphine oxide (TPPO) as described in Section 7.8.1. After that, 0.21 g of FeSO<sub>4</sub>·7H<sub>2</sub>O was dissolved in a few ml of ethanol and de-ionized water, forming slightly opaque pale yellow solution. 0.4 g of Ph<sub>2</sub>PPy was dissolved in ethanol, forming transparent yellow solution. The two solutions were mixed to obtain a precipitate of a chelate complex precipitate of orange-red colour. The chelating reaction is expressed as follows:



Also, the chelating reaction has been conducted using FeCl<sub>3</sub>·6H<sub>2</sub>O in order to study the ability of Ph<sub>2</sub>PPy to form chelate complexes. 0.123 g of FeCl<sub>3</sub>·6H<sub>2</sub>O and 0.4 g of Ph<sub>2</sub>PPy were dissolved in ethanol separately. The two solutions were mixed at a slightly elevated temperature and formed a chelate complex suspension of semi-transparent brown colour. The reaction is expressed as follows:



The suspension was mixed with 0.31 g of the catalyst support pyrolysed at 900 °C, described in Section 7.8.1, ultrasonicated for a few hours, and then dried in the vacuum rotary evaporator. The solid was ground in a mortar with a pestle and heat-treated at 800 °C for 1 hour in flowing N<sub>2</sub> gas. The pyrolysed powder was leached in 0.5 M H<sub>2</sub>SO<sub>4</sub> for 8 hours at 80 °C under reflux conditions. The resulting suspension was filtered, washed with de-ionized water, vacuum-dried and the finally pyrolysed at 800 °C for 1 hour in N<sub>2</sub> flow. The powder was ground and sieved. The obtained material is further referred to as the NP800 catalyst.

## 7.9.2 RRDE Characterisation

The RRDE characterisation of the NP800 catalyst is shown in Figure 7.29. The CVs suggest that in air saturated electrolyte, the catalyst displays significantly higher current density in the peak region than in nitrogen saturated electrolyte. However, the peak potential of circa 0.24 V indicates the existence of a very high overpotential of the ORR on the catalyst. The LSVs show the onset potential of circa 0.50 V and non-defined diffusion limiting currents. The ring currents do not display dependence on the electrode rotation speed, but increase simultaneously with the disk current density

starting from the onset potential. This indicates that the ORR on the synthesized N,P co-doped catalyst proceeds via a two-electron pathway yielding hydrogen peroxide.

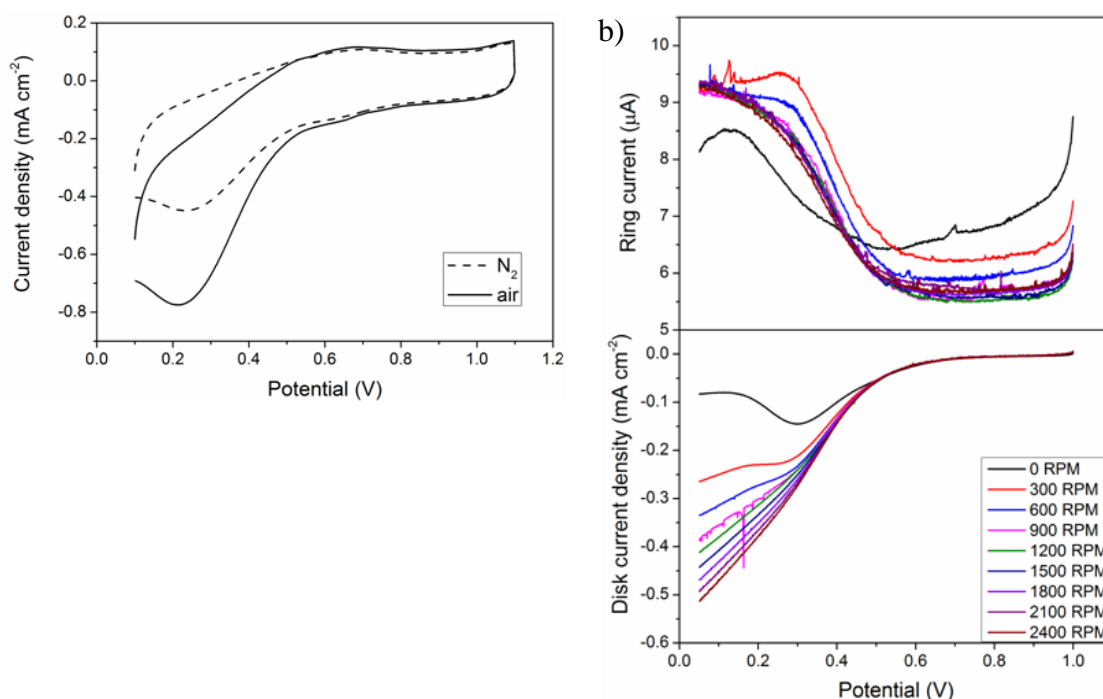


**Figure 7.29** RRDE characterisation of the NP800 catalyst: a) CVs in N<sub>2</sub> and air, and b) LSVs at different electrode rotation speeds.

The RRDE data for the LANL2, LP1-700-3-pyr, NP800 catalysts and carbon black have been overlaid to compare the ORR activity, as illustrated in Figure 7.30. Based on the CVs, the ORR activities of the materials can be arranged in the following order: LANL2  $\gg$  C  $>$  LP1-700-3-pyr  $\gg$  NP800, i.e. the N doped carbon catalyst LANL2 demonstrates significantly higher activity compared to the other alternatives to platinum. Carbon black shows more positive potential of the reduction wave than the LP1-700-3-pyr catalyst, but the surface area and hence capacitance of the latter is higher, since its CV area is greater than that of carbon black.

In the LSVs, the onset potentials of disk current densities on the synthesized catalysts and carbon black confirm the order of catalytic activities derived from the CVs. The ring currents are arranged in the following ascending order: NP800  $<$  LANL2  $<$  carbon black  $<$  LP1-700-3-pyr, i.e. the highest amount of hydrogen peroxide is produced by the P doped carbon catalyst. The low ring current generated by the NP800 catalyst can be assigned to its overall low activity resulting in significantly lower currents. Thus, the LANL2 catalyst shows superior activity and selectivity towards the ORR among the synthesized alternative catalysts and carbon black.

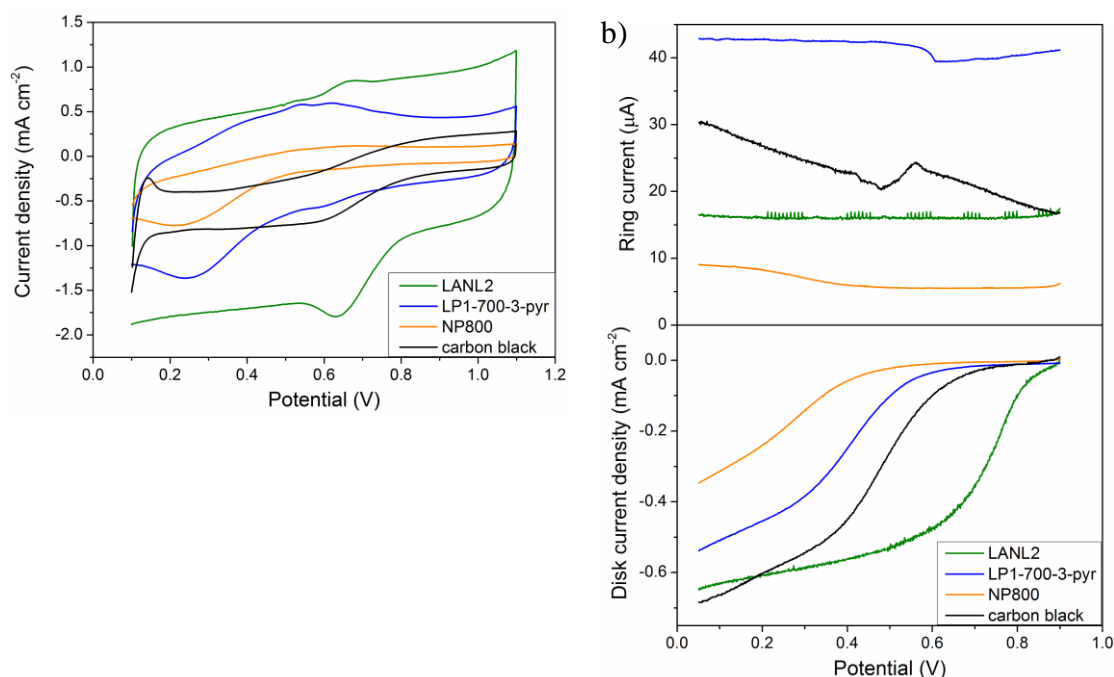


**Figure 7.30** Comparison of the RRDE results for the NP800, LANL2, LP1-700-3-pyr catalysts and carbon black: a) CVs in air, and b) LSVs at 1200 RPM.

### 7.9.3 Physicochemical Characterisation

In order to identify the chemical state of elements and functional groups on the surface of the NP800 catalyst, XPS measurements have been performed. The XPS survey and the deconvoluted high resolution C 1s, N 1s and P 2p spectra are illustrated in Figure 7.31.

The XPS survey spectrum shows discernable peaks of C, O, N, and S, with carbon being the predominant element. The elemental composition of the NP800 catalyst surface is listed in Table 7.3. In addition to the elements whose peaks are visible in the XPS survey, very small amounts of P, Si, Fe and Co are present on the surface. The content of P is 0.18 at.%, which is significantly lower than those of N and O. Thus, the NP800 catalyst synthesis technique did not provide an efficient way of incorporating P into the carbon structure.

**Table 7.3** Elemental composition of the NP800 catalyst derived from the XPS analysis.

Element	C	O	N	S	P	Si	Fe	Co
Content, at. %	96.35	1.64	1.18	0.47	0.18	0.07	0.07	0.03

The high-resolution C 1s peak has been fitted by four peaks with binding energies centred at 284.9, 285.5, 287.9, and 290.1 eV. The sharp peak at 284.9 eV is

assigned to  $sp^2$  hybridised carbon with C=C bonds. This indicates that most of the carbon in the NP800 catalyst exists in graphitic form. The broad peak centred at 285.5 eV correspond to either O=C( $sp^2$ ) or N=C( $sp^2$ ) bonds, since O and N are present in similar amounts. The other two flat peaks are ascribed to O-C( $sp^3$ ) or N-C( $sp^3$ ) and carbonates.

The high-resolution N 1s spectrum has been deconvoluted with three peaks accounting for graphitic N (401.4 eV), pyridinic N (398.7 eV) and pyridinic N-oxide (403.5 eV). The higher intensity of the graphitic N peak indicates that it is the predominant chemical state of N in the catalyst.

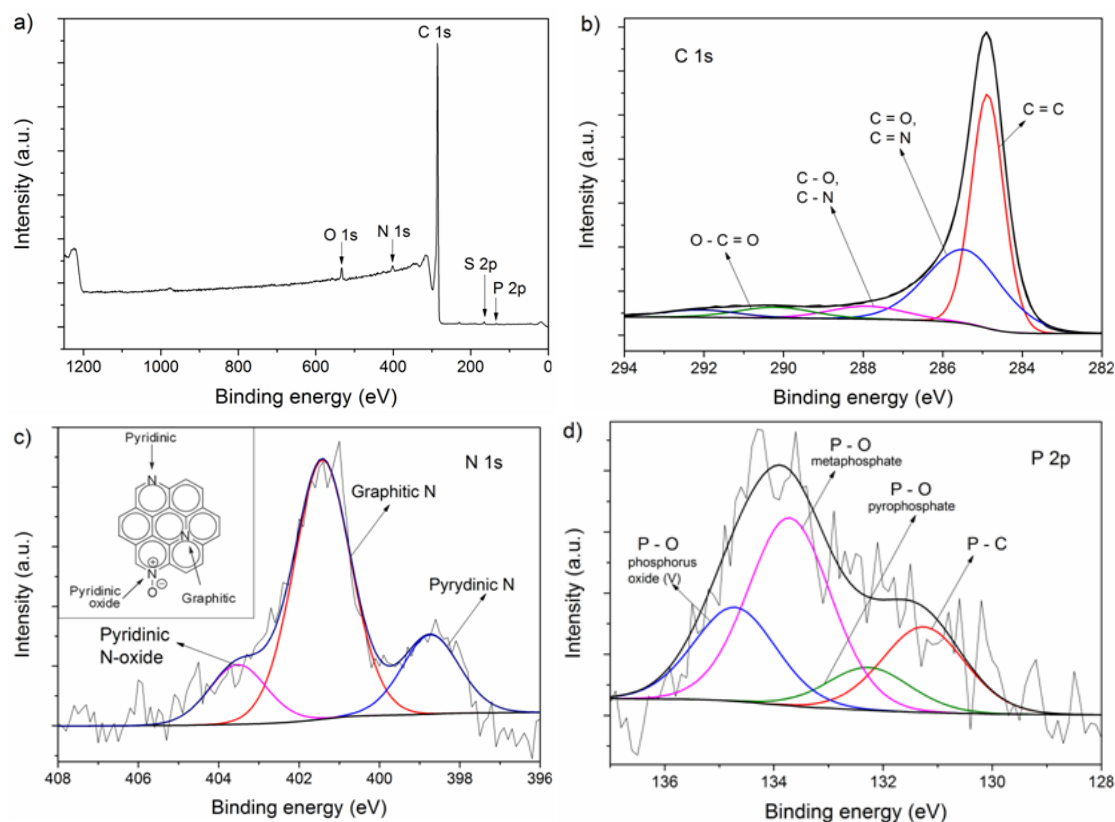


**Figure 7.31** The XPS spectra of the NP800 catalyst: a) XPS survey, and the deconvoluted high resolution b) C 1s, c) N 1s, and d) P 2p spectra.

Similar to the LP1-700-3-pyr catalyst, the high-resolution P 2p spectrum of the NP800 has four deconvoluted contributions appearing at 134.8, 133.7, 132.3 eV and 131.3 eV. The first three peaks are assigned to high oxidation states of P: phosphorus oxide (V), metaphosphate and pyrophosphate, respectively. The peak at 131.3 eV is assigned to P-C bonding of triphenylphosphine-type [247]. Although most of the P is present in oxidized state, a portion of it is incorporated into the carbon structure. However, it can be suggested that such a small content of P on the catalyst surface (0.18 at.%) does not induce an improvement of catalytic activity. Low activity of the

NP800 catalyst may be also determined by a decrease in surface area during the synthesis.

## **7.10 Glow Discharge Method of Synthesis of Phosphorus Doped Carbon Catalyst**

### **7.10.1 Synthesis**

Briefly, a carbon coater is a device with a chamber where carbon fibre is subject to evaporation during glow discharge. A coated material is placed in the bottom of the chamber under the carbon fibre [249]. The chamber is evacuated, and a high-voltage is applied to the carbon fibre, causing it to partially evaporate and precipitate on the coated material.

P doped carbon catalyst has been prepared using the glow discharge method as follows. 20 and 30 mg of red phosphorus was mixed with 980 and 970 mg of carbon fibre to achieve 2 and 3 wt% of phosphorus, respectively. Each of the fibre-phosphorus mixtures was loaded into a glass ampoule, evacuated to  $2 \cdot 10^{-5}$  Torr and then heat treated in a rocking furnace at 800 °C for 10 hours, with a heating rate of 1 °C/min. After the heat treatment, the fibres were cooled down to room temperature. Weights of the initial 2 and 3 wt% mixtures were 984.45 and 975.85 mg, which correspond to 0.45 and 0.60 wt% of phosphorus, respectively. Two carbon paper GDLs were used as substrates. To coat the GDLs, each strand of the P coated carbon fibres was fixed between two electrodes in the carbon coater. The carbon coater's chamber was evacuated to achieve circa 0.001 Torr, and then glow discharge was passed through the fibre. The two coated GDLs are further referred to as the 0.45%P-C and 0.60%P-C.

### **7.10.2 Physicochemical Characterisation**

The coated GDLs have been investigated by physicochemical methods. The 0.45%P-C has been analysed using XRD and SEM EDS. Figure 7.32 shows the XRD patterns of the 0.45%P-C and non-coated GDL for comparison. It can be observed that the XRD patterns of both coated and uncoated GDLs are identical and feature a sharp high peak at  $2\theta = 26.6^\circ$  and smaller peaks at  $2\theta = 42.6, 44.7$  and  $54.8^\circ$  which are characteristic for graphitic carbon. The peak at  $2\theta = 18.2^\circ$  has not been unambiguously ascribed to any compound. Thus, the XRD method did not reveal any difference in chemical composition between the uncoated and the 0.45%P-C coated GDLs.

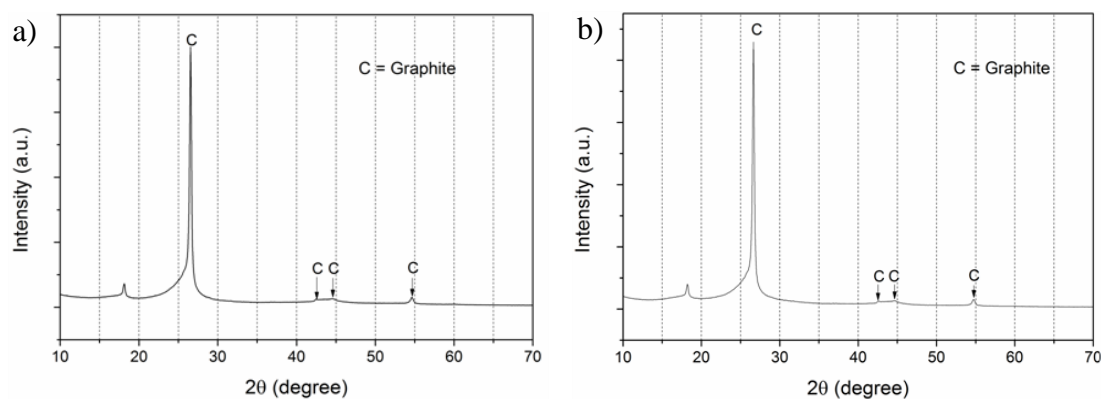


**Figure 7.32** The XRD patterns of a) 0.45%P-C coated, and b) uncoated GDLs.

Further, surface composition of the 0.45%P-C coated and uncoated GDLs have been investigated by scanning electron microscopy (SEM) and energy-dispersive X-ray spectrometry (EDS). The SEM EDX analysis results are shown in Figure 7.33. The SEM images, produced with a 20,000 magnification, demonstrate a successful coating of the GDL with a carbonaceous material.

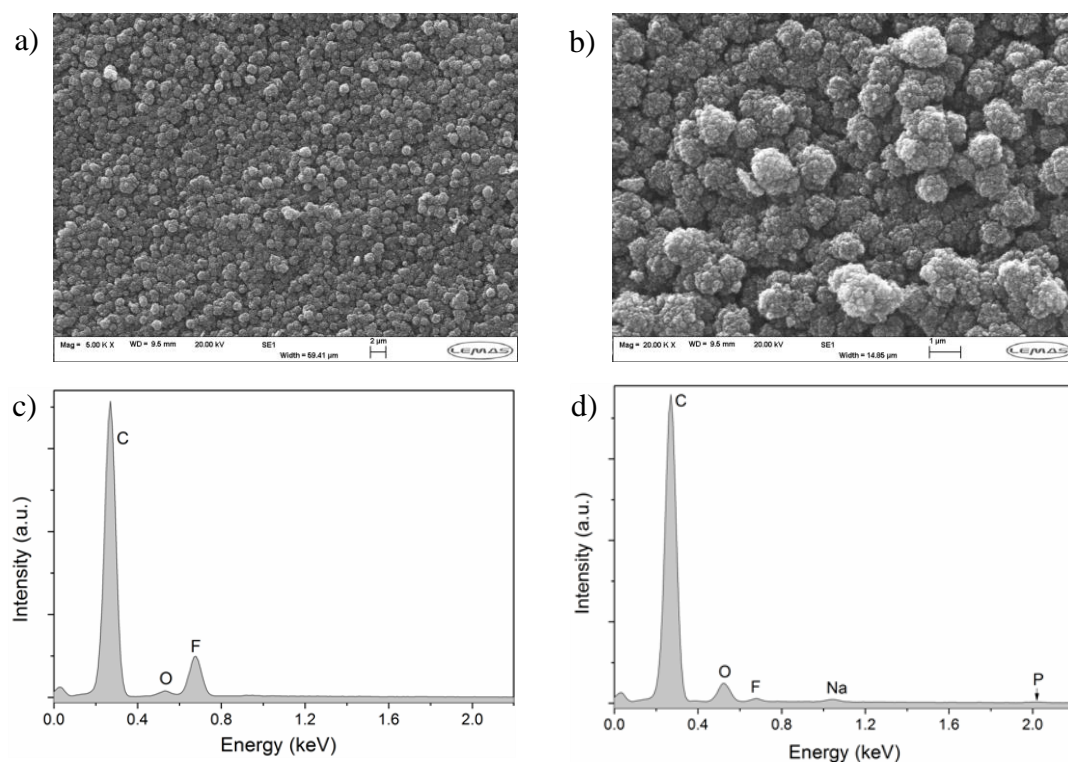


**Figure 7.33** The SEM images of a) non-coated, and b) 0.45% P-C coated GDLs, and EDS spectra of c) non-coated, and d) 0.45%P-C coated GDLs.

The EDS has provided semi-quantitative estimations of elemental composition of the two materials. The obtained EDS spectra illustrate that the uncoated GDL contains a small amount of O and a relatively large amount of F which originates from

Teflon<sup>®</sup> based components of the micro-porous layer (MPL). After coating, the F content decreases, and the O content increases. Also, trace amounts of Na and P have been detected on the 0.45%P-C coated GDL.

Elemental composition of the uncoated and 0.45%P-C coated GDLs derived from the EDS spectra are summarised in Table 7.4. The non-coated GDL mainly consists of C and F with a small amount of O. The 0.45%P-C coated GDL contains a relatively significant amount of O (5.32%), and F, Na and P are present in small amounts. Given the considerable amount of O in the 0.45%P-C coated GDL, C and P may exist partially in oxidized states.

**Table 7.4** Elemental composition of the uncoated and 0.45%P-C coated GDLs derived from the EDS spectra.

Element	Content, at. %	
	Uncoated GDL	Coated GDL
C	88.68	92.89
O	0.62	5.32
F	10.70	0.89
Na		0.51
P		0.39

An MEA was fabricated with the 0.60%P-C coated GDL at the cathode and a GDL coated with standard 20%Pt/C at the anode and then tested in the in-house PEM fuel cell. Figure 7.34 illustrates polarisation and power density curves for the 0.60%P-C coated GDL at the cathode, and also overlaid polarisation curves for MEAs with 0.60%P-C and the LANL2 catalysts for comparison.

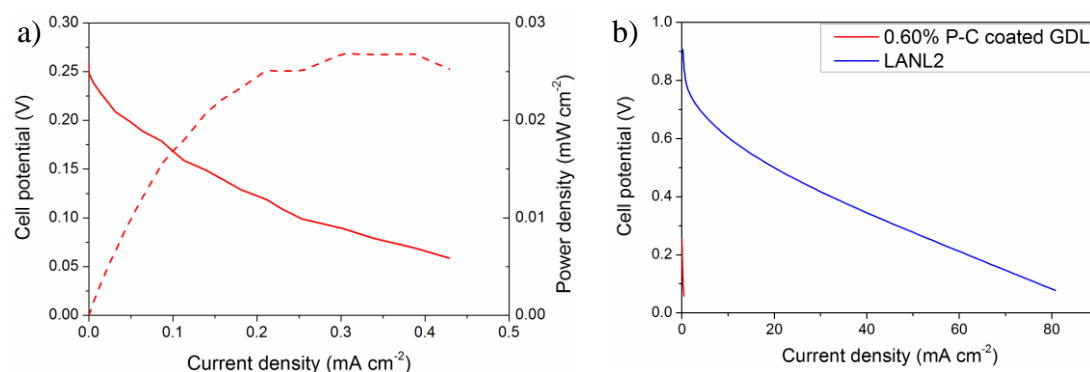


**Figure 7.34** PEM fuel cell test: a) polarisation curve (solid) and power density (dashed) with the 0.60%P-C coated GDL; and b) comparison of polarisation curves with the 0.60%P-C coated GDL and LANL2 as cathode catalysts.

### 7.10.3 PEM Fuel Cell Test

The polarisation and power density curves for the MEA with the 0.60%P-C show that current in the cell starts flowing at a very low potential of 0.25 V, and the maximum power density is 0.03 mW cm<sup>-2</sup>. The cell potential, current and power densities demonstrated by the 0.60%P-C coated GDL at the cathode are extremely low compared to the performance demonstrated by the LANL2 catalyst as PEM fuel cell cathode. Current density in the fuel cell test with the 0.60%P-C cathode catalyst is three orders of magnitude lower than that with the LANL2 cathode catalyst. This may be due to the extremely thin coating and thus low loading of the catalyst, as well as scarcity of necessary active sites, which are proposed to be P atoms in carbon structure of P doped carbon catalysts. As discussed above, the EDS analysis of the catalyst coated GDL revealed only a trace amount of P in carbon and a relatively high amount of oxygen. Therefore, the 0.60%P-C coated GDL does not have active sites for the ORR.

The EIS spectrum has been obtained for the MEA with the 0.60%P-C coated GDL at the cathode. Figure 7.35 presents overlaid EIS spectra of PEM fuel cell tests with 20%Pt/C compared to the LANL2, and the LANL2 compared to the 0.60%P-C coated GDL at the cathode. It is clear that the cell impedance with the 0.60%P-C coated GDL as cathode is a few orders of magnitude higher than that with the LANL2 catalyst, which is in turn a few times higher than impedance with the 20%Pt/C. The extremely high impedance measured with the 0.60%P-C coated GDL cathode may be due to the negligible catalytic activity and hence poor cathode humidification, essential for good conductivity.

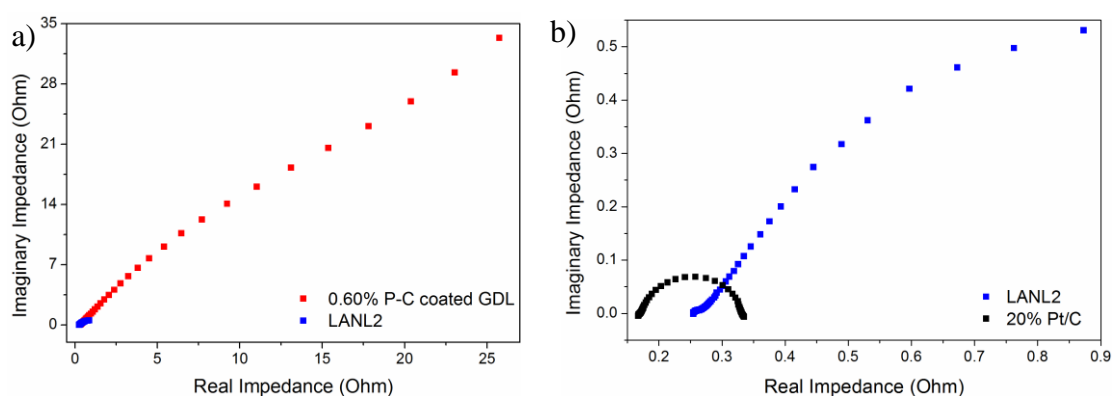


**Figure 7.35** The EIS spectra of a) 0.60% P-C coated GDL compared to the LANL2 catalyst, and b) the LANL2 catalyst compared to 20%Pt/C.

## 7.11 Conclusion

The effect of N or/and P doping of carbon has been investigated with respect to the catalytic activity in the ORR. The N and P doped carbon catalysts were synthesized in the presence of Fe and Co. In addition, a novel technique of synthesis of P doped carbon catalyst was tested using the glow discharge method.

The N doped carbon catalyst has demonstrated the highest activity towards the ORR among the synthesised doped carbon catalysts, with the estimated electron transfer number being close to four. However, the catalyst's performance both in the RRDE and PEM fuel cell tests is still significantly lower than that of platinum. The P doped carbon catalysts have displayed inferior activity in a two-electron mechanism of the ORR compared to the N doped. Furthermore, the glow discharge method of direct synthesis of P doped carbon on a GDL has proved to be inefficient, as evidenced by the PEM fuel cell test and physicochemical characterisation.

The low activity of the P doped carbon catalysts is proposed to be due to high contents of O and negligible fraction of P in the carbon structure. A large portion of P in the catalysts exists in phosphate state and is not active towards the ORR. This indicates that P doping of carbon is considerably more difficult to achieve than N doping, since P forms stronger bonds with O than carbon. Therefore, the techniques of synthesis of P or N doped carbon catalysts should be improved in order to eliminate or reduce the content of O in carbon.

## Chapter 8

### Experimental Investigation of Alternative Supports for PEM Fuel Cell Catalysts

#### 8.1 Introduction

Catalyst support can play a significant role in a catalyst's activity and durability. In order to meet requirements of PEM fuel cell applications, the catalyst support should possess a large surface area and high electronic conductivity. In the previous chapter, carbon black has been utilized as the catalyst support in the syntheses of N and P doped carbon catalysts. However, there are a number of other materials that can be potentially utilized for this purpose.

This chapter describes studies of the effect of alternative catalyst supports on the properties of N doped carbon catalysts. Six support materials have been utilized in the catalyst syntheses: (i) zeolitic imidazolate framework, referred to as ZIF-8 or Bazolite Z1200; (ii) Faujazite zeolite; (iii) molecular sieves; (iv) titanium nitride TiN; (v) tungsten carbide WC; and (vi) multiwall carbon nanotubes, MWCNTs.

ZIF-8 has been reported in the literature as a promising alternative support material used in the synthesis of the most active carbon based catalyst for the ORR [67]. TiN, WC and MWCNTs have high electronic conductivity, sufficient for use in the fuel cell cathodes, as discussed in Section 2.4.6. The utilization of zeolites as alternative support materials in PEM fuel cell catalysts has not been reported so far, to the author's knowledge. Faujazite and molecular sieves are minerals of aluminosilicate-based zeolite group. Although electrically insulating materials, Faujasie and molecular sieves have large surface area. Furthermore, the chemical structure of molecular sieves contains ammonium ions. Thus, during pyrolysis, gaseous ammonia may be released and create active sites in carbon by etching.

#### 8.2 Properties of the Alternative Support Materials

##### 8.2.1 Microporosity and Surface Area

Electronic conductivity, porosity and surface area are important properties of support materials for fuel cell catalysts, as mentioned in Section 2.4.6. The surface area and porosity of the alternative supports have not been measured in this work; however, the reported values are shown in Table 8.1. TiN and WC are powders with particle sizes less than 3 and 2  $\mu\text{m}$ , respectively [250, 251]. The surface area of MWCNTs is dependent on the number of walls and diameter, and the value may vary

between 50 to 1300 m<sup>2</sup>/g, decreasing with the number of walls [252]. Molecular sieves are a porous zeolite powder with large internal surface area varying between 600 and 1000 m<sup>2</sup>/g. The three-dimensional network of pores in molecular sieves takes 25 – 35% of the material's total volume [253, 254]. Similarly, Faujasite is also a zeolite material with high surface area and porosity. ZIF-8 is a subclass of metal-organic frameworks (MOFs) which are a novel class of three dimensional porous crystalline materials composed of metal ions or clusters connected by organic linkers. The high surface area and microporosity of ZIF-8 are the determining factors in selecting it as a catalyst support.

**Table 8.1** Surface area and porosity of the alternative catalyst supports.

Material name	Surface Area, m <sup>2</sup> /g [reference]	Micropore Volume, cm <sup>3</sup> /g, [reference]	Micropore Diameter, nm [reference]
Ketjenblack EC-300J	800 [255]	3.10 – 3.45 [255]	-
MWCNTs	Depend on the number of walls and diameter [252]		
ZIF-8	1300 – 1800 [256]	0.485 [257]	0.4 – 0.6 [257]
Faujasite	567 [258]	0.205 [258]	0.668 [258]
Molecular sieves	700 [253]	-	1 [259]

### 8.2.2 Thermal Stability

Since procedures of catalyst synthesis include pyrolyses, it is important to study thermal stability of the alternative support materials. Thermal stability of ZIF-8, faujazite and molecular sieves has been investigated experimentally in the tube furnace purged with nitrogen gas at 900 °C for 1 hour. Before pyrolysis, masses of the compounds have been weighed to be 0.5 g. After pyrolysis, masses have been measured again, and the mass loss has been calculated using the formula:

$$X = \frac{m_{\text{before pyrolysis}} - m_{\text{after pyrolysis}}}{m_{\text{before pyrolysis}}} \cdot 100\% \quad (8.1)$$

where  $X$  is the mass loss (%), and  $m_{\text{before pyrolysis}}$  and  $m_{\text{after pyrolysis}}$  are the masses before and after the pyrolysis, respectively.

The experimentally measured thermal stabilities are shown in Table 8.2 along with thermal stabilities is reported in the literature. According to the literature, Faujazite is the most thermally stable compound, followed by TiN, WC, molecular sieves and ZIF-8. The experimental study has confirmed that thermal stability of Faujazite is significantly higher than that of molecular sieves. The significant mass losses of molecular sieves and especially ZIF-8 indicate that at the pyrolysis temperature of 900 °C these supports can decompose to a significant extent.

**Table 8.2** Thermal stability of the materials utilized as alternative catalyst supports.

Material name	Chemical formula	Thermal stability, °C [reference]	Mass loss after pyrolysis at 900 °C, %	Appearance before / after pyrolysis
ZIF-8	$C_8H_{12}N_4Zn$	> 550 [260]	80.0	white/black
Faujasite	$(Na_2, Ca, Mg)_{35}[Al_7Si_{17}O_{48}] \cdot 3H_2O$	> 1000 [261]	9.8	white/gray
Molecular sieves	$(NH_3 \cdot Na_2O)_x[SiO_2 \cdot Al_2O_3]_y \cdot ZH_2O$	> 500 [262]	29.5	white/white
Titanium nitride	TiN	> 900 [263]	-	-
Tungsten carbide	WC	> 800 [264]	-	-

### 8.3 ZIF-8 supported N doped catalyst synthesis

#### 8.3.1 Synthesis

The synthesis technique has been the same as in Figure 7.10, but 0.7 g of ZIF-8 was utilized instead of carbon black. After the first pyrolysis, the solid transformed into a black powder (0.132 g), and the amounts of aniline,  $FeCl_3 \cdot 6H_2O$  and  $(NH_4)_2S_2O_4$  were 1 ml, 1.0 g and 1.65 g, respectively. In addition, duration of the final pyrolysis was reduced from 3 hours to 1 hour. The obtained catalyst (0.08 g) is referred to as BLANL1.

In the next synthesis of the ZIF-8 supported catalyst, a few modifications were introduced into the technique: acid leaching after the first pyrolysis has been omitted, because the catalyst is finally acid-leached after the second pyrolysis; in addition, duration of the first two pyrolyses were reduced to 30 minutes and to 1 hour for the final pyrolysis. The modified ZIF-8 supported catalyst is hereafter referred to as the BLANL2. A schematic of the BLANL2 synthesis is presented in Figure 8.1. The catalyst support was synthesized using 0.7 g of ZIF-8, and its mass after the first pyrolysis was 0.18 g. The amounts of aniline,  $FeCl_3 \cdot 6H_2O$  and  $(NH_4)_2S_2O_4$  were 1.35 ml, 1.35 and 2.25 g, respectively.

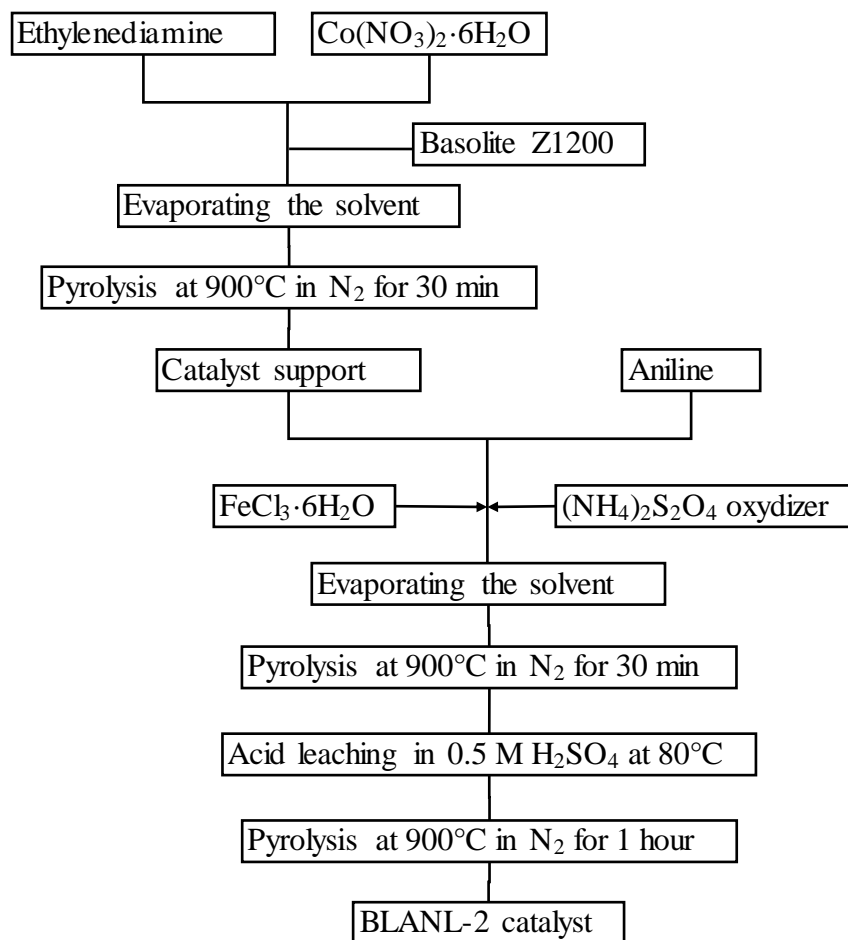


**Figure 8.1** Schematic of the BLANL2 catalyst synthesis.

### 8.3.2 RRDE Characterisation

The BLANL1 and BLANL2 have been characterized electrochemically using the RRDE methods. Figure 8.2 shows CVs in nitrogen and air saturated electrolyte and LSVs for the BLANL1 and BLANL2 catalysts. The CVs of both catalysts have different areas when measured in the nitrogen gas and air saturated electrolyte, indicating that the electrochemical reaction is the ORR. The CVs of the BLANL1 catalyst do not have a reduction peak and thus demonstrate poor activity towards the ORR. In the CVs of the BLANL2, the reduction wave is clearly observed at circa  $0.35 \text{ V}$  and the current density is  $1.0 \text{ mA cm}^{-2}$ . This suggests that the BLANL2 catalyses the ORR more efficiently than the BLANL1. The LSV has been measured only for the BLANL2 catalyst. The onset potential is ca  $0.75 \text{ V}$ , and this is still considerably lower than that of the commercial  $20\% \text{Pt/C}$  catalyst.

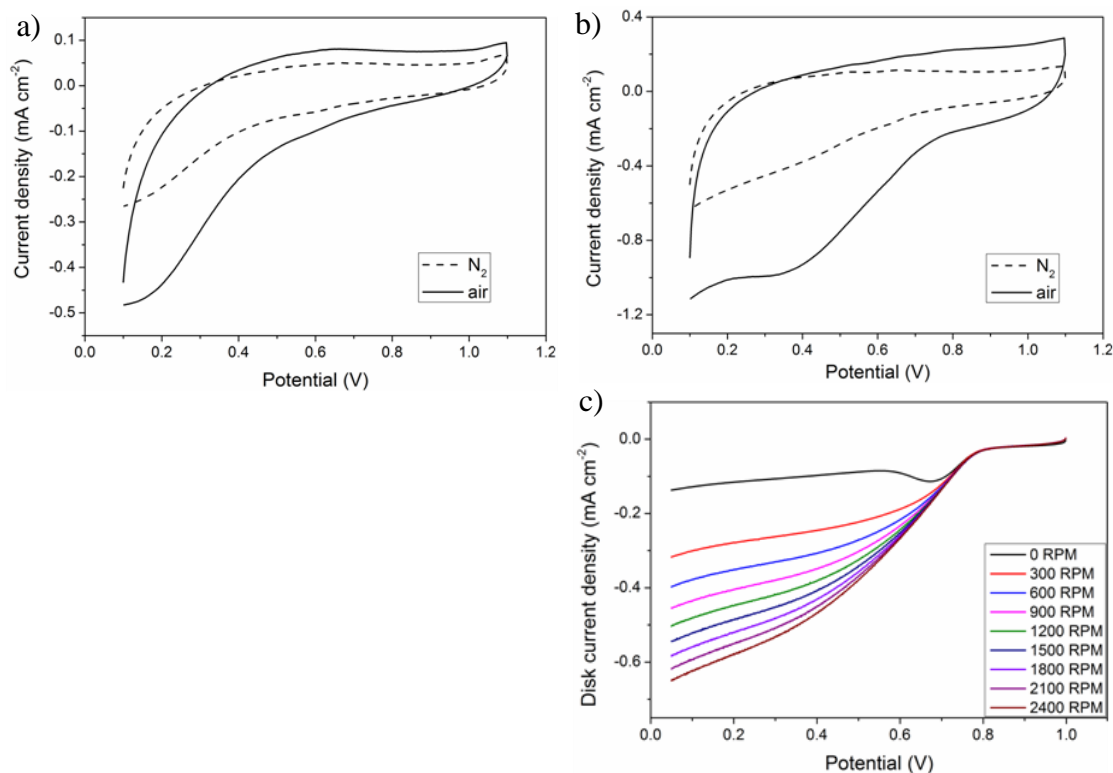


**Figure 8.2** RDE characterisation of the ZIF-8 supported catalysts: a) CVs in N<sub>2</sub> and air for the BLANL1 catalyst; b) CVs in N<sub>2</sub> and air, and c) LSVs at different electrode rotation speeds for the BLANL2 catalyst.

Electrochemical performance of the BLANL2 catalyst has been compared against that of the LANL2 catalyst, as illustrated in Figure 8.3. Compared to the LANL2 catalyst, the reduction peak of the BLANL2 is not clearly defined and is shifted towards more negative potentials. This may be explained by different structure of active sites on the BLANL2 surface. Furthermore, the small CV area and low peak current density of the BLANL2 catalyst evidence a small number of active sites. Although the CVs for the LANL2 and BLANL2 catalysts show a noticeable difference of 0.30 V in the peak potentials, the difference in the onset potentials in the LSVs is only circa 0.10 V. The diffusion limiting current density of the BLANL2 catalyst is 1.4 times lower than that of the fresh LANL2. Thus, the ZIF-8 supported BLANL2 catalyst shows inferior activity towards the ORR than the carbon black supported LANL2.

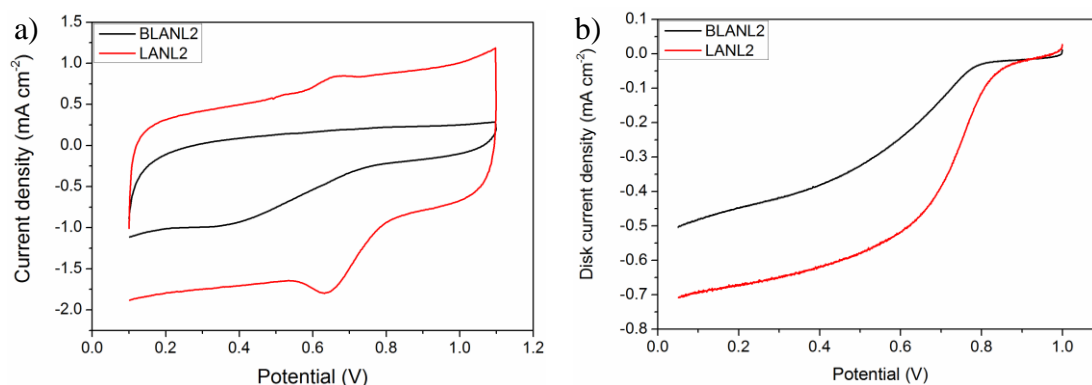


**Figure 8.3** Comparison of the RDE results for the BLANL2 and the LANL2 catalysts: a) CVs in air, and b) LSVs at 1200 RPM.

### 8.3.3 Physicochemical Characterisation

To determine the chemical composition of the BLANL2 catalyst, it has been characterised by XRD and XPS methods. The XRD measurement reveals the composition of crystalline species on the catalyst's surface. Figure 8.4 shows the XRD pattern of the BLANL2 catalyst. The two broad peaks centred at  $2\theta = 25^\circ$  and  $44^\circ$  correspond to the (002) and (100) facets of carbon which are present in the amorphous phase. The sharp peaks are assigned to the metal FeCo alloy and Co. The metals can originate from the Fe and Co salts, which may be reduced in the presence of ammonia or other reducing agents released during thermal decomposition of ZIF-8.

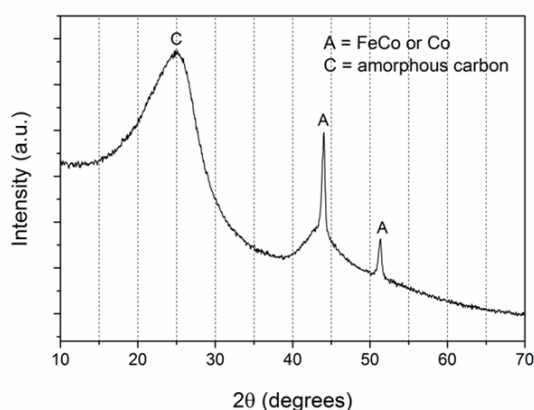


**Figure 8.4** The XRD pattern of the BLANL2 catalyst.

XPS analysis of the BLANL2 catalyst has been performed to identify its chemical composition and functional groups of the catalyst surface. The XPS results are presented in Figure 8.5. The survey spectrum shows a strong C 1s peak and the small O 1s and N 1s peaks, indicating that N has been incorporated into carbon.

Although not discerned in the XPS survey, trace amounts of S, Si, Fe and Co have also been detected.

The XPS-derived elemental composition of the BLANL2 catalyst surface is presented in Table 8.3. The contents of N and O in the BLANL2 are 1.3 and 1.4 times less than in the LANL2 catalyst, respectively, i.e. the degree of N and O doping to carbon has decreased. In addition, the LANL2 catalyst displayed a relatively high content of S (0.77%), while in the BLANL2 catalyst the percentage of S is 77 times lower. It can be hypothesized that the presence of sulphur may significantly improve the ORR performance of N doped carbon.

**Table 8.3** Elemental composition of the BLANL2 catalyst derived from the XPS analysis.

Element	C	O	N	S	Si	Fe	Co
Content, at. %	95.50	2.22	1.97	0.01	0.24	0.03	0.02

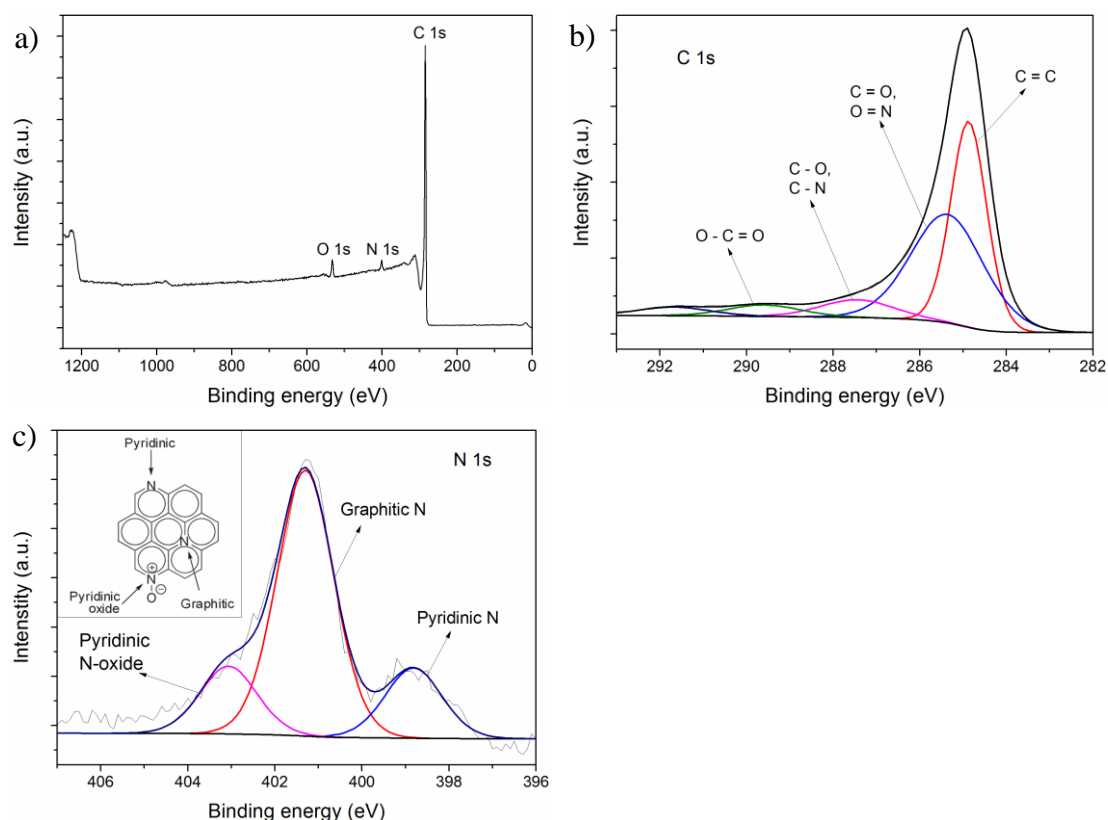


**Figure 8.5** The XPS spectra of the BLANL2 catalyst: a) XPS survey; and the deconvoluted high resolution b) C 1s and c) N 1s spectra.

The high-resolution C 1s spectrum shows the presence of four contributions to the observed peaks. The large peak centred at 284.7 is attributed to the  $sp^2$  hybridised carbon with C=C bonds, and the peak at 285.5 eV is either O=C( $sp^2$ ) or N=C( $sp^2$ )

bonds, since O and N are present in similar amounts. These two states of carbon constitute most of the catalyst's surface, since their contribution to the whole peak is the largest. The small broad peaks at 287.5 and 289.5 eV are ascribed to O-C(sp<sup>3</sup>) or N-C(sp<sup>3</sup>) and carbonates, respectively. The chemical state of the doped N is represented by the high-resolution N 1s spectrum deconvoluted with the three components: graphitic N at 401.4 eV, pyridinic N at 398.8 eV, and pyridinic N-oxide at 403.2 eV. The higher intensity of the graphitic N peak suggests that it is the predominant chemical state of N in the catalyst.

## 8.4 Faujzite and Molecular Sieves Supported N Doped Carbon Catalysts

Faujzite and molecular sieves supported N doped carbon catalysts have been synthesized using the technique shown in Figure 8.1 and further referred to as the FL and ML, respectively. 0.6 g of Faujzite or molecular sieves were utilized instead of ZIF-8 as a catalyst support. The amounts of aniline, FeCl<sub>3</sub>·6H<sub>2</sub>O and (NH<sub>4</sub>)<sub>2</sub>S<sub>2</sub>O<sub>4</sub> were 3 ml, 3.0 g and 5.0 g, respectively.

### 8.4.1 Faujzite Supported Catalyst

The FL catalyst was characterised electrochemically using the RRDE techniques, the results of which are shown in Figure 8.6. The CV does not show a reduction peak or wave, and there is no diffusion limiting current on the LSVs. This demonstrates that Faujzite supported FL catalyst is not efficient as a catalyst for the ORR.

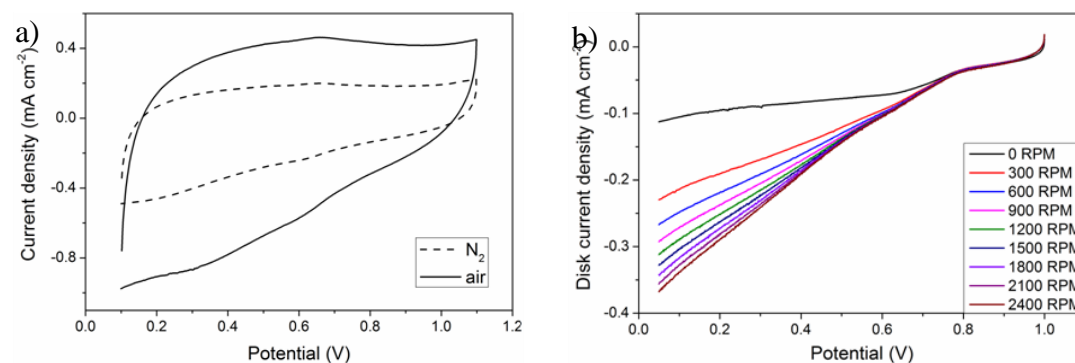


**Figure 8.6** RDE characterisation of the FL catalyst: a) CVs in N<sub>2</sub> and air at 1000 RPM, and b) LSVs at different rotation speeds, shown in the legend.

Physicochemical characterisation of the FL catalyst has been performed in order to understand the reasons of its low activity towards the ORR. The crystalline surface

composition of the FL catalyst has been investigated by powder XRD. In Figure 8.7, the two broad peaks at  $2\theta = 25^\circ$  and  $44^\circ$  correspond to the (002) and (100) diffraction planes of graphite. The broad nature of the peaks indicates a low degree of graphitisation of carbon.

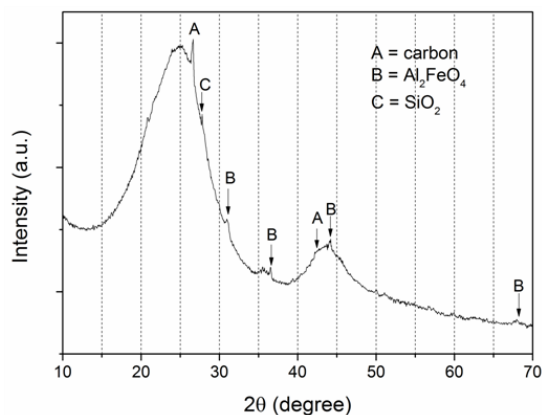


**Figure 8.7** The XRD pattern of the FL catalyst.

The small sharp peaks are assigned to iron aluminium oxide  $\text{Al}_2\text{FeO}_4$  and silicon oxide  $\text{SiO}_2$ . These species may appear during the pyrolysis at  $900^\circ\text{C}$ , when alkaline and alkaline-earth metals (Na, Ca and Mg) are removed from the zeolite structure, since their melting points are below  $900^\circ\text{C}$ . Simultaneously, N-coordinated Fe active sites can be decomposed, and Fe oxides can form. The reaction during pyrolysis of the FL catalyst can be represented schematically as follows:



XPS measurements have been performed to obtain an insight into the chemical composition of the FL catalyst surface, as illustrated in Figure 8.8. The XPS survey spectrum has pronounced O 1s peak, thus indicating a significant amount of O on the surface. In addition, N 1s, S 2p and Si 2p peaks can be clearly observed. The XPS-derived elemental composition of the FL catalyst surface is given in Table 8.4.

**Table 8.4** Elemental composition of the FL catalyst from the XPS analysis.

Element	C	O	N	S	Si	P	Fe	Co
Content, at. %	89.00	6.17	2.84	0.09	1.84	0.03	0.01	0.01

The significant amount of O can be explained by utilising the oxygen-rich Faujasite in the catalyst synthesis. The presence of Si (1.84%) should originate from

the zeolite as well. Notably, the amount of N in the FL catalyst (2.84%) is higher than that in the LANL2 catalyst (2.52%), although the FL does not show sufficient catalytic activity towards the ORR. The S, P, Fe and Co are detected only in trace amounts.

To reveal chemical states of the elements, high-resolution C 1s, N 1s and Si 2p peaks of the XPS spectrum have been investigated. The deconvoluted contributions to the C 1s peak indicate the presence of four states of carbon:  $sp^2$  hybridised carbon with C=C bonds (284.9 eV), O=C( $sp^2$ ) or N=C( $sp^2$ ) bonds (285.5 eV), O-C( $sp^3$ ) bonds (287.4 eV) and carbonates (289.5 eV). It should be noted that the contribution of the 285.5 eV peak is significant, and therefore a substantial portion of carbon exists in the O=C( $sp^2$ ) state owing to the large content of O. The presence of oxidized carbon may be the reason of low activity of the FL catalyst towards the ORR.

The high-resolution N 1s peak has been fitted with three contributions standing for pyridinic N (398.8 eV), graphitic N (401.4 eV) and pyridinic N-oxide (403.9 eV). The high intensities of the graphitic and pyridinic N peaks suggest that these are predominant chemical states of N in the catalyst. The Si 2p peak has been deconvoluted into the two contributions centred at 104 and 102 eV which are assigned to silica and silicones, respectively.

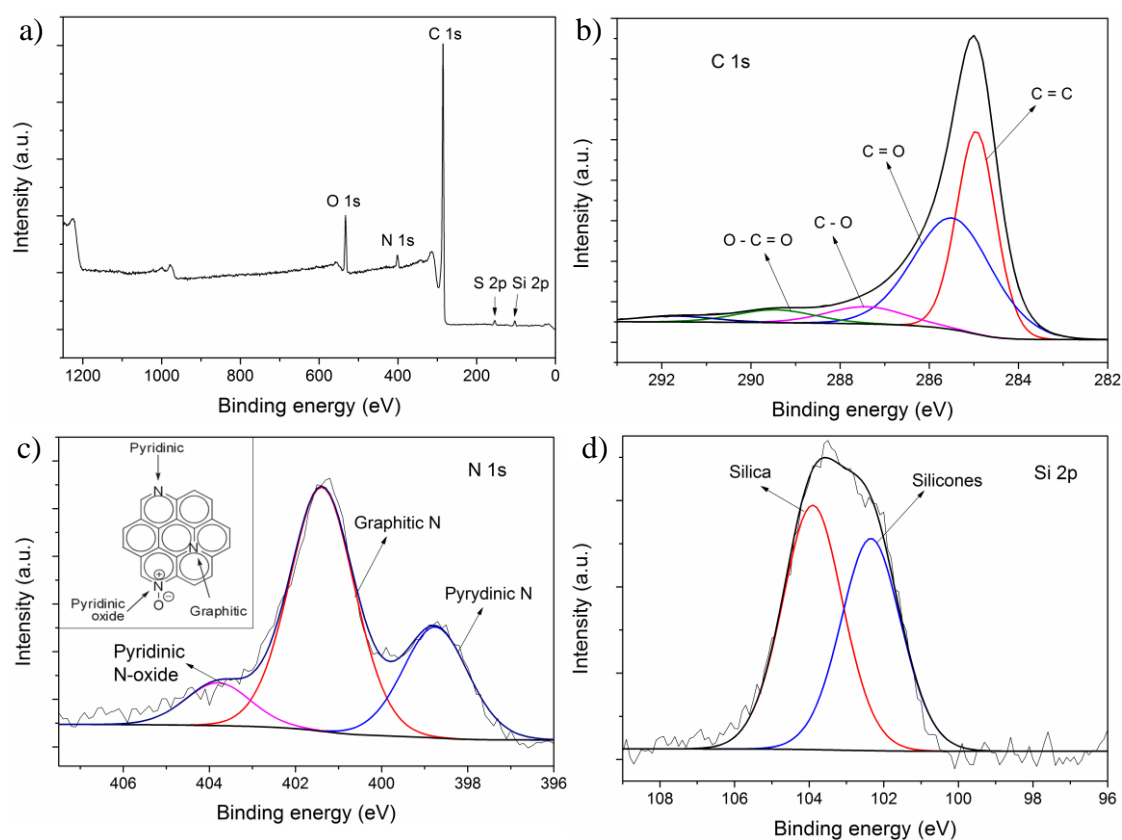


**Figure 8.8** The XPS spectra of the FL catalyst: a) XPS survey, and deconvoluted high resolution b) C 1s, c) N 1s, and d) Si 2p spectra.

### 8.4.2 Molecular Sieves Supported Catalyst

RRDE characterisation of the ML catalyst is shown in Figure 8.9. The CVs indicate that the ML catalyst shows minor activity towards the ORR, since the reduction peak is centred at 0.32 V. In the LSVs, the onset potential of the ORR is circa 0.60 V, and the diffusion limiting current densities are less defined with increasing electrode rotation speed. The ring currents, reflecting hydrogen peroxide formation, start to increase in the region of the onset potential and show slight dependence on the electrode rotation rate. These data suggest that the ORR activity of the ML catalyst is low, and hydrogen peroxide can form.

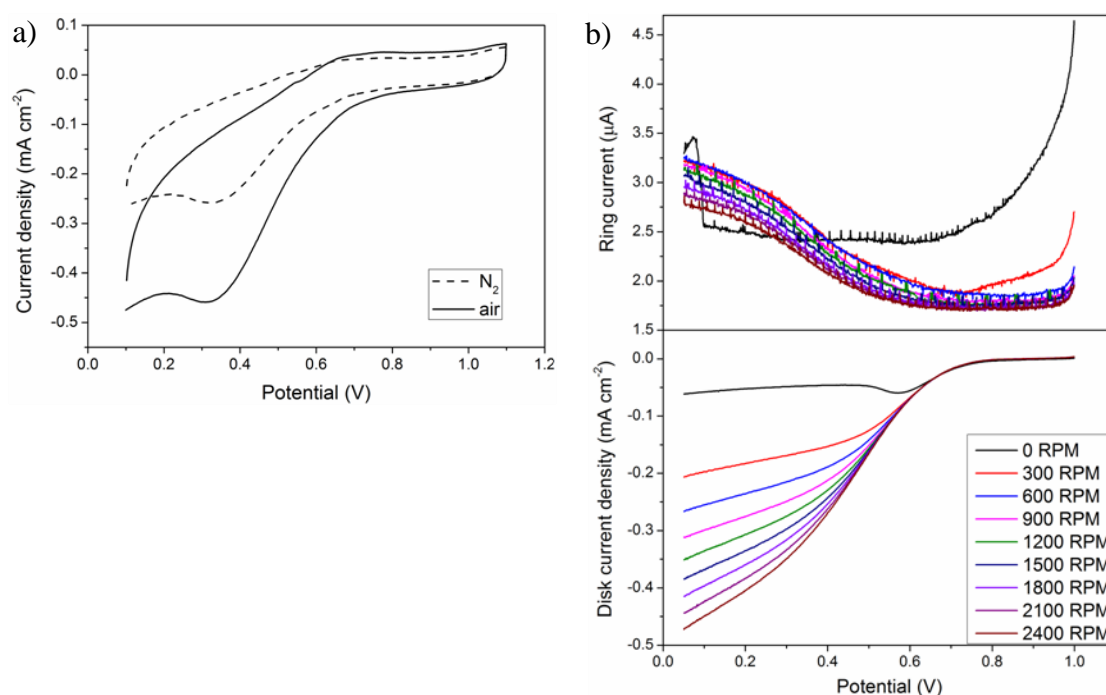


**Figure 8.9** RRDE characterisation of the ML catalyst: a) CVs in  $N_2$  and air at 1000 RPM, and b) LSVs at different rotation speeds, shown in the legend.

The crystal structure of the ML catalyst surface has been examined by the XRD method, as illustrated in Figure 8.10. The XRD pattern displays two broad peaks at  $2\theta = 24^\circ$  and  $44^\circ$ , characteristic for the (002) and (100) crystal planes of amorphous carbon. The two sharp peaks reveal the presence of Co and CoFe alloy particles which may originate from the Fe and Co salts used in the synthesis and reduced to the metal state during the pyrolyses by released ammonia.

XPS analysis has been performed to elucidate chemical composition and functional groups on the ML catalyst surface. The XPS survey spectrum evidences the presence of O, N, S, Si and Co in carbon. A full list of elements detected on the ML catalyst surface is shown in Table 8.5. Relatively high amounts of O (5.19%) and Si

(1.95%), may originate from the zeolitic catalyst support. The ML contains a higher percentage of N (3.11%) compared to the FL catalyst (2.84%).

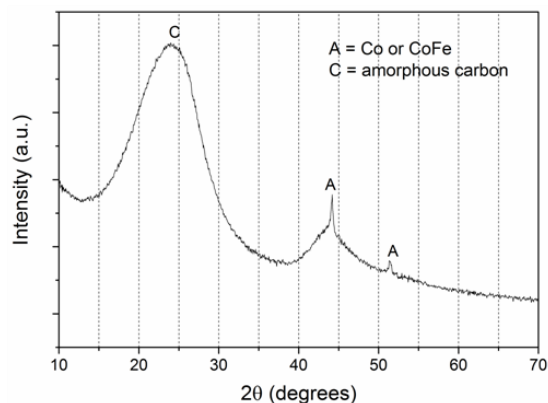


**Figure 8.10** The XRD pattern of the ML catalyst.

**Table 8.5** Elemental composition of the ML catalyst from the XPS analysis.

Element	C	O	N	S	Si	P	Fe	Co
Content, at. %	89.41	5.19	3.11	0.18	1.95	0.03	0.04	0.08

Figure 8.11 presents the high resolution C 1s and N 1s peaks of the ML catalyst. The C 1s peak has been deconvoluted into four contributions centred at 285, 285.6, 287.5 and 289.5 eV. The first two contributions account for the presence of  $sp^2$  hybridised carbon with C=C bonds and O, N doped  $sp^2$  hybridised carbon with O=C( $sp^2$ ) or N=C( $sp^2$ ) bonds. The low broad peaks centred at 287.5 and 289.5 eV account for the O-C( $sp^3$ ) bonds and carbonates, respectively. Considering the significant amount of O in carbon, it can be suggested that there are more O=C( $sp^2$ ) bonds than the N=C( $sp^2$ ) bonds. In addition, the peak accounting for the O=C( $sp^2$ ) bonds have significant contribution to the chemical state of carbon. This indicates that a considerable part of carbon exists in the oxidized state and may be the reason for the low activity of the ML catalyst towards the ORR.

The high-resolution N 1s peak has been fitted with three contributions: pyridinic N (398.8 eV), graphitic N (401.4 eV) and pyridinic N-oxide (403.9 eV). The high intensities of the graphitic and pyridinic N peaks suggest that these are predominant chemical states of N in the catalyst. Notably, N in both the ML and FL catalysts exists in the same chemical state as in the carbon-supported catalysts. Although the ML catalyst contains high amount of graphitic N, its activity towards the ORR is low.

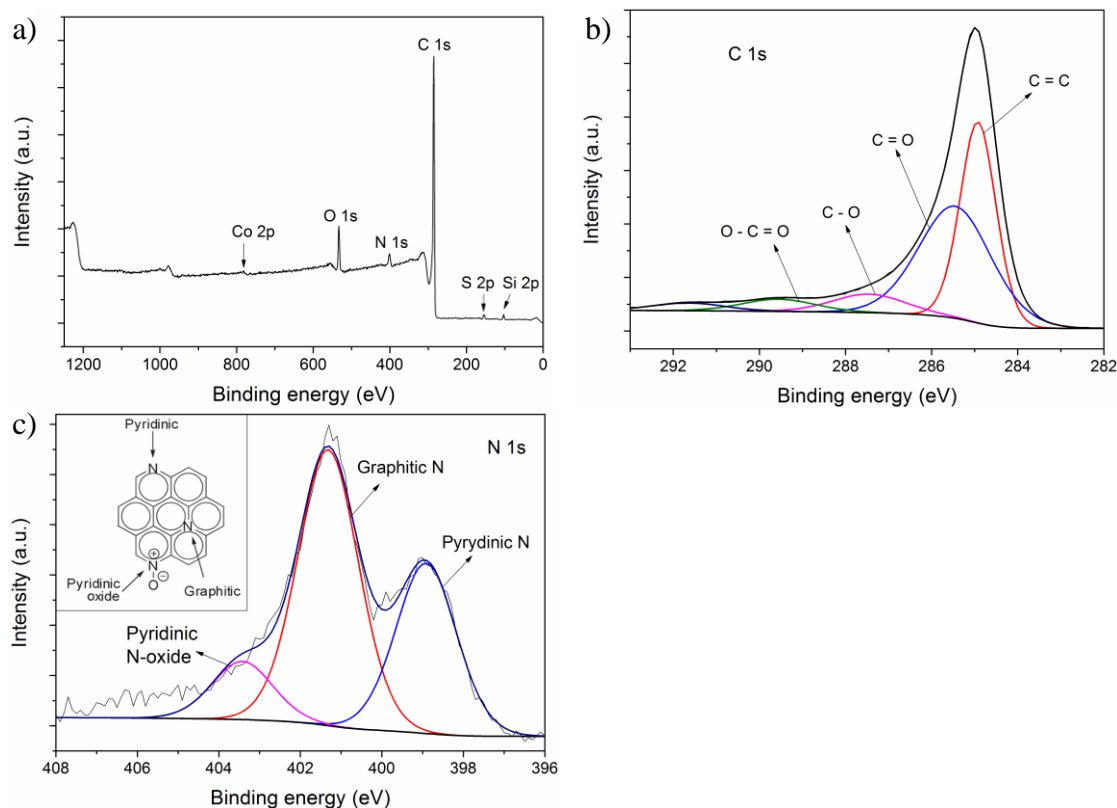


**Figure 8.11** The XPS spectra of the ML catalyst: a) XPS survey; and deconvoluted high-resolution b) C 1s, and c) N 1s spectra.

The ORR activities of the ML and FL catalysts have been compared to those of the LANL2, BLANL2 catalysts and carbon black, as shown in Figure 8.12. In the CVs, it is clear that the LANL2 has superior ORR activity, since it shows the largest CV area and well defined reduction peak compared to the other materials. CV area of the FL catalyst is the second largest, indicating a relatively high surface area. In contrast, CV area of the ML catalyst is the smallest, which indicates that it has the smallest active surface area among these materials. In the LSVs, the FL and ML catalysts display the lowest onset potentials, disk current densities and thus the least activity towards the ORR.

Based on the comparison of both the CVs and LSVs, the activities of the catalysts towards the ORR can be arranged in the following order: LANL2 > carbon black  $\approx$  BLANL2 > ML  $\gg$  FL. The low activities of the ML and FL catalysts may originate from the nature of the aluminosilicate-based catalyst support, which is not electrically conductive and inactive towards the ORR. The zeolite support may be only partially covered by carbon particles bearing active sites, and these particles may also fill pores of the zeolite support and make it impossible to utilise the high surface area of zeolites. Thus, it can be concluded that both Faujasite and molecular sieves are not practical for use as support materials for PEM fuel cell catalysts.

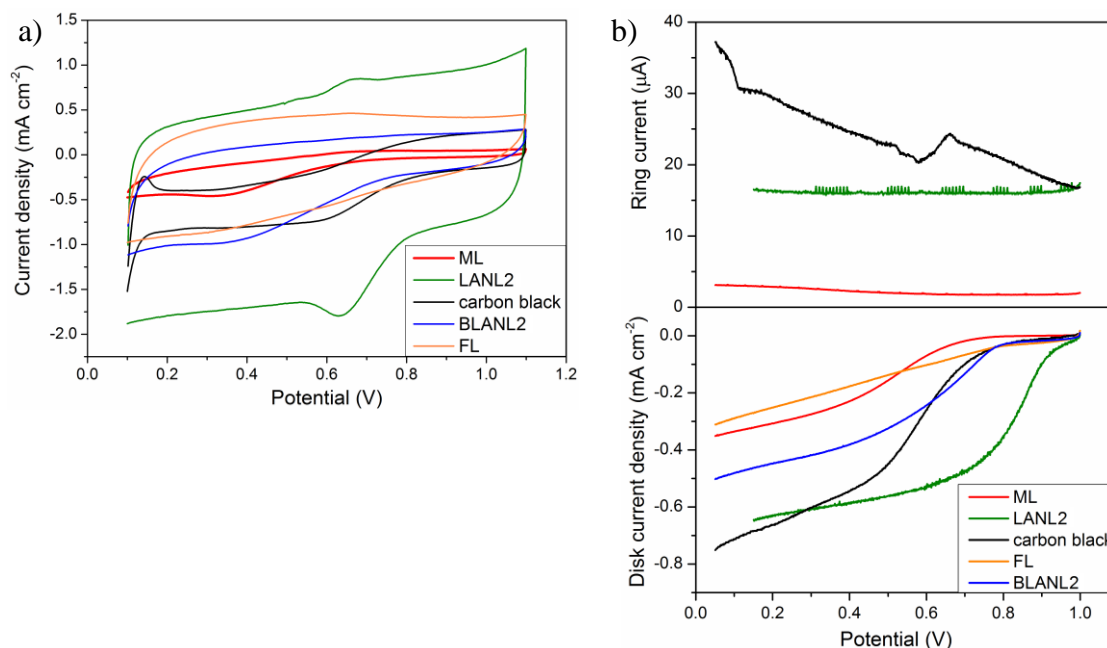


**Figure 8.12** Comparison of the RRDE results for the ML, LANL2, BLANL2, FL catalysts and carbon black: a) CVs, and b) LSVs at 1200 RPM.

## 8.5 Titanium Nitride Supported N doped Carbon Catalysts

The titanium nitride (TiN) supported N doped carbon catalyst has been synthesized using the technique in Figure 8.1 and referred to as the TL. 0.7 g of TiN was utilized instead of ZIF-8. The amounts of aniline,  $\text{FeCl}_3 \cdot 6\text{H}_2\text{O}$  and  $(\text{NH}_4)_2\text{S}_2\text{O}_4$  were 3 ml, 3.0 g and 5.0 g, respectively. After polymerisation of aniline, the resulting black hydrophilic solid was divided into two parts. The first part was processed according to the rest of the synthesis technique to obtain the final TL catalyst. The second part remained as is for electrochemical investigation. This non-pyrolysed solid was in turn divided into two parts, the first of which was ground and sieved and further referred to as the Fe-PANI-CoEDA-TiN catalyst. The second remaining part was acid-leached in 0.5 M  $\text{H}_2\text{SO}_4$  for 7 hours, washed with de-ionized water to a neutral pH of the flush water and dried in a vacuum rotary evaporator. The acid leached material is referred hereafter as the Fe-PANI-CoEDA-TiN-leached catalyst.

### 8.5.1 Non-Pyrolysed Catalyst

The Fe-PANI-CoEDA-TiN catalyst was characterised electrochemically using RRDE methods, as illustrated in Figure 8.13. The shape of obtained CVs displays an unusually pronounced oxidation peak at 0.5 V and a reduction peak at circa 0.85 V along with two smaller oxidation and reduction peaks. This result is markedly

different from those obtained other catalysts. Notably, the CVs in N<sub>2</sub> and air saturated electrolyte almost coincide, and this suggests that the electrochemical reactions at the electrode's surface are not the ORR. Interestingly, a CV measurement in air saturated electrolyte performed on the following day after the first measurement showed no electrochemical activity. LSV measurements performed on the day of the Fe-PANI-CoEDA-TiN catalyst synthesis confirm that the observed electrochemical reaction is not the ORR, since the disk current densities and ring currents rapidly decrease with increasing electrode rotation speed. This indicates that the electrochemical reaction on the Fe-PANI-CoEDA-TiN rapidly declines over time.

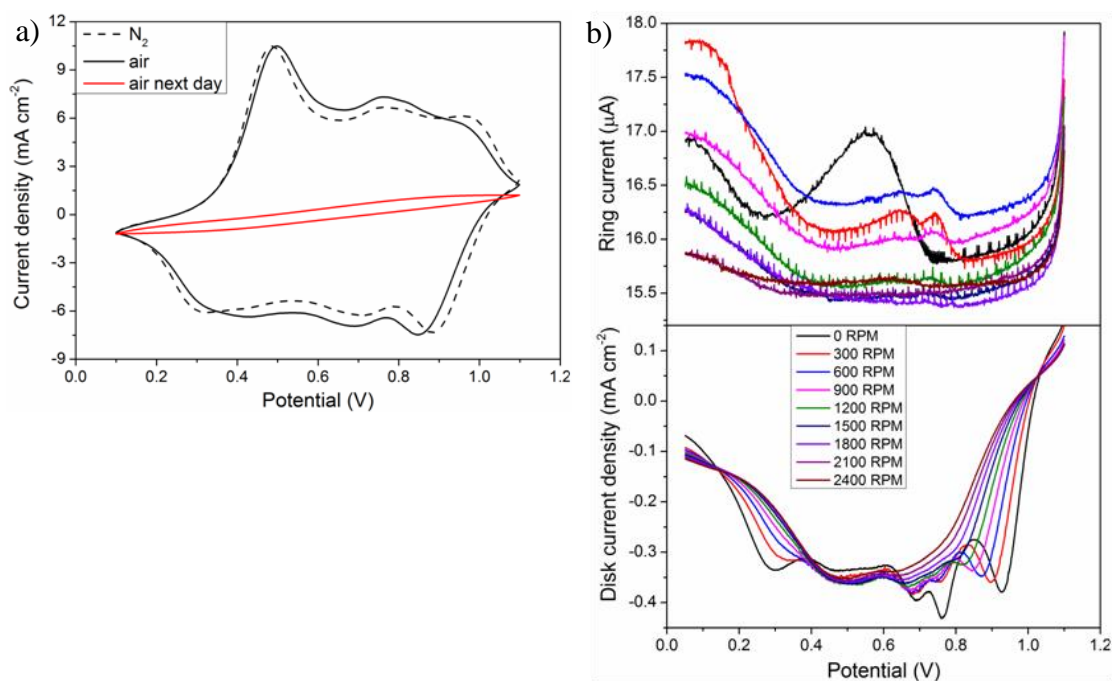


**Figure 8.13** RRDE characterisation of the Fe-PANI-CoEDA-TiN catalyst: a) CVs in N<sub>2</sub> and air at 1000 RPM for the freshly prepared catalyst and on the next day, and b) LSVs at different electrode rotation speeds (shown in the legend).

Further, LSV experiments for the Fe-PANI-CoEDA-TiN catalyst have been repeated in a broader potential range starting from 1.2 V and on the following day of the synthesis. The LSVs shown in Figure 8.14 demonstrate that the electrochemical activity rapidly declines, since the disk current densities continue decreasing with increasing electrode rotation speed. On the following day, the LSV measurements show that both disk current densities and ring currents converge to one line and became independent of the rotation speed. This suggests that the observed electrochemical reaction is independent of mass transport from the electrolyte.

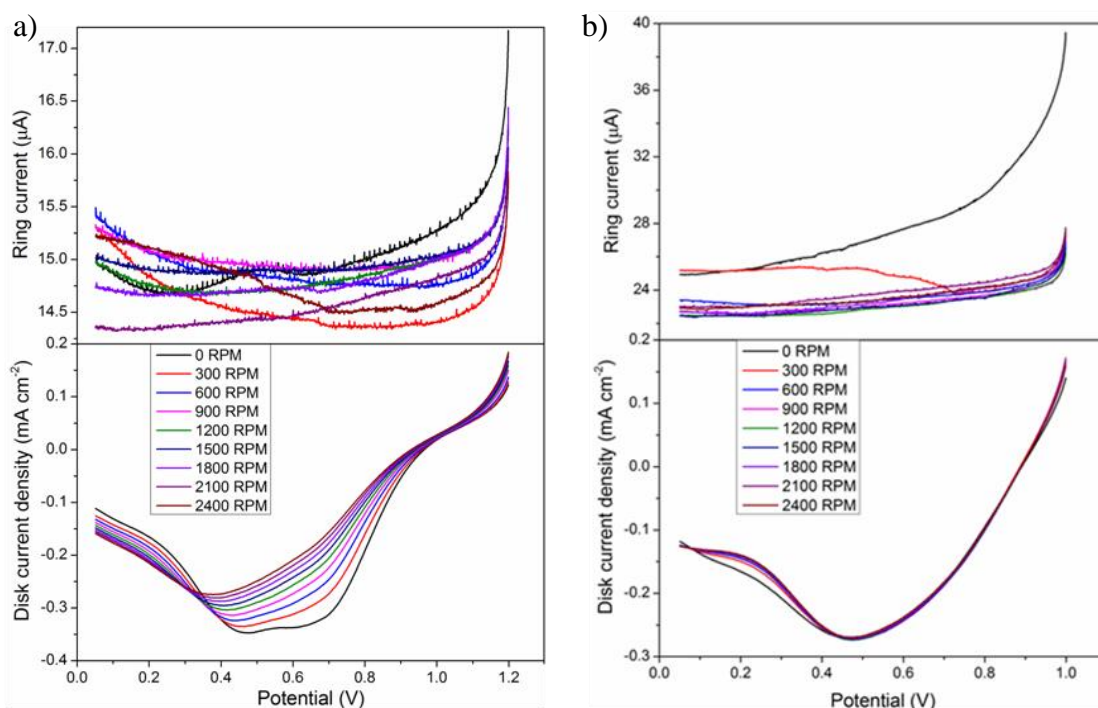


**Figure 8.14** LSVs after the a) second and b) third measurements for the Fe-PANI-CoEDA-TiN catalyst.

Similarly, the Fe-PANI-CoEDA-TiN-leached catalyst has been investigated using the RRDE, as shown in Figure 8.15. The CVs in  $N_2$  and air saturated electrolyte coincide and display pronounced oxidation peak at circa 0.5 V and reduction peak at circa 0.8 V along with smaller oxidation and reduction waves. Both the disk current densities and ring currents in the LSVs decrease with increasing electrode rotation speed, similarly to the results for the non-leached Fe-PANI-CoEDA-TiN catalyst. The RRDE data for both the Fe-PANI-CoEDA-TiN and Fe-PANI-CoEDA-TiN-leached catalysts suggest that the observed electrochemical reaction is not the ORR but possibly oxidation of the polyaniline.

The synthesis technique includes polymerisation of aniline in the presence of the transition metal ions, and the surface of both the Fe-PANI-CoEDA-TiN and Fe-PANI-CoEDA-TiN-leached catalysts should mainly consist of polyaniline with Fe ions trapped in it. The electrochemical reaction observed in the RRDE measurements may be attributed to electrochemical changes in polyaniline during the potential cycling. Due to the highly oxidizing environment in the RRDE experiments, polyaniline may irreversibly transform to an oxidized state. Conductive polymers, such as polyaniline and polypyrrole, with and without incorporated transition metals have been reported in the literature [22, 128] to be effective catalysts for the ORR. However, in this study, polyaniline-derived catalysts showed rapidly declining

current-potential responses in the RRDE experiments and negligible catalytic activity towards the ORR.

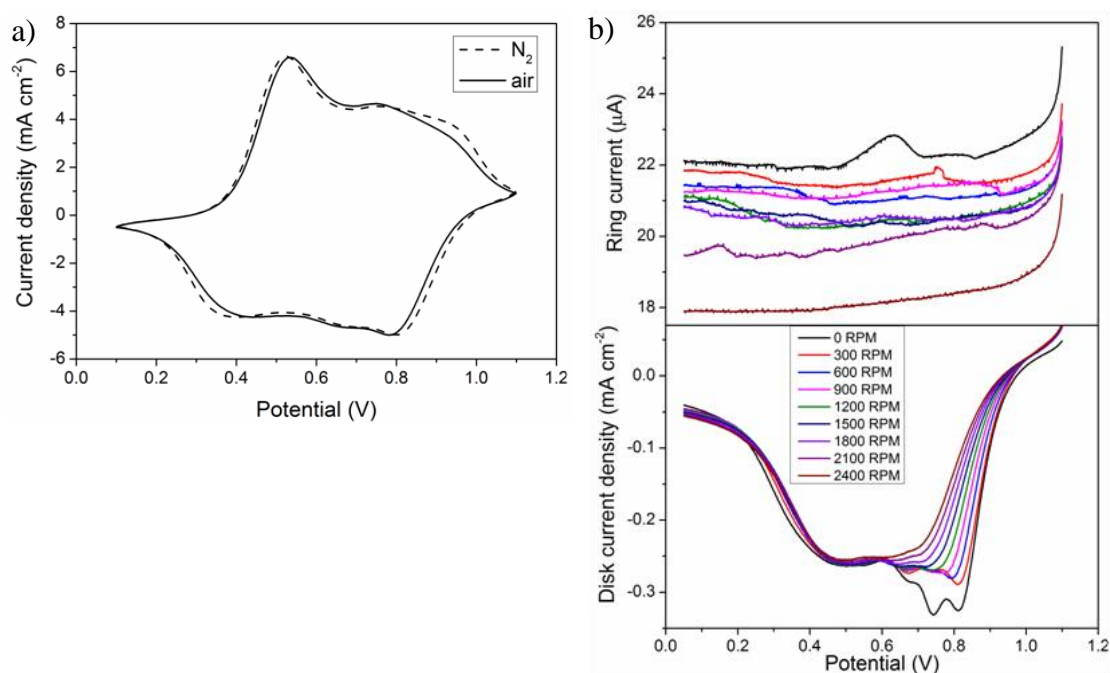


**Figure 8.15** RRDE characterisation of the Fe-PANI-CoEDA-TiN-leached catalyst: a) CVs in N<sub>2</sub> and air at 1000 RPM, and b) LSVs at different rotation speeds (shown in the legend).

### 8.5.2 The Effect of Pyrolysis

Pyrolysis of the polyaniline-based precursor of the TL catalyst dramatically changed its visual appearance, i.e. before the pyrolysis, the Fe-PANI-CoEDA-TiN catalyst was a black hydrophilic solid, while after the pyrolysis it has transformed into a dark-grey hydrophobic powder. The TL catalyst has been characterised electrochemically using the CV technique in N<sub>2</sub> and air saturated electrolyte. Figure 8.16 shows the CVs for the TL overlaid CVs in air for the TL and carbon black for comparison. The TL catalyst CVs show featureless voltammetric currents. Compared to carbon black, the TL catalyst shows very low capacitance and thus active surface area. It is clear that the TL catalyst is significantly less active than carbon black.

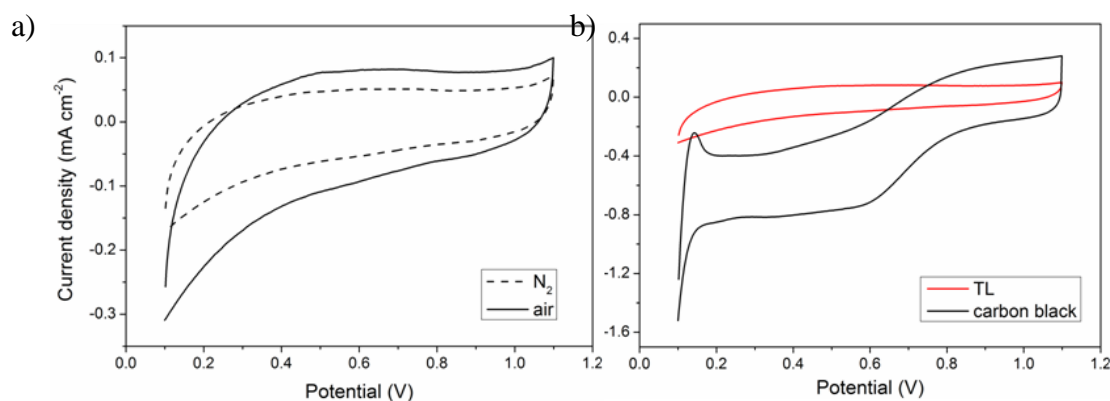


**Figure 8.16** RRDE characterisation of the TL catalysts: a) CVs in  $N_2$  and air at 1000 RPM, and b) overlaid CVs in air for the TL catalyst and carbon black.

### 8.5.3 Physicochemical Characterisation

XRD analysis has been performed for the Fe-PANI-CoEDA-TiN, FePANI-CoEDA-TiN-leached and TL catalysts to reveal the surface crystalline species. In Figure 8.17, the non-pyrolysed catalysts display similar XRD patterns with the same positions of characteristic peaks but slightly different peak intensities, which may be the result of the acid-leaching. The peaks in non-pyrolysed catalysts have been assigned to titanium oxide ( $TiO_2$ ), iron titanium oxide ( $Fe_{1.5}Ti_{0.5}O_3$ ) and ethylenediammonium sulphate ( $C_2H_{10}N_2O_4S$ ). Presence of the latter compound is not certain, since the XRD method is not efficient in detecting organic materials. Notably,  $TiO_2$  has been identified instead of titanium nitride (TiN) in the XRD pattern of the TL catalyst. This suggests that TiN is oxidized during the synthesis, possibly during vacuum drying of the suspension at 100 °C and subsequent pyrolysis. Therefore, the synthesis procedure should be modified in order to prevent oxidation of TiN. During pyrolyses, polyaniline may decompose and act as a reducing agent for  $TiO_2$  at temperature ranging from 800 to 1000°C and normal pressure [265], and carbon can be oxidized and removed from the surface of  $TiO_2$ .

XPS analysis has been performed for the Fe-PANI-CoEDA-TiN-leached catalyst in order to identify the chemical state of its surface. The XPS survey, high resolution C 1s and N 1s signals are illustrated in Figure 8.18. The XPS survey reveals the presence of C, N, O, and S. The Ti peak cannot be visibly discerned, and its position is shown by the arrow. The full elemental composition of the catalyst surface derived from the XPS is presented in Table 8.6. The high contents of N (11.23%) and O (6.36%) are 4.4 and 2 times higher than those on the LANL2 surface, respectively, and can be explained by the presence of oxidized polyaniline. The relatively high content of S may originate from the oxidizing agent,  $(NH_4)_2S_2O_4$ .

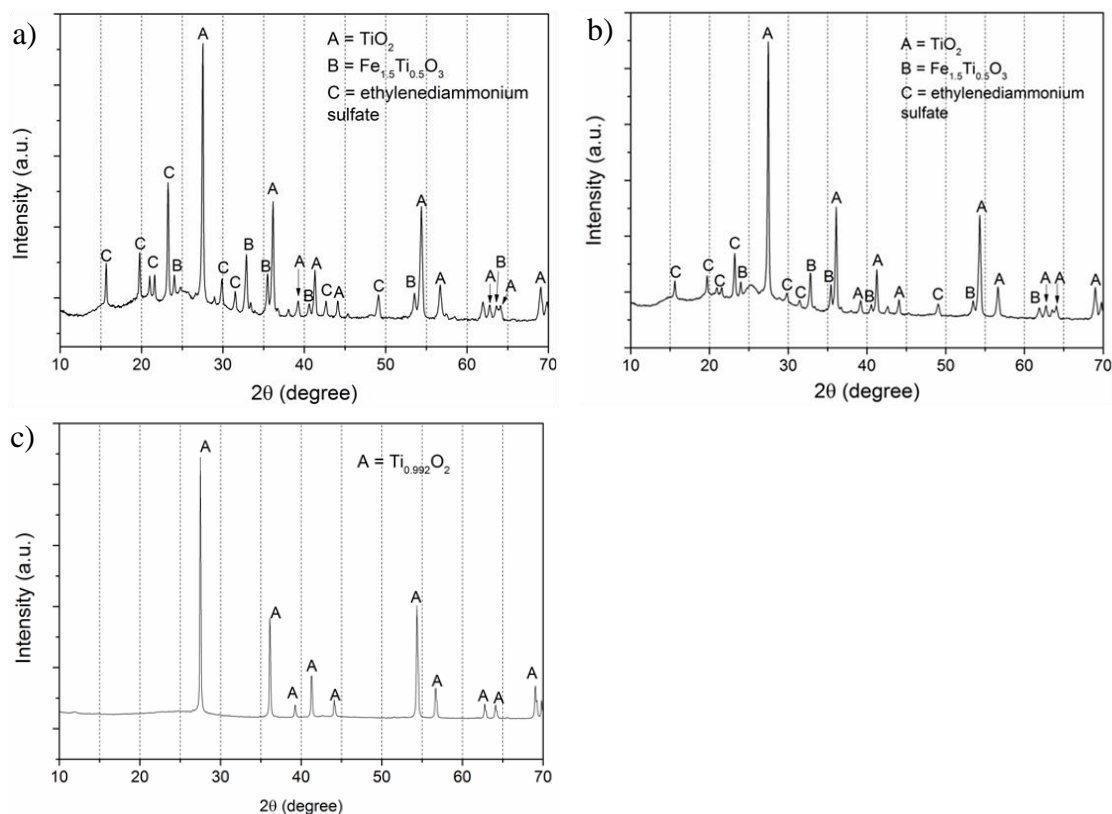


**Figure 8.17** The XRD patterns of a) the FePANI-CoEDA-TiN, b) FePANI-CoEDA-TiN-leached, and c) TL catalysts.

**Table 8.6** Elemental composition of the FePANI-CoEDA-TiN-leached catalyst from the XPS analysis.

Element	C	N	O	S	Si	Ti	Co	P
Content, at. %	80.71	11.23	6.36	1.51	0.11	0.05	0.02	0.01

The C 1s high resolution spectrum has been deconvoluted into four peaks with binding energies centred at 284.5, 285.4, 287.1 and 289.3 eV. The peak at 284.5 eV corresponds to  $sp^2$  hybridised carbon with C=C bonds, and the peak at 285.4 eV corresponds to N or O doped  $sp^2$  hybridised carbon with N=C( $sp^2$ ) and O=C( $sp^2$ ) bonds. The area of the 285.4 eV peak is the largest, and this indicates that most of the carbon exists in either N=C( $sp^2$ ) or O=C( $sp^2$ ) state. Due to the high N content, the contribution of the N=C( $sp^2$ ) bonds should be predominant over the O=C( $sp^2$ ) bonds. The small flat peaks centred at 287.1 and 289.3 eV are assigned to  $sp^3$  hybridised C-N or C-O bonds and carbonates, respectively. The high-resolution N 1s spectrum has been fitted with two peaks at 399.6 and 402.0 eV, assigned to polyaniline and quaternary amine salts [247].

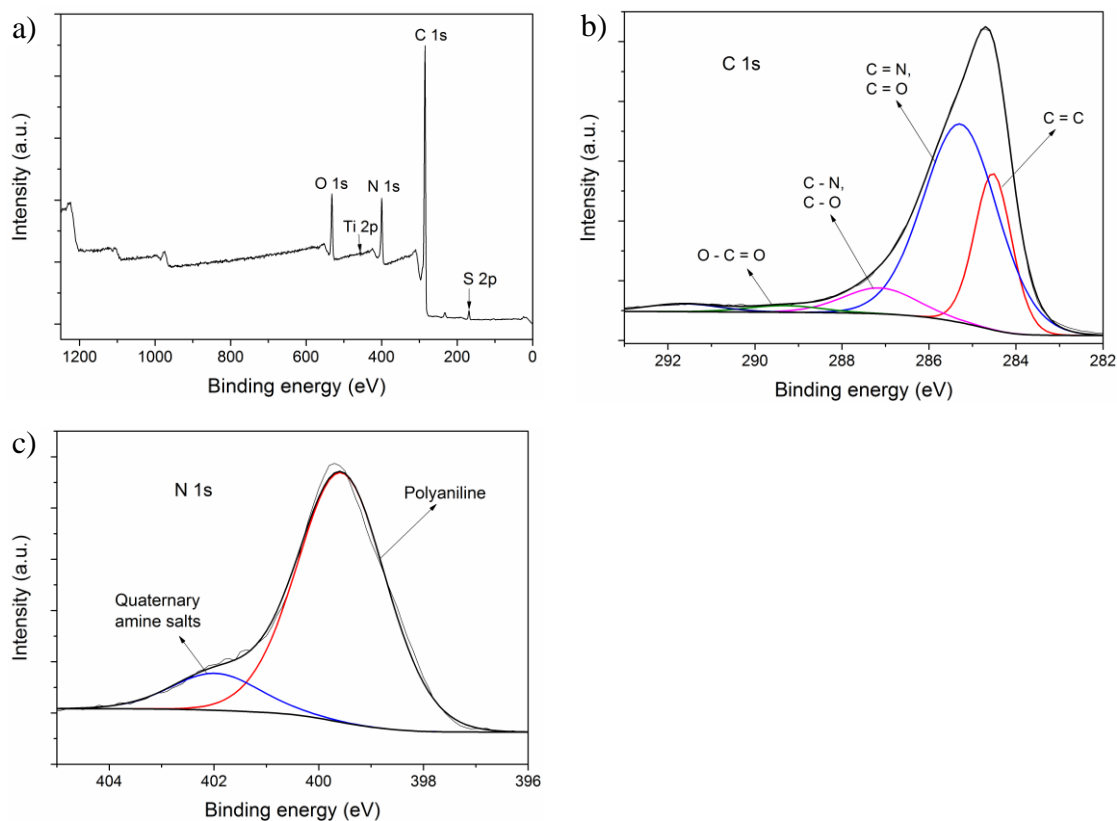


**Figure 8.18** The XPS spectra of the FePANI-CoEDA-TiN-leached catalyst: a) XPS survey, and deconvoluted high-resolution b) C 1s, and c) N 1s spectra.

XPS measurements have been also performed for the TL catalyst, as shown in Figure 8.19. The XPS survey reveals pronounced peaks of C and O, constituting most of the surface, and small peaks of N, S, Si, Ti and Co. Table 8.7 shows the elemental composition of the TL catalyst derived from the XPS survey. The high contents of C and O suggest that significant part of the catalyst's surface is oxidized carbon. Although the content of N is 2.6 times less than that of O, it is still higher than the N content in the LANL2 catalyst (2.52%). A significant amount of Si (2.61%) has been detected. Interestingly, although the XRD analysis of the TL catalyst reveals the presence of TiO<sub>2</sub> only, the XPS shows as little as 0.33% of Ti. This can be explained by the difference in the depth of probing in the XRD and XPS methods: XRD probes a material also under the surface whereas the depth of XPS probing is circa 10 nm.

**Table 8.7** Elemental composition of the TL catalyst from the XPS analysis.

Element	C	O	N	S	Si	P	Ti	Co	Fe
Content, at. %	86.27	7.40	2.79	0.42	2.61	0.04	0.33	0.10	0.04

The C 1s peak has been deconvoluted into the four contributions with binding energies centred at 284.9, 285.4, 287.3 and 289.4 eV. The peak at 284.9 eV is

typically assigned to  $sp^2$  hybridised carbon with C=C bonds of the  $\pi$  conjugated system of graphene lattice. The broad peak at 285.4 eV is assigned to the O=( $sp^2$ )C bonds, and its large area suggests that the fraction of the oxidized carbon on the catalyst surface is significant. The flat peaks at 287.3 and 289.4 eV have minor contribution and account for the presence of O-C( $sp^3$ ) bonds and carbonates, respectively.

The N 1s spectrum has been fitted with three peaks which indicate presence of N in the three chemical states: graphitic N at 401.3 eV, pyridinic N at 398.9 eV, and pyridinic N-oxide at 402.1 eV. The area of the peaks suggests that most of N is present in the graphitic and pyridinic state, and a smaller fraction of N exists in the state of pyridinic N-oxide. In addition, the high resolution Si 2p spectrum has been deconvoluted, since Si is present on the TL surface in the substantial amount of 2.61%. The spectrum is well-fitted with the two peaks centred at 102 and 103.7 eV, which correspond to silicones and silica, respectively [247].

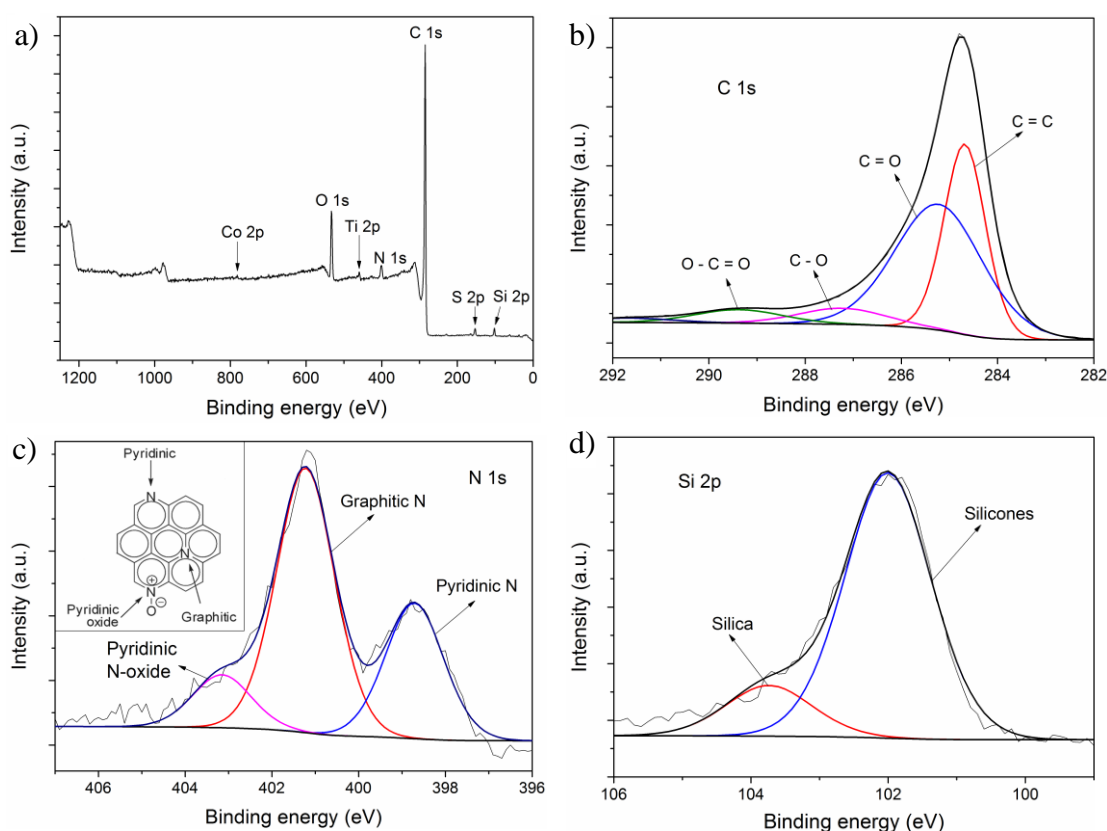


**Figure 8.19** The XPS spectra of the TL catalyst: a) XPS survey and deconvoluted high-resolution b) C 1s, c) N 1s, and d) Si 2p spectra.

### 8.5.4 Modified Synthesis Technique

As follows from the physicochemical characterisation of the TL catalyst, the TiN support transforms into  $TiO_2$  during the synthesis. A possible reason of this

conversion is that TiN is oxidized to TiO<sub>2</sub> in air at elevated temperatures of the pyrolyses [266]. The reason may be that the air in the tube furnace is not fully replaced by purging with N<sub>2</sub> before heat treatments. In order to eliminate air as a source of oxygen, further pyrolyses were performed after purging the tube furnace with N<sub>2</sub> gas for at least 1 hour at a 200 ml/min flow rate. The modified catalyst synthesis technique is illustrated in Figure 8.20, and the synthesis was performed as follows.

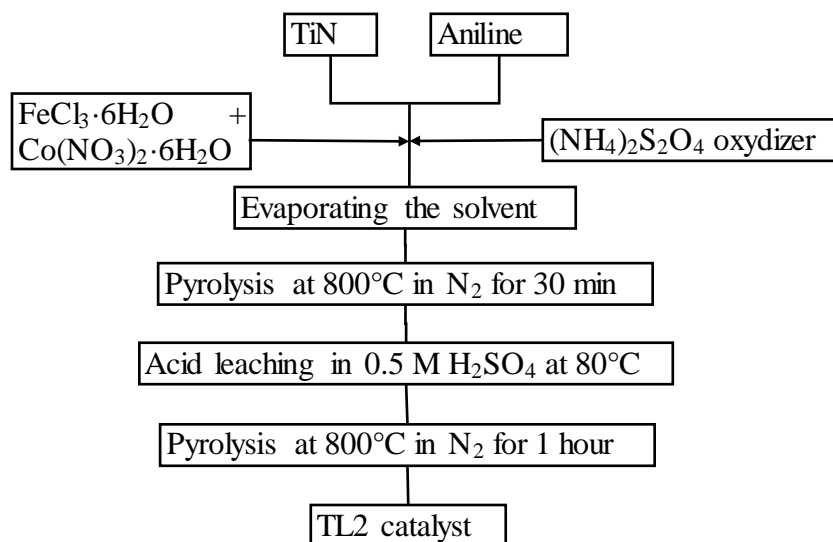


**Figure 8.20** Schematic of the TL2 catalyst synthesis.

3 ml of aniline was dissolved in 10 ml of 0.5 M HCl in a round-bottom flask, and 1 g of TiN added. The suspension was cooled down and kept at a temperature slightly below 10° C. 3 g of FeCl<sub>3</sub>·6H<sub>2</sub>O, 0.5 g of Co(NO<sub>3</sub>)<sub>2</sub>·6H<sub>2</sub>O and 5.0 g of (NH<sub>4</sub>)<sub>2</sub>S<sub>2</sub>O<sub>4</sub> were dissolved in 0.5 M HCl and added to the flask dropwise while stirring for 24 hrs. The resulting suspension was dried in the vacuum rotary evaporator. The solid was placed into a quartz boat in the tube furnace, purged with N<sub>2</sub> for circa 1.5 hours and then pyrolysed at 800 °C for 30 min. When the temperature started to decrease, the N<sub>2</sub> gas flow rate was increased to ensure fast cooling. The pyrolysed solid was acid-leached in 0.5 M H<sub>2</sub>SO<sub>4</sub> while stirring for 8 hours at 80 °C under reflux conditions, then washed with de-ionized water and vacuum-dried. The solid was placed in the tube furnace and purged for 1.5 hours with N<sub>2</sub>, then pyrolysed at 800 °C for 1 hour. When the temperature started to decrease, the N<sub>2</sub> flow rate was increased for faster cooling. After the pyrolysis, the solid was ground and sieved, and the obtained catalyst is hereafter referred to as the TL2.

The TL2 catalyst is a hydrophobic powder and does not form a uniform catalyst ink with ethanol and 5% Nafion<sup>®</sup>, but precipitates quickly from the catalyst ink suspension. For this reason, the GCD was loaded with twice the amount of the TL2

catalyst ink, namely 40  $\mu\text{l}$ . The electrocatalytic performance of the TL2 catalyst was investigated using the RRDE techniques, as shown Figure 8.21.

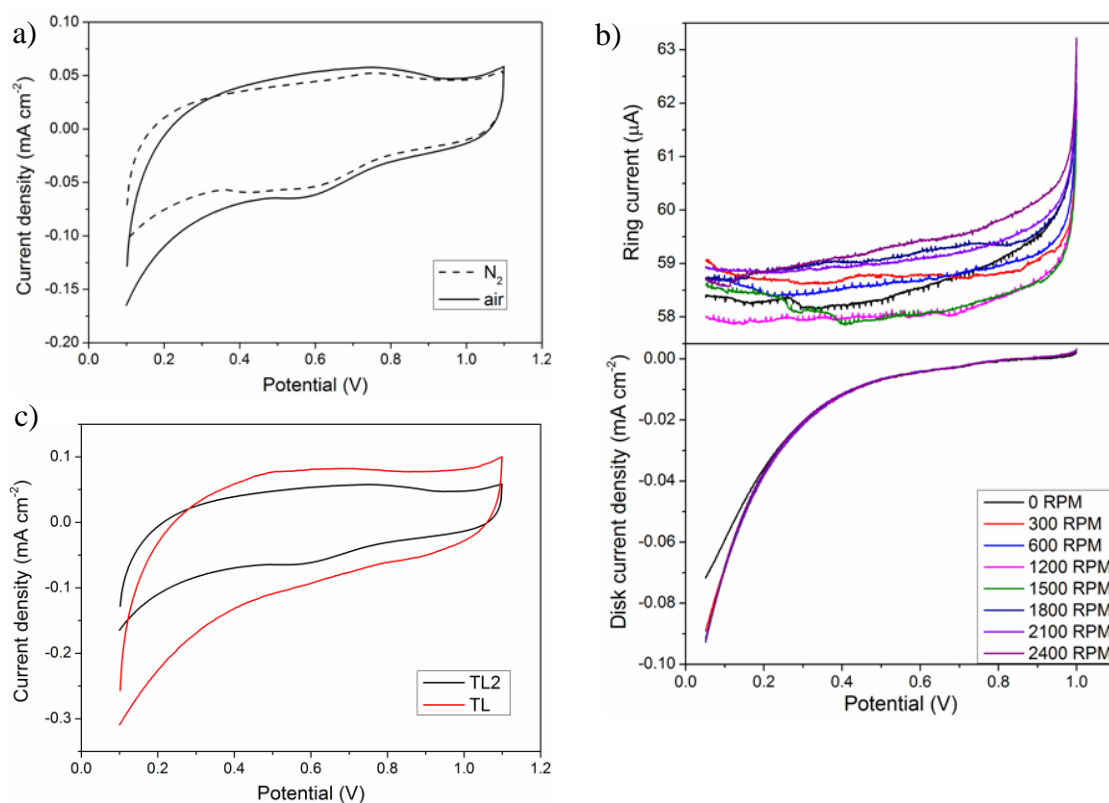


**Figure 8.21** RRDE characterisation of the TL2 catalyst: a) CVs in  $\text{N}_2$  and air at 1000 RPM, b) LSVs at different electrode rotation rates, and c) overlaid CVs in air for the TL and TL2 catalysts.

The CVs of the TL2 in  $\text{N}_2$  and air saturated electrolyte almost coincide and show a slight reduction wave at circa 0.6 V. The LSVs confirm that the TL2 catalyst is not sufficiently active towards the ORR, since the onset potential is very low, circa 0.25 V. The disk current densities are also low and there is no diffusion limited current. The overlaid CVs for the TL and TL2 catalysts evidence a very low catalytic activity towards the ORR for both materials.

XRD measurement was performed in order to elucidate the surface structure of the TL2 catalyst. Figure 8.22 shows the XRD patterns of both the TL and TL2 catalysts. The sharp peaks in the XRD pattern of the TL2 catalyst are characteristic for TiN, whereas the TL has a different peak pattern, which is assigned to  $\text{TiO}_2$ . This evidences that air has been effectively removed during the pyrolyses and no  $\text{TiO}_2$  has been formed. However, TiN is not active towards the ORR and its abundant presence on the surface of the TL2 catalyst may explain the observed low electrochemical activity towards the ORR.

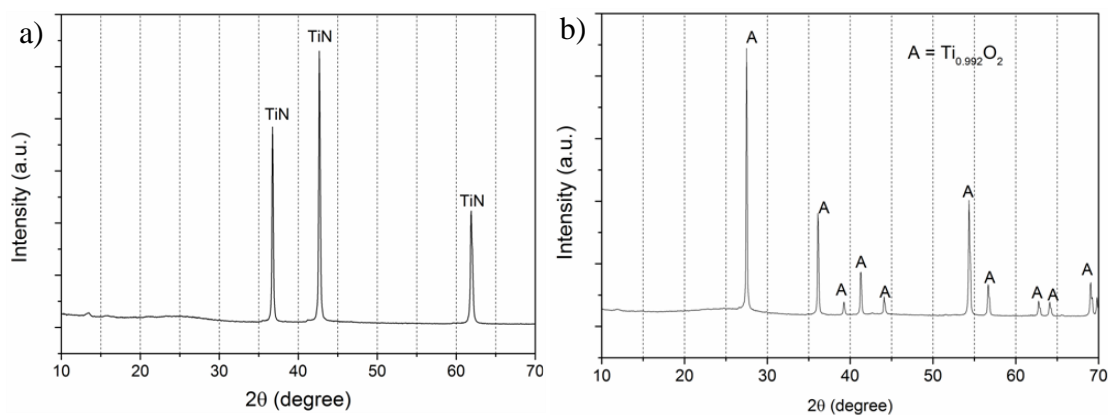


**Figure 8.22** The XRD patterns of the a) TL2 and b) TL catalysts.

Thus, low catalytic activities of the TL and TL2 catalysts indicate that the TiN is not efficient as a catalyst support. The first reason is that both  $\text{TiO}_2$  and TiN are intrinsically inactive towards the ORR and have an insufficient surface area. Furthermore, in syntheses of TiN supported N-doped carbon catalysts, it is difficult to uniformly attach active carbon particles to the non-carbon support. Carbon is eliminated from TiN or  $\text{TiO}_2$  surface during pyrolyses, and the catalytically inactive supports constitute most of the catalyst's surface.

## 8.6 Tungsten Carbide Supported N doped Carbon Catalyst

Tungsten carbide (WC) was utilized in synthesis of the N doped carbon catalyst as an alternative to carbon support using the synthesis technique illustrated in Figure 8.1. 0.7 g of WC was used instead of ZIF-8. The amounts of aniline,  $\text{FeCl}_3 \cdot 6\text{H}_2\text{O}$  and  $(\text{NH}_4)_2\text{S}_2\text{O}_8$  were 2.5 ml, 2.5 g and 4.2 g, respectively. The final product is hereafter referred to as the WL catalyst.

### 8.6.1 RRDE Characterisation

The WL catalyst was tested electrochemically using the RRDE techniques. In Figure 8.23, the CV in air saturated electrolyte show a reduction peak centred at circa 0.2 V, and the LSVs display an onset potential circa 0.5 V. The low peak and onset potentials as well as the absence of diffusion limited disk currents indicate poor activity of the WL catalyst towards the ORR. Furthermore, the WL catalyst demonstrates lower activity than carbon black, as follows from the overlaid CVs.

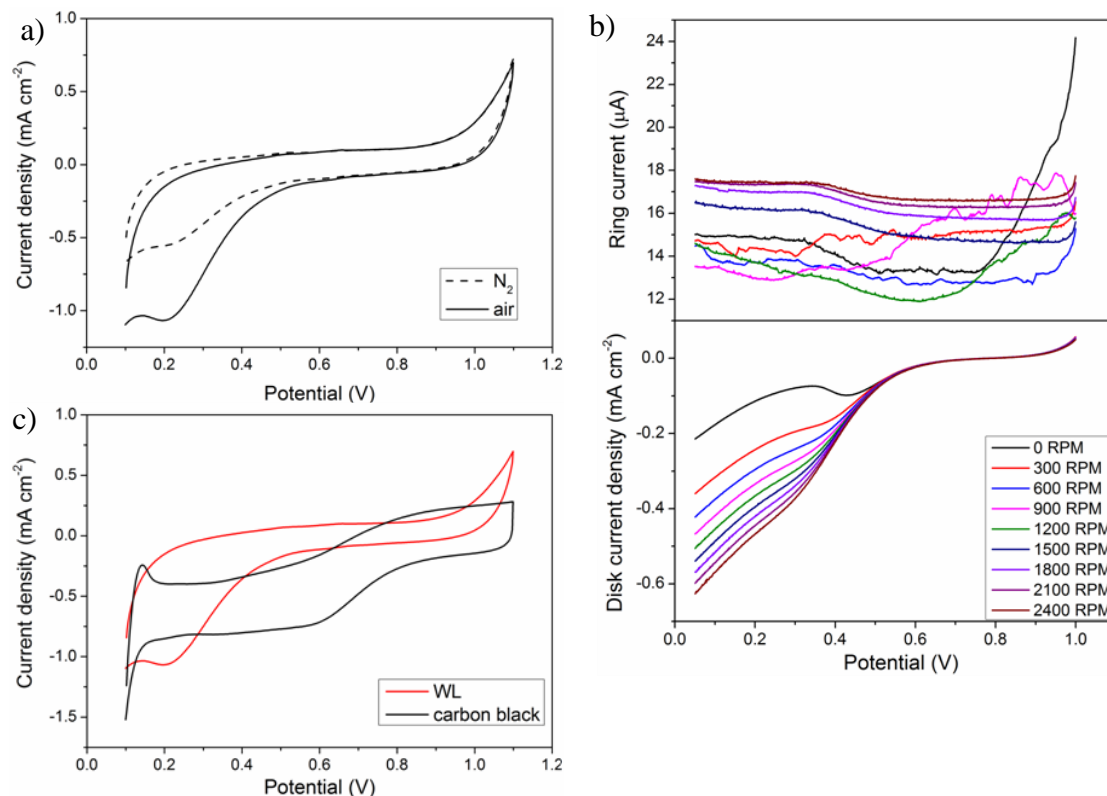


**Figure 8.23** RRDE characterisation of the WL catalyst: a) CVs in  $N_2$  and air at 1000 RPM; b) LSVs at different rotation speeds, and c) overlaid CVs in air for the WL catalyst and carbon black.

### 8.6.2 Physicochemical Characterisation

XRD measurements have been performed to investigate the chemical composition of the WL catalyst at two stages of its synthesis: (i) after polymerisation of aniline and (ii) after the final pyrolysis. Polyaniline coated support is a hydrophilic solid which converts to a hydrophobic powder after pyrolysis with a significant mass loss. Figure 8.24 shows XRD patterns for the two materials, referred to as the FePANI-CoEDA-WC and the WL catalysts, respectively. The XRD pattern of the non-pyrolysed FePANI-CoEDA-WC features sharp peaks corresponding to tungsten carbide (WC) and cobalt tungsten oxide ( $CoWO_4$ ). After final pyrolysis, only WC is detected on the WL surface, and this may be due to thermal reduction of  $CoWO_4$  by carbon. Notably, the XRD method has not detected carbon on the WL catalyst.

In contrast with XRD, XPS analysis has revealed that most of the WL catalyst surface is constituted by carbon and also contains O, N and W with visible peaks (Figure 8.25) and S, Si, P, Fe and Co in relatively small amounts (Table 8.8). This suggests that the WL catalyst may be composed of the WC particles covered by thin layer of carbon which cannot be detected by the XRD.

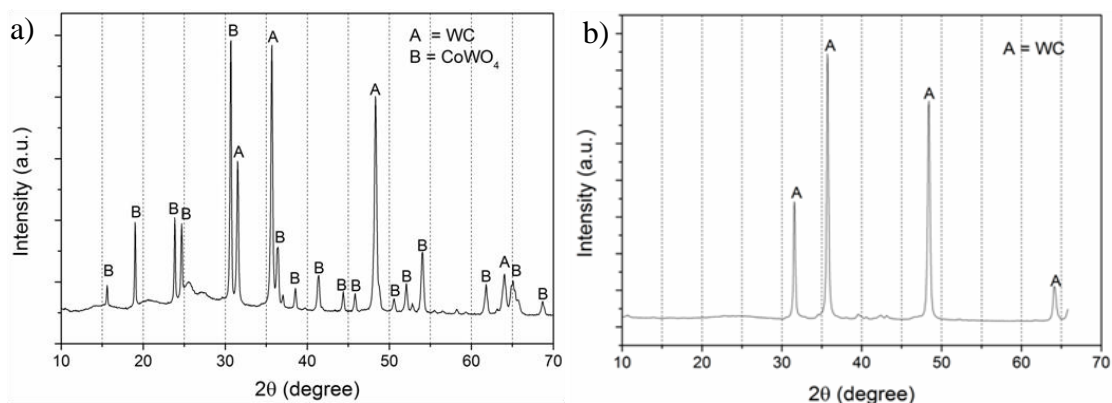


**Figure 8.24** The XRD patterns of a) Fe-PANI-CoEDA-WC and b) WL catalysts.

**Table 8.8** Elemental composition of the WL catalyst from the XPS analysis.

Element	C	O	N	S	Si	P	W	Co	Fe
Content, at. %	93.03	2.87	2.33	0.41	0.16	0.03	1.02	0.08	0.08

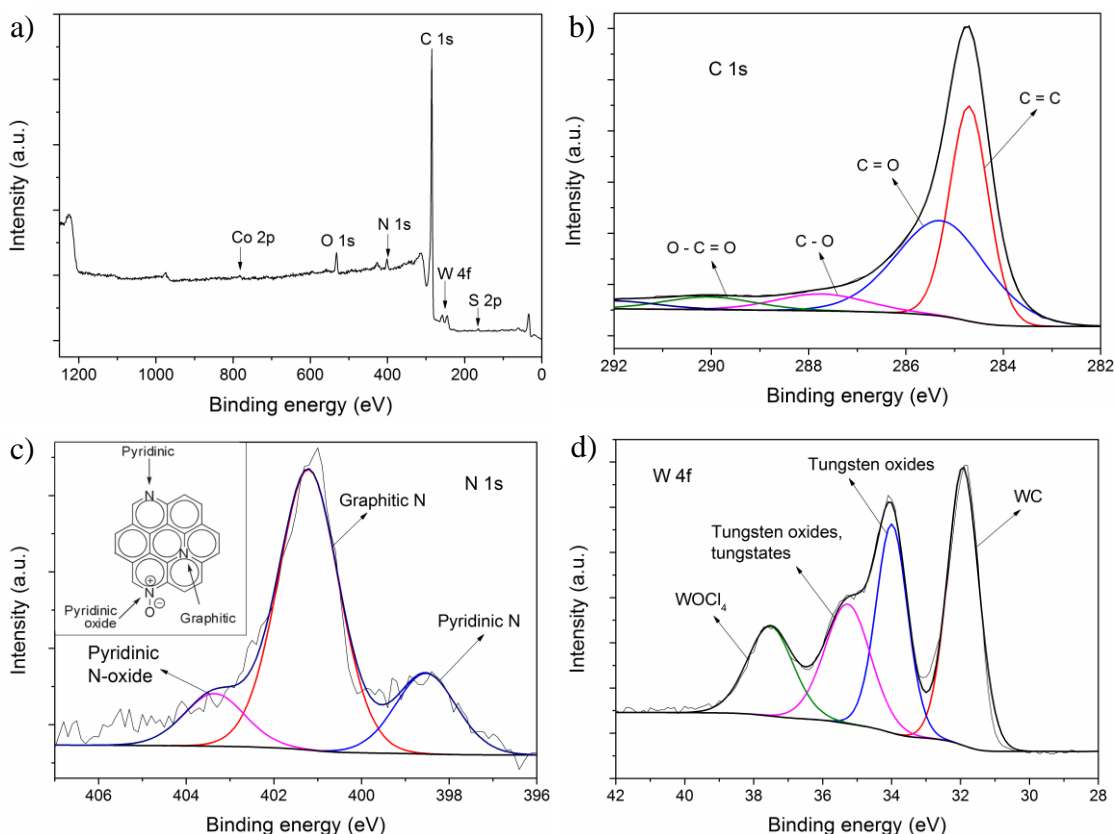


**Figure 8.25** The XPS spectra of the WL catalyst: a) XPS survey and the deconvoluted high resolution b) C 1s, c) N 1s, and d) W 4f spectra.

The deconvoluted high resolution C 1s peak has four contributions centred at 284.8, 285.4, 287.8 and 290 eV. The two low peaks at 287.8 and 290 eV correspond to

the O-C(sp<sup>3</sup>) bonds and carbonates, respectively. The small peak areas indicate that the two species have minor contribution to chemical state of carbon. The sharp peak at 284.8 eV is assigned to the sp<sup>2</sup> hybridised carbon of graphene  $\pi$  conjugated system, and the broad peak at 285.4 eV is either O=(sp<sup>2</sup>)C or N=(sp<sup>2</sup>)C bonds.

The N 1s high resolution spectrum has three contributions: pyridinic N at 398.6 eV, graphitic N at 401.5 eV and pyridinic N-oxide at 403.4 eV. The peak areas indicate that N exists primarily in graphitic form. The high resolution W 4f spectrum has been deconvoluted into four contributions. The peak at 32 eV is assigned to WC, and the peaks centred at 34, 35.3 and 37.7 eV correspond to tungsten oxides, tungstates and tungsten (VI) oxytetrachloride (WOCl<sub>4</sub>), respectively [247].

In summary, the synthesised WC supported N doped carbon catalyst showed insufficient catalytic performance towards the ORR. Physicochemical analysis suggests that the catalyst is constituted in bulk by WC which is covered by a thin layer of carbon atoms. Low surface area and intrinsic low ORR activity of WC is the most probable reason of insufficient activity of the WL catalyst. Therefore, tungsten carbide is not suitable as an alternative support for carbon-based catalysts.

## 8.7 Multiwall Carbon Nanotubes Supported N Doped Carbon Catalyst

Multiwall carbon nanotubes (MWCNTs) were utilized as an alternative support material for the N doped carbon catalyst using the synthesis technique shown in Figure 8.1. 0.4 g of MWCNTs were used as the catalyst support instead of ZIF-8. The amounts of aniline, FeCl<sub>3</sub>·6H<sub>2</sub>O and (NH<sub>4</sub>)<sub>2</sub>S<sub>2</sub>O<sub>4</sub> have been 3 ml, 3.0 g and 5.0 g, respectively. The final product is hereafter referred to as the NL catalyst.

RRDE measurements have been performed to investigate catalytic properties of the NL catalyst in the ORR. In Figure 8.26, the CVs show a significant increase of current densities at low potentials, with the wave peak at about 0.15 V. The disk current densities in the LSVs show onset potential at circa 0.45 V, which is far less than that of the LANL2 catalyst (0.83 V). The ring currents increase, starting from the onset potential, and this indicates that the electrochemical reaction at the electrode is oxygen reduction. Nevertheless, the low onset potential and absence of diffusion limiting current in the ORR on the NL catalyst indicates that it is not an efficient alternative to platinum.

The crystalline composition of the NL catalyst has been studied using the XRD method, as shown in Figure 8.27. The two broad peaks centred at  $2\theta = 24^\circ$  and  $44^\circ$  are characteristic for the (002) and (100) planes of amorphous carbon. The few sharp

peaks are characteristic for cobalt oxide (CoO), originating from Co salt used in the synthesis.

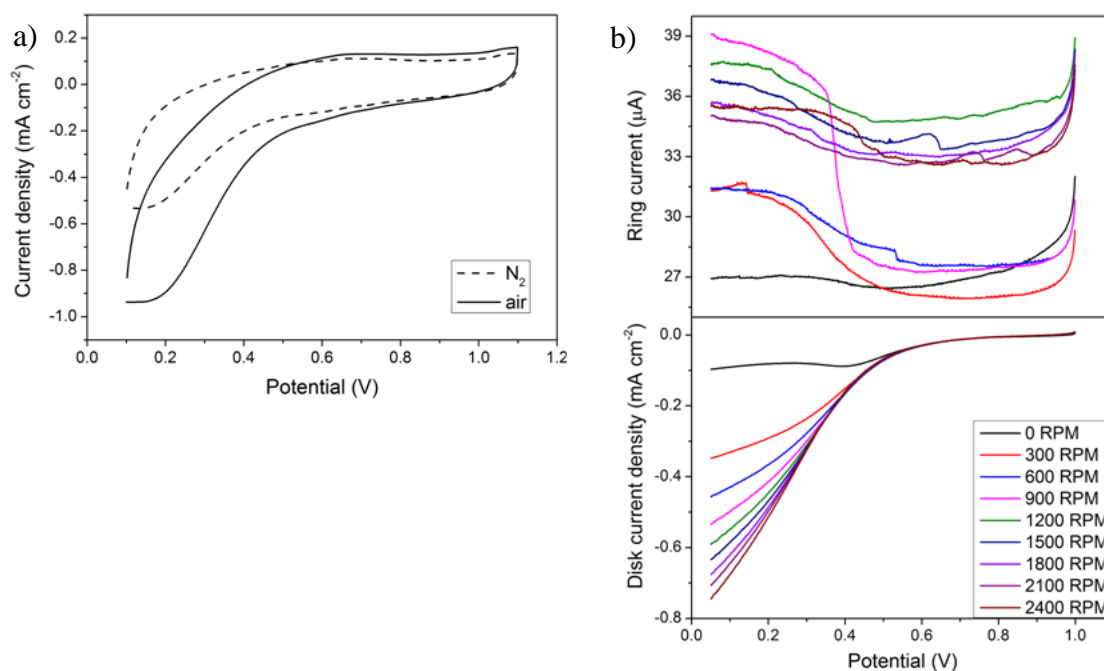


**Figure 8.26** RRDE characterisation of the NL catalyst: a) CVs in N<sub>2</sub> and air at 1000 RPM, and b) LSVs at different rotation speeds (shown in the legend).

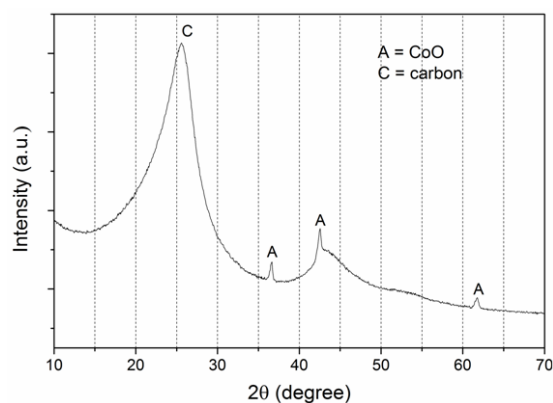


**Figure 8.27** The XRD pattern of the NL catalyst.

## 8.8 Compared Activity of the Synthesised Catalyst

The catalytic activity of the NL, LANL2, LP1-700-3-pyr, NP800, BLANL2, FL catalysts and carbon black has been compared by overlaying the RRDE results, as shown in Figure 8.28. The TL and ML catalysts have not been included because these materials showed almost negligible ORR activity. According to the CV data, the

activity towards the ORR of the synthesized catalysts and carbon black can be arranged in the following descending order:

LANL2 >> carbon black > BLANL2 > LP1-700-3-pyr > FL > NL  $\approx$  NP800

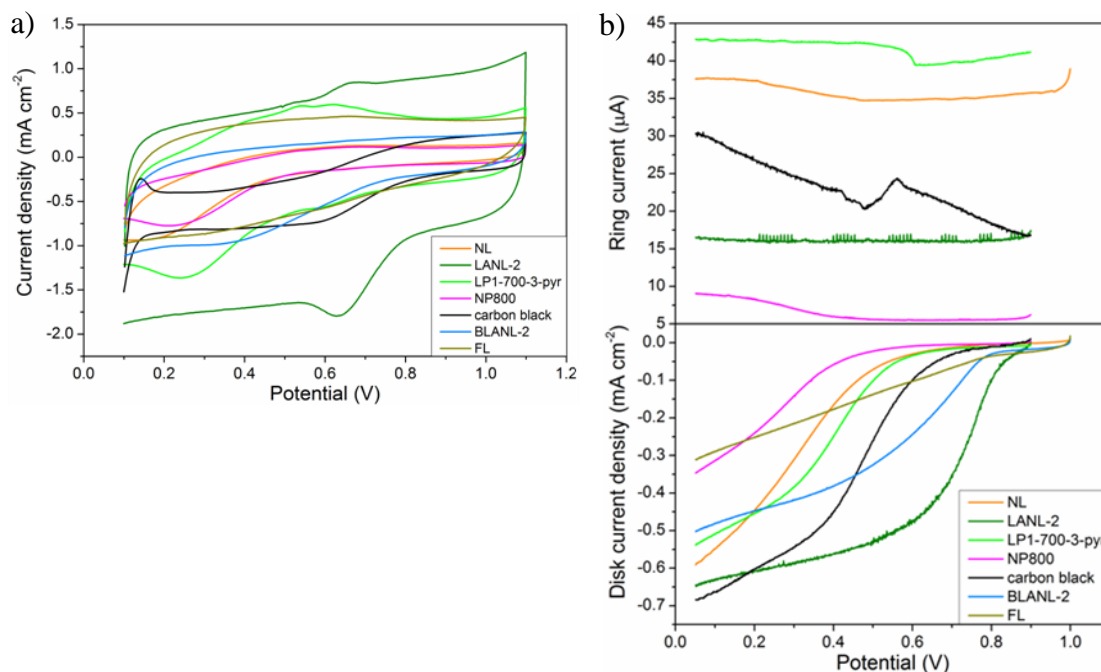


**Figure 8.28** Comparison of the RRDE results for NL, LANL2, LP1-700-3-pyr, NP800, BLANL2, FL catalysts and carbon black: a) CVs, and b) LSVs at 1200 RPM.

Based on the LSVs, the activities towards the ORR of the synthesized catalysts have been ranked as follows:

LANL2 >> BLANL2 > carbon black > LP1-700-3-pyr > NL > NP800 > FL

The ring currents on the LSVs indicate the amount of hydrogen peroxide formed during the oxygen reduction, and therefore can be used for qualitative assessment of catalyst selectivity. High ring currents imply high hydrogen peroxide yield and low catalyst selectivity. The catalyst selectivity has been arranged in the following descending order:

LANL2 > carbon black > NL > LP1-700-3-pyr

In summary, the most efficient catalyst for oxygen reduction synthesised so far is the N doped carbon catalyst LANL2. P doped carbon catalysts demonstrate very

low activity and selectivity in RRDE measurements, and this may be due to the presence of oxidized carbon and the low level of P doping. Carbon black is the most efficient material as a catalyst support. Utilizing ZIF-8 support has resulted in lower activity and selectivity, and MWCNTs, WC and TiN are inefficient support materials for carbon based catalysts.

## 8.9 Conclusion

The effect of alternative non-carbon support materials has been investigated in the synthesis of N doped carbon catalyst. The catalytic performance has been evaluated using the RRDE techniques, while the morphology and chemical composition have been studied using the XRD and XPS methods.

Carbon black is found to be the best support material among the investigated carbon and non-carbon supports. Metalorganic framework and multiwall carbon nanotubes are significantly less efficient as catalyst support than carbon black. Metallorganic framework decomposes significantly during pyrolyses and does not efficiently retain nitrogen functional groups in carbon. The inorganic conductive and non-conductive materials, i.e. tungsten carbide titanium nitride, zeolites and molecular sieves can easily oxidize or decompose during pyrolysis in the presence of air. In addition, these materials may interact with carbon at high temperatures and facilitate removal of the active carbon based layer from the surface. The electrochemical performance of catalysts supported on the investigated alternative compounds is very low, making them unsuitable for PEM fuel cell applications.

## Chapter 9

### Conclusions and Future Work

#### 9.1 Theoretical Findings

This thesis describes theoretical and experimental studies of alternative catalysts for the ORR in PEM fuel cells. The theoretical studies have focused on carbon based catalysts, simulated using simple finite-size model systems. Active sites in the catalysts have been modelled using either graphene fragments doped with heteroatoms or well known structures of transition metal macrocycles within a carbon framework. The catalytic potential of these active sites has been evaluated by simulating molecular oxygen chemisorption and mechanistic pathways of the ORR. First principles calculations have been used to investigate the reactivity of graphene in the basal planes as well as graphene sheet edges toward molecular oxygen chemisorption.

##### 9.1.1 Doped Graphene Edge Sites

Simulated graphene edges were both non-doped and mono-heteroatom doped with nitrogen, boron, phosphorus, aluminium, oxygen, sulphur or selenium. It was shown that carbon edges are more reactive than basal planes, especially in the presence of valence unsaturated carbon atoms, which enables molecular oxygen chemisorption regardless of the influence of heteroatom doping.

The theoretical results also suggest that oxygen, sulphur or selenium doped carbon edges do not facilitate molecular oxygen binding compared to non-doped carbon edges, and lead to an irreversible oxidation and thus chemical degradation of the carbon edge structure. Hence, oxygen, sulphur or selenium doped carbon is predicted to be inefficient and unstable as a catalyst for the ORR in fuel cells. In boron doped carbon edge sites, various B-O-C species may form during molecular oxygen chemisorption, thus causing changes in the chemical structure of a boron doped carbon catalyst. Oxidation of aluminium doped carbon edge sites is also very likely due to aluminium's strong affinity for oxygen. Therefore it is concluded that boron or aluminium doped carbon edge sites should have insufficient chemical stability as catalysts for the ORR.

Nitrogen and phosphorus doped carbon edges enhance molecular oxygen chemisorption compared to non-doped heteroatom doped carbon edges. It is shown that the presence of graphitic nitrogen on the edges enables molecular oxygen chemisorption on the adjacent carbon atoms without the presence of valence electrons on the unsaturated carbon atoms. Graphitic rather than pyridinic nitrogen improves the

catalytic properties of carbon edges, since the lone-electron pair of graphitic nitrogen is in-plane with the aromatic  $\pi$  electron system and donates electron density to the adjacent carbon atoms. Pyridinic nitrogen does not improve catalytic activity of carbon edges, because its lone-electron pair is not in-plane with the aromatic delocalized  $\pi$  electron system. Instead, pyridinic nitrogen withdraws electron density from carbon atoms, making molecular oxygen chemisorption on them less favourable. In phosphorus doped carbon edges, substituted phosphorus atoms can serve as molecular oxygen chemisorption sites. Phosphorus doped carbon edges retain their structure in interaction with molecular oxygen, and thus may be an efficient and stable catalyst.

### 9.1.2 Doped Graphene Planes

The catalytic activity of heteroatom doped graphene planes was studied using graphene model systems doped with nitrogen, phosphorus, boron and sulphur, and the effect of both mono and dual heteroatom doping was investigated. The catalytic activity of heteroatom doped graphene planes is found to be lower than that of carbon edge sites, since mono nitrogen, phosphorus or boron doped graphene planes do not bind molecular oxygen, whereas even non-doped carbon edge sites can bind it. In addition, graphene co-doped with nitrogen and either of phosphorus, boron or sulphur is found to be inactive towards molecular oxygen chemisorption.

Dual nitrogen doped graphene planes provide a site for molecular oxygen binding, which is a carbon atom between two substituent nitrogen atoms. In dual phosphorus, as well as phosphorus and sulphur co-doped graphene planes, the substituent phosphorus atoms are potential active sites. The calculated binding energies and activation barriers of molecular oxygen chemisorption on these dual doped graphene systems vary from 0.10 to 0.70 eV, and 0.03 to 0.14 eV, respectively. These values are comparable to those reported for platinum in the literature.

### 9.1.3 Transition Metal Macrocycles

The catalytic activity of transition metal macrocycle active sites were studied by modelling mechanistic pathways of the oxygen reduction reaction. The effect of macrocycle structure was studied by modelling molecular oxygen binding to four well-known macrocycle types either with iron, cobalt or manganese in the centre. The effect of the central transition metal atom has been investigated by obtaining the thermodynamics and kinetics of the oxygen reduction reaction mechanisms.

The theoretical results suggest that the central transition metal atom is the reaction centre, and the molecular oxygen chemisorption depends primarily on the nature of the metal. The chemisorption strength increases in the order of  $\text{Co} < \text{Fe} < \text{Mn}$ .

Also, the macrocycle structure influences the molecular oxygen binding and hence the efficiency of the active sites, but its effect is less pronounced than that of the metal centre. In a macrocycle active site, the metal centre should be terminated by a functional group on one side, e.g. a hydroxyl group, which decreases the binding capacity of the metal centre. The oxygen reduction should proceed on the other free side.

Iron macrocycle active sites are predicted to have the highest catalytic activity, since the simulated four-electron oxygen reduction pathway has negligibly small calculated activation energy on the rate limiting step. Further, cobalt and manganese macrocycle active sites have the same calculated activation energies on the rate limiting steps for the two metal centres (0.14 eV) and therefore similar activities in the four-electron oxygen reduction. However, the manganese macrocycle active sites may provide an accessible route to a two-electron oxygen reduction pathway producing undesirable hydrogen peroxide. Although iron macrocycle active sites are predicted to be the most promising for PEM fuel cells, the five-coordinated metal organic compound structure is unlikely to be stable during the highly oxidative fuel cell operation conditions. Furthermore, transition metal macrocycles are not likely to survive high temperatures of pyrolysis, which is an essential step in the catalyst synthesis process.

## **9.2 Experimental Findings**

The experimental study has focused on the synthesis and testing of alternative non-platinum catalysts to investigate the nature of active sites and the effect of alternative non-carbon support materials. Since the theoretical studies have predicted that nitrogen or phosphorus doped carbon as well as iron and cobalt macrocycle active sites should be the most efficient towards the ORR, the experimental studies have focussed on nitrogen and phosphorus doped catalysts synthesized in the presence of iron and cobalt salts.

Nitrogen doped carbon catalysts have demonstrated the best performance among the synthesized materials, but they are still substantially inferior compared to the catalytic performance of platinum. In contrast with the theoretical predictions, the catalytic activity of synthesized phosphorus doped as well as phosphorus and nitrogen co-doped carbon towards the oxygen reduction is inferior compared to nitrogen doped carbon catalysts. The experimentally observed low activity is explained by a high content of oxidized carbon and a negligible fraction of phosphorus in the carbon structure. Phosphorus in the catalyst exists predominantly in an oxidized state and therefore is not active towards the oxygen reduction. A novel technique of phosphorus

doped carbon catalyst preparation has been evaluated using a glow discharge method. In this technique, the catalyst is directly applied onto a gas diffusion layer for fuel cells. The technique as implemented proved to be inefficient, since the deposited carbon contains a considerable amount of oxygen and negligible amounts of phosphorus.

Among the investigated catalyst support materials, carbon black provides the best results in the electrochemical tests, while metalorganic frameworks and multiwall carbon nanotubes have demonstrated significantly lower activity when used as catalyst supports. Utilization of inorganic conductive and non-conductive materials, such as tungsten carbide, titanium nitride, zeolites and molecular sieves, result in very low catalytic performance, making these supports unsuitable for PEM fuel cell application. This may be due to oxidation or decomposition of these materials during pyrolysis in the presence of remaining air. In addition, these materials may interact with carbon at high temperatures and facilitate the removal of the active carbon layer from the surface.

### **9.3 Future work**

This thesis has presented a promising comprehensive approach to the development of novel alternative carbon based catalysts for the oxygen reduction reaction. This involved modelling the catalytic behaviour of the proposed catalyst compounds, as well as the synthesis and evaluation of the proposed compounds.

So far the oxygen reduction reaction has been simulated in a vacuum, or using the polarized continuum model, representing the solvent implicitly. Therefore it is recommended that future models should account explicitly for ambient water to increase the accuracy in predicting the energies of the proton transfer steps in the oxygen reduction reaction. The effect of the electric field on the catalyst-electrolyte interface also offers further research possibilities.

Currently the origin of the reactivity of the active sites has been investigated by an analysis of the atomic spin density and charge distribution on the model systems. Although spin density on atoms is an important factor in determining catalytic activity, the results shown in this thesis are in disagreement with those reported in the literature. It has been found that possible active sites have a lower spin density than inactive sites, in contradiction to the conclusions drawn elsewhere in the literature. Therefore a more detailed investigations and accurate methods that can predict the spin density and charge distribution on catalyst candidate compounds is required.

Given the contrast between the predicted and observed activity of the synthesised catalysts, future experimental work should be focused on improving the

synthesis process. The catalytic activity of a nitrogen doped catalyst may increase as a result of the heat treatment in a reductive atmosphere, such as ammonia to reduce the oxidized carbon and increase the catalytic activity and surface area.

Further study should be dedicated to the retention of, or an increase in the number of, transition metal macrocycle active sites that are highly active towards the oxygen reduction reaction. This includes the development of new or improved synthesis techniques using different compounds as sources of iron and nitrogen.

The experimental results have further shown that phosphorus doping of carbon is considerably more difficult than nitrogen doping of carbon, since phosphorus exhibits a higher affinity towards oxygen than carbon. All phosphorus doped catalysts reported in the literature and in the present thesis contain a significant fraction of oxygen, rather than just phosphorus. New synthesis techniques that exclude oxygen from the catalyst by utilizing a reductive atmosphere during pyrolyses may be the route to functional phosphorus doped catalysts.

## References

- [1] F. Barbir, PEM Fuel Cells: Theory and Practice, Elsevier Academic Press (2005).
- [2] J. Zhang, PEM Fuel Cell Electrocatalysts and Catalyst Layers, Springer (2008).
- [3] L.O. Vasquez, Fuel Cell Research Trends, Nova Science Publishers Inc., New-York (2007).
- [4] B. Smitha, S. Sridhar, A.A. Khan, Journal of Membrane Science, 259 (2005) 10-26.
- [5] M.M. Mench, Fuel Cell Engines, John Wiley & Sons Inc. (2008).
- [6] K. Epping Martin, J.P. Kopasz, K.W. McMurphy, 1040 (2010) 1-13.
- [7] I. EG&G Technical Services Inc., Fuel Cell Handbook, 7-th edition, Morgantown, (2004).
- [8] S. Lee, J.G. Speight, S.K. Loyalka, Handbook of Alternative Fuel Technology, CRC Press (2007).
- [9] M. Ehsani, Y. Gao, S.E. Gay, A. Emadi, Modern Electric, Hybrid Electric, and Fuel Cell Vehicles: Fundamentals, Theory, and Design, CRC Press (2004).
- [10] F.H. Yang, R.T. Yang, Carbon, 41 (2003) 2149-2158.
- [11] C.G. Arges, V. Ramani, P.N. Pintauro, The Electrochemical Society Interface, (2010).
- [12] J. Larminie, A.L. Dicks, Fuel Cell Systems Explained, John Wiley & Sons (2003).
- [13] X. Li, Encyclopedia of Energy Engineering and Technology, Taylor and Francis Group, LLC (2007).
- [14] G. Hoogers, Fuel Cell Technology Handbook, CPC Press (2003).
- [15] F. de Bruijn, Green Chemistry, 7 (2005) 132.
- [16] S. Thomas, M. Zalbowitz, Fuel Cells -Green Power, US Department of Energy, Los Alamos, New Mexico (1999).

- [17] S. Litster, G. McLean, *Journal of Power Sources*, 130 (2004) 61-76.
- [18] K.R. Lee, K.U. Lee, J.W. Lee, B.T. Ahn, S.I. Woo, *Electrochemistry Communications*, 12 (2010) 1052-1055.
- [19] J.M. Ziegelbauer, T.S. Olson, S. Pylypenko, F. Alamgir, C. Jaye, P. Atanassov, S. Mukerjee, *J. Phys. Chem. C*, 112 (2008) 8839-8849.
- [20] A. Velázquez-Palenzuela, L. Zhang, L. Wang, P.L. Cabot, E. Brillas, K. Tsay, J. Zhang, *Electrochimica Acta*, 56 (2011) 4744-4752.
- [21] L. Wang, L. Zhang, J. Zhang, *Electrochimica Acta*, 56 (2011) 5488-5492.
- [22] Z. Chen, D. Higgins, A. Yu, L. Zhang, J. Zhang, *Energy & Environmental Science*, 4 (2011) 3167.
- [23] C.-H. Huang, S.-J. Liu, W.-S. Hwang, *Energy*, 36 (2011) 4410-4414.
- [24] G. Wu, K.L. More, C.M. Johnston, P. Zelenay, *Science*, 332 (2011) 443-447.
- [25] L. Zhu, D. Susac, M. Teo, K. Wong, P. Wong, R. Parsons, D. Bizzotto, K. Mitchell, S. Campbell, *Journal of Catalysis*, 258 (2008) 235-242.
- [26] J. Maruyama, N. Fukui, M. Kawaguchi, I. Abe, *Journal of Power Sources*, 182 (2008) 489-495.
- [27] K. Ono, Y. Yasuda, K. Sekizawa, N. Takeuchi, T. Yoshida, M. Sudoh, *Electrochimica Acta*, 97 (2013) 58-65.
- [28] C. Jin, X. Cao, L. Zhang, C. Zhang, R. Yang, *Journal of Power Sources*, 241 (2013) 225-230.
- [29] M.H. Robson, A. Serov, K. Artyushkova, P. Atanassov, *Electrochimica Acta*, 90 (2013) 656-665.
- [30] A.B. Anderson, R. Jinnouchi, J. Uddin, *J. Phys. Chem. C*, 117 (2013) 41-48.
- [31] K. Srinivasu, S.K. Ghosh, *The Journal of Physical Chemistry C*, 117 (2013) 26021-26028.
- [32] Y. Wang, H.-P. Cheng, *The Journal of Physical Chemistry C*, 117 (2013) 2106-2112.
- [33] A. G. Saputro, H. Kasai, K. Asazawa, H. Kishi, H. Tanaka, *Journal of the Physical Society of Japan*, 82 (2013) 114704.

- [34] K.-Y. Yeh, M.J. Janik, *Journal of Computational Chemistry*, 32 (2011) 3399-3408.
- [35] M.J. Janik, C.D. Taylor, M. Neurock, *Journal of The Electrochemical Society*, 156 (2009) B126.
- [36] Z. Shi, H. Liu, K. Lee, E. Dy, J. Chlistunoff, M. Blair, P. Zelenay, J. Zhang, Z.-S. Liu, *The Journal of Physical Chemistry C*, 115 (2011) 16672-16680.
- [37] Z. Shi, J. Zhang, Z.-S. Liu, H. Wang, D.P. Wilkinson, *Electrochimica Acta*, 51 (2006) 1905-1916.
- [38] J.K. Norskov, J. Rossmeisl, A. Logadottir, L. Lindquist, *J. Phys. Chem. B*, 108 (2004) 17886-17892.
- [39] T. Ikeda, M. Boero, S.F. Huang, K. Terakura, M. Oshima, J. Ozaki, *Journal of Physical Chemistry C*, 112 (2008) 14706-14709.
- [40] L. Qi, J. Li, *Journal of Catalysis*, 295 (2012) 59-69.
- [41] H.-Y. Su, Y. Gorlin, I.C. Man, F. Calle-Vallejo, J.K. Nørskov, T.F. Jaramillo, J. Rossmeisl, *Physical Chemistry Chemical Physics*, 14 (2012) 14010.
- [42] A.B. Anderson, *Physical Chemistry Chemical Physics*, 14 (2012) 1330.
- [43] H. Dorsett, A. White, *Overview of Molecular Modelling and Ab initio Molecular Orbital Methods Suitable for Use with Energetic Materials*, Defence Science and Technology Organisation Salisbury, Australia (2000).
- [44] E.B. Butyrskaya, *Computational Chemistry: The Basics of Theory and Working with Gaussian and GaussView Programmes*, Moscow (2011).
- [45] J.B. Foresman, A. Frisch, *Exploring Chemistry with Electronic Structure Methods*, Gaussian, Inc., Pittsburgh, PA (1996).
- [46] G.M. Painter, *Multiscale Modeling of Polymer Bond Scission*, Case Western Reserve University (2009).
- [47] W. Goddard, B. Merinov, A. van Duin, T. Jacob, M. Blanco, V. Molinero, S.S. Jang, Y.H. Jang, *Molecular Simulation*, 32 (2006) 251-268.
- [48] M.J.T. Frisch, G. W.; Schlegel, H. B.; Scuseria, G. E.; Robb, M. A.; Cheeseman, J. R.; Scalmani, G.; Barone, V.; Mennucci, B.; Petersson, G. A.; Nakatsuji, H.; Caricato, M.; Li, X.; Hratchian, H. P.; Izmaylov, A. F.; Bloino, J.; Zheng, G.; Sonnenberg, J. L.; Hada, M.; Ehara, M.; Toyota, K.; Fukuda, R.; Hasegawa, J.; Ishida, M.; Nakajima, T.; Honda, Y.; Kitao, O.; Nakai, H.; Vreven, T.; Montgomery, J. A., Jr.; Peralta, J. E.; Ogliaro, F.; Bearpark, M.; Heyd, J. J.; Brothers, E.; Kudin, K. N.;

Staroverov, V. N.; Kobayashi, R.; Normand, J.; Raghavachari, K.; Rendell, A.; Burant, J. C.; Iyengar, S. S.; Tomasi, J.; Cossi, M.; Rega, N.; Millam, N. J.; Klene, M.; Knox, J. E.; Cross, J. B.; Bakken, V.; Adamo, C.; Jaramillo, J.; Gomperts, R.; Stratmann, R. E.; Yazyev, O.; Austin, A. J.; Cammi, R.; Pomelli, C.; Ochterski, J. W.; Martin, R. L.; Morokuma, K.; Zakrzewski, V. G.; Voth, G. A.; Salvador, P.; Dannenberg, J. J.; Dapprich, S.; Daniels, A. D.; Farkas, Ö.; Foresman, J. B.; Ortiz, J. V.; Cioslowski, J.; Fox, D. J., Gaussian 09, Revision D.01, Gaussian, Inc., Pittsburgh, PA (2009).

[49] Oxygen reduction reaction on platinum using DFT, <http://electronicstructure.wikidot.com/oxygen-reduction-reaction-on-platinum-using-dft>, accessed in 2014.

[50] T. Li, P.B. Balbuena, *J. Phys. Chem. B*, 105 (2001) 9943-9952.

[51] L. Ou, F. Yang, Y. Liu, S. Chen, *J. Phys. Chem. C*, 113 (2009) 20657-20665.

[52] R.A. Sidik, A.B. Anderson, *J. Electroanalytical Chemistry*, 528 (2002) 69-76.

[53] M.P. Hyman, J.W. Medlin, *J. Phys. Chem. B*, 110 (2006) 15338-15344.

[54] T. Li, P.B. Balbuena, *Chemical Physics Letters*, 367 (2003) 439-447.

[55] M.A. Petersen, S.J. Jenkins, D.A. King, *J. Phys. Chem. B*, 110 (2006) 11962-11970.

[56] Y. Xu, A. Ruban, M. Mavrikakis, *Journal of American Chemical Society*, 126 (2004) 4717-4725.

[57] V. Tripković, E. Skúlason, S. Siahrostami, J.K. Nørskov, J. Rossmeisl, *Electrochimica Acta*, 55 (2010) 7975-7981.

[58] Y. Wang, P.B. Balbuena, *J. Phys. Chem. B*, 109 (2005).

[59] M.T.M. Koper, *Molecular-Level Modeling of Anode and Cathode Electrocatalysis for PEM Fuel Cells*, in S.J. Paddison, K.S. Promislow (Eds.) *Device and Materials Modeling in PEM Fuel Cells*, Springer Science+Business Media, LLC (2009).

[60] I.E.L. Stephens, A.S. Bondarenko, U. Grønbjerg, J. Rossmeisl, I. Chorkendorff, *Energy & Environmental Science*, 5 (2012) 6744.

[61] P. Matter, L. Zhang, U. Ozkan, *Journal of Catalysis*, 239 (2006) 83-96.

[62] Z.-H. Sheng, H.-L. Gao, W.-J. Bao, F.-B. Wang, X.-H. Xia, *Journal of Materials Chemistry*, 22 (2012) 390.

[63] Z. Yang, Z. Yao, G. Li, G. Fang, H. Nie, Z. Liu, X. Zhou, X. Chen, S. Huang, *AcsNano*, 6 (2012) 205-211.

[64] J. Ozaki, T. Anahara, N. Kimura, A. Oya, *Carbon*, 44 (2006) 3358-3361.

[65] V.V. Strelko, V.S. Kuts, P.A. Thrower, *Carbon*, 38 (2000) 1499-1524.

[66] V.V. Strelko, N.T. Kartel, I.N. Dukhno, V.S. Kuts, R.B. Clarkson, B.M. Odintsov, *Surface Science*, 548 (2004) 281-290.

[67] E. Proietti, F. Jaouen, M. Lefèvre, N. Larouche, J. Tian, J. Herranz, J.-P. Dodelet, *Nature Communications*, 2 (2011) 416.

[68] K.A. Kurak, A.B. Anderson, *J. Phys. Chem. C*, 113 (2009) 6730-6734.

[69] R.A. Sidik, A.B. Anderson, N.P. Subramanian, S.P. Kumaraguru, B.N. Popov, *J. Phys. Chem. B*, 110 (2006) 1787-1793.

[70] D.W. Boukhvalov, Y.-W. Son, *Nanoscale*, 4 (2012) 417.

[71] J. Zhang, Z. Wang, Z. Zhu, *Journal of Molecular Modeling*, 19 (2013) 5515-5521.

[72] L. Zhang, Z. Xia, *J. Phys. Chem. C*, 115 (2011) 11170-11176.

[73] X. Bao, X. Nie, D.v. Deak, E.J. Biddinger, W. Luo, A. Asthagiri, U.S. Ozkan, C.M. Hadad, *Topics in Catalysis*, 56 (2013) 1623-1633.

[74] F. Studt, *Catalysis Letters*, 143 (2013) 58-60.

[75] N.P. Subramanian, X. Li, V. Nallathambi, S.P. Kumaraguru, H. Colon-Mercado, G. Wu, J.-W. Lee, B.N. Popov, *J. Power Sources*, 188 (2009) 38-44.

[76] P.H. Matter, E. Wang, M. Arias, E.J. Biddinger, U.S. Ozkan, *Journal of Molecular Catalysis A: Chemical*, 264 (2007) 73-81.

[77] D.-e. Jiang, B.G. Sumpter, S. Dai, *Journal of Chemical Physics*, 126 (2007) 134701.

[78] D. Yu, L. Wei, W. Jiang, H. Wang, B. Sun, Q. Zhang, K. Goh, R. Si, Y. Chen, *Nanoscale*, 5 (2013) 3457.

[79] H.-S. Oh, J.-G. Oh, W.H. Lee, H.-J. Kim, H. Kim, *International Journal of Hydrogen Energy*, 36 (2011) 8181-8186.

- [80] W.Y. Wong, W.R. Wan Daud, A.B. Mohamad, A.A.H. Kadhun, K.S. Loh, E.H. Majlan, *Colloquium on Humanities, Science & Engineering Research*, (2012).
- [81] F. Gao, G.-L. Zhao, S. Yang, J.J. Spivey, *Journal of the American Chemical Society*, 135 (2013) 3315-3318.
- [82] L. Feng, L. Yang, Z. Huang, J. Luo, M. Li, D. Wang, Y. Chen, *Scientific Reports*, 3 (2013) 3306.
- [83] Z. Lin, M.-k. Song, Y. Ding, Y. Liu, M. Liu, C.-p. Wong, *Physical Chemistry Chemical Physics*, 14 (2012) 3381.
- [84] J. Zhu, C. He, Y. Li, S. Kang, P.K. Shen, *Journal of Materials Chemistry A*, 1 (2013) 14700.
- [85] L. Lai, J.R. Potts, D. Zhan, L. Wang, C.K. Poh, C. Tang, H. Gong, Z. Shen, J. Lin, R.S. Ruoff, *Energy & Environmental Science*, 5 (2012) 7936.
- [86] Y. Okamoto, *Applied Surface Science*, 256 (2009) 335-341.
- [87] L. Ferrighi, M. Datteo, C. Di Valentin, *J. Phys. Chem. C*, 118 (2014) 223-230.
- [88] M. Kaukonen, A.V. Krashennnikov, E. Kauppinen, R.M. Nieminen, *ACS Catalysis*, 3 (2013) 159-165.
- [89] L. Zhang, J. Niu, M. Li, Z. Xia, *The Journal of Physical Chemistry C*, 118 (2014) 3545-3553.
- [90] J. Ozaki, N. Kimura, T. Anahara, A. Oya, *Carbon*, 45 (2007) 1847-1853.
- [91] Y. Liu, S. Chen, X. Quan, H. Yu, H. Zhao, Y. Zhang, G. Chen, *The Journal of Physical Chemistry C*, 117 (2013) 14992-14998.
- [92] C.H. Choi, M.W. Chung, H.C. Kwon, S.H. Park, S.I. Woo, *Journal of Materials Chemistry A*, 1 (2013) 3694.
- [93] C.H. Choi, S.H. Park, S.I. Woo, *Acs Nano*, 6 (2012) 7084-7091.
- [94] Y. Zhao, L. Yang, S. Chen, X. Wang, Y. Ma, Q. Wu, Y. Jiang, W. Qian, Z. Hu, *Journal of the American Chemical Society*, 135 (2013) 1201-1204.
- [95] L. Yang, S. Jiang, Y. Zhao, L. Zhu, S. Chen, X. Wang, Q. Wu, J. Ma, Y. Ma, Z. Hu, *Angewandte Chemie International Edition*, 50 (2011) 7132-7135.
- [96] Z.-W. Liu, F. Peng, H.-J. Wang, H. Yu, W.-X. Zheng, J. Yang, *Angewandte Chemie International Edition*, 50 (2011) 3257-3261.

- [97] D.-S. Yang, D. Bhattacharjya, S. Inamdar, J. Park, J.-S. Yu, *J. American Chemical Society*, 134 (2012) 16127-16130.
- [98] J. Wu, Z. Yang, X. Li, Q. Sun, C. Jin, P. Strasser, R. Yang, *Journal of Materials Chemistry A*, 1 (2013) 9889.
- [99] C.H. Choi, S.H. Park, S.I. Woo, *Journal of Materials Chemistry*, 22 (2012) 12107.
- [100] X. Bao, D.v. Deak, E.J. Biddinger, U.S. Ozkan, C.M. Hadad, *Chemical Communications*, 46 (2010) 8621.
- [101] S.-A. Wohlgemuth, R.J. White, M.-G. Willinger, M.-M. Titirici, M. Antonietti, *Green Chemistry*, 14 (2012) 1515.
- [102] J.-e. Park, Y.J. Jang, Y.J. Kim, M.-s. Song, S. Yoon, D.H. Kim, S.-J. Kim, *Physical Chemistry Chemical Physics*, 16 (2014) 103.
- [103] A.B. Anderson, R.A. Sidik, *J. Phys. Chem. B*, 108 (2004) 5031-5035.
- [104] F. Calle-Vallejo, J.I. Martínez, J. Rossmeisl, *Physical Chemistry Chemical Physics*, 13 (2011) 15639.
- [105] G. Wang, N. Ramesh, A. Hsu, D. Chu, R. Chen, *Molecular Simulation*, 34 (2008) 1051-1056.
- [106] W. Orellana, *Chemical Physics Letters*, 541 (2012) 81-84.
- [107] H. He, Y. Lei, C. Xiao, D. Chu, R. Chen, G. Wang, *J. Phys. Chem. C*, 116 (2012) 16038-16046.
- [108] X. Chen, F. Li, X. Wang, S. Sun, D. Xia, *J. Phys. Chem. C*, 116 (2012) 12553-12558.
- [109] X. Chen, S. Sun, X. Wang, F. Li, D. Xia, *J. Phys. Chem. C*, 116 (2012) 22737-22742.
- [110] L. Xiao, B. Huang, L. Zhuang, J. Lu, *RSC Advances*, 1 (2011) 1358.
- [111] J. Greeley, I.E.L. Stephens, A.S. Bondarenko, T.P. Johansson, H.A. Hansen, T.F. Jaramillo, J. Rossmeisl, I. Chorkendorff, J.K. Nørskov, *Nature Chemistry*, 1 (2009).
- [112] A.A. Gewirth, M.S. Thorum, *Inorganic Chemistry*, 49 (2010) 3557-3566.

- [113] P. Nekooi, M. Akbari, M.K. Amini, *International Journal of Hydrogen Energy*, 35 (2010) 6392-6398.
- [114] Y. Feng, A. Gago, L. Timperman, N. Alonso-Vante, *Electrochimica Acta*, 56 (2011) 1009-1022.
- [115] H. Wang, Y. Liang, Y. Li, H. Dai, *Angewandte Chemie International Edition*, 50 (2011) 10969-10972.
- [116] B.N. Popov, *Novel Non-precious Metal Catalysts for PEMFC: Catalyst Selection Through Molecular Modelling and Durability Studies*, University of South Carolina (2009).
- [117] J. Tian, L. Birry, F. Jaouen, J.P. Dodelet, *Electrochimica Acta*, 56 (2011) 3276-3285.
- [118] L.N. Ramavathu, K.K. Maniam, K. Gopalram, R. Chetty, *Journal of Applied Electrochemistry*, 42 (2012) 945-951.
- [119] L. Ding, X. Dai, R. Lin, H. Wang, J. Qiao, *Journal of The Electrochemical Society*, 159 (2012) F577-F584.
- [120] S. Wirth, F. Harnisch, A. Quade, M. Brüser, V. Brüser, U. Schröder, N.A. Savastenko, *Plasma Processes and Polymers*, 8 (2011) 914-922.
- [121] M. Yuasa, T. Kondo, D. Mori, S. Arikawa, *Polymers for Advanced Technologies*, 22 (2011) 1235-1241.
- [122] U.I. Kosłowski, I. Abs-Wurmbach, S. Fiechter, P. Bogdanoff, *J. Phys. Chem. C*, 112 (2008).
- [123] S.-T. Chang, C.-H. Wang, H.-Y. Du, H.-C. Hsu, C.-M. Kang, C.-C. Chen, J.C.S. Wu, S.-C. Yen, W.-F. Huang, L.-C. Chen, M.C. Lin, K.-H. Chen, *Energy & Environmental Science*, 5 (2012) 5305.
- [124] C.-H. Wang, C.-T. Wang, H.-C. Huang, S.-T. Chang, F.-Y. Liao, *RSC Advances*, 3 (2013) 15375.
- [125] H.-C. Huang, C.-H. Wang, I. Shown, S.-T. Chang, H.-C. Hsu, H.-Y. Du, L.-C. Chen, K.-H. Chen, *Journal of Materials Chemistry A*, 1 (2013) 14692.
- [126] S.-T. Chang, H.-C. Hsu, H.-C. Huang, C.-H. Wang, H.-Y. Du, L.-C. Chen, J.-F. Lee, K.-H. Chen, *International Journal of Hydrogen Energy*, 37 (2012) 13755-13762.
- [127] F. Jaouen, S. Marcotte, J.-P. Dodelet, G. Lindbergh, *J. Phys. Chem. B*, 107 (2003).

- [128] R. Othman, A.L. Dicks, Z. Zhu, *International Journal of Hydrogen Energy*, 37 (2011) 357-372.
- [129] D. Chu, R. Jiang, *Solid state Ionics*, 148 (2002) 591-599.
- [130] A. Serov, M.H. Robson, M. Smolnik, P. Atanassov, *Electrochimica Acta*, 109 (2013) 433-439.
- [131] F. Jaouen, F. Charreteur, J.P. Dodelet, *Journal of The Electrochemical Society*, 153 (2006) A689.
- [132] J. Wang, H. Qin, J. Liu, Z. Li, H. Wang, K. Yang, A. Li, Y. He, X. Yu, *The Journal of Physical Chemistry C*, 116 (2012) 20225-20229.
- [133] D. Nguyen-Thanh, A.I. Frenkel, J. Wang, S. O'Brien, D.L. Akins, *Applied Catalysis B: Environmental*, 105 (2011) 50-60.
- [134] P.-A. Pascone, D. Berk, J.-L. Meunier, *Catalysis Today*, 211 (2013) 162-167.
- [135] S.-H. Liu, J.-R. Wu, C.-J. Pan, B.-J. Hwang, *Journal of Power Sources*, 250 (2014) 279-285.
- [136] M. Lefevre, E. Proietti, F. Jaouen, J.P. Dodelet, *Science*, 324 (2009) 71-74.
- [137] G. Liu, X. Li, P. Ganesan, B.N. Popov, *Electrochimica Acta*, 55 (2010) 2853-2858.
- [138] V. Nallathambi, J.-W. Lee, S.P. Kumaraguru, G. Wu, B.N. Popov, *Journal of Power Sources*, 183 (2008) 34-42.
- [139] H.-S. Oh, H. Kim, *Journal of Power Sources*, 212 (2012) 220-225.
- [140] D. Higgins, Z. Chen, Z. Chen, *Electrochimica Acta*, 56 (2011) 1570-1575.
- [141] G. Wu, K. Artyushkova, S.D. Conradson, C.M. Johnston, J.S. Lezama-Pacheco, N.H. Mack, K. More, M. Nelson, P. Zelenay, *Synthesis and Performance of Polyaniline-Me-C Non-Precious Metal Cathode Catalysts for Oxygen Reduction in Fuel Cells*, Los Alamos National Laboratory (2009).
- [142] S. Gubin, S. Tkachev, *Graphene and Related Nanoforms of Carbon*, Moscow (2011).
- [143] X.-K. Kong, C.-L. Chen, Q.-W. Chen, *Chemical Society Reviews*, 43 (2014) 2841.

- [144] Z. Yang, H. Nie, X.a. Chen, X. Chen, S. Huang, *Journal of Power Sources*, 236 (2013) 238-249.
- [145] Z. Zuo, W. Li, A. Manthiram, *Journal of Materials Chemistry A*, 1 (2013) 10166.
- [146] S. Yang, X. Feng, X. Wang, K. Müllen, *Angewandte Chemie International Edition*, 50 (2011) 5339-5343.
- [147] K. Gong, F. Du, Z. Xia, M. Durstock, L. Dai, *Science*, 323 (2009) 760-764.
- [148] Z. Lin, G.H. Waller, Y. Liu, M. Liu, C.-p. Wong, *Carbon*, 53 (2013) 130-136.
- [149] W.Y. Wong, W.R.W. Daud, A.B. Mohamad, A.A.H. Kadhum, K.S. Loh, E.H. Majlan, *International Journal of Hydrogen Energy*, 38 (2013) 9370-9386.
- [150] H. Li, W. Kang, L. Wang, Q. Yue, S. Xu, H. Wang, J. Liu, *Carbon*, 54 (2013) 249-257.
- [151] R. Silva, D. Voiry, M. Chhowalla, T. Asefa, *Journal of the American Chemical Society*, 135 (2013) 7823-7826.
- [152] J. Yan, H. Meng, F. Xie, X. Yuan, W. Yu, W. Lin, W. Ouyang, D. Yuan, *Journal of Power Sources*, 245 (2014) 772-778.
- [153] Z. Mo, R. Zheng, H. Peng, H. Liang, S. Liao, *Journal of Power Sources*, 245 (2014) 801-807.
- [154] Q. Liu, H. Zhang, H. Zhong, S. Zhang, S. Chen, *Electrochimica Acta*, 81 (2012) 313-320.
- [155] M.S. Ahmed, S. Jeon, *Journal of Power Sources*, 218 (2012) 168-173.
- [156] Y. Tang, S.C. Burkert, Y. Zhao, W.A. Saidi, A. Star, *The Journal of Physical Chemistry C*, 117 (2013) 25213-25221.
- [157] M. Sevilla, L. Yu, T.P. Fellingner, A.B. Fuertes, M.-M. Titirici, *RSC Advances*, 3 (2013) 9904.
- [158] S. Ci, Y. Wu, J. Zou, L. Tang, S. Luo, J. Li, Z. Wen, *Chinese Science Bulletin*, 57 (2012) 3065-3070.
- [159] A.U. Nilekar, M. Mavrikakis, *Surface Science*, 602 (2008) L89-L94.
- [160] S.K. Ramasahayam, U.B. Nasini, V. Bairi, A.U. Shaikh, T. Viswanathan, *RSC Advances*, 4 (2014) 6306.

- [161] C.H. Choi, M.W. Chung, S.H. Park, S.I. Woo, *Physical Chemistry Chemical Physics*, 15 (2013) 1802.
- [162] L. Chen, X. Cui, Y. Wang, M. Wang, R. Qiu, Z. Shu, L. Zhang, Z. Hua, F. Cui, C. Wei, J. Shi, *Dalton Transactions*, 43 (2014) 3420.
- [163] J. Xu, Y. Zhao, C. Shen, L. Guan, *ACS Applied Materials & Interfaces*, 5 (2013) 12594-12601.
- [164] Z. Jin, H. Nie, Z. Yang, J. Zhang, Z. Liu, X. Xu, S. Huang, *Nanoscale*, 4 (2012) 6455.
- [165] X. Li, L. Liu, J.-W. Lee, B.N. Popov, *Journal of Power Sources*, 182 (2008) 18-23.
- [166] C.H. Choi, M.W. Chung, Y.J. Jun, S.I. Woo, *RSC Advances*, 3 (2013) 12417.
- [167] Y. Zhao, K. Watanabe, K. Hashimoto, *Journal of Materials Chemistry*, 22 (2012) 12263.
- [168] X. Sun, Y. Zhang, P. Song, J. Pan, L. Zhuang, W. Xu, W. Xing, *ACS Catalysis*, 3 (2013) 1726-1729.
- [169] X. Sun, P. Song, Y. Zhang, C. Liu, W. Xu, W. Xing, *Scientific Reports*, 3 (2013).
- [170] Z. Yao, H. Nie, Z. Yang, X. Zhou, Z. Liu, S. Huang, *Chemical Communications*, 48 (2012) 1027.
- [171] B.N. Popov, X. Li, G. Liu, J.-W. Lee, *International Journal of Hydrogen Energy*, 36 (2011) 1794-1802.
- [172] K. Kamiya, K. Hashimoto, S. Nakanishi, *Chemical Communications*, 48 (2012) 10213.
- [173] S. Li, Y. Hu, Q. Xu, J. Sun, B. Hou, Y. Zhang, *Journal of Power Sources*, 213 (2012) 265-269.
- [174] L. Xu, G. Zhang, J. Chen, Y. Zhou, G.e. Yuan, F. Yang, *Journal of Power Sources*, 240 (2013) 101-108.
- [175] X. Fu, Y. Liu, X. Cao, J. Jin, Q. Liu, J. Zhang, *Applied Catalysis B: Environmental*, 130-131 (2013) 143-151.
- [176] Q. Liu, J. Zhang, *Langmuir*, 29 (2013) 3821-3828.

- [177] H. Tang, H. Yin, J. Wang, N. Yang, D. Wang, Z. Tang, *Angewandte Chemie International Edition*, 52 (2013) 5585-5589.
- [178] J.-Y. Choi, D. Higgins, Z. Chen, *Journal of The Electrochemical Society*, 159 (2012) B87.
- [179] Z. Xu, H. Li, G. Cao, Z. Cao, Q. Zhang, K. Li, X. Hou, W. Li, W. Cao, *Journal of Materials Chemistry*, 20 (2010) 8230.
- [180] D. Deng, L. Yu, X. Chen, G. Wang, L. Jin, X. Pan, J. Deng, G. Sun, X. Bao, *Angewandte Chemie International Edition*, 52 (2013) 371-375.
- [181] C. Arbizzani, S. Righi, F. Soavi, M. Mastragostino, *International Journal of Hydrogen Energy*, 36 (2011) 5038-5046.
- [182] Y. Yuan, B. Zhao, Y. Jeon, S. Zhong, S. Zhou, S. Kim, *Bioresource Technology*, 102 (2011) 5849-5854.
- [183] J.Y. Cheon, C. Ahn, D.J. You, C. Pak, S.H. Hur, J. Kim, S.H. Joo, *Journal of Materials Chemistry A*, 1 (2013) 1270.
- [184] A.A. Mikhaylova, E.K. Tusseeva, N.A. Mayorova, A.Y. Rychagov, Y.M. Volkovich, A.V. Krestinin, O.A. Khazova, *Electrochimica Acta*, 56 (2011) 3656-3665.
- [185] M. Jahan, Q. Bao, K.P. Loh, *Journal of the American Chemical Society*, 134 (2012) 6707-6713.
- [186] D. Zhao, J.-L. Shui, C. Chen, X. Chen, B.M. Repragle, D. Wang, D.-J. Liu, *Chemical Science*, 3 (2012) 3200.
- [187] A. Rabis, P. Rodriguez, T.J. Schmidt, *ACS Catalysis*, 2 (2012) 864-890.
- [188] H. Liu, Y. Liu, D. Zhu, *Journal of Materials Chemistry*, 21 (2011) 3335.
- [189] R. Wang, X. Li, H. Li, Q. Wang, H. Wang, W. Wang, J. Kang, Y. Chang, Z. Lei, *International Journal of Hydrogen Energy*, 36 (2011) 5775-5781.
- [190] R. Wang, J. Jia, H. Li, X. Li, H. Wang, Y. Chang, J. Kang, Z. Lei, *Electrochimica Acta*, 56 (2011) 4526-4531.
- [191] A. Serov, M.H. Robson, K. Artyushkova, P. Atanassov, *Applied Catalysis B: Environmental*, 127 (2012) 300-306.
- [192] A. Serov, M.H. Robson, M. Smolnik, P. Atanassov, *Electrochimica Acta*, 80 (2012) 213-218.

- [193] M. Lu, L. Guo, S. Kharkwal, H. Wu, H.Y. Ng, S.F.Y. Li, *Journal of Power Sources*, 221 (2013) 381-386.
- [194] S.-Y. Huang, P. Ganesan, B.N. Popov, *ACS Catalysis*, 2 (2012) 825-831.
- [195] L. Chevallier, A. Bauer, S. Cavaliere, R. Hui, J. Rozière, D.J. Jones, *ACS Applied Materials & Interfaces*, 4 (2012) 1752-1759.
- [196] K. Kakinuma, Y. Wakasugi, M. Uchida, T. Kamino, H. Uchida, S. Deki, M. Watanabe, *Electrochimica Acta*, 77 (2012) 279-284.
- [197] Y. Bing, V. Neburchilov, C. Song, R. Baker, A. Guest, D. Ghosh, S. Ye, S. Campbell, J. Zhang, *Electrochimica Acta*, 77 (2012) 225-231.
- [198] X. Li, C. Liu, W. Xing, T. Lu, *Journal of Power Sources*, 193 (2009) 470-476.
- [199] W. Wang, O. Savadogo, Z.-F. Ma, *Journal of Applied Electrochemistry*, 42 (2012) 857-866.
- [200] D.T. Dam, K.-D. Nam, H. Song, X. Wang, J.-M. Lee, *International Journal of Hydrogen Energy*, 37 (2012) 15135-15139.
- [201] M. Chisaka, A. Ishihara, K. Suito, K.-i. Ota, H. Muramoto, *Electrochimica Acta*, 88 (2013) 697-707.
- [202] I.J. Hsu, Y.C. Kimmel, Y. Dai, S. Chen, J.G. Chen, *Journal of Power Sources*, 199 (2012) 46-52.
- [203] K. Jiang, Q. Jia, M. Xu, D. Wu, L. Yang, G. Yang, L. Chen, G. Wang, X. Yang, *Journal of Power Sources*, 219 (2012) 249-252.
- [204] J. Feng, Y. Liang, H. Wang, Y. Li, B. Zhang, J. Zhou, J. Wang, T. Regier, H. Dai, *Nano Research*, 5 (2012) 718-725.
- [205] Z. Yang, X. Zhou, H. Nie, Z. Yao, S. Huang, *ACS Applied Materials & Interfaces*, 3 (2011) 2601-2606.
- [206] Y. Tan, C. Xu, G. Chen, X. Fang, N. Zheng, Q. Xie, *Advanced Functional Materials*, 22 (2012) 4584-4591.
- [207] M. Lu, S. Kharkwal, H.Y. Ng, S.F.Y. Li, *Biosensors and Bioelectronics*, 26 (2011) 4728-4732.
- [208] J.-S. Lee, G.S. Park, H.I. Lee, S.T. Kim, R. Cao, M. Liu, J. Cho, *Nano Letters*, 11 (2011) 5362-5366.

- [209] G. Liu, H.M. Zhang, M.R. Wang, H.X. Zhong, J. Chen, *Journal of Power Sources*, 172 (2007) 503-510.
- [210] Y. Ohgi, A. Ishihara, K. Matsuzawa, S. Mitsushima, K.-i. Ota, M. Matsumoto, H. Imai, *Electrochimica Acta*, 68 (2012) 192-197.
- [211] R. Ohnishi, K. Takanabe, M. Katayama, J. Kubota, K. Domen, *The Journal of Physical Chemistry C*, 117 (2013) 496-502.
- [212] M. Chisaka, T. Iijima, Y. Ishihara, Y. Suzuki, R. Inada, Y. Sakurai, *Electrochimica Acta*, 85 (2012) 399-410.
- [213] U.I. Kramm, I. Herrmann-Geppert, P. Bogdanoff, S. Fiechter, *J. Phys. Chem. C*, 115 (2011) 23417-23427.
- [214] S. Takenaka, H. Matsumori, H. Matsune, M. Kishida, *Applied Catalysis A: General*, 409-410 (2011) 248-256.
- [215] D. Geng, H. Liu, Y. Chen, R. Li, X. Sun, S. Ye, S. Knights, *Journal of Power Sources*, 196 (2011) 1795-1801.
- [216] C.V. Rao, C.R. Cabrera, Y. Ishikawa, *Journal of Physical Chemistry Letters*, 1 (2010) 2622-2627.
- [217] J. Zhang, S. Tang, L. Liao, W. Yu, *Chinese Journal of Catalysis*, 34 (2013) 1051-1065.
- [218] L. Zhang, J. Zhang, D.P. Wilkinson, H. Wang, *Journal of Power Sources*, 156 (2006) 171-182.
- [219] Z.-Y. Yang, Y.-X. Zhang, L. Jing, Y.-F. Zhao, Y.-M. Yan, K.-N. Sun, *Journal of Materials Chemistry A*, 2 (2014) 2623.
- [220] M. Ferrandon, X. Wang, A.J. Kropf, D.J. Myers, G. Wu, C.M. Johnston, P. Zelenay, *Electrochimica Acta*, 110 (2013) 282-291.
- [221] X. Yuan, X.-X. Hu, X.-L. Ding, H.-C. Kong, H.-D. Sha, H. Lin, W. Wen, G. Shen, Z. Guo, Z.-F. Ma, Y. Yang, *Nanoscale Research Letters*, 8 (2013) 478.
- [222] Y. Hu, X. Zhao, Y. Huang, Q. Li, N.J. Bjerrum, C. Liu, W. Xing, *Journal of Power Sources*, 225 (2013) 129-136.
- [223] N. Larouche, R. Chenitz, M. Lefèvre, E. Proietti, J.-P. Dodelet, *Electrochimica Acta*, 115 (2014) 170-182.
- [224] F. Jaouen, M. Lefevre, J.-P. Dodelet, M. Cai, *J. Phys. Chem. B*, 110 (2006) 5553-5558.

- [225] D. Chen, H. Feng, J. Li, *Chemical Reviews*, 10 (2012) 1021.
- [226] N. Chen, R.T. Yang, *Carbon*, 36 (1998) 1061-1070.
- [227] N. Chen, R.T. Yang, *J. Physical Chemistry A*, 102 (1998) 6348-6356.
- [228] J.A. Dean, *Lange's Handbook of Chemistry*, 15-th edition, McGraw-Hill Inc. (1999).
- [229] E.D. Glendening, A.E. Reed, J.E. Carpenter, F. Weinhold, NBO Version 3.1.
- [230] F. Jensen, *Introduction to Computational Chemistry*, Wiley-Blackwell (2007).
- [231] Pine Instrument Company, Educator's Reference Guide for Electrochemistry, <https://www.pineinst.com/echem/viewproduct.asp?ID=46265>, accessed 2013.
- [232] Bio-Logic Science Instruments, Calculation of the Platinum's Active Surface, <http://www.bio-logic.info/potentiostat-electrochemistry-ec-lab/apps-literature/application-notes/general-electrochemistry/>, accessed 2013.
- [233] Z. Mo, H. Peng, H. Liang, S. Liao, *Electrochimica Acta*, 99 (2013) 30-37.
- [234] ALS Co. Ltd, *Electrochemical Electrodes and Accessories*, <http://www.als-japan.com/1295.html>, accessed 2013.
- [235] V. Vishnyakov, *Vacuum*, 80 (2006) 1053-1065.
- [236] H.-J. Zhang, X. Yuan, L. Sun, J. Yang, Z.-F. Ma, Z. Shao, *Electrochimica Acta*, 77 (2012) 324-329.
- [237] R.M. Nix, *An Introduction to Surface Chemistry*, <http://www.chem.qmul.ac.uk/surfaces/scc/>, accessed 2014.
- [238] B. Hafner, *Scanning Electron Microscopy Primer*, University of Minnesota (2007).
- [239] B. Hafner, *Energy Dispersive Spectroscopy on the SEM: A Primer*, University of Minnesota (2007).
- [240] K.N. Bozhilov, *Introduction to Energy Dispersive X-ray Spectrometry (EDS)*, University of California, <http://micron.ucr.edu/>, accessed 2014.
- [241] F.A. de Bruijn, V.A.T. Dam, G.J.M. Janssen, *Fuel Cells*, 8 (2008) 3-22.
- [242] D.J. Myers, X. Wang, N. Garland, *Polymer Electrolyte Fuel Cell Lifetime Limitations: The Role of Electrocatalyst Degradation*, annual Progress Report (2010).

[243] P. Zelenay, G. Wu, Nitrogen-Doped Carbon-Supported Cobalt-Iron Oxygen Reduction Catalyst, patent, Los Alamos (2011).

[244] Gamry Instruments, RDE710 Rotating Electrode Instruction Manual, <http://www.gamry.com/products/accessories/rde710-rotating-electrode/>, accessed 2013.

[245] Pine Research Instrumentation, RRDE Efficiency Calculator, [https://www.pineinst.com/echem/files/RRDE\\_EFFICIENCY.XLS](https://www.pineinst.com/echem/files/RRDE_EFFICIENCY.XLS), accessed 2013.

[246] B.P. Vinayan, S. Ramaprabhu, *Nanoscale*, 5 (2013) 5109.

[247] J.F. Moulder, W.F. Stickle, P.E. Sobol, K.D. Bomben, *Handbook of X-ray Photoelectron Spectroscopy*, Perkin-Elmer Corporation (1992).

[248] P.T. Ndifon, M.O. Agwara, Y. Hayashi, A. Uehara, *Bulletin of the Chemical Society of Ethiopia*, 22 (2008) 253-260.

[249] Quorum Technologies, CC7650 Carbon Coater Operating Manual, <http://www.quorumtech.com/customer-support/discontinued-product-manuals-and-circuit-diagrams.html>, accessed 2014.

[250] Sigma-Aldrich, Tungsten Carbide Specification Sheet, <http://www.sigmaaldrich.com/catalog/product/aldrich/241881?lang=en&region=GB>, accessed 2014.

[251] Sigma-Aldrich, Titanium Nitride Specification Sheet, <http://www.sigmaaldrich.com/catalog/product/aldrich/595063?lang=en&region=GB>, accessed 2014.

[252] A. Peigney, C. Laurent, E. Flahaut, R.R. Basca, A. Rousset, *Carbon*, 39 (2001) 507-514.

[253] D.P. Roelofsen, *Molecular Sieve Zeolites: Properties and Applications in Organic Synthesis*, Delft (1972).

[254] Shanghai MLC Molecular Sieve Ltd., *Introduction to Molecular Sieve*, <http://www.shmlc.com/pls.htm>, accessed 2014.

[255] AzkoNobel, Ketjenblack EC-300J Product Data Sheet, [http://www.polymerpds.akzonobel.com/PolymerChemicalsPDS/showPDF.aspx?pds\\_id=1024](http://www.polymerpds.akzonobel.com/PolymerChemicalsPDS/showPDF.aspx?pds_id=1024), accessed 2014.

[256] Sigma-Aldrich, Bazolite Z1200 Product Data Sheet, <http://www.sigmaaldrich.com/catalog/product/aldrich/691348?lang=en&region=GB>, accessed 2014.

- [257] Princeton University, View Structure: ZIF-8,  
[http://helios.princeton.edu/mofomics/cgi-bin/view\\_structure.pl?src=zif&id=ZIF-8&token=30c2cbc36c01166bb76f3b16dbd6ff5c](http://helios.princeton.edu/mofomics/cgi-bin/view_structure.pl?src=zif&id=ZIF-8&token=30c2cbc36c01166bb76f3b16dbd6ff5c), accessed 2014.
- [258] Sigma-Aldrich, Faujasite Type Zeolite Material Data Sheet,  
<http://www.sigmaaldrich.com/catalog/product/fluka/bcr704?lang=en&region=GB>,  
accessed 2014.
- [259] Rochester University, Molecular Sieves,  
<http://chem.chem.rochester.edu/~nvd/molecularsieves.html>, accessed 2014.
- [260] K.S. Park, Proceedings of the National Academy of Sciences, 103 (2006)  
10186-10191.
- [261] C.-Y. Li, L.V.C. Rees, Zeolites, 6 (1986).
- [262] G.T. Kerr, Journal of Catalysis, 15 (1969).
- [263] F.H. Pollard, P. Woodward, Transactions of the Faraday Society, 46 (1950).
- [264] J. Nerz, B. Kushner, A. Rotolico, Journal of Thermal Spray Technology, 1  
(1992).
- [265] F. Yang, V. Hlavacek, Metallurgical and Materials Transactions B, 29B (1998).
- [266] Knowledge Base Nanomaterials, Titanium Nitride,  
<http://www.nanopartikel.info/cms/lang/en/Wissensbasis/Titannitrid>, accessed 2014.

## Appendix A

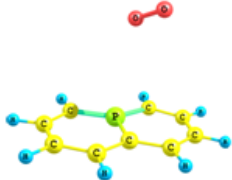
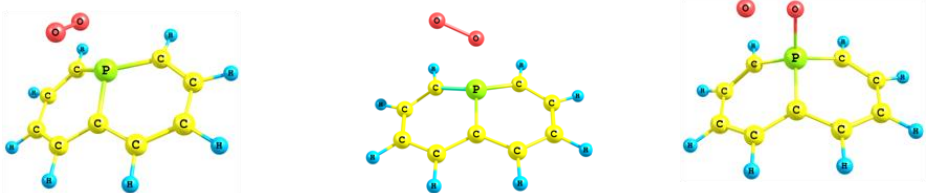
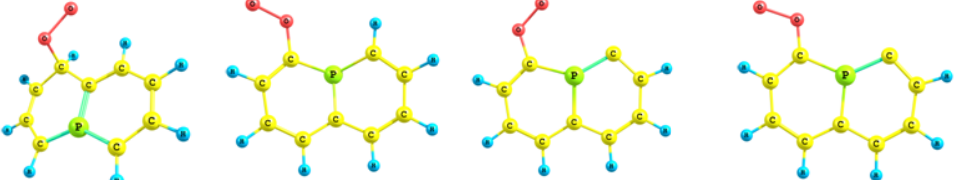
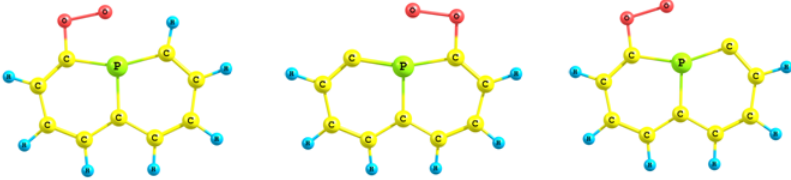
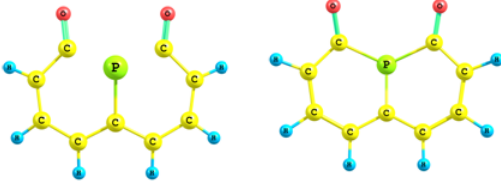
### DFT Study of Molecular Oxygen Binding to P, Al, S or Se Doped Carbon Edge Sites

Figures A1 - A3 show the potential energy profiles of molecular oxygen binding to the P, Al doped naphthalene-type and the S and Se doped anthracene-type model systems. The modifications of the P and Al doped systems are (i) a (-1) charge, (ii) one H atom removed, (iii) two H atoms removed, and (iv) two H atoms removed and a (-1) charge. The modifications of the S and Se doped systems are (i) two H atoms removed, and (ii) two H atoms removed and a (-1) charge.

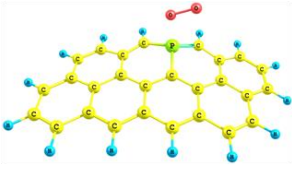
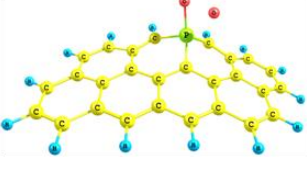
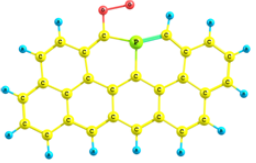
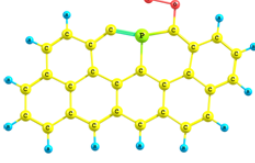
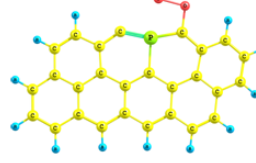
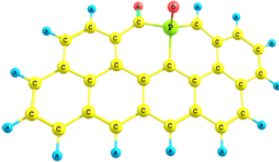
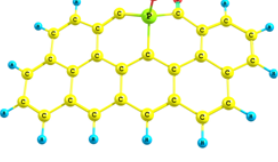
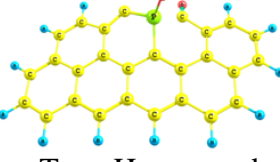
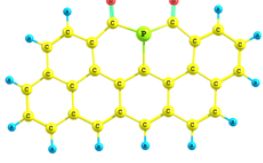
In the case of the P and Al doped systems, the scanned coordinates have been the distances between one of the atoms of the oxygen molecule and either (i) the doped heteroatom, or (ii) the adjacent C atom. The O-P and O-Al distances were decremented from 3.5 Å to 1.5 and 1.6 Å, respectively, and the O-C distance was decremented from 3.5 Å to 1.2 Å. In the case of the S and Se doped anthracene-type systems, the scanned coordinates have been the distances between one of the atoms of the oxygen molecule and either (i) the valence unsaturated C atom at the edge, or (ii) the C atom adjacent to the heteroatom. The distances were decremented from 3.0 to 1.3 Å, and from 2.3 to 1.1 Å, respectively. In the scan calculations, the step size has been set to 0.1 Å. A step size of 0.025 Å has been used in several calculations to obtain very fine resolution potential energy profiles.

In order to account for the triplet spin state of the molecular oxygen, the spin multiplicities in the scan calculations have been chosen either 3 or 4, depending on the electronic structure. The relative energies in the potential energy profiles of molecular oxygen binding have been calculated as the energy difference between each scan point and the minimum energy point. The structures of energy minima, maxima, as well as start and end of the scan calculations are shown adjacent to the corresponding points of the potential energy profiles.

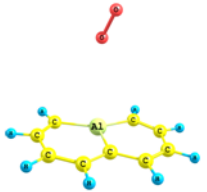
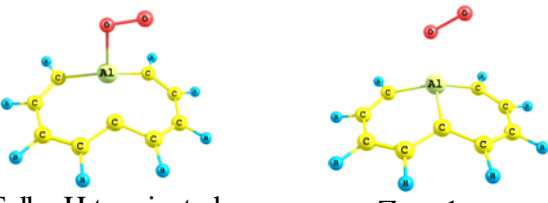
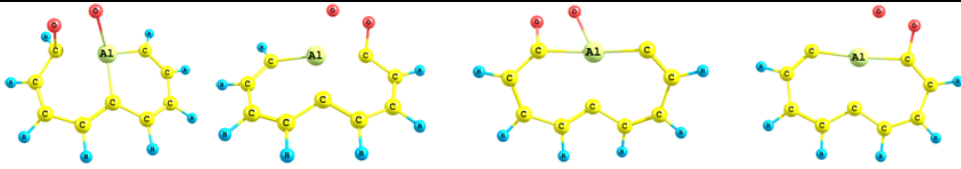
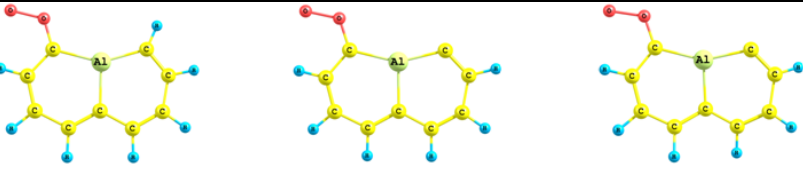
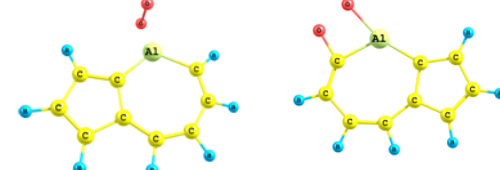
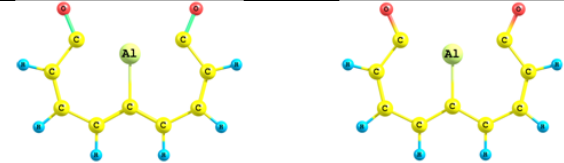
**Table A1** Optimised products of molecular oxygen binding to the P doped naphthalene-type systems.

Product label	Structures
A	 <p>Fully H terminated</p>
B	 <p>Fully H terminated                      Z = -1                      Z = -1</p>
C	 <p>Z = -1                      One H removed                      Two H removed                      Two H removed and Z = -1</p>
D	 <p>One H removed                      Two H removed                      Two H removed and Z = -1</p>
E	 <p>Two H removed                      Two H removed and Z = -1</p>

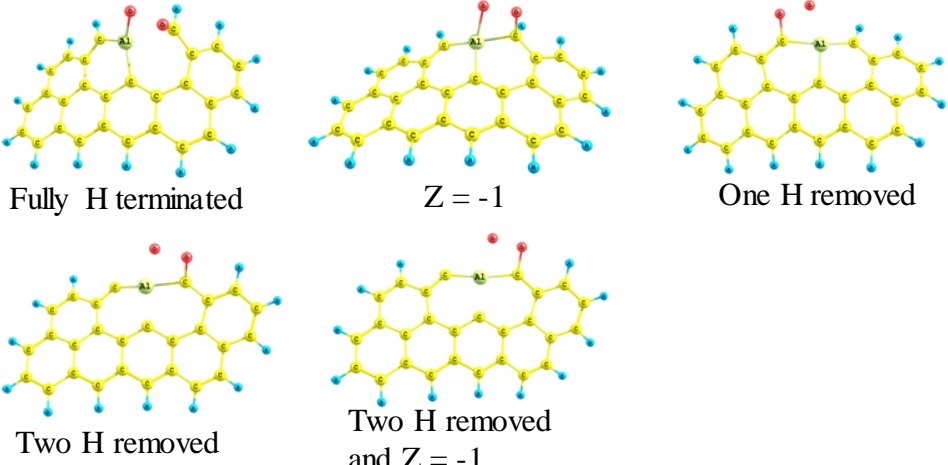
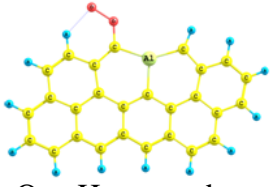
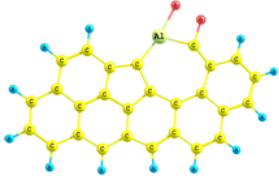
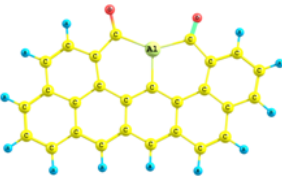
**Table A2** Optimised products of molecular oxygen binding to the P doped graphene-type systems.

Product label	Structures		
<b>B</b>	 <p data-bbox="499 566 740 600">Fully H terminated</p>		 <p data-bbox="932 566 1018 600"><math>Z = -1</math></p>
<b>D</b>	 <p data-bbox="464 786 663 819">One H removed</p>	 <p data-bbox="799 786 999 819">Two H removed</p>	 <p data-bbox="1142 786 1342 853">Two H removed and <math>Z = -1</math></p>
<b>F</b>	 <p data-bbox="464 1048 663 1081">One H removed</p>	 <p data-bbox="799 1048 999 1081">Two H removed</p>	 <p data-bbox="1142 1048 1342 1115">Two H removed and <math>Z = -1</math></p>
<b>E</b>	 <p data-bbox="464 1339 679 1406">Two H removed and <math>Z = -1</math></p>		

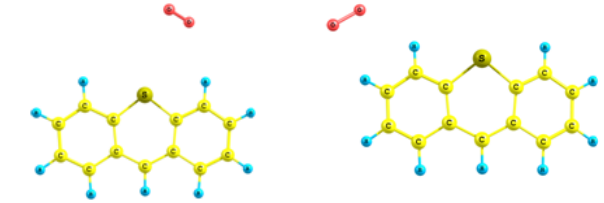
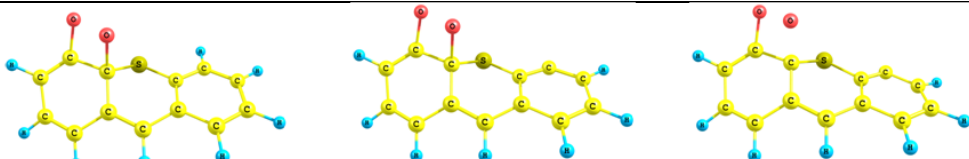
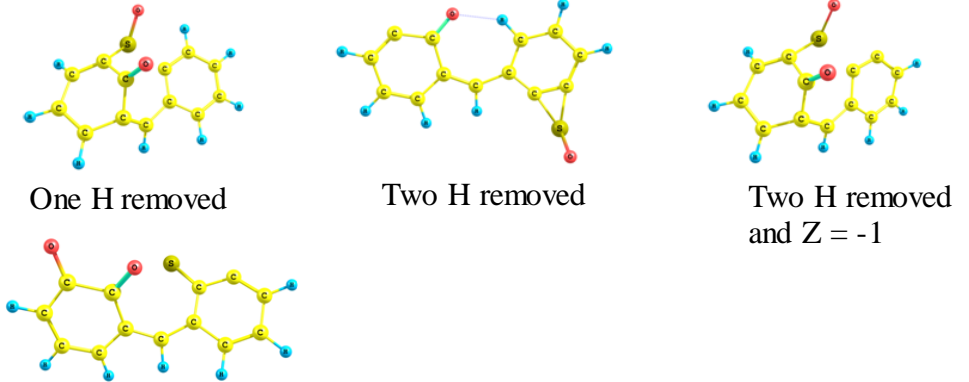
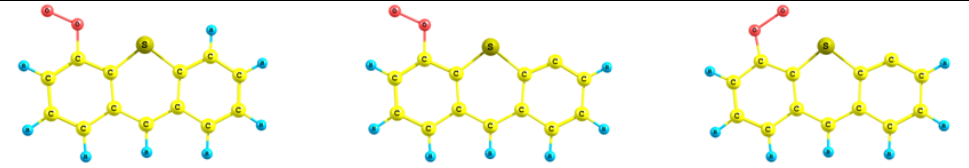
**Table A3** Optimised products of molecular oxygen binding to the Al doped naphthalene-type systems.

Product label	Structures
A	 <p>Fully H terminated</p>
B	 <p>Fully H terminated                      Z = -1</p>
D	 <p>Z = -1              One H removed              Two H removed              Two H removed and Z = -1</p>
C	 <p>One H removed              Two H removed              Two H removed and Z = -1</p>
G	 <p>One H removed              Two H removed and Z = -1</p>
H	 <p>One H removed</p>
E	 <p>Two H removed              Two H removed and Z = -1</p>

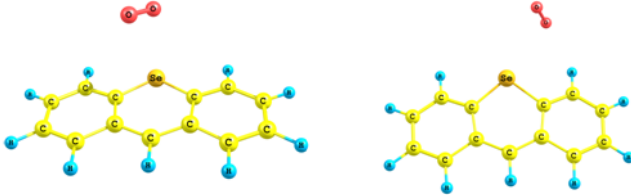
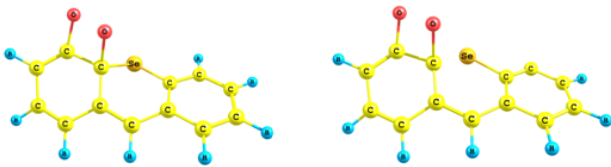
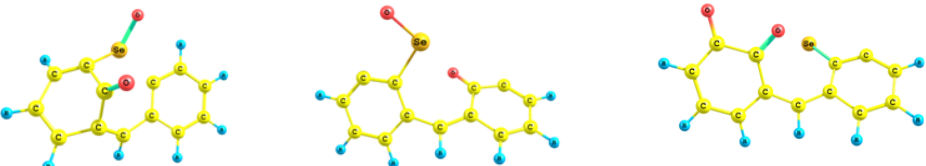
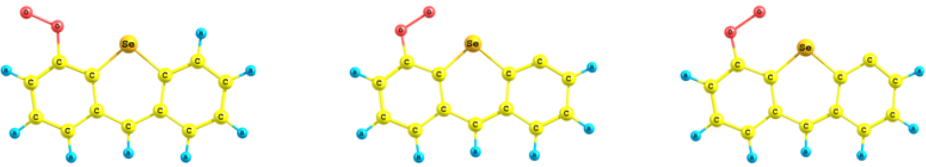
**Table A4** Optimised products of molecular oxygen binding to the Al doped graphene-type systems.

Product label	Structures
<b>D</b>	 <p>Fully H terminated      <math>Z = -1</math>      One H removed</p> <p>Two H removed      Two H removed and <math>Z = -1</math></p>
<b>C</b>	 <p>One H removed</p>
<b>G</b>	 <p>Two H removed and <math>Z = -1</math></p>
<b>E</b>	 <p>Two H removed and <math>Z = -1</math></p>

**Table A5** Optimised products of molecular oxygen binding to the S doped anthracene-type systems.

Product label	Structures		
A	 <p>Fully H terminated <span style="margin-left: 200px;">Z = -1</span></p>		
D	 <p>One H removed <span style="margin-left: 100px;">Two H removed</span> <span style="margin-left: 100px;">Two H removed and Z = -1</span></p>		
I	 <p>One H removed <span style="margin-left: 100px;">Two H removed</span> <span style="margin-left: 100px;">Two H removed and Z = -1</span></p> <p>Two H removed and Z = -1</p>		
C	 <p>One H removed <span style="margin-left: 100px;">Two H removed</span> <span style="margin-left: 100px;">Two H removed and Z = -1</span></p>		

**Table A6** Optimised products of molecular oxygen binding to the Se doped anthracene-type systems.

Product label	Structures		
A	 <p>Fully H terminated                      Z = -1</p>		
D	 <p>One H removed                      Two H removed and Z = -1</p>		
I	 <p>One H removed                      Two H removed                      Two H removed and Z = -1</p>		
C	 <p>One H removed                      Two H removed                      Two H removed and Z = -1</p>		

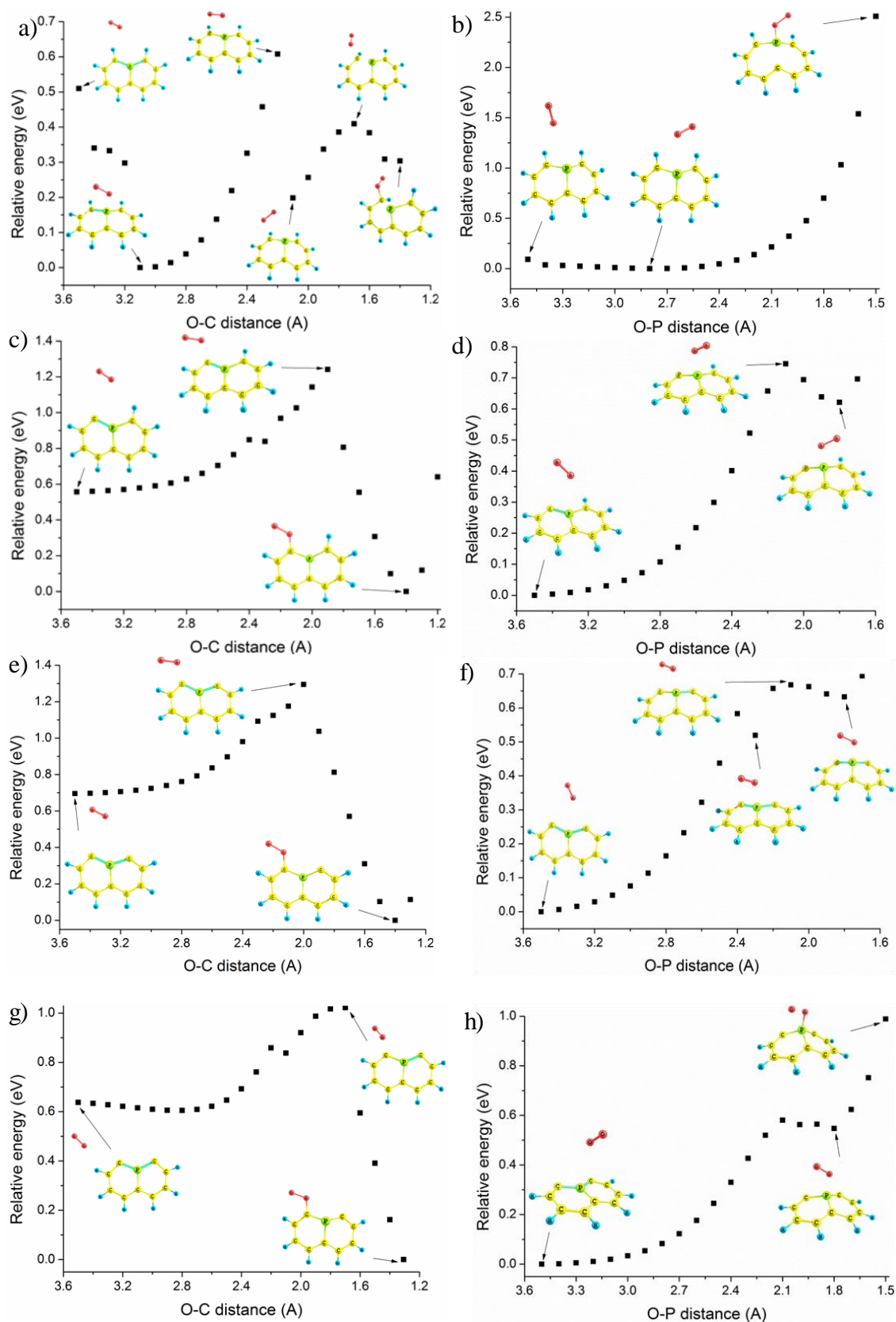


**Figure A1** Potential energy profiles of molecular oxygen binding to the modifications of the P doped naphthalene-type systems with a), b) a (-1) charge, c), d) one H removed, e), f) two H removed, and g), h) two H removed and a (-1) charge. The C, P, O and H atoms are designated by the yellow, green, red and cyan colours, respectively.

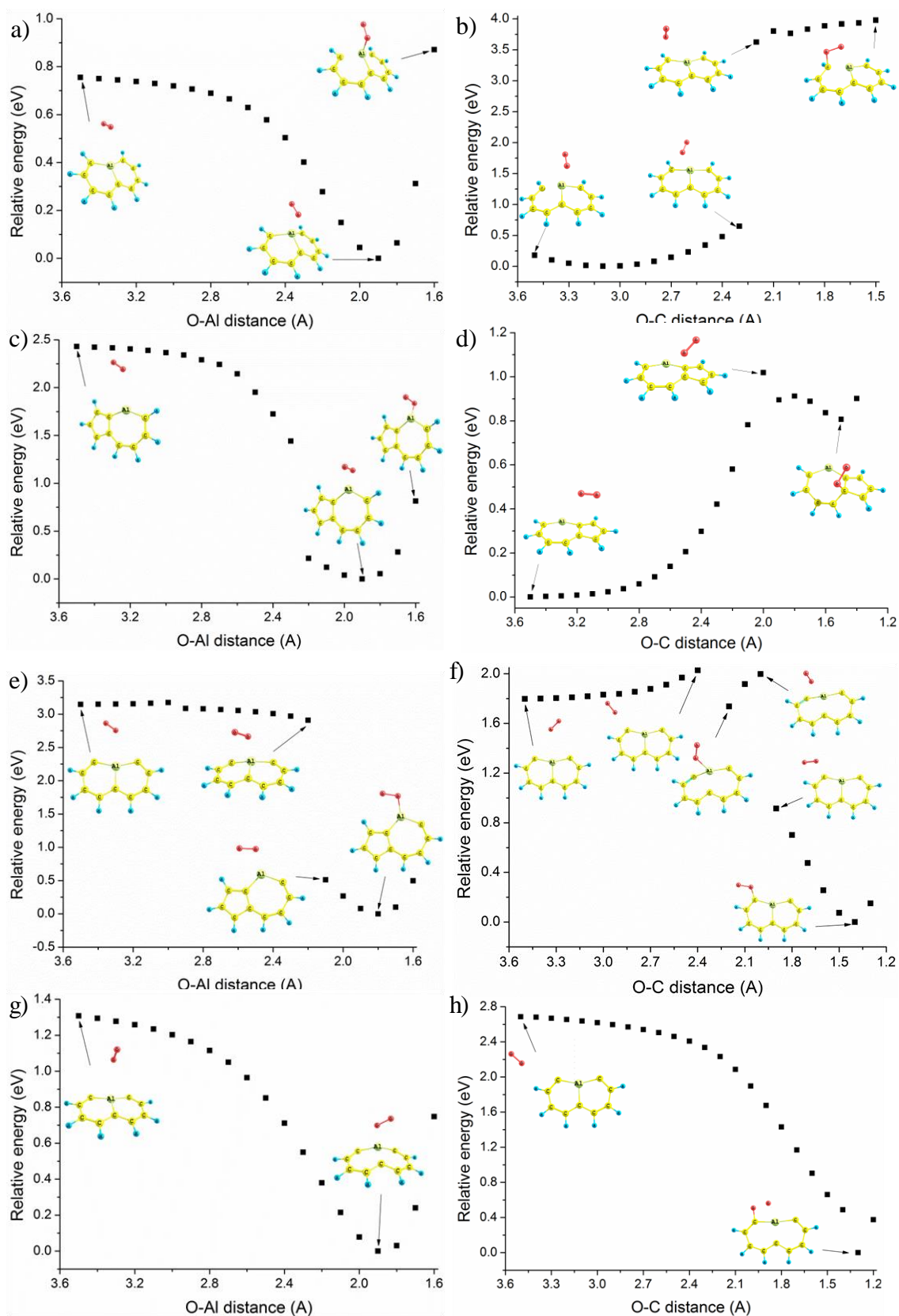


**Figure A2** Potential energy profiles of molecular oxygen binding to the modifications of the Al doped naphthalene-type systems with a), b) (-1) charge, c), d) one H removed, e), f) two H removed, g), h) two H removed and a (-1) charge. The C, Al, O and H atoms are designated by the yellow, pale-green, red and cyan colours, respectively.

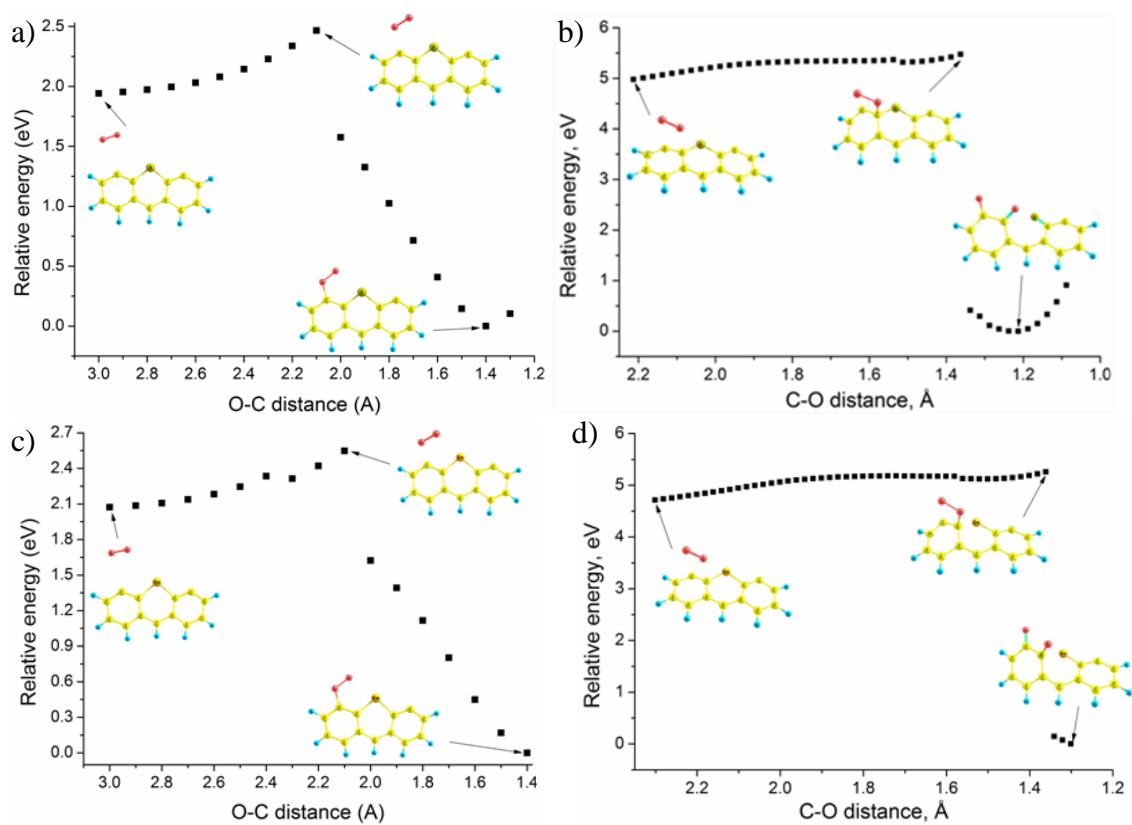


**Figure A3** Potential energy profiles of molecular oxygen binding to a), b) S doped, and c), d) Se doped anthracene-type systems in the end-on mode and with disruption of the heterocycle ring. The C, S, Se, O and H atoms are designated by the yellow, olive, orange, red and cyan colours, respectively.